DOE/ET/27002-8

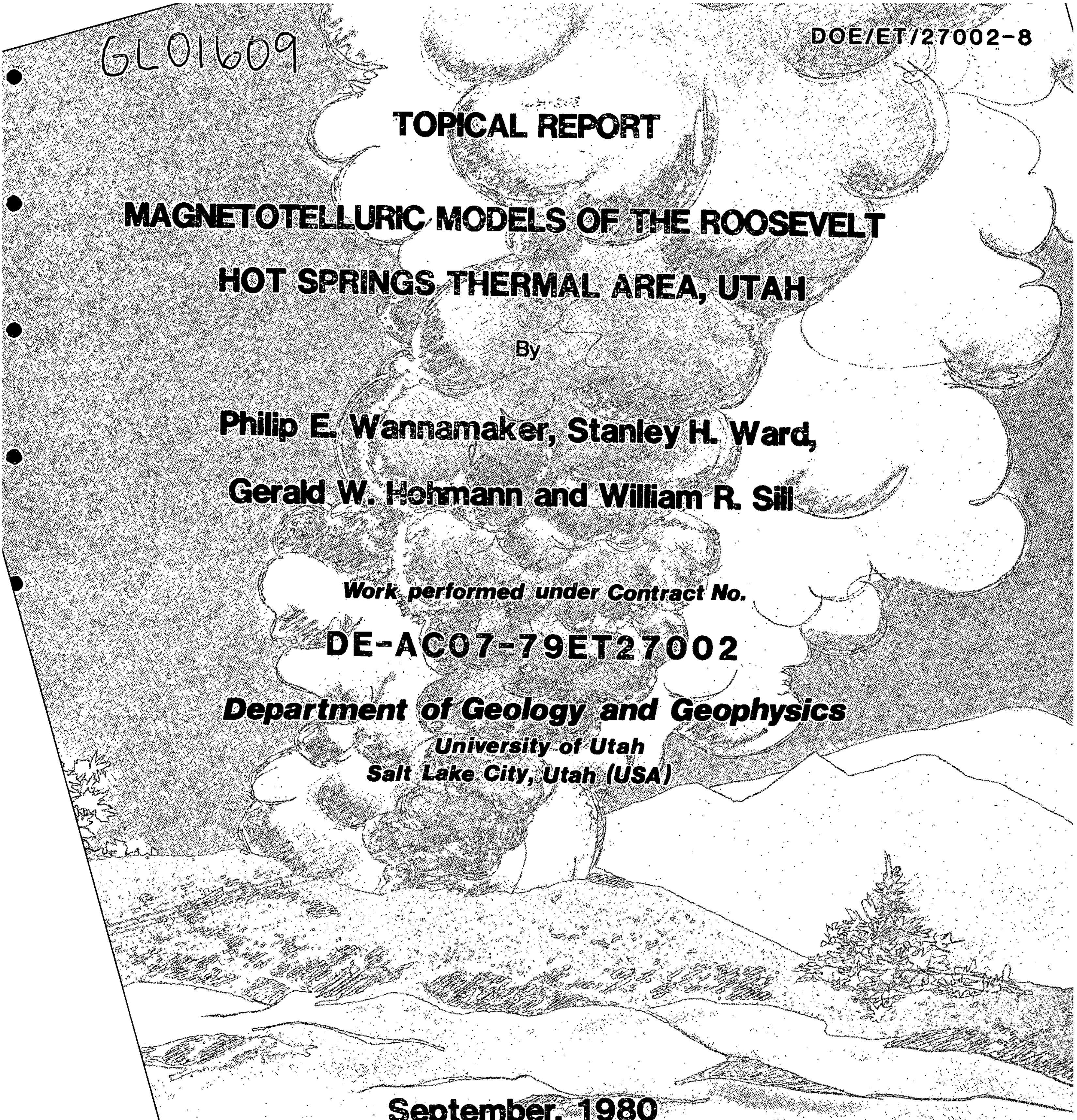

TOPICAL REPORT

MAGNETOTELLURIC MODELS OF THE ROOSEVELT HOT SPRINGS THERMAL AREA, UTAH

By

Philip E. Wannamaker, Stanley H. Ward,
Gerald W. Hohmann and William R. Sill

Work performed under Contract No.

DE-AC07-79ET27002

Department of Geology and Geophysics
University of Utah
Salt Lake City, Utah (USA)

September, 1980

Prepared for
DEPARTMENT OF ENERGY
Division of Geothermal Energy

DOE/ET/27002-8

MAGNETOTELLURIC MODELS OF THE ROOSEVELT HOT SPRINGS THERMAL AREA, UTAH

by

Philip E. Wannamaker, Stanley H. Ward,
Gerald W. Hohmann and William R. Sill

September, 1980

PREPARED FOR THE
U.S. DEPARTMENT OF ENERGY
ASSISTANT SECRETARY FOR ENERGY TECHNOLOGY
DIVISION OF GEOTHERMAL ENERGY

UNDER CONTRACT NO. DE-AC07-79ET27002

NOTICE

This report was prepared to document work sponsored by the United States Government. Neither the United States nor its agent, the United States Department of Energy, nor any Federal employees, nor any of their contractors, subcontractors or their employees, makes any warranty, express or implied, or assumes any legal liability or responsibility for the accuracy, completeness, or usefulness of any information, apparatus, product or process disclosed, or represents that its use would not infringe privately owned rights.

NOTICE

Reference to a company or product name does not imply approval or recommendation of the product by the University of Utah or the U.S. Department of Energy to the exclusion of others that may be suitable.

TABLE OF CONTENTS

ABSTRACT

The Roosevelt Hot Springs (RHS) thermal area, which includes a hot-water-dominated fracture zone prospect, near the eastern margin of the Basin-Range tectonic province, conceivably possesses a whole family of resistivity structures that includes the following: deep hot brine reservoirs, deep-seated partially molten heat sources in the crust or upper mantle that drive the convective system, near-surface hydrothermal alteration zones, wet sedimentary fill in valleys, and a regional, apparently one-dimensional resistivity profile of the crust and upper mantle. This complex resistivity makeup, particular to RHS but probably similar to that at other geothermal areas in the Great Basin, must be treated as being fully three-dimensional (3-D). In an attempt to understand these structures, we have obtained broadband (10^{-3} to 10^{2} Hz) tensor magnetotelluric (MT) data including apparent resistivities (ρ_a), impedance phases (ϕ) and vertical magnetic field transfer functions for 93 sites in the vicinity of this resource area.

The preservation of normal current density combined with the finite lateral extent of 3-D bodies results in discontinuities in electric field regardless of polarization or frequency of incident field. Such effects are referred to as polarization charge or current-gathering phenomena. Distortions in any apparent resistivity or vertical admittance element magnitudes around a 3-D body will approach a non-zero, essentially frequency independent function below some low-frequency limit. This is not so for tipper element magnitudes as well, generally, as anomalies in phases of all MT functions, which

diminish below this limit. Furthermore, small-scale geologic noise may cause anomalies in apparent resistivity, tipper element magnitudes and the phases of all functions as pronounced as those of large bodies, though the spatial extent of the former will be relatively confined. We emphasize that ρ_a soundings near such noise may be distorted sufficiently so that 1-D and 2-D transverse electric (TE) interpretations aimed at describing a deeper feature of interest may be subject to serious errors. However when comparing the responses of large and small structures, the frequency ranges over which their respective anomalies in any MT quantity occur are separated roughly according to the square of the scale change between the structures. This may hence encourage use of tipper element magnitudes and the phases of all MT quantities in order to observe more directly the presence of larger structure buried beneath small-scale geologic noise.

An integral equation numerical simulation of variable hydrothermal alteration and valley sedimentary fill by conducting prisms in a conducting half-space shows that, at relatively high frequencies, rather complicated signatures result relating to an outwardly propagating secondary wavefront. Below our defined low frequency limit, the MT quantities are to first order those of a static electric dipole in the earth. For variable hydrothermal alteration and other geologic noise, this limit is met below about 1 Hz. The distortion in low frequency apparent resistivities over representative 3-D geological noise may approach two orders of magnitude and as such would have a very deleterious effect upon the results of 1-D or 2-D TE interpretation.

Current-gathering in the valley is reflected in a regional distortion of the electric field affecting all stations at RHS to arbitrarily low frequencies. MT quantities around valley sedimentary fill reach their low frequency limit at about 0.01 Hz. The valley induces a large ρ_a anisotropy near its edge where the bulk of the soundings at RHS are located. The anisotropy does not vanish as frequency diminishes; both principal apparent resistivities are nearly equidistant from the background apparent resistivity of the 1-D host. This strong anisotropy, along with the distorting effects of small-scale geologic noise, invalidates 1-D interpretation at RHS. In terms of active convective hydrothermal systems, polarization charges in and around the near-surface conductivity structure within a thermal area created by the upward convection of hot brines with attendant hydrothermal alteration of rocks and alluvium may themselves be the cause of an apparent but false deep conductor beneath the system, suggestive of a partially molten heat source, if ρ_a soundings within this shallow structure are interpreted with a 1-D inverse algorithm.

Model studies have also pointed out severe limitations to the application of 2-D TE algorithms even for evaluating valley sediments. Corresponding 3-D and 2-D TE apparent resistivity and impedance phase signatures depart significantly below about 0.3 Hz. However, for centrally located profiles across geometricaly regular 3-D prisms, the principal quantities ρ_{yx} and ϕ_{yx}, where x is the direction normal to the profiles, may be interpreted successfully using a 2-D transverse magnetic (TM) algorithm. A variety of MT strike estimators may be used to select which data may be treated as the transverse magnetic mode.

For interpreting deeper, larger structure in the face of geologic noise, we favor an estimator based upon maximizing the magnitude of tipper element K_{zy}. If reliable tipper element estimates are not available, rotation of co-ordinate axes to a uniform direction compatible with regional geologic trends should give roughly equivalent results.

Based upon the insight derived from the 3-D model studies, we have modeled two, east-west profiles of soundings across the eastern edge of the Milford Valley with a 2-D TM finite element algorithm. The first profile, some 6 km north of the hot springs, provides mainly information on the valley sediments and the regional resistivity profile. The stations of the second profile directly over the hot springs concentrate on structure beneath the thermal anomaly such as the brine reservoir or deep heat source. Generally excellent fits of computed results to observed data along with detailed but overall well-resolved geoelectric cross sections have been obtained. Very conductive sediments ($\rho = 1.1$ Ω-m), probably mostly Quaternary Lake Bonneville clays, appear in the Milford Valley to a depth approaching 700 m. Below this, great thicknesses (>1 km) of modest resistivity material ($\rho = 25$ Ω-m), possibly Tertiary semiconsolidated sediments, are believed to exist, although resolution of this feature is not good.

In the upper 300 m of the finite element cross-section beneath the hot springs, the resistivity sequence progresses downward from 50 Ω-m material of 100 m maximum thickness through more conductive units (2 to 6 Ω-m) into a resistive medium of 450 Ω-m, a sequence comparing favorably to that determined by DC resistivity and controlled-source audiomagnetotelluric surveys. Below this at a depth of 400 m, a deeply extending (2 km), highly resistive (50,000 Ω-m) prism was included in the section in an attempt to fit the data below 10 Hz directly over the thermal anomaly. A significant lack of fit to the measurements remains so that we are not convinced that such a highly resistive structure exists. Sensitivity tests of the data suggest that a geometrically regular reservoir of conductive brine beneath the thermal anomaly is quite unlikely so that our search for any economic thermal reservoir at RHS must be considered unsuccessful at this point. No lateral resistivity anomalies below 3 km affect that mode of data identified as TM at RHS. Hence, our search for any deep heat source must also be considered unsuccessful to this time. If a structure of high resistivity contrast representing such a source exists beneath the hot springs, its east-west extent is too narrow to be resolved by the TM algorithm. A future, fully 3-D evaluation utilizing all measured ρ_a's and ϕ's along with vertical magnetic field functions will be attempted to assess both any deep heat source and any economic thermal reservoir.

We have, however, succeeded in estimating the apparently 1-D regional resistivity profile to depths in excess of 100 km. Considering the total profile, we observe a rise in resistivity from a few hundred Ω-m to about 3000 Ω-m as we leave the surface to a depth of 11 km. Subsequently, the resistivity falls, probably in a smooth manner, to some 200 Ω-m at 35 km. Encountered next is an abrupt drop to 20 Ω-m material, which remains seemingly uniform to a depth of 65 km, where an equally abrupt rise to 200 Ω-m introduces an apparently basal half-space. Sensitivity computations indicate that this deep conductive layer exists and its estimated depth to top is accurate to <10 km. We presently endorse the following physical model. The conduction mechanism of the upper 15 km of crust in the region is dominantly electrolytic conduction in aqueous pore and fracture fluids. Increasing pressure and temperature with depth causes solid-state crustal mineral semiconduction to be henceforth most important leading to rather uniform decrease in resistivity to 35 km. The 20 Ω-m layer isolated from 35 to 65 km in the upper mantle is of particular interest. Presuming a mantle of uniform composition and downward increasing temperature, an order-of-magnitude rise to 200 Ω-m at 65 km cannot be explained by considering only solid state semiconduction. We thus propose electrolytic conduction in an interconnected partial melt layer of low melt fraction (∿2%) to represent the medium from 35 to 65 km. This layer may be a manifestation of a N-S trending reservoir of basaltic liquid in the upper mantle of the eastern Great Basin supplying the repeated volcanism here for the past 10 m.y. Semiconduction is favored though as the most important mechanism for the lowermost medium of 200 Ω-m. Possible high lateral resistivity contrasts, such as may be associated with the Basin-Range to Colorado Plateau lithosphere transition about 100 km to the east, do not appear to have a measureable effect on our observations at RHS. However, this transition as well as other characteristics of the tectonics and physical state of the Great Basin interior, its eastern margin and the Colorado Plateau itself should be accurately determined by a series of MT measurements along an ESE trend from central Nevada to the Four Corners area.

ACKNOWLEDGMENTS

We would like to express our appreciation to several people who contributed substantially to this work. In particular, the discussions and reviews of Drs. J. R. Bowman, D. S. Chapman, S. H. Evans, Jr., W. P. Nash and W. T. Parry were invaluable. Also, one of the authors (P.E.W.) wishes to thank S. C. Ting, T. J. Killpack and C. Nutter for instruction in use of the 3-D modeling algorithm and its adaptation to the Prime 400 minicomputer. The manuscript was typed patiently and competently by Lori Icke and Nancy Stroud. A clear drafting of often difficult figures was accomplished by Sandra Bromley, William Holmes, Tawny Isakson and Paul Onstott.

Research on electrical methods applied to geothermal exploration has been conducted under the following grants and contracts:

NSF	AER-74-01043-A01
	AER-76-11155-A
DOE	DE-AC07-78ET28392
	DE-AC07-79ET27002
	EY-76-S-07-1601

Data used in this report relates to all mentioned contracts and grants. This report is submitted here as a deliverable under DE-AC07-79ET27002, but acknowledgment of funding assistance to all other contracts is hereby made.

LIST OF FIGURES

INTRODUCTION

There is keen interest in geophysical methods that can describe possible resistivity structure associated with geothermal prospects in the Basin-Range tectonic province of the western United States. The Roosevelt Hot Springs (RHS) thermal area, which includes a hot water-dominated fracture zone prospect, conceivably possesses a whole family of resistivity structures (Ward and Sill, 1976; Ward et al, 1978). Family members may include the following: deep hot brine reservoirs, deep-seated partially molten heat sources in the crust or upper mantle that drive the convective system, near-surface hydrothermal alteration zones, wet sedimentary fill in valleys, and a regional, apparently one-dimensional resistivity profile of the crust and upper mantle.

A wide range of intrinsic resistivities and characteristic lengths is represented by this group. With the exception of the regional profile, all the above features may have resistivities as low as a few Ω-m due to electrolytic conduction in aqueous or magmatic pore fluids and along mineral surfaces. The resistivities of the regional profile, determined by electrolytic conduction in pore fluids and solid-state semiconduction in minerals, may be as high as thousands of Ω-m or as low as tens of Ω-m (Brace, 1971; this report). The upper few kilometers of this regional layering, usually possessing values of a few hundred Ω-m or more, constitutes a host for most of the other features resulting in an overall assemblage of high resistivity contrast. Characteristic dimensions of hydrothermal alteration zones at RHS are a few hundred meters to a couple of kilometers while those of any deep brine reservoir may be a few to several kilometers. On the other hand, dimensions of a postulated deep-seated heat source, valley sediments or regional profile might be tens of kilometers. While there may be some preferred orientation of resistivity boundaries paralleling major N-S trending block faulting (Stewart, 1978), strike lengths of the conductive bodies of interest are comparable in magnitude to their widths.

Magnetotelluric (MT) measurements are affected by the resistivity makeup of the subsurface, potentially to depths of hundreds of kilometers (Swift, 1967; Word et al, 1971; Vozoff, 1972; Larsen, 1975; Jupp and Vozoff, 1976). During a three-year period extending from 1976 to 1978, 93 tensor MT soundings were monitored in the central Mineral Mountains and Milford Valley in the vicinity of RHS (see Figure 1). The data collection and processing were performed by Geotronics Corp. of Austin, Texas, the University of Texas at Austin and Lawrence Berkeley Laboratories of the University of California at Berkeley. Tensor apparent resistivities (ρ_a), impedance phases (ϕ) and the vertical magnetic field transfer functions and strike estimators were provided over a frequency range of 10^{-3} to 10^{2} Hz.

The interpretation of magnetotellurics most commonly involves the inversion of observed apparent resistivity and phase results for each sounding to obtain a one-dimensional (1-D) resistivity distribution, i.e. a distribution that is horizontally isotropic (e.g. Vozoff, 1972; Petrick et al, 1977;, Stanley et al, 1977). Observed vertical magnetic fields, apparent resistivity anisotropy, and site-to-site variations in

Figure 1. Magnetotelluric site location map for the Mineral Mountains-Roosevelt Hot Springs study. Outcrop pattern of sedimentary, igneous and metamorphic rocks bounding the Milford Valley sediments is lightly stippled while the solid contour is the 400 mWm^{-2} thermal contour. Station numbers referred to in the text have been prefixed according to the year in which they were occupied, except for the Berkeley sites which are prefixed by a B.

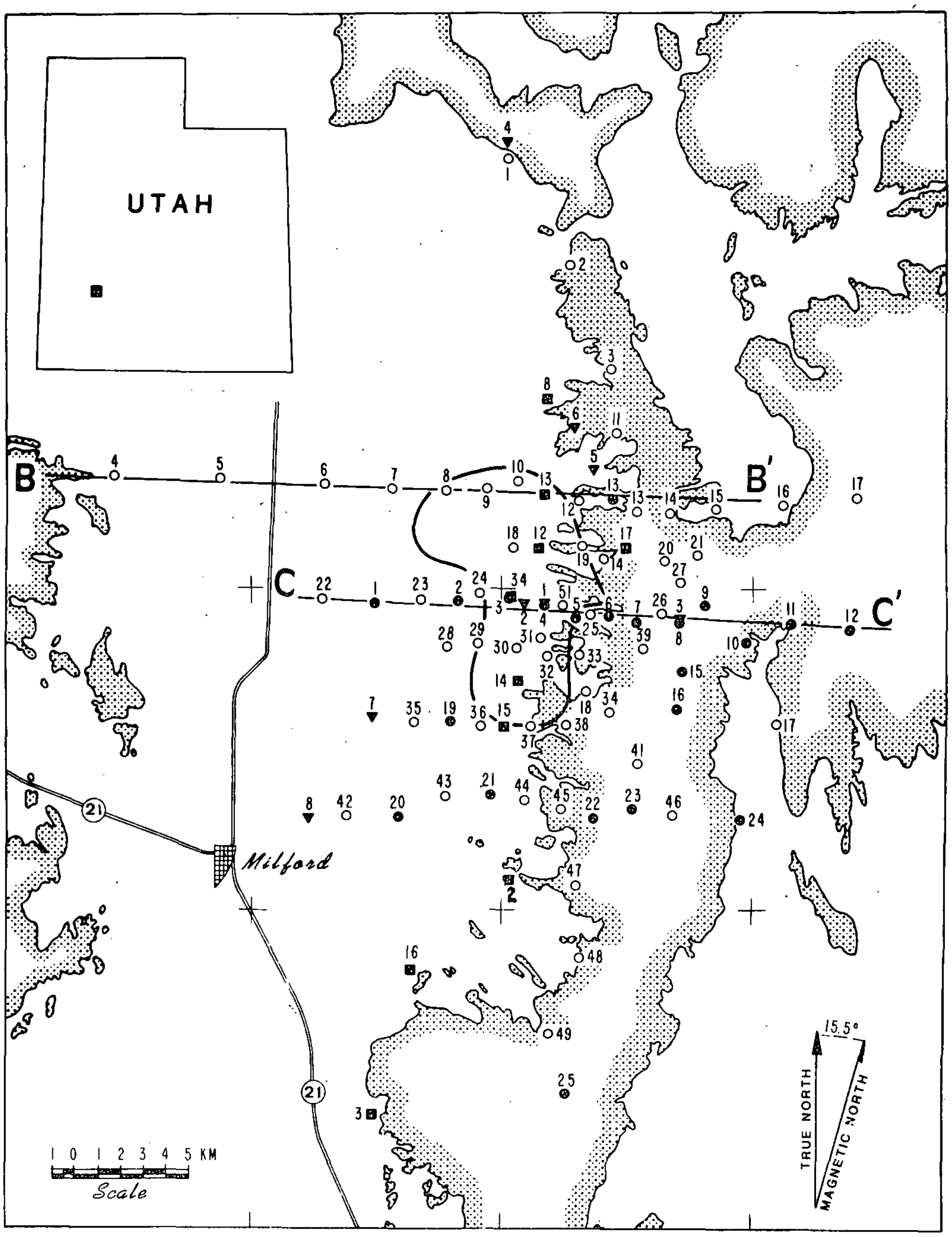

● GEOTRONICS CORP. (1976)

○ GEOTRONICS CORP. (1978)

■ UNIV. OF TEXAS AT AUSTIN (1977)

▼ UNIV. OF CALIFORNIA AT BERKELEY (1979)

MT./AMT. STATIONS
ROOSEVELT HOT SPRINGS KGRA, UTAH

tensor quantities and their principal axes are indications that this 1-D model is incorrect. When such indications occur, that mode of the ρ_a and ϕ data identified as transverse electric (TE) is generally subjected to such a 1-D evaluation. This is because small-scale near-surface resistivity variations from a horizontally isotropic earth can be shown not to distort this mode of MT observations to arbitrarily low frequencies, provided such variations are purely two-dimensional (2-D) with uniform strike directions. For the strictly 1-D approach, the remaining results, including the transverse magnetic (TM) ρ_a's and ϕ's, more often undergo just a qualitative evaluation. The application of 2-D modeling algorithms to measured quantities can yield a better approximation to natural resistivity composition, although substantial computing facilities are required to handle complicated geoelectric cross-sections. Both TE and TM quantities may be interpreted (for example, Kurtz and Garland, 1976; Rooney and Hutton, 1977). However, under the 2-D assumption, the TE mode is preferred for the same reason that applied in the 1-D case.

There are two major reasons why 1-D and 2-D approaches are employed for data that are, strictly speaking, responses to 3-D resistivity geometry. First, 3-D modeling algorithms require enormous computing resources to accommodate a complex resistivity environment, resources not readily available. The second reason, related in part to the first, is that there is a lack of concensus concerning the errors in interpretation which take place when simpler 1-D and 2-D schemes are used to approximate a three-dimensional assembly. When one deals with relatively uncomplicated geometries, for instance undisturbed sedimentary basins, these errors may be not be serious. However, there was described in the opening two paragraphs of this introduction an ensemble of geoelectric structures of high resistivity contrast and limited strike extent, specific to RHS but probably conceptually similar to that at other geothermal areas in the Great Basin, that is due to a series of severe tectonic disturbances. One should not be surprised if attempts to gain satisfactory data fits and reasonable geoelectric sections by using 1-D and 2-D TE approaches fail at RHS, and such has been our experience (Wannamaker, 1978).

Our difficulties with these simpler interpretation schemes have forced us to treat the Roosevelt Hot Springs area as being fully three-dimensional in its resistivity makeup. The proposed brine reservoir and deep-seated heat source are the primary targets of this electromagnetic investigation. However, the alteration zones, valley sediments and regional layering, though considered to be secondary features, may determine the major characteristics of the total magnetotelluric response. An understanding of these secondary structures is necessary before an evaluation of the principal targets is possible. A hydrothermal alteration zone, a body of characteristic dimensions comparable to or smaller than the average MT station spacing, and the Milford Valley sedimentary fill, a body of characteristic dimensions much larger than the average station spacing, have been simulated numerically using conductive rectangular prisms in a conductive half-space host. Theoretical considerations and computed multifrequency responses provide basic insight into the behavior of MT quantities around these 3-D bodies as well as pointing out the limited applicability of 1-D and 2-D modeling algorithms to three-dimensional observations.

One important result of these calculations is the demonstration that profiles of stations across geometrically regular 3-D prisms may be modeled successfully with a 2-D TM program. Using observed ρ_a and data, identified as the transverse magnetic mode and where co-ordinate axes lie in a uniform direction, such a restricted 2-D modeling approach has been used to interpret realistic geoelectric sections for two profiles at RHS. Published laboratory determinations of the electrical properties of fluids and minerals as a function of temperature and pressure in conjunction with recent estimations of the regional 1-D temperature distribution of the Basin and Range crust are compared to our interpreted geoelectric sections. With this comparison, we establish some limits to the material properties and geometry of any possible brine reservoir or deep-seated heat source as well as the regional resistivity layering in this area. While our interpretation is incomplete, the studies to this point have yielded much useful information about this geothermal prospect and provide direction for future work on MT observations in this environment and others within the Basin-Range province.

MAGNETOTELLURIC THEORY FOR THREE-DIMENSIONAL (3-D) BODIES IN A LAYERED CONDUCTING EARTH

The three-dimensionality of a conductive body in the earth may have a profound effect upon its magnetotelluric response. Finite horizontal extent in any direction requires that the total electric field exhibit discontinuities at some resistivity boundaries regardless of polarization or frequency of incident fields in order to preserve total normal current density. Associated with these discontinuities are boundary distributions of free charge. The secondary electromagnetic (EM) fields scattered by a 3-D inhomogeneity are hence due to both anomalous volume currents and surface charges. Especially at lower frequencies, the charge distribution is roughly dipolar[1]. The effect of such a charge buildup on the ends of an inhomogeneity is to reduce the total electric field within the body from the incident field, $\vec{E}_i$. On the other hand, the total electric field outside the ends is enhanced. This process has given rise to the popular concept of "current-gathering" or "current-channeling". The magnified electric field outside the ends of the body results in a commensurate increase in current density.

---

[1] Stratton (1941, p 563-573) discusses EM field distribution for a classical geometry in his section 'Diffraction of a Plane Wave by a Sphere'. See also his presentation 'A Multipole Expansion' (p 431-434).

Some consequences of current-gathering upon active-source measurements over 3-D conductors have been pointed out by Lajoie and West (1975) and Hohmann (1975). Current-gathering effects in magnetotelluric observations have also been recognized in the literature. Porath (1971a), in a review of deep crustal sounding research, warned that current-channeling in sedimentary basins may detrimentally influence attempts to sound the electrical properties of the deep crust and upper mantle. Frequency (f) independent distortion of electric field in observed MT soundings due to small-scale, near-surface inhomogeneities were observed by Kemmerle (1977). These distortions tended to bias adjacent ρ_a vs f curves upwards or downwards with respect to one another while leaving the phase estimates (ϕ vs f) relatively intact. Berdichevskiy and Dmitriev (1976) concluded that current-channeling is generated by excess charges, does not vanish as frequency decreases, and that false conductors and false basement relief may result. These phenomena are apparent in soundings at RHS as will be presented in subsequent model results and field data.

Electromagnetic Field Relations

We elaborate next upon the characteristics of the EM fields scattered by an arbitrary three-dimensional conductor in a layered conducting earth. By considering the differential equations governing the fields everywhere along with tensor relations between secondary and incident fields, the role of boundary charge and volume current distributions is demonstrated in determining EM responses for general geoelectric structures.

Governing Differential Equations: In Figure 2, a 3-D body is excited by an incident, uniform, vertically propagating EM plane wave, which is the conventional MT source. An exp($i\omega t$) time dependence is assumed. The body has an admittivity (Harrington, 1961) $\hat{y}_b = \sigma_b + i\omega\varepsilon$ and is situated within the jth layer of an n-layered conducting earth with $\hat{y}_j = \sigma_j + i\omega\varepsilon$. We regard the dielectric permittivity, ε, as constant in the earth. The concept of admittivity relates total current density, $\vec{J}_t = \vec{J}_c + \vec{J}_d$, to total electric field $\vec{E}_t$ at any point by combining conduction current density, $\vec{J}_c = \sigma\vec{E}_t$, and displacement current density, $\vec{J}_d = i\omega\varepsilon E_t$. It will be convenient to divide the total electric and magnetic fields ($\vec{E}_t$, $\vec{H}_t$) around the 3-D conductor into an incident set ($\vec{E}_i$,$\vec{H}_i$) and a secondary set ($\vec{E}_s$, $\vec{H}_s$). The former pertains to upward and downward propagating plane waves which would exist in the layered host in the absence of the body while the latter concerns secondary fields scattered by the inhomogeneity (Harrington, 1961, p 126). In the manner of Lorrain and Corson (1970, p 448), it may be shown straightforwardly that the incident and secondary fields in any layer m obey the wave equations

$$(\bar{\nabla}^2 + k_m^2)\vec{E}_i = 0 \qquad , \qquad (1a)$$

$$(\bar{\nabla}^2 + k_m^2)\vec{H}_i = 0 \qquad , \qquad (1b)$$

$$(\bar{\nabla}^2 + k_m^2)\vec{E}_s = 0 \qquad m \neq j \; , \qquad (2a)$$

$$(\bar{\nabla}^2 + k_m^2)\vec{H}_s = 0 \qquad m \neq j \; , \qquad (2b)$$

$$(\bar{\nabla}^2 + k_j^2)\vec{E}_s = \frac{1}{\varepsilon}\,\bar{\nabla}\rho + \hat{z}\vec{J}_s \qquad (3a)$$

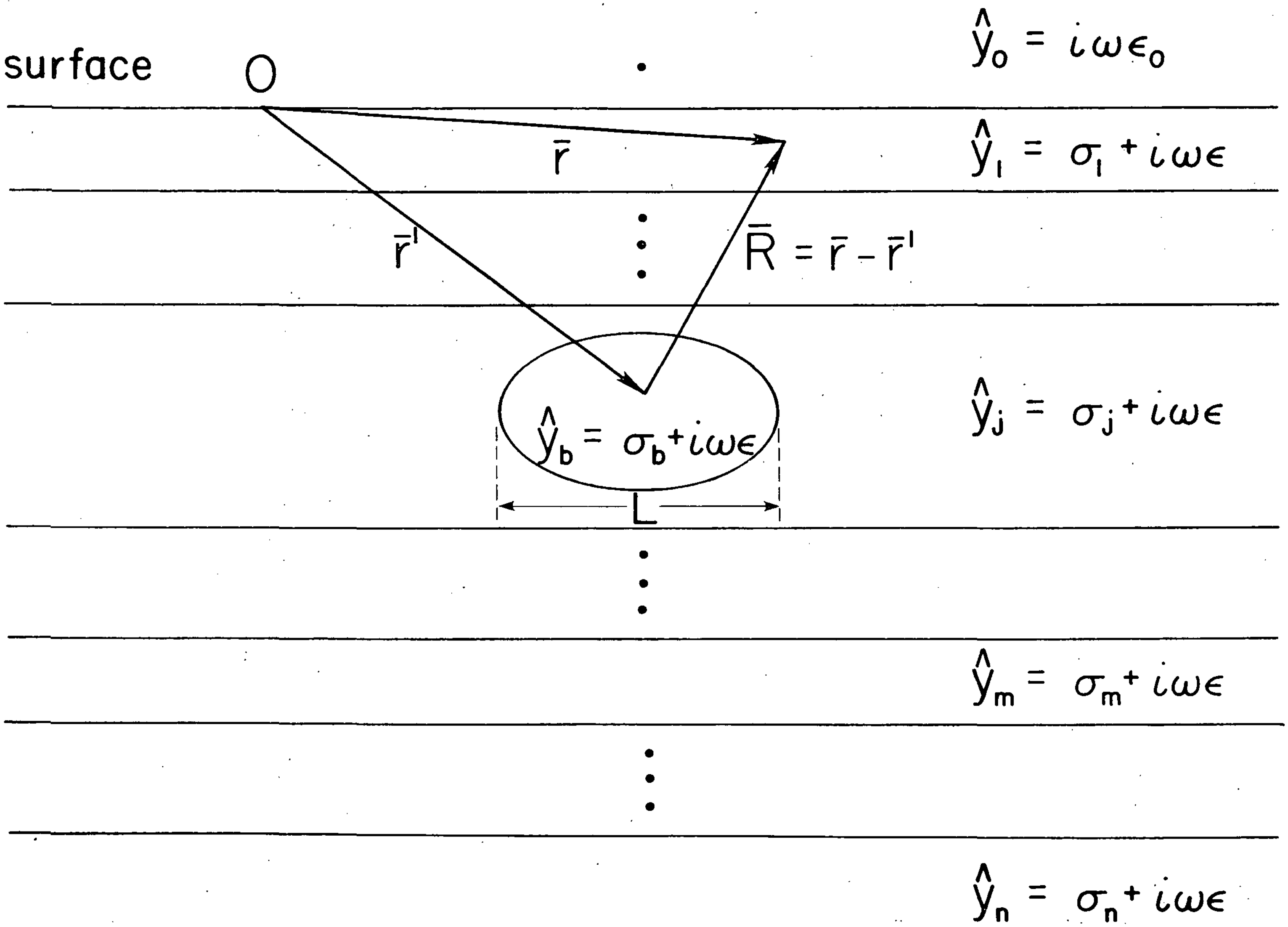

Figure 2. Schematic three-dimensional inhomogeneity in a conductive layered earth. L is any characteristic dimension of the inhomogeneity while $\bar{R} = \bar{r} - \bar{r}'$ is the observation vector from any point in the body to a point on the surface or within the earth.

and

$$(\bar{\nabla}^2 + k_j^2)\vec{H}_s = -\bar{\nabla}\times\vec{J}_s \tag{3b}$$

with $k_m = \sqrt{-\hat{z}\hat{y}_m}$ the spatial wavenumber and $\hat{z} = i\omega\mu$ the impedivity. The magnetic susceptibility μ is taken to be μ_0, that of free space, throughout the earth. $\vec{J}_s$ is an equivalent volume scattering current and exists only within the 3-D conductor. It may be considered an impressed source that replaces the inhomogeneity as far as secondary fields are concerned. This scattering current is defined as

$$\vec{J}_s = (\hat{y}_b - \hat{y}_j)\vec{E}_b \quad , \tag{4}$$

where $\vec{E}_b$ is the total electric field within the 3-D body. $\vec{E}_b$ in turn is governed by the wave equation

$$(\bar{\nabla}^2 + k_b^2)\vec{E}_b = 0 \tag{5}$$

which applies only within the inhomogeneity and where $k_b = \sqrt{-\hat{z}\hat{y}_b}$. The quantity ρ in (3a) is a density of free charge appearing over the boundary of the body to effect continuity of total normal current density and discontinuity of total normal electric field. As pointed out by Price (1973), this charge is periodic in time and is supplied by a periodic divergence of the conduction current density, i.e.

$$\bar{\nabla}\cdot\vec{J}_c = -i\omega\rho = -\nabla\cdot\vec{J}_d \quad . \tag{6}$$

Realizing that $\vec{E}_i$ is continuous everywhere and using our definition of $\vec{J}_d$, it follows that the charge is related to discontinuities in secondary electric field by

$$\bar{\nabla}\cdot\vec{E}_s = \rho/\varepsilon \quad . \tag{7}$$

The charge distribution may also be related to our definition of the scattering current density $\vec{J}_s$ by taking the divergence of both sides of equation (3a);

$$\bar{\nabla}\cdot\vec{E}_s = \rho/\varepsilon = \frac{-1}{\hat{y}_j}\,\bar{\nabla}\cdot\vec{J}_s \quad . \tag{8}$$

This allows us to rewrite (3a) as

$$(\bar{\nabla}^2 + k_j^2)\vec{E}_s = (\frac{-1}{\hat{y}_j}\,\bar{\nabla}\bar{\nabla}\cdot + \hat{z})\vec{J}_s \quad . \tag{9}$$

The gist of the development so far is that the secondary electric field in (3a) has two sources, boundary charges and volume currents. Near-field, induction and radiation contributions to the secondary EM fields all must be considered important (Harrington, 1961, p 77-81). The volume current contribution, $\hat{z}\vec{J}_s$, is to first order proportional to frequency and hence will become decreasingly important in determining $\vec{E}_s$ as frequency is lowered. Concerning charges, the divergence of conduction current in (6) is on the order of displacement currents and is very small compared to the magnitude of $\vec{J}_c$. However, the charge distribution, weighted by $1/\varepsilon$ in (3a) strongly affects the electric field and will not vanish as frequency falls.

<u>Tensor Field Relations</u>: The general solution to equations (1) through (3) and (9) for the total electric and magnetic fields at any point in the earth exterior to an inhomogeneity of volume v are

$$\vec{E}_t(\bar{r}) = \vec{E}_i(\bar{r}) + \int_v \tilde{G}_E(\bar{r};\bar{r}')\cdot\vec{J}_s(\bar{r}')dv' \quad . \tag{10a}$$

and

$$\vec{H}_t(\bar{r}) = \vec{H}_i(\bar{r}) + \int_V \tilde{G}_H(\bar{r};\bar{r}')\cdot\vec{J}_s(\bar{r}')dv' \ . \qquad (10b)$$

The quantities $\tilde{G}_E(\bar{r};\bar{r}')$ and $\tilde{G}_H(\bar{r};\bar{r}')$ are tensor Green's functions relating the electric and magnetic fields at $\bar{r}$ in the layered earth due to a scattering current element at $\bar{r}'$ in the 3-D body (ibid.) The elements of these tensors for a current element in a whole-space and a half-space are given by Hohmann (1975). Van Blaedel (1961) has shown that (10a) is valid even within the current volume, so that $\vec{E}_t(\bar{r})$ would in this case be $\vec{E}_b(\bar{r})$. Considering that and the linear equations (4) and (10a) we presume that there exists the linear relation

$$\vec{J}_s(\bar{r}') = \tilde{J}_s^n(\bar{r}')\cdot\vec{E}_i^\circ \qquad (11)$$

with $\tilde{J}_s^n(\bar{r}')$ a 3x2 normalized scattering current tensor and $\vec{E}_i^\circ$ the incident normal electric vector uniform over the earth's surface. Substitution of (11) into (10a) and (10b) gives

$$\vec{E}_t^\circ(\bar{r}) = \vec{E}_i^\circ + \tilde{P}_s^\circ(\bar{r})\cdot\vec{E}_i^\circ \qquad (12a)$$

and

$$\vec{H}_t^\circ(\bar{r}) = \vec{H}_i^\circ + \tilde{Q}_s^\circ(\bar{r})\cdot\vec{E}_i^\circ \qquad (12b)$$

with

$$\tilde{P}_s^\circ(\bar{r}) = \int_V \tilde{G}_E^\circ(\bar{r};\bar{r}')\cdot\tilde{J}_s^n(\bar{r}')dv' \quad . \qquad (13a)$$

and

$$\tilde{Q}_s^\circ(\bar{r}) = \int_V \tilde{G}_H^\circ(\bar{r};\bar{r}')\cdot\tilde{J}_s^n(\bar{r}')dv' \quad . \qquad (13b)$$

The superscript ∘ indicates that we are now concerned with the observation vector $\bar{r}$ at the surface of the earth. $\tilde{P}_s^\circ(\bar{r})$ and $\tilde{Q}_s^\circ(\bar{r})$ are

3x2 normalized scattered field tensors which are unique for a specified conductivity anomaly, a specified layered host and a specified frequency. Their forms are

$$\tilde{P}_s^\circ(\bar{r}) = \left[\begin{array}{c} \tilde{P}_h^\circ(\bar{r}) \\ \hline \tilde{P}_v^\circ(\bar{r}) \end{array}\right] = \left[\begin{array}{cc} P_{xx}^\circ & P_{yy}^\circ \\ P_{yx}^\circ & P_{yy}^\circ \\ \hline P_{zx}^\circ & P_{zy}^\circ \end{array}\right] \tag{14a}$$

and

$$\tilde{Q}_s(\bar{r}) = \left[\begin{array}{c} Q_h^\circ(\bar{r}) \\ \hline \tilde{Q}_v^\circ(\bar{r}) \end{array}\right] = \left[\begin{array}{cc} Q_{xx}^\circ & Q_{xy}^\circ \\ Q_{yx}^\circ & Q_{yy}^\circ \\ \hline Q_{zx}^\circ & Q_{zy}^\circ \end{array}\right] \tag{14b}$$

E- and H-field tensor approaches have also been considered by Larsen (1975; 1977). The apparent impedance of the host medium (Ward, 1967, p 117-124) may be used to relate the primary electric and magnetic fields at the earth's surface through

$$\vec{E}_i^\circ = \tilde{Z}_\ell \cdot \vec{H}_i^\circ \tag{15}$$

in which

$$\tilde{Z} = \begin{bmatrix} 0 & Z_\ell \\ -Z_\ell & 0 \end{bmatrix} \tag{16}$$

The total horizontal observed fields become

$$\vec{E}_t^{\circ}(\bar{r}) = [\tilde{I} + \tilde{P}_h^{\circ}(\bar{r})]\cdot\vec{E}_i^{\circ} \qquad (17a)$$

and

$$\vec{H}_t^{\circ}(\bar{r}) = [\tilde{I} + \tilde{Q}_h^{\circ}(\bar{r})\cdot\tilde{Z}_\ell]\cdot\vec{H}_i^{\circ} \qquad (17b)$$

where $\tilde{I}$ is the 2x2 identity tensor.

Low Frequency Conditions: It is illuminating to study field behavior as frequency decreases. Suppose that the frequency is sufficiently low so that the observation distance from the inhomogeneity, $\bar{R} = \bar{r}-\bar{r}'$ in Figure 2, is insignificant compared to a wave-length in any layer m of the host medium, i.e., $|k_m\bar{R}| \ll 1$ for such m. This is the near-field or quasistationary condition. The previous wave equations become

$$\bar{\nabla}^2\vec{E}_i \simeq 0 \qquad , \qquad (18a)$$

$$\bar{\nabla}^2\vec{H}_i \simeq 0 \qquad , \qquad (18b)$$

$$\bar{\nabla}^2\vec{E}_s \simeq 0 \qquad m\neq j \quad , \qquad (19a)$$

$$\bar{\nabla}^2\vec{H}_s \simeq 0 \qquad m\neq j \quad , \qquad (19b)$$

$$\bar{\nabla}^2\vec{E}_s \simeq \frac{1}{\varepsilon}\bar{\nabla}\rho \qquad (20a)$$

and

$$\bar{\nabla}^2\vec{H}_s \simeq -\bar{\nabla}\times\vec{J}_s \qquad (20b)$$

which are Laplace's and Poisson's equations. The secondary electric field is determined only by the boundary charge distribution appearing over the surface of the inhomogeneity; there are negligible radiation or induction contributions from the scattering current. The tensor Green's functions $\tilde{G}_E^o(\bar{r};\bar{r}')$ and $\tilde{G}_H^o(\bar{r};\bar{r}')$ become those relating the fields at $\bar{r}$ on the surface to a static current element at $\bar{r}'$ and are essentially real functions independent of frequency. We caution however that the condition of long wavelength in the host, while a necessary condition, is not sufficient to allow interpretation of observed MT quantities in terms of static electric and magnetic fields. From equations (4) and (8) it is apparent that the source term of charge in (12a) is intimately associated with the total electric field within the 3-D body. This field, according to relation (5), may not obey Laplace's equation for very conductive inhomogeneities even though $|k_m\bar{R}|<<1$ exterior to the body. If the interior long wavelength condition $|k_bL|<<1$, where L is some characteristic dimension of the 3-D conductor, is met then we may assume

$$\bar{\nabla}^2\vec{E}_b \simeq 0 \quad . \tag{21}$$

When both long wavelength criteria are satisfied, $\vec{J}_S(\bar{r}')$, $\tilde{P}_S^o(\bar{r})$ and $\tilde{Q}_S^o(\bar{r})$ will be in phase with $\vec{E}_i^o$ and independent of frequency and it will be valid to use zero-frequency interpretation approaches.

Equation (17a) indicates that the total electric field at the surface of the earth in the vicinity of a three-dimensional conductivity inhomogeneity will remain distorted no matter how low the frequency of the incident applied field. Surface charge distributions required to preserve total normal current density are responsible. Such a permanent distortion is not the case for the total magnetic field at the earth's surface. Differentiation of the expression for the impedance of an n-layered conducting earth (Ward, 1967, p 120) will show that $|Z_\ell|$, appearing in equation (16), is a monotonically decreasing function for decreasing frequency. In particular the impedance of a uniform, conducting half-space

$$\begin{aligned} Z_\ell &= \frac{\omega\mu_o}{k} \\ &\simeq \sqrt{\mu_o\omega/\sigma} \end{aligned} \tag{22}$$

is proportional to $\omega^{1/2}$. Since at low frequencies $\tilde{Q}^o_h(\bar{r})$ approaches a real constant bounded by physical constraints, it is apparent that the contribution of the secondary magnetic field in (17b) to the total observed magnetic field will likewise become a monotonically decreasing function for sufficiently low frequencies. The frequency at which the total H-field can be considered essentially constant may depend strongly on the behavior of Z_ℓ. If a resistive basement below the body is being sensed, such that $|Z_\ell|$ is decreasing only slightly with decreasing frequency, the total H-field may remain distorted to relatively lower frequencies. If a conductive basement is being sensed, such that $|Z_\ell|$ is decreasing rather rapidly as frequency falls, the total horizontal H-field may become uniform at relatively higher frequencies.

Magnetotelluric Tensor Quantities

The previously described behavior of electromagnetic fields over an arbitrary 3-D inhomogeneity may be extended to magnetotelluric quantities that would be observed over that body. In particular, we investigate the low frequency asymptotes of the tensor elements as these will pertain most directly to the effects of small-scale geologic noise upon MT observations.

Impedance Tensor: The existence and structure of the general impedance tensor, defined by

$$\vec{E}^{\circ}_{t}(\bar{r}) = \tilde{Z}(\bar{r})\cdot\vec{H}^{\circ}_{t}(\bar{r}) \tag{23}$$

where

$$\tilde{Z}(\bar{r}) = \begin{bmatrix} Z_{xx} & Z_{xy} \\ Z_{yx} & Z_{yy} \end{bmatrix} \tag{24}$$

may be shown by combining equations (15) and (17). One obtains

$$\tilde{Z}(\bar{r}) = [\tilde{I} + \tilde{P}^{\circ}_{h}(\bar{r})]\cdot\tilde{Z}_{\ell}\cdot[\tilde{I} + \tilde{Q}^{\circ}_{h}(\bar{r})\cdot\tilde{Z}_{\ell}]^{-1} \quad . \tag{25}$$

Using the definitions of $\tilde{P}^{\circ}_{h}(\bar{r})$, $\tilde{Q}^{\circ}_{h}(\bar{r})$ and $\tilde{Z}_{\ell}$ given by (14) and (16), the elements of $\tilde{Z}(\bar{r})$ become

$$Z_{xx} = Z_{\ell}\left[\frac{(1+P^{\circ}_{xx})Z_{\ell}Q^{\circ}_{yy} - P^{\circ}_{xy}(1+Z_{\ell}Q^{\circ}_{yx})}{(1-Z_{\ell}Q^{\circ}_{xy})(1+Z_{\ell}Q^{\circ}_{yx}) + Z^{2}_{\ell}Q^{\circ}_{xx}Q^{\circ}_{yy}}\right] \quad , \tag{26a}$$

$$Z_{xy} = Z_{\ell}\left[\frac{P^{\circ}_{xy}Z_{\ell}Q^{\circ}_{xx} + (1+P^{\circ}_{xx})(1-Z_{\ell}Q^{\circ}_{xy})}{(1-Z_{\ell}Q^{\circ}_{xy})(1+Z_{\ell}Q^{\circ}_{yx}) + Z^{2}Q^{\circ}_{xx}Q^{\circ}_{yy}}\right] \quad , \tag{26b}$$

$$Z_{yx} = Z_{\ell}\left[\frac{P^{\circ}_{yx}Z_{\ell}Q^{\circ}_{yy} - (1+P^{\circ}_{yy})(1+Z_{\ell}Q^{\circ}_{yx})}{(1-Z_{\ell}Q^{\circ}_{xy})(1+Z_{\ell}Q^{\circ}_{yx}) + Z^{2}_{\ell}Q^{\circ}_{xx}Q^{\circ}_{yy}}\right] \tag{26c}$$

and

$$Z_{yy} = Z_{\ell}\left[\frac{(1+P^{\circ}_{yy})Z_{\ell}Q^{\circ}_{xx} + P^{\circ}_{yx}(1-Z_{\ell}Q^{\circ}_{xy})}{(1-Z_{\ell}Q^{\circ}_{xy})(1+Z_{\ell}Q^{\circ}_{yx}) + Z^{2}_{\ell}Q^{\circ}_{xx}Q^{\circ}_{yy}}\right] \quad . \tag{26d}$$

When no inhomogeneity is present, all elements of $\tilde{P}_h^\circ(r)$ and $\tilde{Q}_h^\circ(r)$ are zero and hence $Z_{xx} = Z_{yy} = 0$ and $Z_{xy} = -Z_{yx} = Z_\ell$. Whenever observation points are on and measurement axes are parallel to axes of symmetry for 3-D bodies, $P_{xy}^\circ = P_{yx}^\circ = Q_{xx}^\circ = Q_{yy}^\circ = 0$ so that $Z_{xx} = Z_{yy} = 0$ and

$$Z_{xy} = Z_\ell \left[\frac{(1+P_{xx}^\circ)}{(1+Z_\ell Q_{yx}^\circ)} \right] \tag{27a}$$

and

$$Z_{yx} = -Z_\ell \left[\frac{(1+P_{yy}^\circ)}{(1-Z_\ell Q_{xy}^\circ)} \right] \quad . \tag{27b}$$

Observation points are always on planes of symmetry for 2-D geometries. The low frequency asymptotes of Z_{ij} warrant examination. For $|k_m\bar{R}|$, $|k_bL|$ and $|Z_\ell Q_{ij}^\circ| \ll 1$ we have

$$Z_{xx} = -Z_\ell P_{xy}^\circ \quad , \tag{28a}$$

$$Z_{xy} = Z_\ell(1+P_{xx}^\circ) \quad , \tag{28b}$$

$$Z_{yx} = -Z_\ell(1+P_{yy}^\circ) \tag{28c}$$

and

$$Z_{yy} = Z_\ell P_{yx}^\circ \quad . \tag{28d}$$

All four elements of the tensor become purely linear functions of the impedance of the layered host medium and the normalized electric tensor elements. For the special case of the x-axis parallel to the strike of a two-dimensional inhomogeneity, $\vec{E}_x$ is parallel to all resistivity contacts and no surface charges exist. This is the well-known transverse electric (TE) mode of excitation. For sufficiently low frequencies, the wave equation (3a) for E_x becomes homogeneous, $P^o_{xy} = P^o_{yx} = 0$, $P^o_{xx} \rightarrow 0$ and so $Z_{xy} \rightarrow Z_\ell$. On the other hand, a significant component of E_y will be perpendicular to contacts, non-vanishing surface changes will exist, P^o_{yy} remains non-zero, and Z_{yx} will be as given in (28c). Because of the charge distribution, this transverse magnetic (TM) polarization may be considered as exhibiting two-dimensional current-gathering phenomena.

For the general 3-D body, the apparent resistivity functions at low frequencies

$$\rho_{xx} = \frac{1}{\omega\mu_o}|Z_\ell|^2 \cdot |P^\circ_{xy}|^2 \quad , \tag{29a}$$

$$\rho_{xy} = \frac{1}{\omega\mu_o}|Z_\ell|^2 \cdot |1+P^\circ_{xx}|^2 \quad , \tag{29b}$$

$$\rho_{yx} = \frac{1}{\omega\mu_o}|Z_\ell|^2 \cdot |1+P^\circ_{yy}|^2 \tag{29c}$$

and

$$\rho_{yy} = \frac{1}{\omega\mu_o}|Z_\ell|^2 \cdot |P^\circ_{yx}|^2 \tag{29d}$$

result. Like the impedance elements Z_{ij}, the apparent resistivities will be distorted to arbitrarily low frequencies by polarization charge effects. At this Poisson's equation limit, all four ρ_{ij}'s are magnitude-scaled images of the apparent resistivity of the layered earth host, differing by only a multiplicative constant. However since the elements P^o_{ij} become purely real at this low frequency limit, the phases of all impedance elements ($\phi_{xx}, \phi_{xy}, \phi_{yx}, \phi_{yy}$) asymptote to the phase of the layered host and are no longer affected by the body.

Vertical H-field Tensors: A similar analysis is possible for the vertical magnetic transfer functions, defined by

$$\vec{H}_z^{\circ}(\bar{r}) = \tilde{K}_z(\bar{r}) \cdot \vec{H}_t^{\circ}(\bar{r}) \tag{32}$$

and

$$\vec{H}_z^{\circ}(\bar{r}) = \tilde{Y}_z(\bar{r}) \cdot \vec{H}_t^{\circ}(\bar{r}) \tag{33}$$

where

$$\tilde{K}_z(\bar{r}) = [K_{zx} \; K_{zy}]$$

and

$$\tilde{Y}_z(\bar{r}) = [Y_{zx} \; Y_{zy}] \quad .$$

From equations (14), (15) and (17), the transfer functions are expressed as

$$\tilde{K}_z(\bar{r}) = \tilde{Q}_v^{\circ}(\bar{r}) \cdot Z_{\ell} \cdot [\tilde{I} + \tilde{Q}_h^{\circ}(\bar{r}) \cdot \tilde{Z}_{\ell}]^{-1} \tag{34}$$

and

$$\tilde{Y}_z(\bar{r}) = \tilde{Q}_v^{\circ}(\bar{r}) \cdot [\tilde{I} + \tilde{P}_h^{\circ}(\bar{r})]^{-1} \tag{35}$$

Using the definitions of $\tilde{Q}_v^{\circ}(\bar{r})$, $\tilde{P}_h^{\circ}(\bar{r})$, $\tilde{Q}_h^{\circ}(\bar{r})$ and $\tilde{Z}_{\ell}$ given by (14) and (16), the elements of $\tilde{K}_z(\bar{r})$, and $\tilde{Y}_z(\bar{r})$ become

$$K_{zx} = Z_{\ell} \left[\frac{Q_{zx}^{\circ} Z_{\ell} Q_{yy}^{\circ} - Q_{zy}^{\circ}(1+Z_{\ell} Q_{yx}^{\circ})}{(1-Z_{\ell} Q_{xy}^{\circ})(1+Z_{\ell} Q_{yx}^{\circ}) + Z_{\ell}^2 Q_{xx}^{\circ} Q_{yy}^{\circ}} \right] \quad , \tag{36a}$$

$$K_{zy} = Z_{\ell} \left[\frac{Q_{zy}^{\circ} Z_{\ell} Q_{xx}^{\circ} + Q_{zx}^{\circ}(1-Z_{\ell} Q_{xy}^{\circ})}{(1-Z_{\ell} Q_{xy}^{\circ})(1+Z_{\ell} Q_{yx}^{\circ}) + Z_{\ell}^2 Q_{xx}^{\circ} Q_{yy}^{\circ}} \right] \quad , \tag{36b}$$

$$Y_{zx} = \left[\frac{Q_{zx}^{\circ}(1+P_{yy}^{\circ}) - Q_{zy}^{\circ} P_{yx}^{\circ}}{(1+P_{xx}^{\circ})(1+P_{yy}^{\circ}) - P_{xy}^{\circ} P_{yx}^{\circ}} \right] \tag{37a}$$

and

$$Y_{zy} = \left[\frac{Q^\circ_{zy}(1+P^\circ_{xx}) - Q^\circ_{zx}P^\circ_{xy}}{(1+P^\circ_{xx})(1+P^\circ_{yy}) - P^\circ_{xy}P^\circ_{yx}} \right] \quad . \qquad (37b)$$

When no inhomogeneity is present all elements of $\tilde{P}^\circ_s(\bar{r})$ and $\tilde{Q}^\circ_s(\bar{r})$ are zero and hence $K_{zx} = K_{zy} = Y_{zx} = Y_{zy} = 0$. Whenever observation points are on and a measurement axis is parallel to, say, the y'-axis of symmetry, $P^\circ_{xy} = P^\circ_{yx} = Q^\circ_{xx} = Q^\circ_{yy} = Q^\circ_{zy} = 0$ so that $K_{zx} = Y_{zy} = 0$ and

$$K_{zy} = Z_\ell \left[\frac{Q^\circ_{zx}}{(1+Z_\ell Q^\circ_{yx})} \right] \qquad (38)$$

and

$$Y_{zx} = \left[\frac{Q^\circ_{zx}}{(1+P^\circ_{xx})} \right] \quad . \qquad (39)$$

The low frequency asymptotes of the transfer function estimates are

$$K_{zx} = -Z_\ell Q^\circ_{zy} \quad , \qquad (40a)$$

$$K_{zy} = Z_\ell Q^\circ_{zx} \quad , \qquad (40b)$$

$$Y_{zx} = \left[\frac{Q^\circ_{zx}(1+P^\circ_{yy}) - Q^\circ_{zy}P^\circ_{yx}}{(1+P^\circ_{xx})(1+P^\circ_{yy}) - P^\circ_{xy}P^\circ_{yx}} \right] \quad , \qquad (41a)$$

and

$$Y_{zy} = \left[\frac{Q^\circ_{zy}(1+P^\circ_{xx}) - Q^\circ_{zx}P^\circ_{xy}}{(1+P^\circ_{xx})(1+P^\circ_{yy}) - P^\circ_{xy}P^\circ_{yx}} \right] \qquad (41b)$$

Both K_{zx} and K_{zy} become purely linear functions of the impedance of the layered host medium and the normalized magnetic tensor components.

These elements hence approach zero for sufficiently low frequencies. Their phases will also asymptote to that of the impedance of the host since Q°_{zx} become purely real as Poissons's equation becomes the governing relation. On the other hand, $|Y_{zx}|$ and $|Y_{zy}|$ remain permanently distorted as frequency falls because of non-vanishing current-gathering phenomena, although the phases should asymptote to zero (or 180° depending upon the signs of the denominators of (41)).

The tipper (Vozoff, 1972), relating the vertical magnetic field to both horizontal magnetic components, is a function with a magnitude defined by

$$|T| = [|K_{zx}|^2 + |K_{zy}|^2]^{\frac{1}{2}} \quad . \tag{42}$$

This quantity is invariant under co-ordinate rotation. From equation (40), this becomes, in the low frequency limit

$$|T| = |Z_{\ell}|\cdot[|Q_{zy}|^2 + |Q^{\circ}_{zx}|^2]^{\frac{1}{2}} \tag{43}$$

Because of the factor $|Z_{\ell}|$, the tipper strength will approach zero for sufficiently low frequencies.

Behavior of MT Quantities under EM Scaling: We have shown that MT functions involving magnitudes of electric fields are affected to arbitrarily low frequencies by current-gathering in conductive inhomogeneities, even though these inhomogeneities may be small and considered as geologic noise. This effect pertains to the impedance element magnitudes, apparent resistivities and vertical admittance magnitudes such that principal axis estimations along with structural interpretations using these functions, based upon 1-D or 2-D TE schemes, might be misleading. The discussion however has so far limited itself to a single inhomogeneity in a layered earth. At the Roosevelt Hot Springs, a variety of 3-D bodies combine to determine the MT signatures at a given sounding. Some basic investigations of the relative contributions of large and small inhomogeneities in a given host to the total MT response can be made using electromagnetic scaling arguments (Grant and West, 1965, p 479-482; Stratton, 1941, p 488-491). For ease of understanding, we confine the discussion to prisms in a half-space, although a generalization to bodies in a layered host can be made.

Let us consider two separate conductivity structures, each consisting of a conductive inhomogeneity in a conducting half-space, where one of the structures is an exact replica of the other except that all its linear dimensions are smaller than those of the other by an arbitrary factor ξ. This scaling of dimensions will apply to the position vectors $\bar{r}$, $\bar{r}'$ and $\bar{R}$, as defined in Figure 2, and not just the size and depth of the buried 3-D body. We choose for this discussion however not to transform in any way the admittivities of the half-space host and the body such that corresponding media in the two overall structures remain equal in this regard. Now suppose the two structures are subject to incident fields, $\vec{E}^{o}_{i1}$, $\vec{H}^{o}_{i1}$, $\vec{E}^{o}_{i2}$ and $\vec{H}^{o}_{i2}$, at the surface which are of different frequencies such that $\omega_1/\omega_2 = \xi^2$. Subscripts 1 and 2 refer herein to physical quantities associated with the smaller and larger structures respectively. Under these conditions, an induction number

$$\bar{\Theta} = \omega_1\mu_o\hat{y}|\bar{r}_1|^2\hat{r} = \omega_2\mu_o\hat{y}|\bar{r}_2|^2\hat{r} \quad , \qquad (44)$$

where $\bar{r}_1$ and $\bar{r}_2 = \xi\bar{r}_1$ are the equivalent observation vectors, $\hat{r}$ is a unit vector in the direction of $\bar{r}_1$ or $\bar{r}_2$ and $\hat{y}$ is the admittivity at equivalent points in the two structures, remains invariant. Making the admittivities of corresponding media equal for the two postulated structures leads to a rather restrictive definition of the induction number, since appropriate scaling of $\hat{y}$ will still preserve ξ. However, we are concerned with the effects upon MT quantities of different inhomogeneities in a given host so that keeping admittivities fixed is necessary.

When such a scaling transformation as above is considered, the secondary electric field tensor $\tilde{P}_s^o(\bar{\theta})$, defined in a manner analogous to $\tilde{P}_s^o(\bar{r})$ in equation (12) by

$$\vec{E}_s^o(\bar{r}_1) = \tilde{P}_s^o(\bar{\Theta})\cdot\vec{E}_{i1}^o \tag{45a}$$

or

$$\vec{E}_s^o(r_2) = \tilde{P}_s^o(\bar{\Theta})\cdot\vec{E}_{i2}^o \tag{45b}$$

remains unchanged by the transformation. Stated literally, two resistivity structures that are geometrically similar with equal admittivities in corresponding media will scatter secondary electric fields which are likewise geometrically similar, provided the frequency of excitation for the larger structure is less than that of the smaller by the square of the dimension scale change ξ. Furthermore, the amplitudes of the respective secondary fields at the equivalent observation vectors $\bar{r}_1$ and $\bar{r}_2$, normalized by the amplitudes of the respective incident fields $\vec{E}_{i1}^o$ and $\vec{E}_{i2}^o$, are the same. An identical conclusion applies concerning the secondary H-field tensor $\tilde{R}_s^o(\bar{\Theta})$, the same in structure as $\tilde{P}^{o}_{s}(\bar{r})$ in equation (14), i.e.

$$\vec{H}^{o}_{s}(\bar{r}_1) = \tilde{R}^{o}_{s}(\bar{\Theta})\cdot\vec{H}^{o}_{i1} \tag{46a}$$

and

$$\vec{H}^{o}_{s}(\bar{r}_2) = \tilde{R}^{o}_{s}(\bar{\Theta})\cdot\vec{H}^{o}_{i2} \quad . \tag{46b}$$

From equations (12b) and (15), $\tilde{R}^{o}_{s}(\bar{\Theta})$ is also shown to be

$$\tilde{R}^{o}_{s}(\bar{\Theta}) = \tilde{Q}^{o}_{s}(\bar{r}_1)\cdot\tilde{Z}_{\ell 1} = \tilde{Q}^{o}_{s}(\bar{r}_2)\cdot\tilde{Z}_{\ell 2} \quad . \tag{47}$$

$\tilde{Q}^{o}_{s}(\bar{r}_1)$, $\tilde{Z}_{\ell 1}$, $\tilde{Q}^{o}_{s}(\bar{r}_2)$ and $\tilde{Z}_{\ell 2}$ cannot individually be written as a function of $\bar{\Theta}$. With $\omega_1 = \xi^2\omega_2$, it follows from equation (22) for the half-space that

$$\tilde{Z}_{\ell 1} = \xi\tilde{Z}_{\ell 2} \quad . \tag{48}$$

Relation (48) can be shown to be valid even for an n-layered impedance and, since ξ is purely real, it follows that the layered earth impedance phase can be written solely as a function of induction number. It is apparent then from (47) and (48) that if $\tilde{R}^{o}_{s}(\bar{\Theta})$ is to depend only upon $\bar{\Theta}$ that

$$\tilde{Q}^{o}_{s}(\bar{r}_1) = \frac{1}{\xi}\tilde{Q}^{o}_{s}(\bar{r}_2) \quad . \tag{49}$$

It is important to conclude that, other things being equal, the scattered H-field tensor $\tilde{Q}^{o}_{s}(\bar{r})$ increases with increased size of the inhomogeneity, although the frequency dependence will shift to lower frequencies.

Substitution of relations (45), (48) and (49) into the impedance expression (25) will show, for a specified $\bar{\Theta}$, that

$$\tilde{Z}(\bar{r}_1) = \xi\tilde{Z}(\bar{r}_2) \quad . \tag{50}$$

General apparent resistivity functions though, defined in a manner analogous to equation (29), are invariant under scaling, i.e.

$$\rho_{ij1} = \rho_{ij2} = \rho_{ij}(\bar{\Theta}) \quad . \tag{51}$$

Likewise, because the host impedance phase and all elements of $P_S^{\circ}(\bar{\Theta})$ are functions only of induction number, the phases of the individual impedance elements of (25) follow as

$$\phi_{ij1} = \phi_{ij2} = \phi_{ij}(\bar{\Theta}) \quad . \tag{52}$$

However, vertical admittance values due to large structures generally exceed those due to smaller structures. One sees

$$\tilde{Y}_z(\bar{r}_1) = \frac{1}{\xi}\tilde{Y}_z(\bar{r}_2) \tag{53}$$

by use of (35), (45) and (49). Finally it can be demonstrated for our hypothetical construction from (34) and (49) that

$$\tilde{K}_z(\bar{r}_1) = \tilde{K}_z(\bar{r}_2) = \tilde{K}_z(\bar{\Theta}) \quad . \tag{54}$$

As stated before, we have been building this discussion of scaling around large and small bodies in identical half-spaces in order to compare the relative contributions of these bodies in a common host to the overall MT response. However, relations (44) through (54) can be shown to be correct for inhomogeneities in a layered host provided the thicknesses of all corresponding layers in the two structures are related by the previously defined scale transformation.

The behavior of MT quantities under scaling is relevant to the problem of near-surface geologic noise and we continue with the postulated, geometrically similar large and small bodies in half-space hosts. Equation (50) indicates that, all other things being equal, a very small lateral inhomogeneity may cause an apparent resistivity anomaly as pronounced as that of a large body which will not decrease as frequency decreases, though the spatial extent of the former is relatively small. An apparent resistivity sounding obtained near such a small body may be distorted sufficiently so that 1-D and 2-D TE interpretations aimed at describing a deeper feature of interest may be subject to serious errors. However, any of the impedance phases ϕ_{ij} for a smaller body should generally approach that of the host, as frequency falls, but at a higher frequency than those of a larger body; in our hypothetical situation the frequency should be higher by a factor of ξ^2. This separation of phase signatures might allow one to "see through" geologic noise to observe more clearly the presence of deeper features.

Comparisons of the vertical H-field transfer functions in this context is also useful. Suppose ω_1 and ω_2 are low enough such that $\tilde{Y}_z(\bar{r}_1)$ and $\tilde{Y}_z(\bar{r}_2)$ have essentially asymptoted to the constant values of equation (41). In that instance for the assumed half-space host the relation

$$\tilde{Y}_z(\bar{r}_1) \simeq \frac{1}{\xi}\tilde{Y}_z(\bar{r}_2) \tag{55}$$

is valid when $\omega_1 = \omega_2$. Concerning the tipper elements, if the same low frequency conditions are invoked such that equation (40) applies, then for a half-space host

$$\tilde{K}_z(\bar{r}_1) \simeq \frac{1}{\xi}\tilde{K}(\bar{r}_2) \tag{56}$$

for $\omega_1 = \omega_2$. Though tipper elements for both the large and the small body are decreasing monotonically now as frequency falls, their ratio at a given frequency remains essentially $1/\xi$, which is that for the vertical admittance just described. Although this simple scaling argument suggests that the relative distortion of the vertical admittance by geologic noise might be no worse than that of the tipper elements, coupling between the inhomogeneities as considered in the next section will invalidate this. Finally, as for the impedance element phases ϕ_{ij}, the phases of the vertical admittance and tipper elements should approach their respective low frequency values for the smaller postulated body at a frequency that is higher than for the larger body by a factor of ξ^2.

Coupled Body Considerations

The concept of EM scaling cannot be applied directly to the Roosevelt Hot Springs because there is a single, layered, apparently regional resistivity profile which is the host for all lateral inhomogeneities at RHS. The simple geometric scaling of secondary fields from small to large bodies, as given in equations (45) and (46), does not occur so that straightforward relations like (55) and (56) are not strictly applicable. Futhermore, the conductive inhomogeneities at RHS are electromagnetically coupled so that it is unwise to examine the MT functions over only one structure at a time. The following approximation to the coupling between large and small structures allows some relief from the above shortcomings. A larger body, perhaps exemplifying conductive valley sediments, can be viewed as scattering secondary EM fields which, together with the incident, vertically propagating plane wave, constitute total source fields for a small, nearby inhomogeneity, for instance zones of variable hydrothermal alteration. Such a view presumes that the role of the smaller conductor in determining the scattering current distribution within the larger is negligible and that the secondary fields from the larger body are essentially uniform and horizontal over the smaller. Under these assumptions, we generate analytic expressions for the MT quantities over such a two-body geometry in terms only of scattered field tensors, exemplified by equation (14), that apply to the large and small bodies independently. Numerical results presented in Appendix A show the accuracy of the approximation for the valley-alteration zone composition.

Horizontal Field Relations: The horizontal secondary field vectors $\vec{E}^{o}_{ss}(\bar{r})$ and $\vec{H}^{o}_{ss}(\bar{r})$ at the earth's surface scattered by a small conductor alone are uniquely related to the incident planar electric field vector $\vec{E}_i$ upon the center of the small body by

$$\vec{E}^{o}_{ss}(\bar{r}) = \tilde{P}_{hs}(\bar{r})\cdot\vec{E}_i \tag{57a}$$

and

$$\vec{H}^{o}_{ss}(\bar{r}) = \tilde{Q}_{hs}(\bar{r})\cdot\vec{E}_i \quad . \tag{57b}$$

Let the total horizontal electric field due to the large body alone which would exist at the location of the center of the small body be denoted as $\vec{E}_{t\ell}(\bar{r}_b)$. Under the assumptions stated previously, the perturbed horizontal secondary electric and magnetic fields scattered to the surface by the smaller body in the presence of the larger are

$$\vec{E}^{o\prime}_{ss}(\bar{r}) \simeq \tilde{P}_{hs}(\bar{r})\cdot\vec{E}_{t\ell}(\bar{r}_b) \tag{58a}$$

and

$$\vec{H}^{o\prime}_{ss}(\bar{r}) \simeq \tilde{Q}_{hs}(\bar{r})\cdot\vec{E}_{t\ell}(\bar{r}_b) \quad . \tag{58b}$$

The total approximate impedance $\tilde{Z}(\bar{r})$ is now defined by

$$[\vec{E}^{o}_{t\ell}(\bar{r}) + \vec{E}^{o\prime}_{ss}(\bar{r})] \simeq \tilde{Z}(\bar{r})\cdot[\vec{H}^{o}_{t}(\bar{r}) + \vec{H}^{o\prime}_{ss}(\bar{r})] \tag{59}$$

where $\vec{E}^{o}_{t\ell}(\bar{r})$ and $\vec{H}^{o}_{t\ell}(\bar{r})$ are the total electric and magnetic fields at the earth's surface around the large conductor without the smaller. If we allow

$$\vec{E}^{o}_{s\ell}(\bar{r}) = \tilde{P}^{o}_{h\ell}(\bar{r})\cdot\vec{E}^{o}_{i} \quad , \tag{60a}$$

$$\vec{H}^{o}_{s\ell}(\bar{r}) = \tilde{Q}^{o}_{h\ell}(\bar{r})\cdot\vec{E}^{o}_{i} \tag{60b}$$

and

$$\vec{E}_{s\ell}(\bar{r}_b) = \vec{E}_{t\ell}(\bar{r}_b) - \vec{E}_{i} = \tilde{P}_{h\ell}(\bar{r}_b)\cdot\vec{E}^{o}_{i}$$

then the impedance estimate Z(r) of (59) may be written

$$\tilde{Z}(\bar{r}) \simeq \{\tilde{I} + \tilde{P}^{o}_{h\ell}(\bar{r}) + \tilde{P}_{hs}(\bar{r})\cdot[d\tilde{I} + \tilde{P}_{h\ell}(\bar{r}_b)]\}\cdot\tilde{Z}_{\ell}$$

$$\cdot\{\tilde{I} + \tilde{Q}^{o}_{h\ell}(\bar{r})\cdot\tilde{Z}_{\ell} + \tilde{Q}_{hs}(\bar{r})\cdot[d\tilde{I} + \tilde{P}_{h\ell}(\bar{r}_b)]\cdot\tilde{Z}_{\ell}\}^{-1} \quad . \tag{62}$$

Due to dissipation of the incident plane wave with depth in the earth, the complex scalar d is required before some unit tensors, implying $\vec{E}_i = d\vec{E}^{o}_i$.

The quantity $\tilde{P}_{hs}(\bar{r})$ can be quite important in the neighborhood of the small body. To the degree that relation (62) is accurate, $\tilde{P}_{hs}(\bar{r})$ can be said to alter the relative contributions of each element of $\tilde{P}_{h\ell}(\bar{r}_b)$ to each element of $\tilde{Z}(\bar{r})$ from receiver to receiver. This is true even at low frequencies where $\tilde{P}_{hs}(\bar{r})$ is essentially real and independent of frequency. Inasmuch as $\tilde{P}^{o}_{h\ell}(\bar{r})$ differs from $\tilde{P}_{h\ell}(\bar{r}_b)$ and the latter is not a diagonal tensor, then the anisotropic impedance phase as well as the apparent resistivity responses of the larger body may be distorted in the vicinity of the small body. If the smaller structure resides near any planes of symmetry of the larger structure where $\tilde{P}^{o}_{h\ell}(\bar{r})$ and $\tilde{P}_{h\ell}(\bar{r}_b)$ are entirely diagonal (true provided measurement axes parallel symmetry axes), distortions of the impedance phase response of the larger body will be at a minimum. This is in contrast to the effects of a single body in the earth, as described by (28), where the host impedance phase is little affected by an inhomogeneity below a certain frequency. Contributions of the scattered magnetic field of the small body to $\tilde{Z}(\bar{r})$ are however not considered important even when large and small bodies are coupled in this manner, unless magnitudes of elements of $\tilde{P}_{h\ell}(\bar{r}_b)$ become much greater than unity. EM scaling arguments given earlier indicate $\tilde{Q}^{o}_{h\ell}(\bar{r})$ should be much greater than $\tilde{Q}_{hs}(\bar{r})$ as long as the sizes of the large and small structures are quite different.

<u>Vertical H-field Relations</u>: The vertical magnetic field tensors $\tilde{Y}_z(\bar{r})$ and $\tilde{K}_z(\bar{r})$ are similarly derived. The vertical magnetic field scattered by the small conductor alone is related to $\vec{E}_i$ by

$$\vec{H}^{o\prime}_{zs}(\bar{r}) = \tilde{Q}_{zs}(\bar{r})\cdot\vec{E}_i \quad . \qquad (63)$$

The perturbed secondary vertical magnetic fields over the smaller inhomogeneity in the presence of the larger are approximately

$$\vec{H}^{o\prime}_{zs}(\bar{r}) \simeq \tilde{Q}_{zs}(\bar{r})\cdot\vec{E}_t(\bar{r}_b) \quad . \qquad (64)$$

The estimates of the vertical field tensors become defined by

$$[\vec{H}^{o}_{z\ell}(\bar{r}) + \vec{H}^{o\prime}_{zs}(\bar{r})] \simeq \tilde{K}_z(\bar{r})\cdot[\vec{H}^{o}_{t\ell}(\bar{r}) + \vec{H}^{o\prime}_{ss}(\bar{r})] \qquad (65)$$

and

$$[\vec{H}^{o}_{z\ell}(\bar{r}) + \vec{H}^{o\prime}_{zs}(\bar{r})] \simeq \tilde{Y}_z(\bar{r})\cdot[\vec{E}^{o}_{t\ell}(\bar{r}) + \vec{E}^{o\prime}_{ss}(\bar{r})] \qquad (66)$$

where $\vec{H}^{o}_{z\ell}$ is the vertical magnetic field at the earth's surface around the larger conductor without the smaller. If we allow

$$\vec{H}^{o}_{z\ell}(\bar{r}) = \tilde{Q}^{o}_{z\ell}(\bar{r})\cdot\vec{E}^{o}_{i} \qquad (67)$$

then using (58), (59) and (61) the estimates of $\tilde{Y}_z(\bar{r})$ and $\tilde{K}_z(\bar{r})$ may be written

$$\tilde{K}_z(\bar{r}) \simeq \{\tilde{Q}^{o}_{z\ell}(\bar{r}) + \tilde{Q}_{zs}(\bar{r})\cdot[d\tilde{I} + \tilde{P}_{h\ell}(\bar{r}_b)]\}\cdot\tilde{Z}_\ell$$

$$\cdot\{\tilde{I} + \tilde{Q}^{o}_{h\ell}(\bar{r})\cdot\tilde{Z}_\ell + \tilde{Q}_{hs}(\bar{r})\cdot[d\tilde{I} + \tilde{P}_{h\ell}(\bar{r}_b)]\cdot\tilde{Z}_\ell\}^{-1}. \qquad (68)$$

and

$$\tilde{Y}_z(\bar{r}) \simeq \{\tilde{Q}^{o}_{z\ell}(\bar{r}) + \tilde{Q}_{zs}(\bar{r})\cdot[d\tilde{I} + \tilde{P}_{h\ell}(r_b)]\}$$

$$\cdot\{\tilde{I} + \tilde{P}^{o}_{h\ell}(\bar{r}) + \tilde{P}_{hs}(\bar{r})\cdot[d\tilde{I} + \tilde{P}_{h\ell}(\bar{r}_b)]\}^{-1} \quad . \qquad (69)$$

The remarks following equation (62) apply equally well to equation (68). We suspect that the anisotropic vertical admittance phases as well as their amplitudes for the larger body may be distorted to some extent in the vicinity of the small body, especially for sites distant from symmetry planes of the larger. This is in contrast to the effects of a single body in the earth, as described by equation (41). However, even when the large and small structures are coupled in our approximate manner, the small feature does not significantly distort the magnitudes and phases of the tipper element due to the larger feature at low frequencies, unless magnitudes of elements of $\tilde{P}_{h\ell}(\bar{r}_b)$ in equation (69) become greater than unity.

Summary of MT Theory

To close this examination of theory, we stress that 3-D lateral inhomogeneities may have marked effects upon MT measurements to arbitrarily low frequencies, even though these inhomogeneities may be smaller than one's station spacing. Polarization charge or current-gathering phenomena at lateral resistivity discontinuities disturb most importantly the magnitude of total electric field in their vicinity. Current-gathering may well be very important for 3-D bodies at high frequencies but is by far dominant at low frequencies. However, the phase of the total electric field as well as magnitude and phase of the total magnetic field approach those of the layered earth host under low frequency conditions defined previously and are no longer affected by the inhomogeneity. The frequency below which the horizontal magnetic field appears nearly uniform may depend strongly, for a given inhomogeneity, upon the layered host makeup.

The MT quantities affected most severely by 3-D structures appear to be the apparent resistivity and the vertical admittance element magnitudes as they involve relations between magnitudes of E-fields. For single bodies though, tipper element magnitudes and the phases of all MT functions approach those of the layered earth at low frequencies. At the same time, an apparent resistivity sounding constructed from any impedance element observed around a single body resembles that of the layered earth but differs by a multiplicative, real, positive constant. The errors in any 1-D model obtained from such a sounding are directly proportional to the distortion of the total E-field by an inhomogeneity.

EM scaling considerations indicate that, other things being equal, small bodies may cause anomalies in apparent resistivity, tipper element magnitudes and the phases of all functions as pronounced as those of large bodies, though the spatial extent of an anomaly of a little body will be relatively small. Larger anomalies in vertical admittance magnitudes generally accompany larger structures. However, the frequency ranges over which such anomalies occur are separated generally according to the square of the scale change between bodies. This may encourage use of tipper element magnitudes and the phases of all MT quantities in order to observe more directly the presence of larger and perhaps more interesting structure buried beneath small-scale geologic noise, since these functions are not distorted through decreasing frequencies by polarization charge phenomena.

Approximations to coupling between large and small bodies show that caution is required before interpreting at least the impedance and vertical admittance element phases in this manner. In general, these phases around a large structure will be affected by small features unless one is near planes of symmetry of the larger body and measurement axes are parallel to these planes. Tipper element magnitudes and phases on the other hand, at any point around a large structure with any orientation of measurement axes, are not so disturbed by geologic noise through diminishing frequencies. In the face of such noise, we recommend strike estimations using tipper element magnitudes for giving the most consistent estimates of major geoelectric trends in the face of geologic noise.

THREE-DIMENSIONAL MAGNETOTELLURIC MODEL STUDIES

In this section, the conclusions of the previous theoretical development are illustrated using the calculated magnetotelluric (MT) responses of conductive prisms in a half-space. These bodies will represent the hydrothermal alteration zones and the Milford graben sediments. The model studies are intended to demonstrate the severity of the effects of these secondary features upon MT soundings near RHS and in the Mineral Mountains and also to suggest ways of accommodating properly such features in the interpretation of economic targets like the brine reservoir or deep heat source. Although we are presently restricted to bodies in a half-space instead of in a layered earth, we believe the results presented do provide basic insight into the behavior of MT quantities around arbitrary three-dimensional (3-D) inhomogeneities.

The Modeling Algorithm

Our modeling algorithm is based upon equation (10a) of the previous section, an integral equation formulation of the unknown electric field within the inhomogeneity (Hohmann, 1975). Using the method of moments, $\vec{J}_s(\bar{r}')$ is approximated by cubic pulse basis functions over the body and is obtained by solving a dense matrix equation. Once the scattering current in the body has been solved, total fields at the surface will result from numerical integration of equations (10a) and (10b). MT quantities may be determined as per Jones and Vozoff (1978) if total fields are computed for two independent polarizations of $\vec{E}_i(\bar{r})$. Although the alteration zones and valley sediments at RHS outcrop, prisms modeled with this routine must be buried somewhat to achieve accurate results. Details of the formulation for a plane-wave source and a discussion of the solution accuracy are given by Hohmann and Ting (1978) and Ting and Hohmann (1980).

Alteration Zone Model

The geometry of a prismatic conductor representing a near-surface hydrothermal alteration zone appears in Figure 3. It is a small feature, 1200 m by 400 m by 250 m thick with a depth to top of 50 m. The intrinsic resistivity of the prism is 10 Ω-m while that of its half-space host is 100 Ω-m. The scattering current within the conductor was approximated by 72 cubic cells of varying sizes. Forming and solving the matrix equation for the interior current required about 3 hrs CPU time per frequency on a Prime 400 Series minicomputer while calculating the secondary fields at the surface required an additional 3 hrs.

Plan maps of off-diagonal apparent resistivities show the strong effect of small, moderate-contrast features over a wide range of frequencies (see Figure 4). For these and all subsequent MT functions presented for this model, the data measurement axes are coincident with the x'-y' symmetry axes of the body. Due to symmetry of the body, only the upper right quadrant of the calculations is presented; the plan outline of the inhomogeneity is shown with dots. The basic electric dipolar nature of the anomalies is apparent for both 1 Hz and 100 Hz,

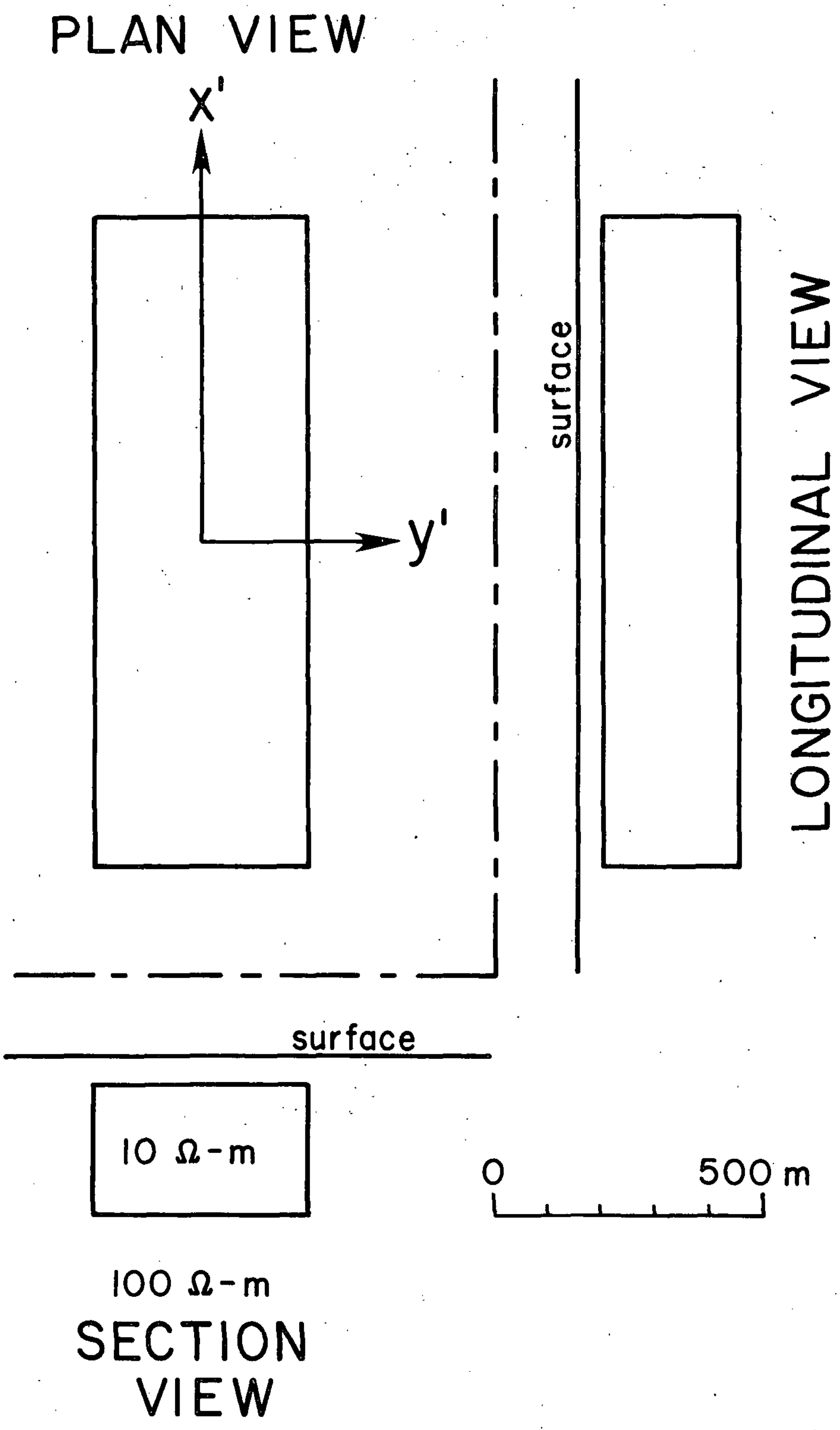

Figure 3. Conductive prism in conductive half-space used to represent a near-surface hydrothermal alteration distribution. Dimensions may be inferred from the scale provided or taken from main text.

Figure 4. Plan maps of contoured apparent resistivity at 100 Hz and 1 Hz for the shallow 3-D conductor of Figure 3. Due to the two symmetry planes of the conductor, only the upper right quadrant of results need be plotted for these results and those of the next five figures. Contour values are in Ω-m and the plan view outline of the conductor is shown in dots.

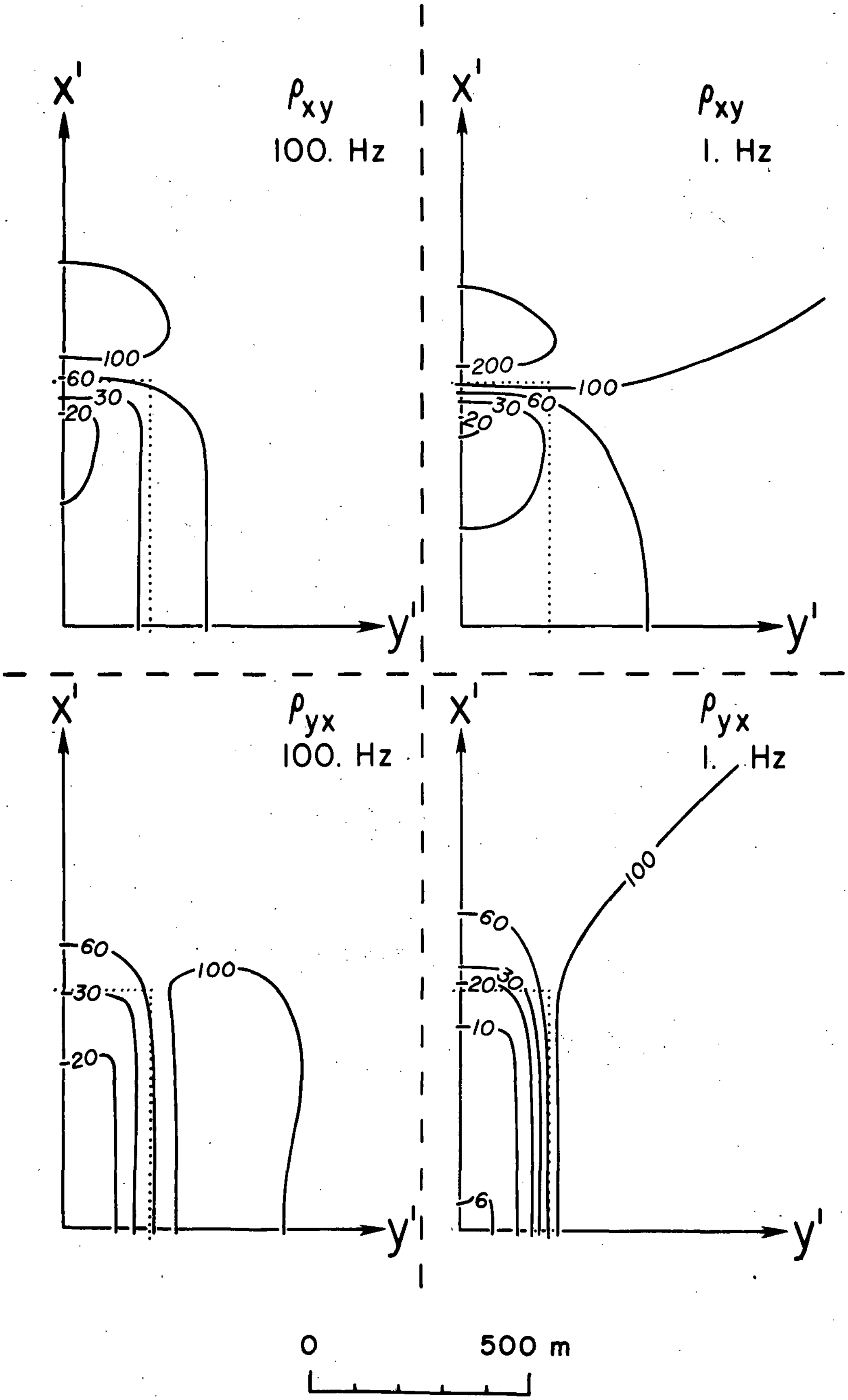
x'
ρxy
100. Hz
100
60
30
20
y'
x'
ρxy
1. Hz
200
100
60
30
20
y'
x'
ρyx
100. Hz
60
100
30
20
y'
x'
ρyx
1. Hz
100
60
30
20
10
6
y'
0
500 m

with undershoots and overshoots in magnitudes occurring over the ends of the body for ρ_{xy} and over the sides for ρ_{yx}. Outside the body, the apparent resistivities are smoothly varying functions of position. This is in contrast to the results of Reddy et al (1977) where irregularities in ρ_a appear outside their model. At 1 Hz, where the low frequency conditions leading to equation (28) apply, the anomalies are essentially independent of frequency and are actually magnified substantially compared to those at 100 Hz. Polarization charges on the ends or along the sides, of particular importance at the lower frequency, are responsible for apparent resistivities varying spatially by a factor of forty, as described by equation (29). In general, one expects commensurate distortions of interpreted intrinsic resistivities and interface depths for 1-D inversions performed on data gathered around such features.

Boundary polarization charges have no such persistent affect upon impedance phases, as shown in Figure 5. At the upper frequency, anomalies in excess of 15° from the phase of the host, 45° in this half-space case, may appear. At 1 Hz, secondary E-fields are essentially in phase with $\vec{E}_i^o$, the total horizontal H-field is roughly uniform and phase anomalies barely reach 5° from the normal 45° for ϕ_{yx}. Impedance phase anomalies for small-scale geoelectric noise, as exemplified by this feature, are limited in frequency range.

In Figure 6, the magnitudes of the elements of the vertical admittance tensor $\tilde{Y}_z(\bar{r})$, defined by relations (31), (33) and (35), are given again for 100 and 1 Hz. Peaks in $|Y_{zx}|$ and $|Y_{zy}|$ appear over the sides and ends of the conductor respectively. The anomalies in

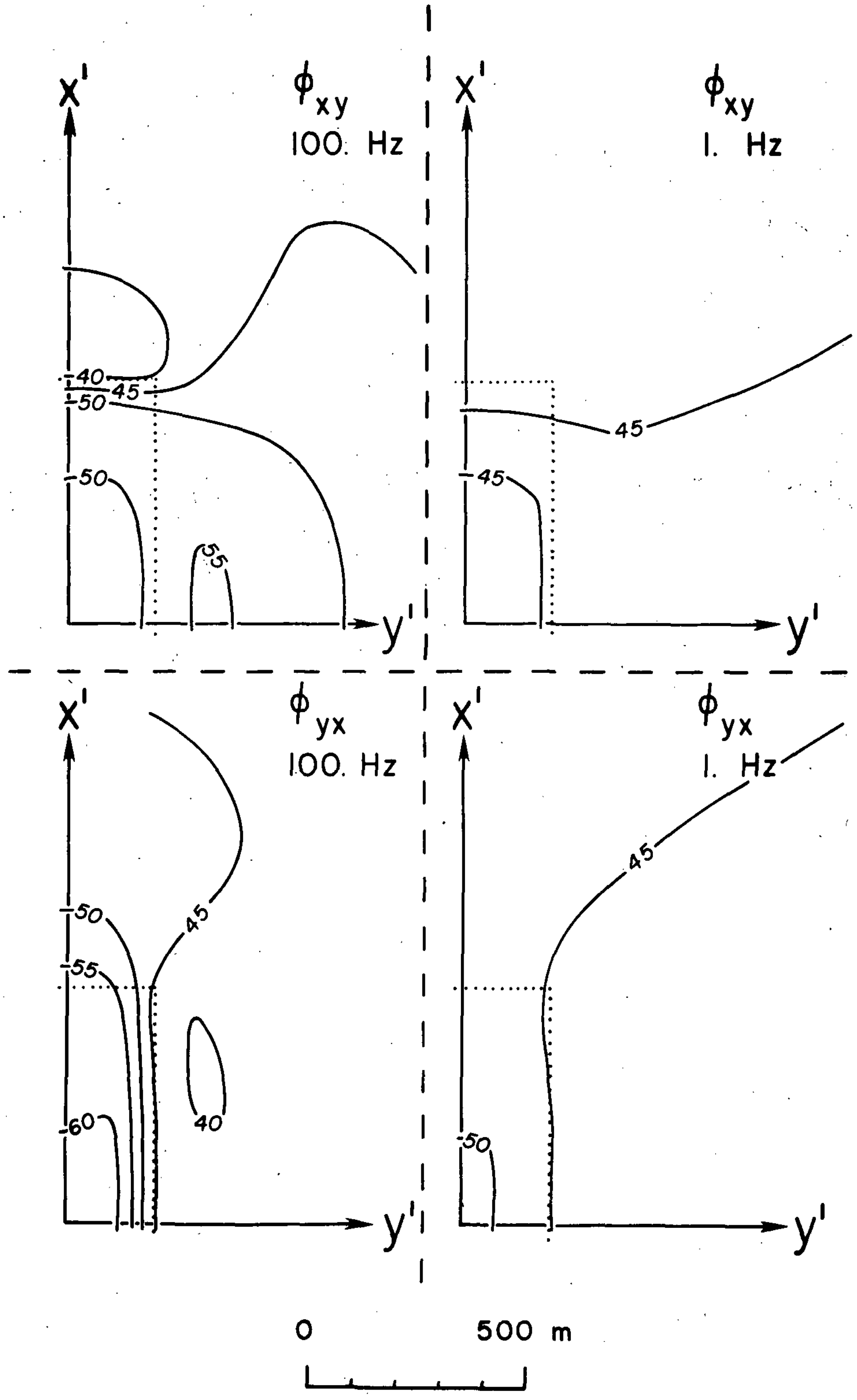

Figure 5. Plan maps of contoured impedance phase (degrees) over upper right quadrant of 3-D body of Figure 3 at 100 Hz and 1 Hz.

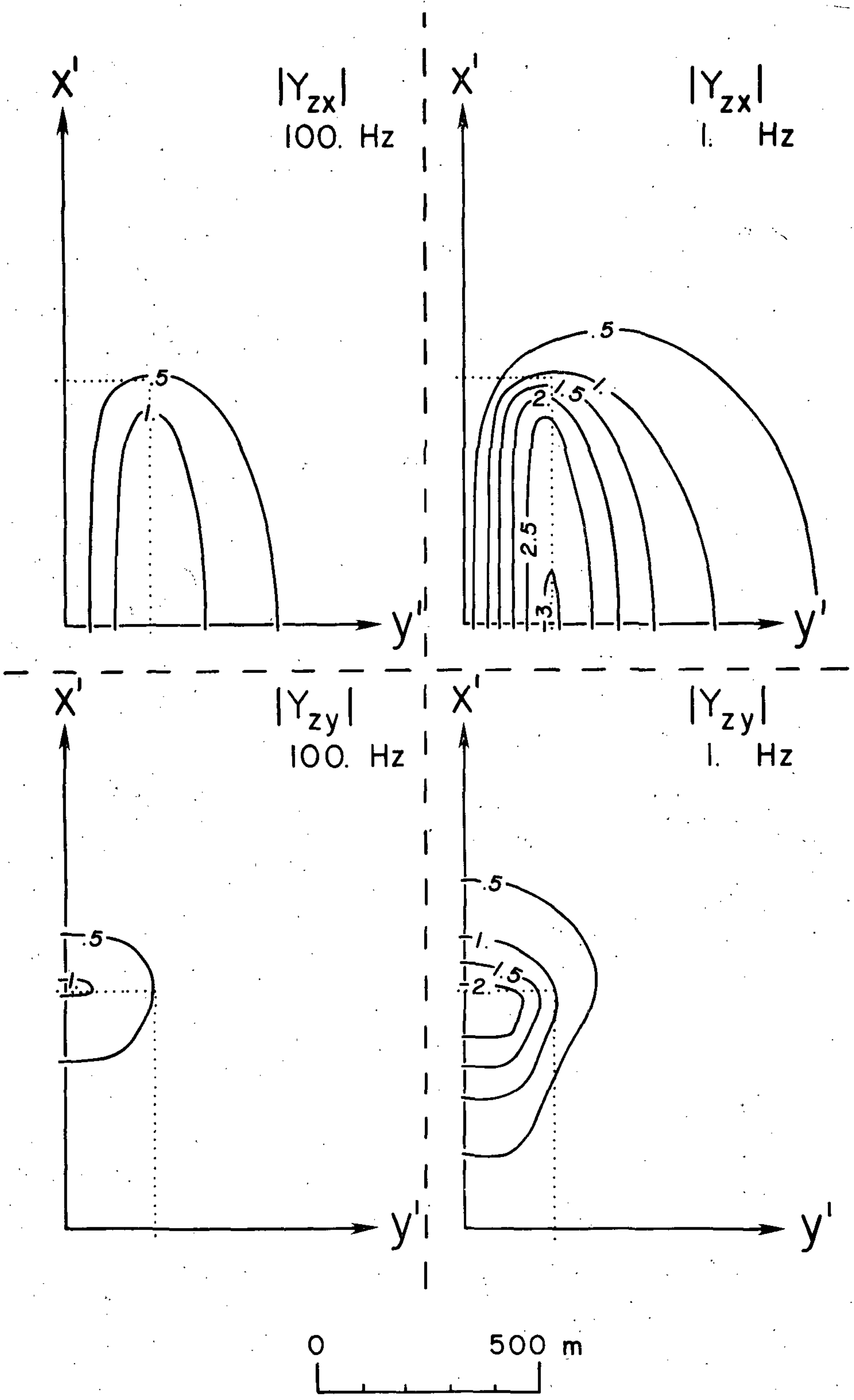

Figure 6. Plan maps of contoured vertical admittance magnitudes over upper right quadrant of 3-D body of Figure 3 at 100 Hz and 1 Hz. Contour values are in S/m.

admittance magnitudes are substantially greater at 1 Hz than at 100 Hz since, at the upper frequency, a skin depth in the host is about 500 m, comparable to the depth extent of the body. There is a lesser volume of scattering current in relation to the incident electric field and scattered fields from currents near the bottom of the conductor are more attenuated as they propagate to the surface for 100 Hz.

Complicated anomalies in admittance phase appear in Figure 7 for 100 Hz. To the rather complex behavior over the prism, it is difficult to assign physical significance. Something may be noted however concerning the rather linear spacing of the phase contours at 100 Hz at distances of 800 m or more from the center of the inhomogeneity. With the skin depth in the host being close to 500 m, far field or radiation contributions to the secondary fields are important in this region. Furthermore, due to electromagnetic and geometric attenuation of the secondary fields, the vertical admittance tensor at this distance is roughly a relation between the secondary vertical magnetic field and the horizontal primary electric field, $\vec{E}_i^o$. Hence this linear phase transition represents the outward propagation of a secondary EM wavefront from this essentially electric dipole scatterer. At 1 Hz, as expected from equation (41), the admittance phase has asymptoted to near 180° for Y_{zx} and zero for Y_{zy}.

Plan maps of tipper element magnitudes (Figure 8) agree with equation (40). At 100 Hz anomalies in excess of 0.25 appear over the side of the body for $|K_{zy}|$ and in excess of 0.15 over the end of the body for $|K_{zx}|$. At 1 Hz though, the values have decreased markedly, barely exceeding 0.05 for $|K_{zy}|$. This effect, which is in contrast to

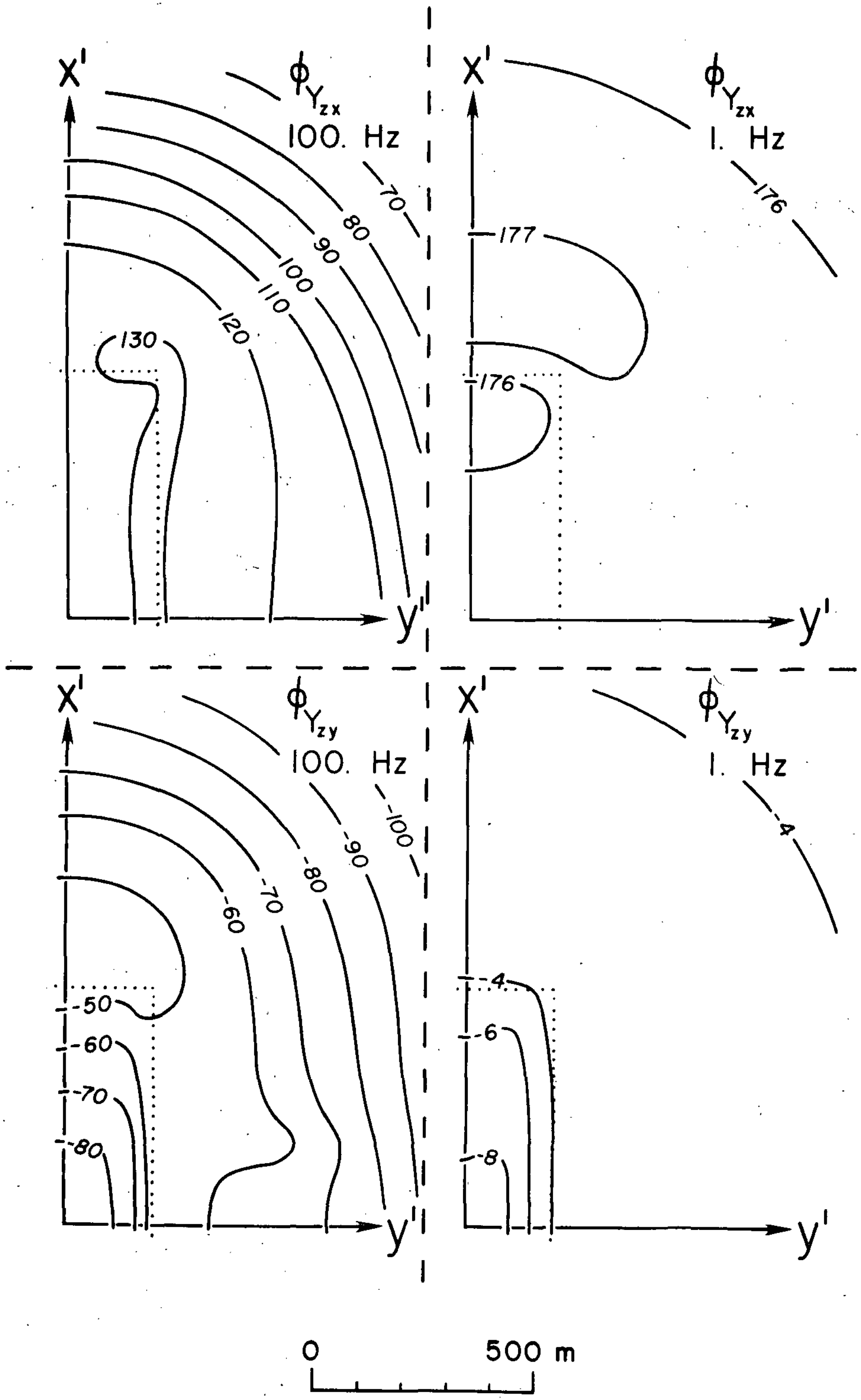

Figure 7. Plan maps of contoured vertical admittance phase (degrees) over upper right quadrant of 3-D body of Figure 3 at 100 Hz and 1 Hz.

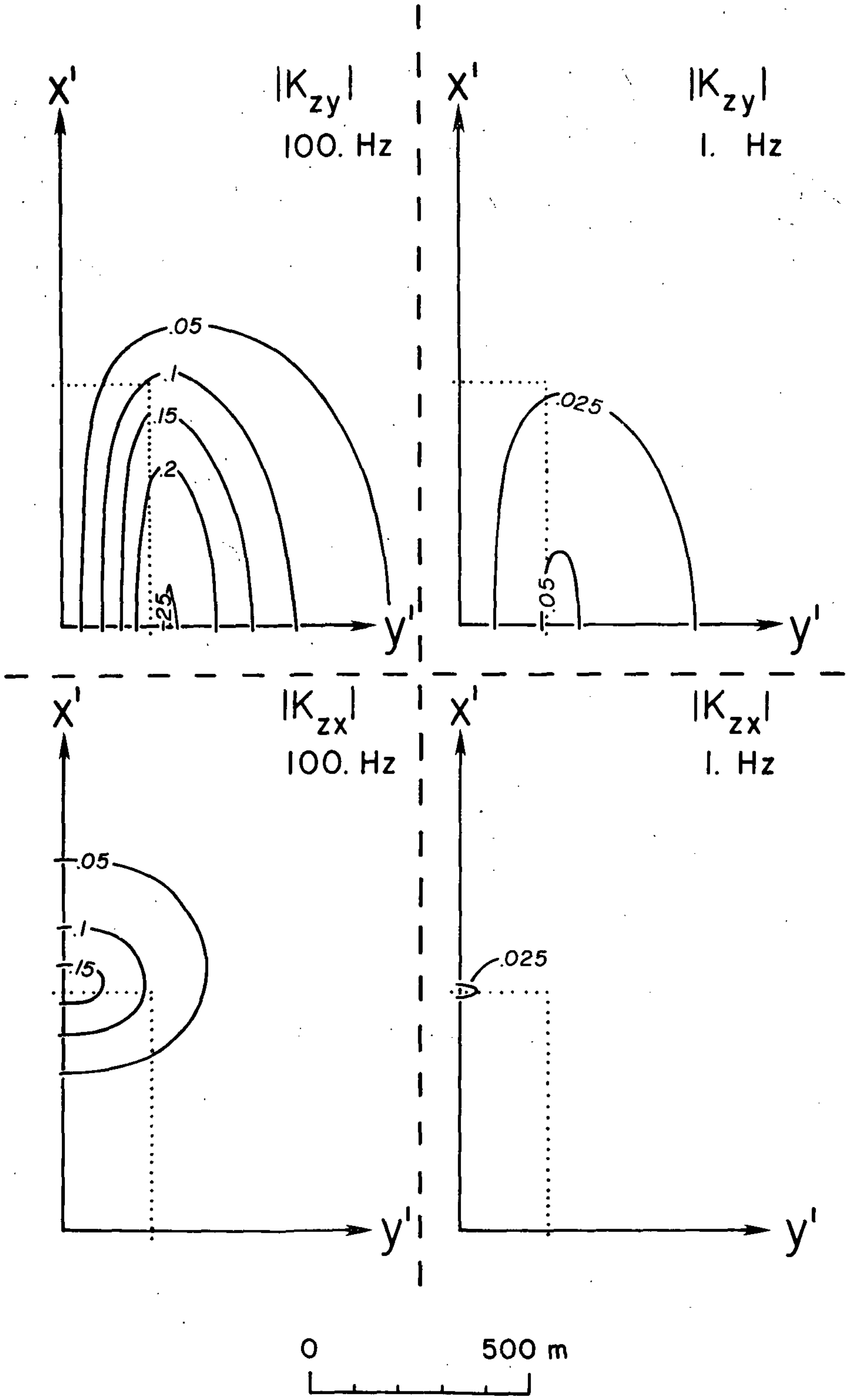

Figure 8. Plan maps of contoured tipper element magnitudes over upper right quadrant of 3-D body of Figure 3 at 100 Hz and 1 Hz. Contours are dimensionless.

that of the vertical admittance elements which are larger at 1 Hz, is overwhelmingly due to the attenuation of Z_ℓ in equations (22) and (40). The tipper, as defined by relation (42), can roughly be obtained from a superposition of the anomalies of K_{zx} and K_{zy} in Figure 8 and hence one expects its behavior at lower frequencies to be consistent with (43).

As in the case of the vertical admittance elements, the phases of the Tipper elements at high frequency are complicated functions of position, especially right over the body as shown in Figure 9. Again though, the outward linear variation of phase at distances of 800 m or so from the center of the prism represents the outward propagation of the secondary wavefront. At 1 Hz, as anticipated, the phases of the elements approach that of the host, which is 45° in this half-space case.

Valley Sediments Model

After considering the effects of the prism chosen to represent an alteration zone, herein considered to constitute near surface geoelectric noise when attempting to model deep structures at RHS, we now wish to examine a feature of a much bigger scale (see Figure 10). On the basis of gravity, seismic refraction and DC resistivity surveys, the Milford Valley sediments may be simulated by a large plate, 36 km long by 14 km wide by 1 km thick (Ward et al, 1978; Gertson and Smith, 1979). The interior resistivity is 2 Ω-m while that of the host is 400 Ω-m. To get good numerical results, the plate has been buried 1 km, nevertheless the basic behavior of a sediment-filled graben for MT will still be apparent. The scattering current within the conductor was

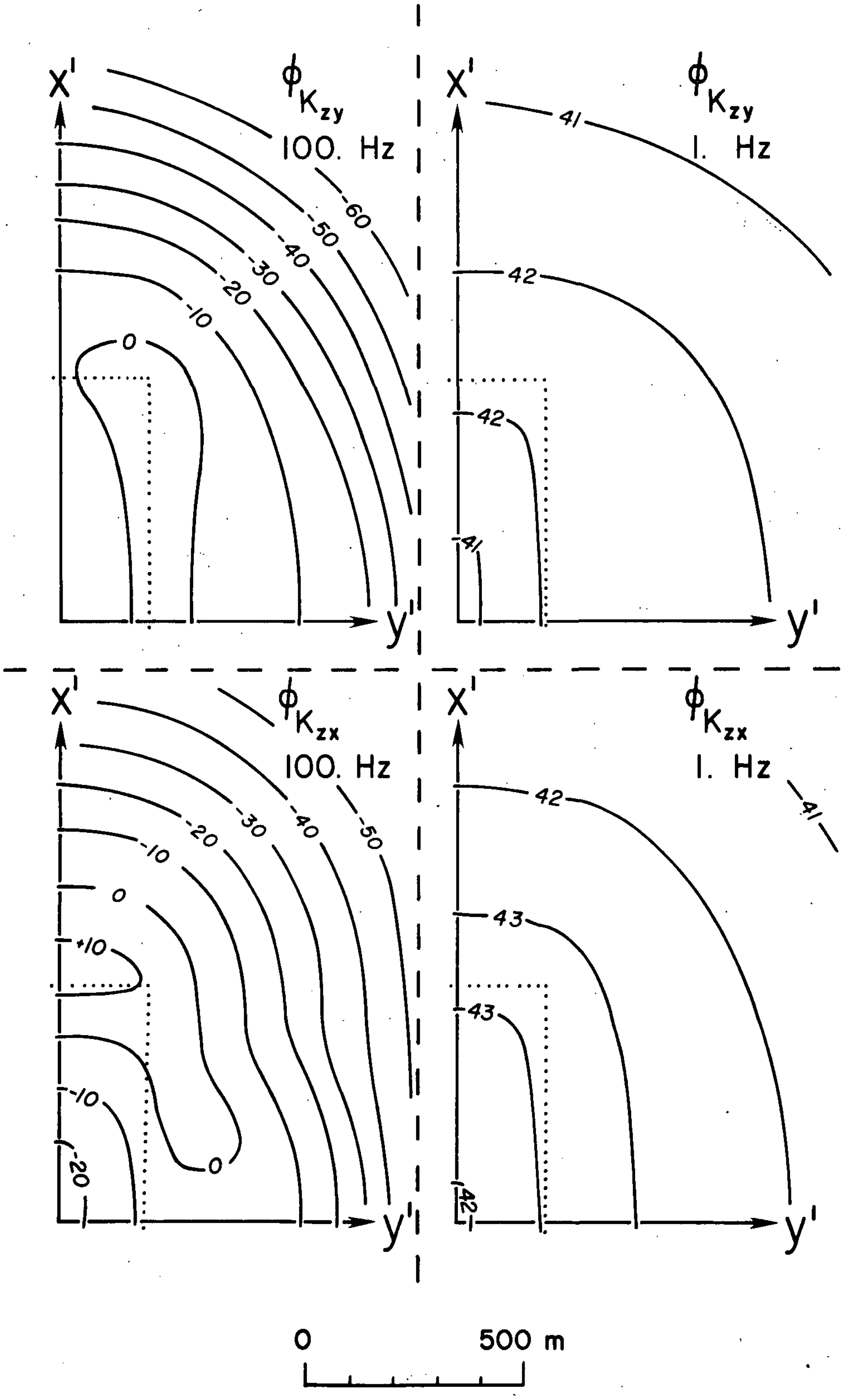

Figure 9. Plan maps of contoured tipper element phase (degrees) over upper right quadrant of 3-D body of Figure 3 at 100 Hz and 1 Hz.

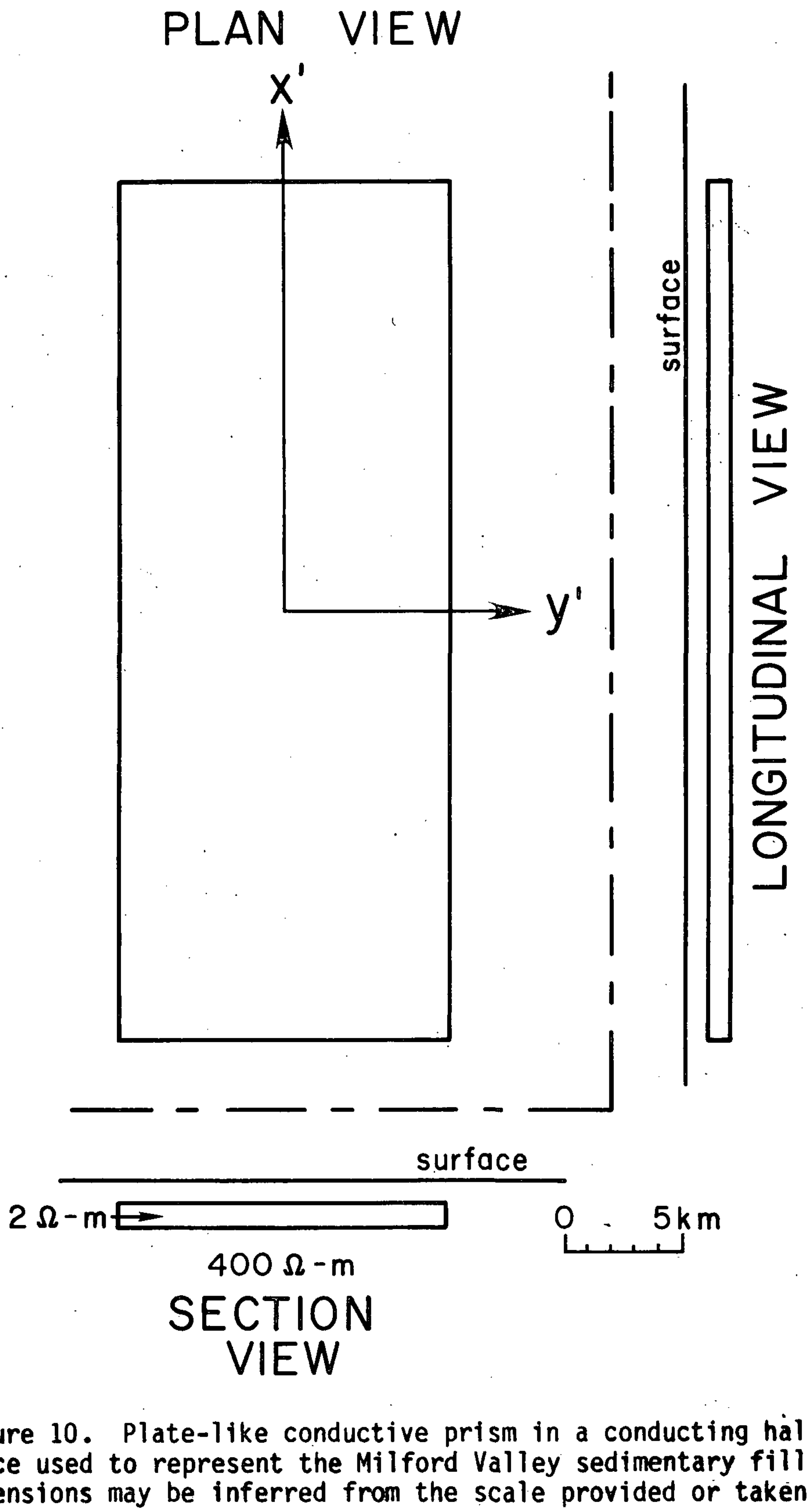

Figure 10. Plate-like conductive prism in a conducting half-space used to represent the Milford Valley sedimentary fill. Dimensions may be inferred from the scale provided or taken from main text.

approximated by 126 cubic cells 1 km each in size. Forming and solving the matrix for the interior current required about 14 hrs CPU time per frequency on the minicomputer while calculating the secondary fields at the surface required an additional 7 hrs.

<u>Regional Current-Gathering</u>: In Figures 11a and 11b, total electric field polarization ellipses for two directions of incident E-field vector show the important consequences of the valley sediments upon MT observations in the area. As with the alteration zone model, symmetry allows us to present only the upper right quadrant of results. The ellipses are shown for a rather low frequency, 0.003 Hz, and are hence virtually linear, distorted only in relative magnitude and orientation from the incident electric vectors at the surface, shown in the legends. Due to boundary charges, current-gathering along the sides of the valley for $\vec{E}^{o}_{i1}$ and along the ends for $\vec{E}^{o}_{i2}$ results in a regional distortion of the electric field within the valley sediments and to distances of 20 km or more from the valley center. This E-field behavior, notably the undershoots and overshoots across the sides for $\vec{E}^{o}_{t1}$ and across the ends for $\vec{E}^{o}_{t2}$, is the determinative factor in the apparent resistivity signatures, to be discussed soon, and will be seen to invalidate 1-D and 2-D TE interpretation schemes.

<u>MT Strike Estimations</u>: MT strike estimations can be useful for identifying preferred geoelectric directions along with significant variations in those directions. Four such estimations around the valley prism appear in Figure 12, two involving the secondary vertical magnetic field (K_z- and Y_z-strike) and two involving an off-diagonal impedance element (Z- and ϕ-strike). In 12a, the solid and dashed

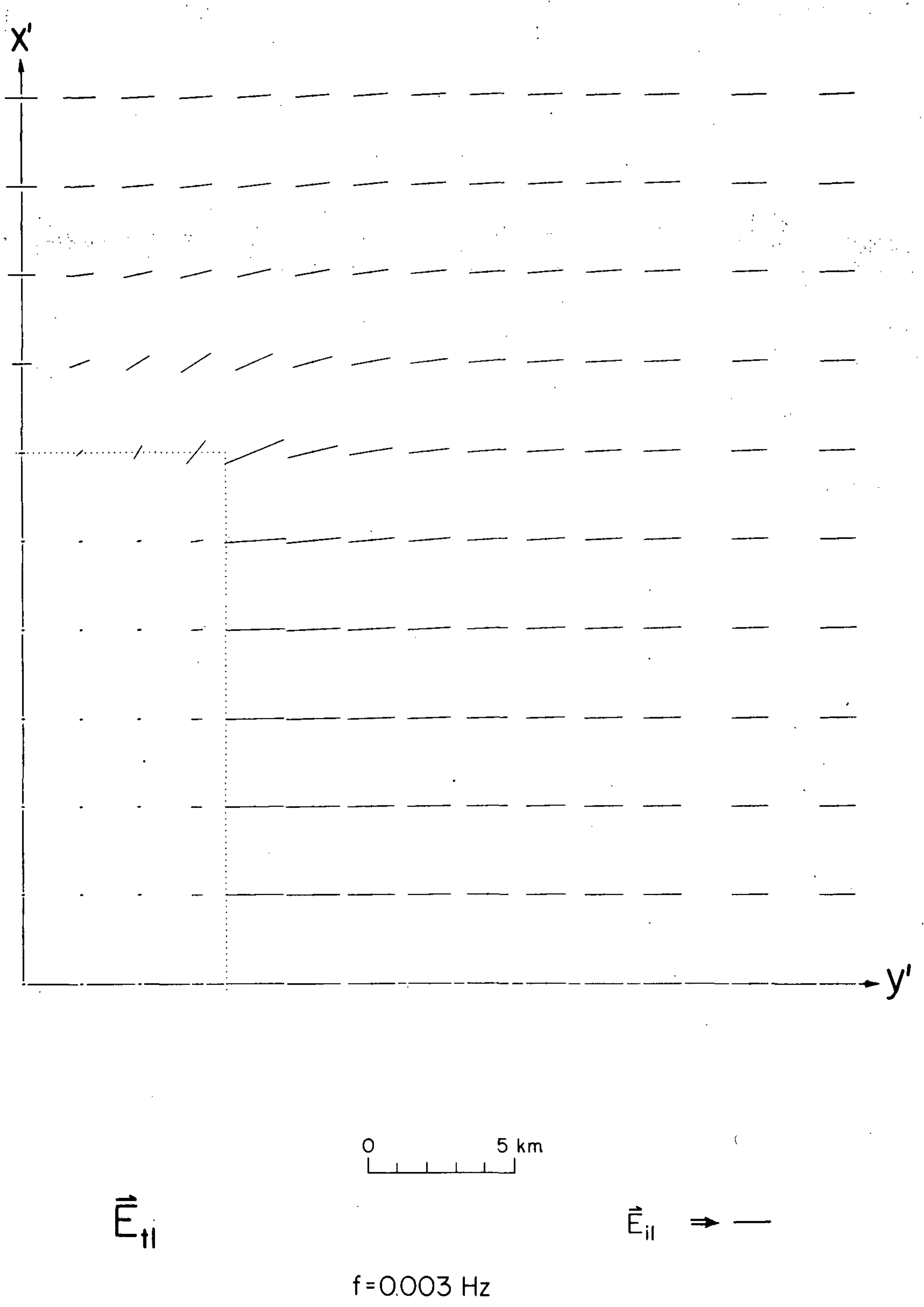

Figure 11a. Total electric field polarization ellipses at the surface over the upper right quadrant of 3-D body of Figure 10. The orientation and amplitude of the incident field at the surface is shown in the lower right corner. The frequency is also 0.003 Hz.

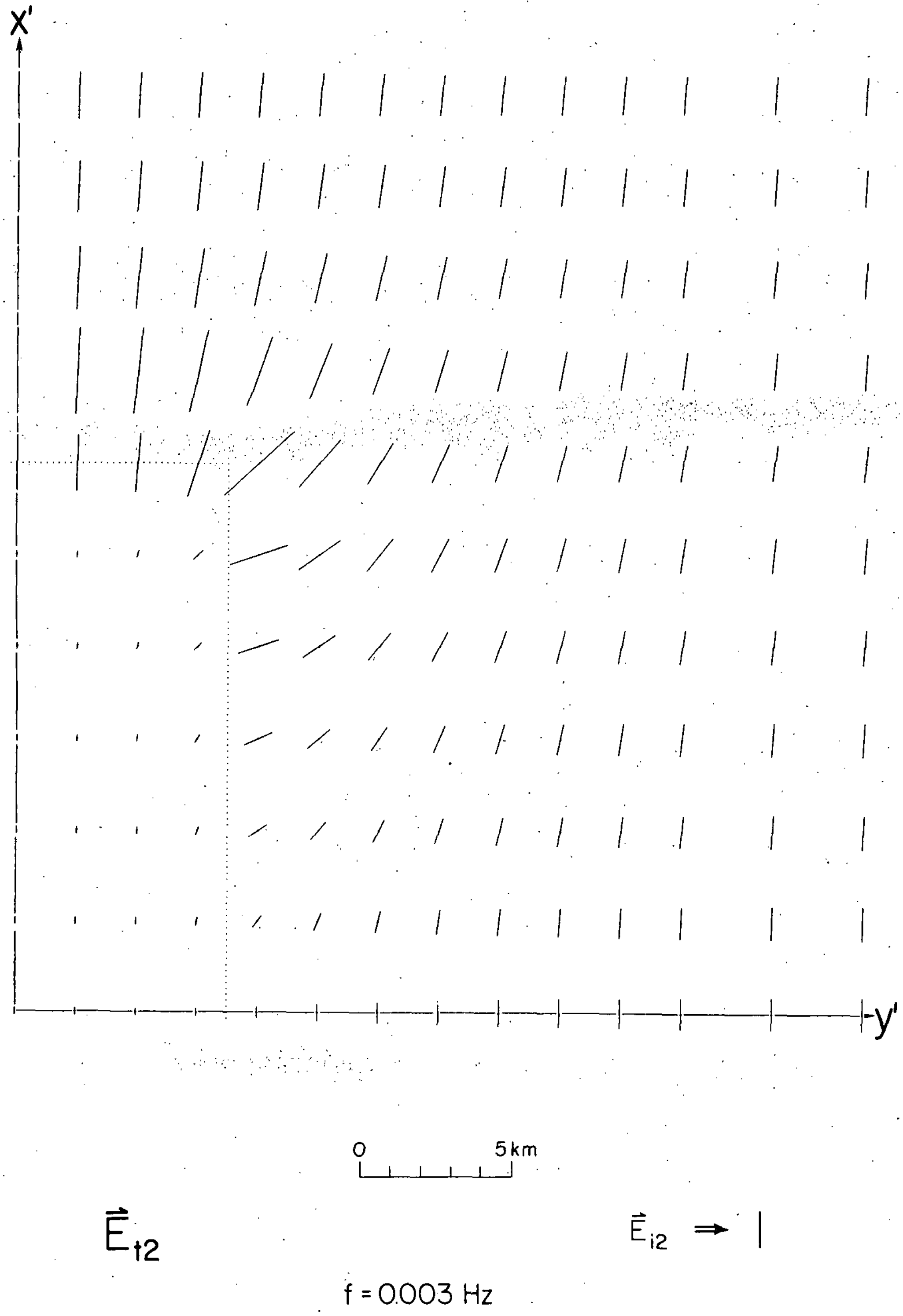

Figure 11b. Total electric field polarization ellipses at the surface over the upper right quadrant for a different polarization of $\vec{E}_i$. Frequency is also 0.003 Hz.

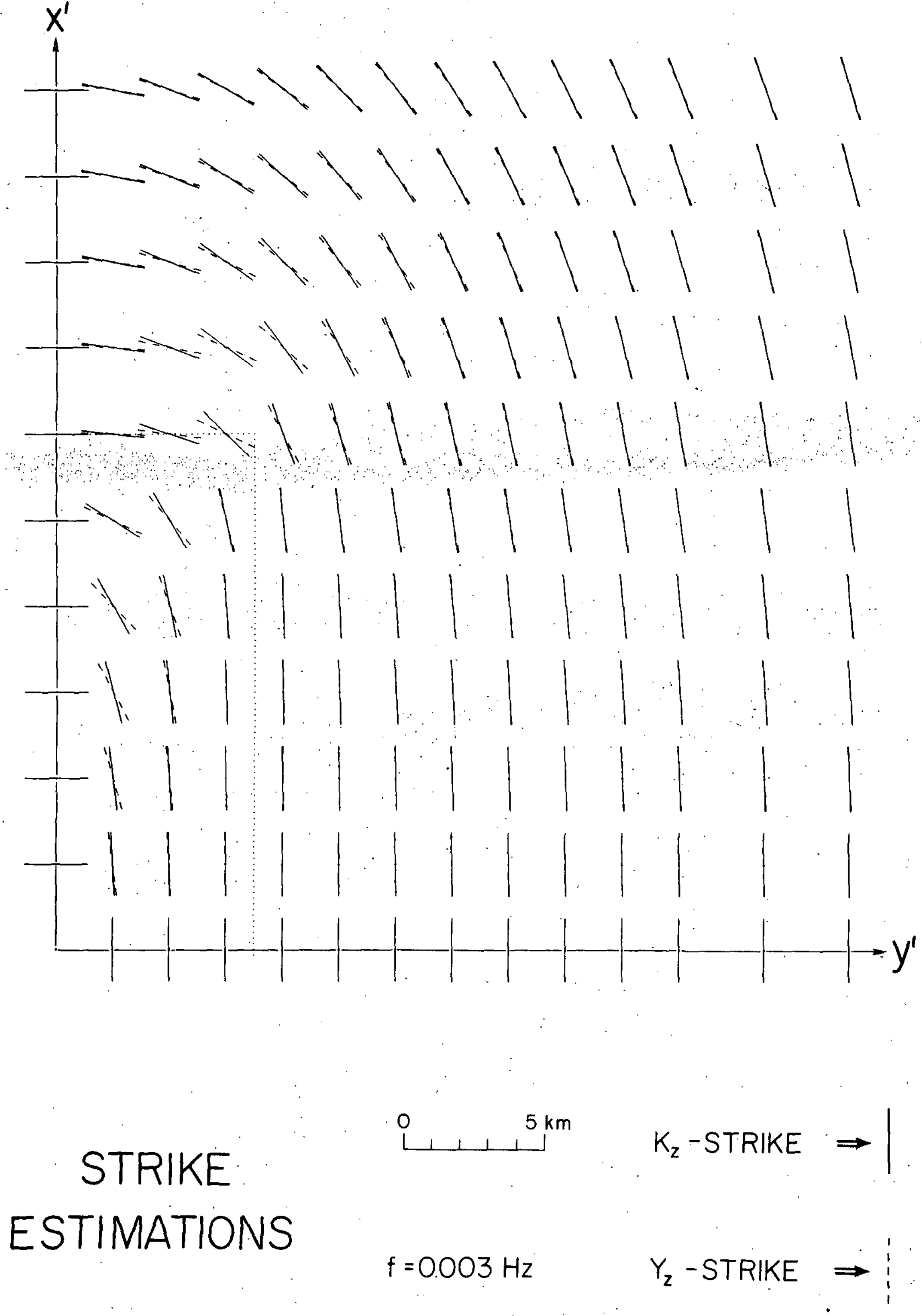

Figure 12a. Azimuths of MT strike estimations around 3-D prism of Figure 10 based upon maximizing $|K_{zy}|$ and $|Y_{zx}|$. The frequency is 0.003 Hz.

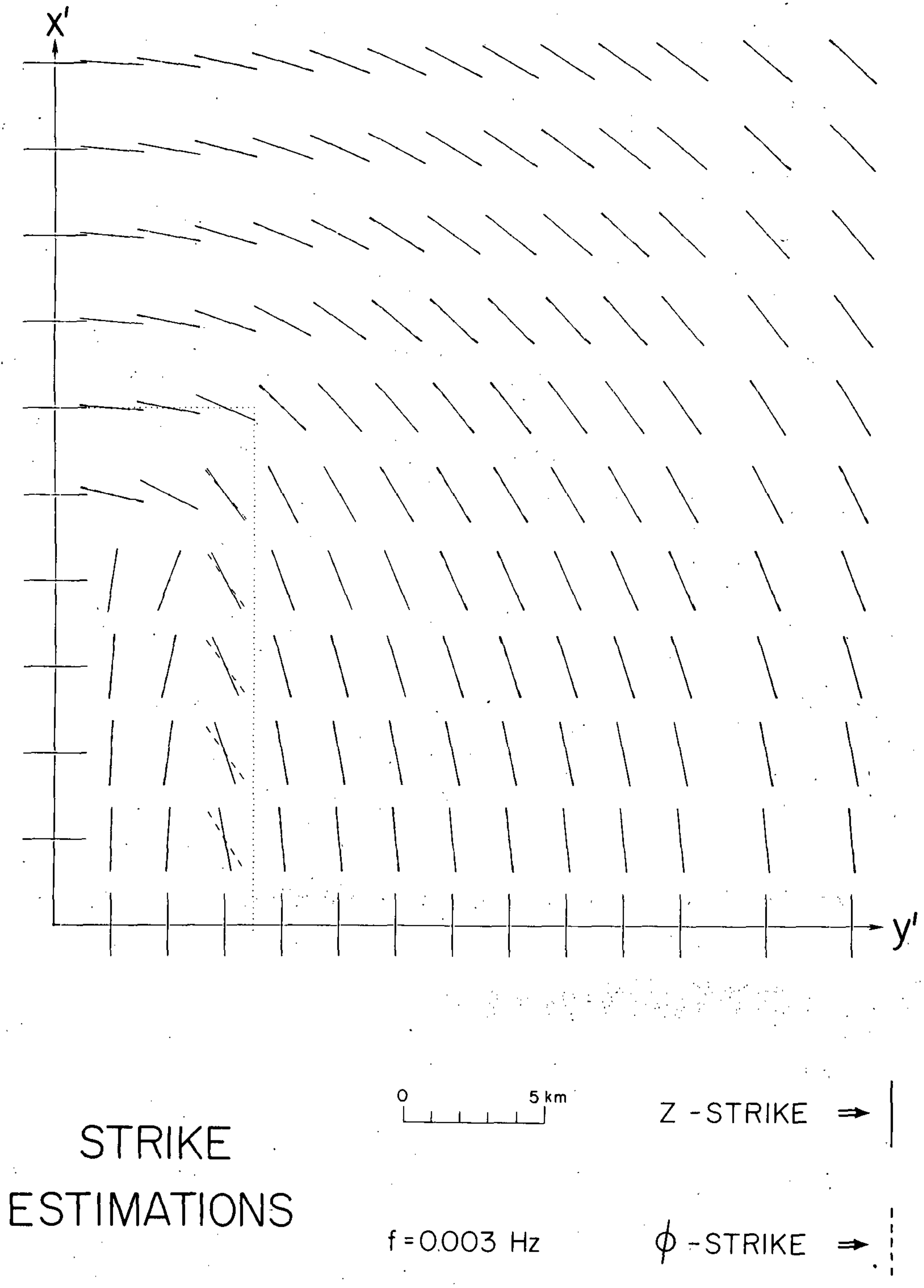

Figure 12b. Azimuths of MT strike estimations around 3-D prism of Figure 10 based upon maximizing $|Z_{xy}|$ and $|\phi_{xy}|$. The frequency is 0.003 Hz.

lines were obtained respectively by an incremental rotation (1° increments) of the data axes until $|K_{zy}|$ and $|Y_{zx}|$ were maximized. For a 2-D geometry, these elements maximize when the x data axis parallels structural strike, and at this point as well $|K_{zx}|$ and $|Y_{zy}|$ become zero. For the 3-D valley prism, both the estimators are not uniform throughout the quadrant but swing from the x'-direction as one leaves the y'-axis and parallel the y'-direction as one approaches the x'-axis. The agreement between the two estimators is quite close for this single body. Both mimic the N-S trend of the eastern edge of the prism for receiver positions generally to the east of its center, where the majority of soundings in the RHS area would be situated.

In Figure 12b, the solid and dashed lines were obtained by maximizing $|Z_{xy}|$ and $|\phi_{xy}|$, respectively. If a resultant axis varied by more than 45° from K_z-strike at a given receiver location, 90° was added to this value so it could be considered a true strike estimation. Such an addition was required generally for Z-strike over and exterior to the plate's right-hand edge and for ϕ-strike directly over the area of the plate. For a 2-D geometry, these latter two estimators also parallel structural strike. Furthermore, similar behavior to that for K_z- and Y_z-strike occurs for the 3-D model where the estimator directions swing through 90° as one leaves the y'-axis and approaches the x'-axis. Z- and ϕ-strike are somewhat less consistent in their azimuths than the other two estimators, particularly over the valley prism itself, but in general they do a reasonable job. We should mention at this point that the direction which maximizes $|\phi_{xy}|$ is not necessarily 90° away from that which minimizes $|\phi_{yx}|$ for an arbitrary

3-D geometry, though it should be fairly close. We have no good reason at present to favor the maximizing direction and this matter will be pursued in future model studies.

Apparent Resistivities and Impedance Phases: Multifrequency profiles in Figures 13 and 14 of apparent resistivities and impedance phases for the 3-D valley model further our understanding of the limitations of 1-D and 2-D methods of interpretation in the RHS area. In Figure 13 for ρ_{xy} and ϕ_{xy} we compare first for the 3-D case results of a profile at x' = 0 km, directly over the center of the prism, with results at x' = 9 km, half-way towards the end of the prism. For x' = 9 km, the responses drawn with short dashes correpond to receiver site x-axes parallel to K_Z-strike while responses drawn with dots correspond to ϕ-strike. Symmetry of the conductor permits us to show just the calculations extending along the y'-axis from y' = 0 over the center. Figure 12 has shown that K_Z-strike, Y_Z-strike and the x'-axis of the inhomogeneity are all close to parallel for these two profiles so that what one says concerning MT quantities rotated according to K_Z-strike will also apply for the other two directions. One may make a similar statement concerning ϕ-strike and Z-strike. The three 3D profiles of Figure 13 for ρ_{xy} and ϕ_{xy} all agree well with each other at all frequencies. At 0.003 Hz, a small irregularity in ρ_{xy} is observed for the ϕ-strike direction, this being due to small variations in this strike estimator as one crosses the edge of the plate.

The 3-D curves are compared to the 2-D TE counterpart for a valley model of infinite strike length in the x'-direction (Rijo, 1977; Stodt, 1978). At 0.3 Hz, the 2-D TE and 3-D signatures agree to a large

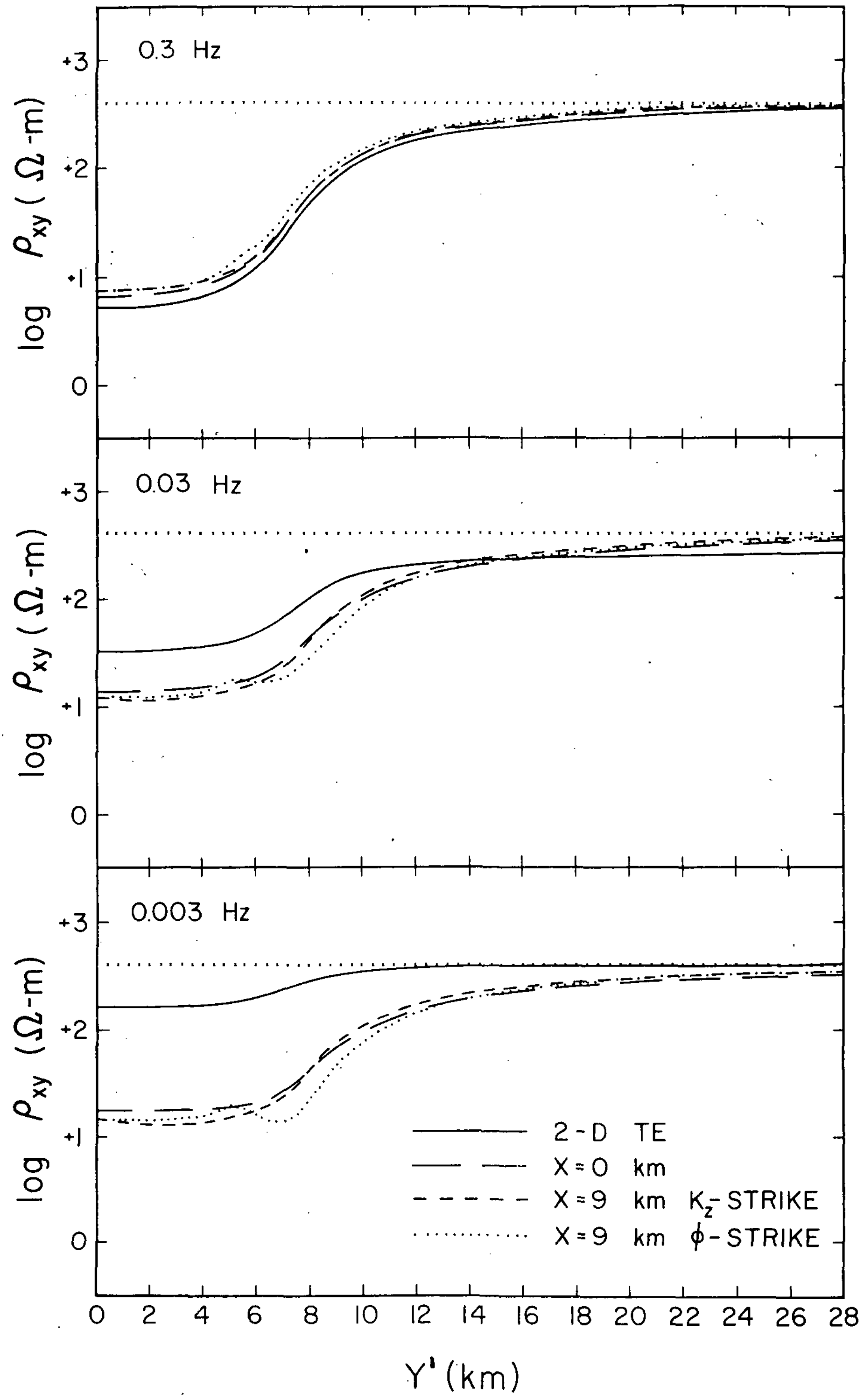

Figure 13a. Profiles of ρ_{xy} extending from center of valley prism along its y'-axis at x' = 0. The 2-D TE curve is compared as a solid line. Horizontal rows of tiny x's represents the host apparent resistivity of 400 Ω-m.

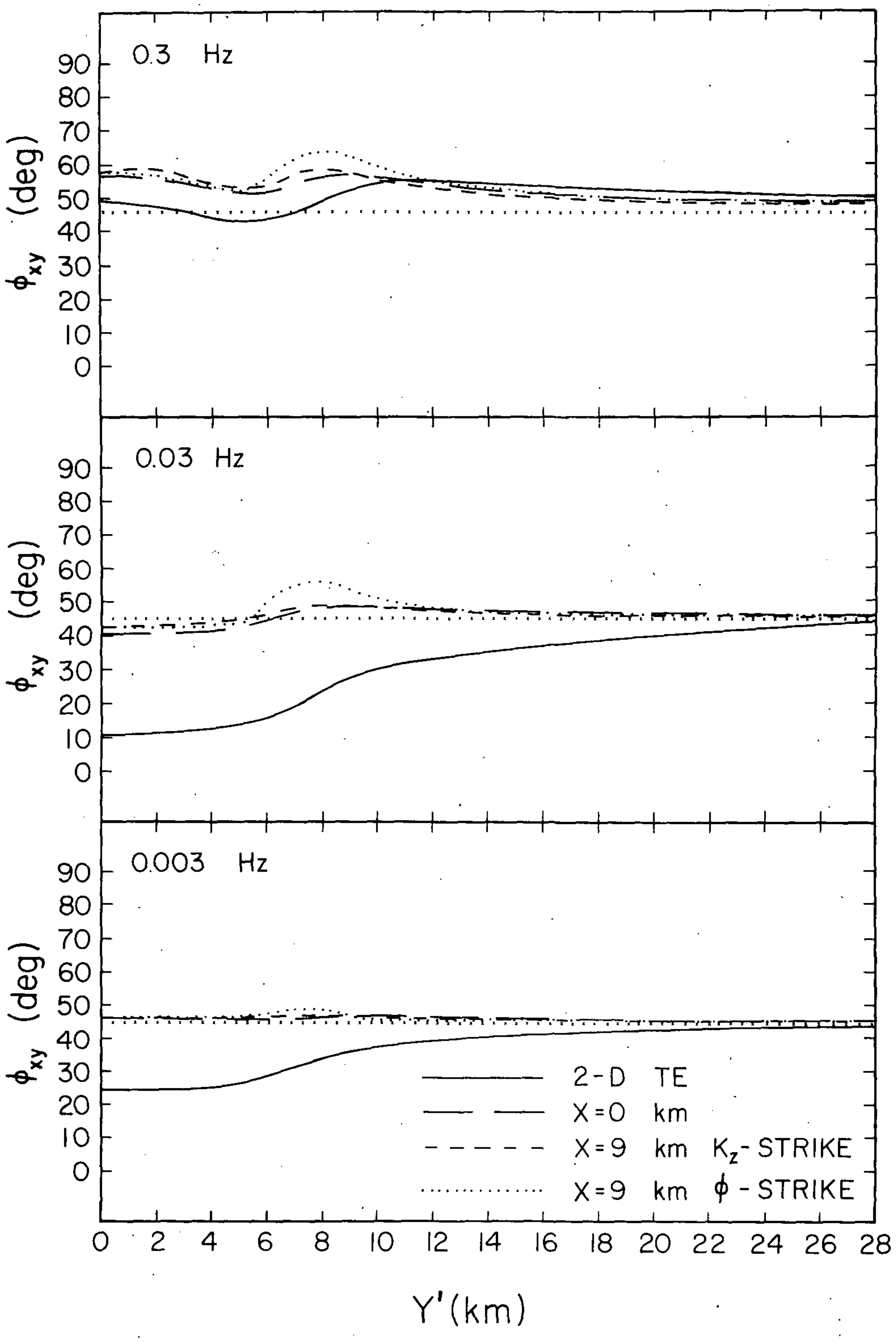

Figure 13b. Profiles of ϕ_{xy} extending from center of valley prism along its y'-axis at x' = 0. The 2-D TE curve is again compared as a solid line. Horizontal rows of tiny x's represent the host impedance phase of 45°.

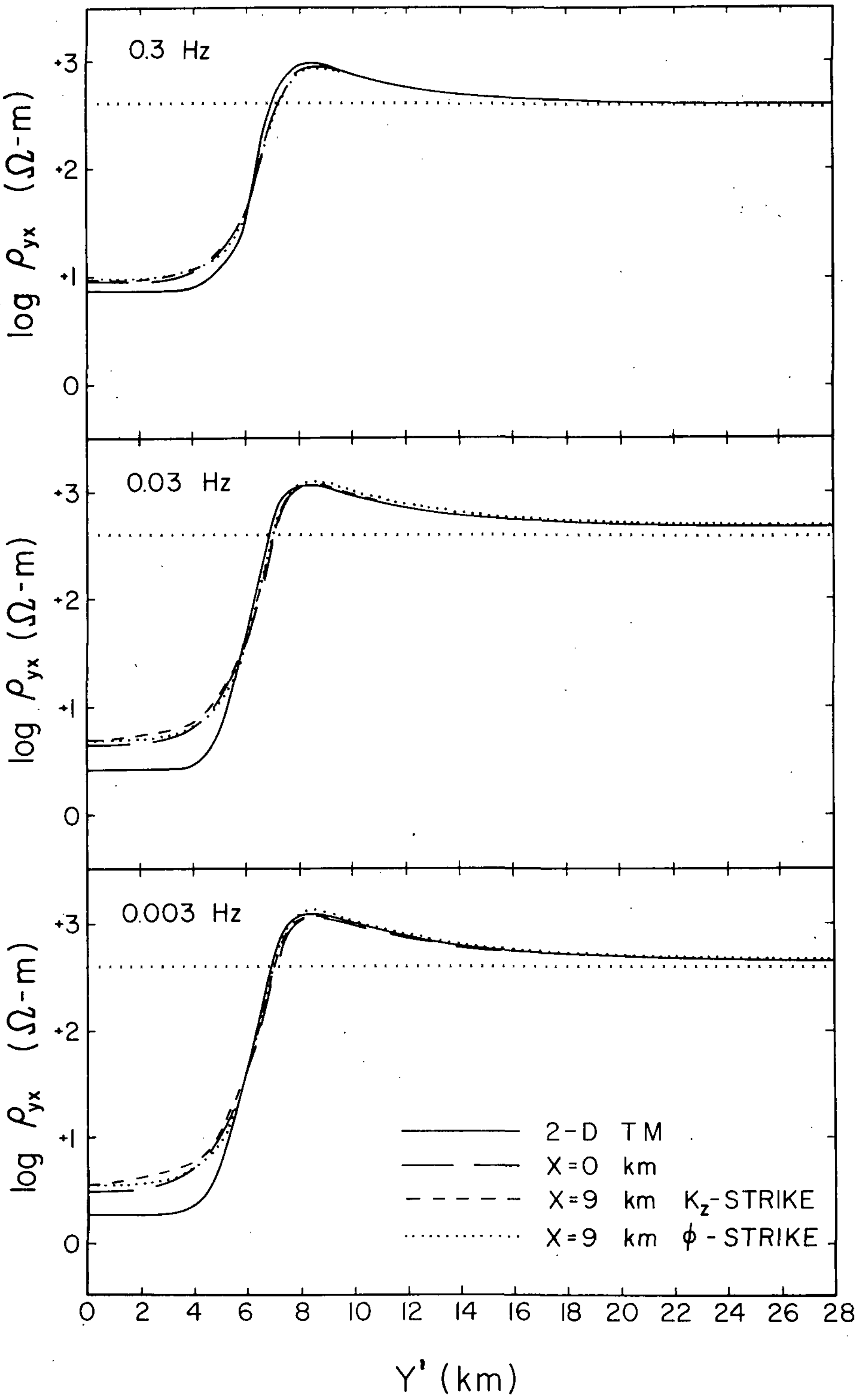

Figure 14a. Profiles of ρ_{yx} extending from center of valley prism along its y'-axis at x' = 0. The 2-D TM curve is compared as a solid line. Horizontal rows of tiny x's represent the host apparent resistivity of 400 Ω-m.

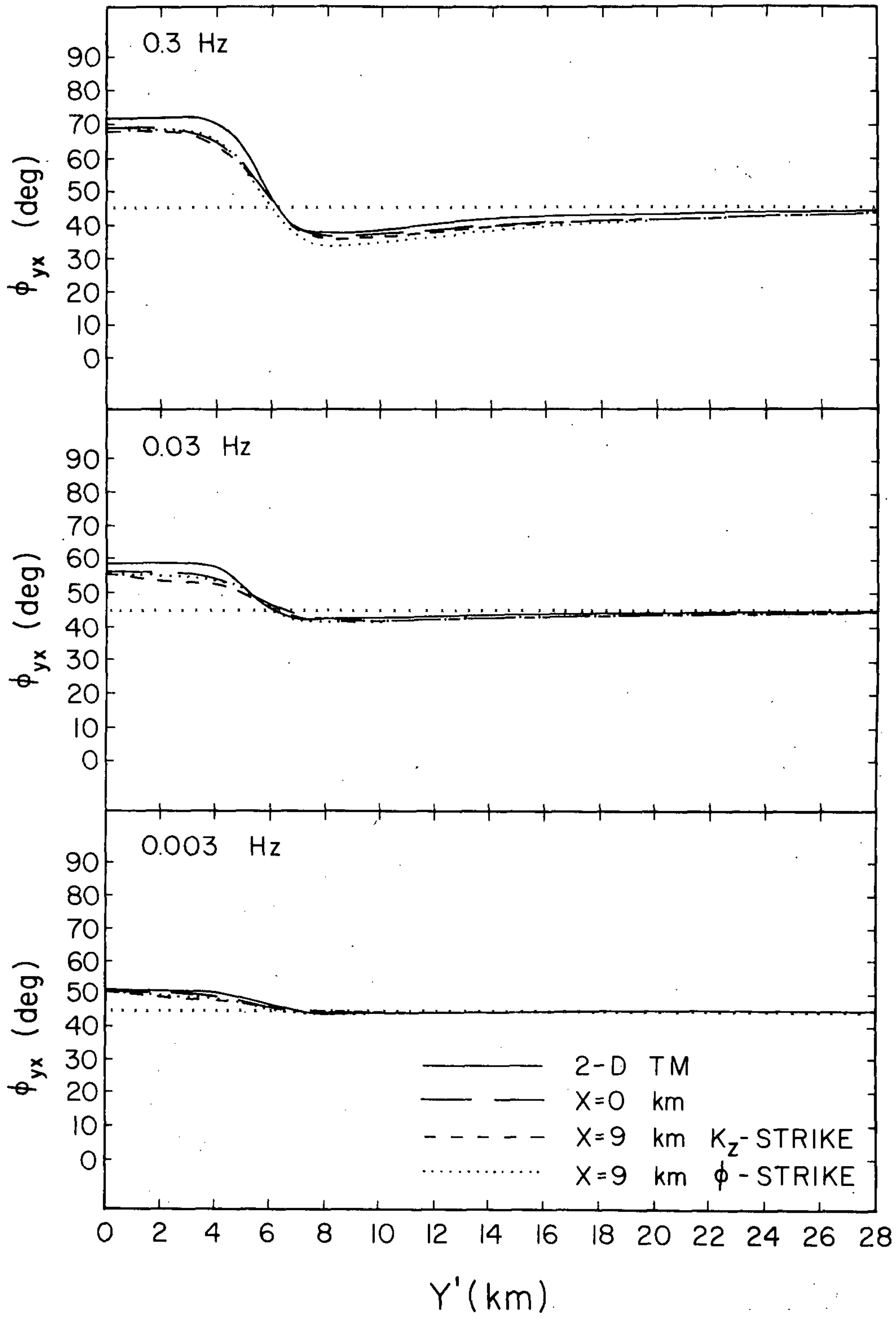

Figure 14b. Profiles of ϕ_{yx} extending from center of valley prism along its y'-axis at x' = 0. The 2-D TM curve is again compared as a solid line. Horizontal rows of tiny x's represent the host impedance phase of 45°.

extent, particularly for ρ_{xy}. There is some departure observed in ϕ_{xy} right over the valley and we believe that 0.3 Hz is the frequency for this valley model below which 2-D TE anomalies differ significantly from their 3-D counterparts. At lower frequencies, the disagreement is outstanding, especially at 0.03 Hz for ϕ_{xy} and 0.003 Hz for ρ_{xy}. Since in the 2-D TE formulation electric fields are everywhere parallel to resistivity contacts, surface charges do not appear. Due to this and the diminishing importance of volume currents at low frequencies, the wave equation (3a) for E_{sx} of the section on theory will hence approach the homogeneous Laplace's equation and the secondary electric fields will vanish. The contribution of the secondary magnetic field, as given by equation (17b), will also decrease at low frequencies. This combined behavior of electric and magnetic fields will eventually result in a decay of the 2-D TE responses to those of the host medium, which is 400 Ω-m for ρ_{xy} and 45° for ϕ_{xy}. The 2-D signatures though are still rather far from their low frequency limits at 0.003 Hz in Figure 13 and we note that it is variations in the total H-field that are responsible for the anomalies in ρ_{xy} and ϕ_{xy} at this frequency. Laplace's equation does approximately hold now for electric fields yet the volume currents within the 2-D prism are large enough to cause a substantial secondary H-field, essentially in phase with the incident E-field at the surface. However since this secondary H-field is not in phase with the primary H-field, variations in both ρ_{xy} and ϕ_{xy} occur. Concerning the 3-D model, boundary charges occurring mainly along the ends of the valley prism are primarily responsible for the differences in 2-D and 3-D signatures. Such charges cause a depression of the total E-field within the valley, as shown in Figure 11b, lasting to arbitrarily low frequencies. A similar depression in ρ_{xy} follows. The finite strike length of the prism also appears responsible for the 3-D values of ϕ_{xy} approaching 45° of a higher frequency than is the case for the 2-D model. The relatively small values of electric field at any point within the valley prism mean relatively small values of the scattering current density. This and the lesser total volume of scattering currents for the finite strike length conductor result in a rather small secondary magnetic field compared to the primary H-field. Along with the fact that Poisson's equations (20) and (21) roughly govern E- and H-fields at 0.003 Hz, the relative uniformity of the horizontal magnetic field results in frequency-independent behavior of ρ_{xy} and values of ϕ_{xy} near 45° for the 3-D body.

In Figure 14 we compare ρ_{yx} and ϕ_{yx} for the 3-D geometry along the same profiles at $x' = 0$ km and $x' = 9$ km and for the same strike estimators K_z-strike and ϕ-strike. The three 3-D profiles again all agree closely with each other at all frequencies. Furthermore, they all compare well with the 2-D TM signatures for an infinite strike length valley model. The 2-D ρ_{yx} appears somewhat smaller than its 3-D counterparts right over the valley while the 2-D ϕ_{yx} appears somewhat larger than that of the 3-D curves but we do not believe the discrepancy is significant. The secondary electric field at the surface, which is what the 3-D routine initially computes, nearly cancels the incident E-field over the prism so that small errors in the secondary field may lead to large errors in the total field. A disagreement of $\sim$2% between the secondary electric fields of the 2-D and 3-D programs is sufficient to cause the observed discrepancies in ρ_{yx} and ϕ_{yx}. We can by no means guarantee better accuracy than that with the modeling algorithms. The reason for the good comparison between 2-D and 3-D responses for this model is twofold. First, the transverse magnetic mode for the 2-D body includes boundary charges in its formulation. Current-gathering along the sides of the structure hence occurs in both 2-D and 3-D cases. Second, the condition of finite strike length causes very little secondary magnetic field along the two profiles considered for this mode. In the purely 2-D TM polarization, no secondary magnetic fields occur.

Multiple Body Model

Figure 12 has demonstrated that use of any of the four strike estimators shown yields reasonable estimates of preferred geoelectric trends for the single, geometrically regular 3-D valley prism. Figures 13 and 14 indicate that a 2-D TE algorithm would be restricted to frequencies above 0.3 Hz for modeling the valley structure over the profiles considered but that 2-D TM routine might be applied successfully at any frequency. Nonetheless, it is important to inquire whether small-scale shallow geologic noise in the vicinity of a larger structure like the valley sediments invalidates any of the previous conclusions in the immediate neighborhood of these conductors. In Figure 15 we show a rather more complicated inhomogeneity with three relatively conductive (6 Ω-m) small prisms enclosed in a less conductive plate-like host of 40 Ω-m which itself exists in a resistive medium of 400 Ω-m. The interior prisms have lengths of 1200 m and

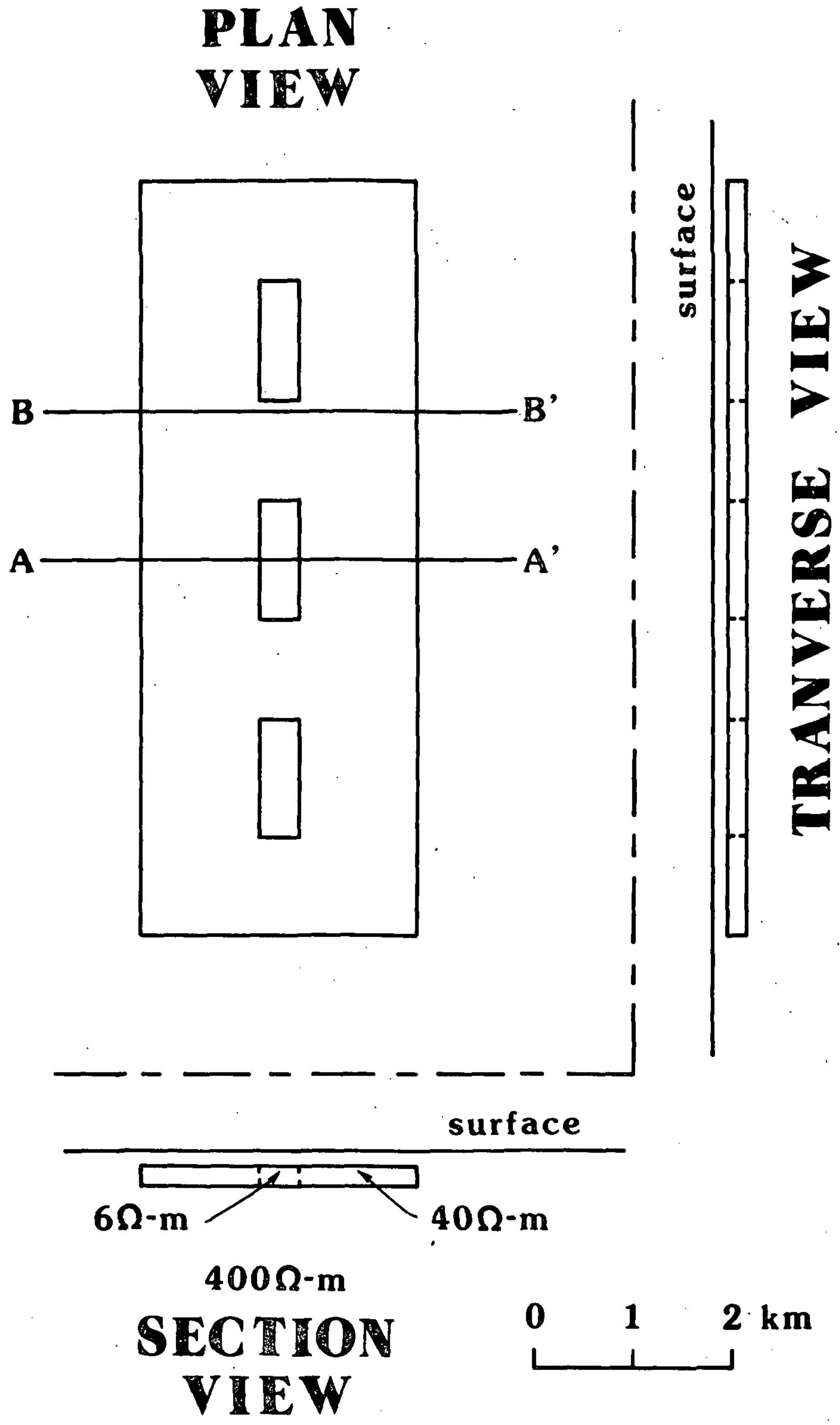

Figure 15. 3-D inhomogeneity representative of variable near-surface hydrothermal alteration coincident with the observed thermal anomaly at RHS. MT quantities along profiles A-A' and B-B' are discussed in text.

widths of 400 m while the larger surrounding structure is some 7600 m long by 2800 m wide. The composite feature has a thickness of 200 m and a depth to top of 150 m. Such a construction is crudely representative of the northward oriented series of variable hydrothermal alteration zones surrounded by brine-saturated, partially altered alluvium and/or bedrock (Tripp et al, 1978). This feature is modeled in conjunction with the valley sediments prism of Figure 11 and its center is positioned along the y'-axis of the valley model at y' = 10500 m. Such a simultaneous consideration allows a study of how seriously small-scale geoelectric noise may distort MT quantities due to large structures to arbitrarily low frequencies.

The inhomogeneity of Figure 15 was approximated by 126 cubic cells each 200 m in size. Computation times on the Prime minicomputer for this body by itself are essentially the same as for the valley model previously described. The calculations involving the valley and this alteration model together were accomplished using the multiple body approximation described in the section on coupled body considerations. The total fields around the valley alone were used as source fields for the smaller lateral inhomogeneity. Such an approach assumes that the smaller feature does not affect the scattering currents in the larger and that the fields from the larger are essentially uniform and horizontal over the smaller. A test case for this scheme is presented in Appendix A. For the valley-alteration zones juxtaposition we believe this approximate method introduces a further numerical uncertainty to the computations of at most 10%.

The two body response was calculated at a frequency of 0.3 Hz.

This is a fairly high frequency as far as the valley prism is concerned and one observes pronounced anomalies in both off-diagonal apparent resistivities and impedance phases as well as in magnitude and phase of the vertical admittance and tipper elements. It is though a fairly low frequency for the smaller structure such that secondary fields scattered by it alone are close to in-phase with $\vec{E}_i^o$. This is a good frequency therefore to study the distortions of complex quantities arising from larger more distant structure due to nearly frequency independent current-gathering in small-scale geologic noise.

Strike Estimations: The first consequence of the smaller feature to be examined will be that upon strike estimations around the larger feature. In Figure 16 are presented the estimators K_Z-strike, Y_Z-strike, Z-strike and ϕ-strike, all defined earlier, at various locations over the smaller complicated structure. For reference, a portion of the right-hand edge of the valley is included towards the left side of the figure. In Figure 16a, we see K_Z-strike displaying a greater uniformity of azimuth than Y_Z-strike, particularly around corners of the interior conductive prisms. Even though previous EM scaling arguments for independent bodies suggested that the contribution of a large structure to $\tilde{Y}_Z(\bar{r})$ would be much greater than that of a small inhomogeneity below a certain frequency, distortions of the magnitude of the electric field around these small features are sufficient to distort the total vertical admittance function, as explained in the discussion on coupled body considerations. Over the area shown in Figure 16a, Y_Z-strike values vary from -25° to +18° from the x'-axis (positive sense clockwise), a range of 43°. On the other

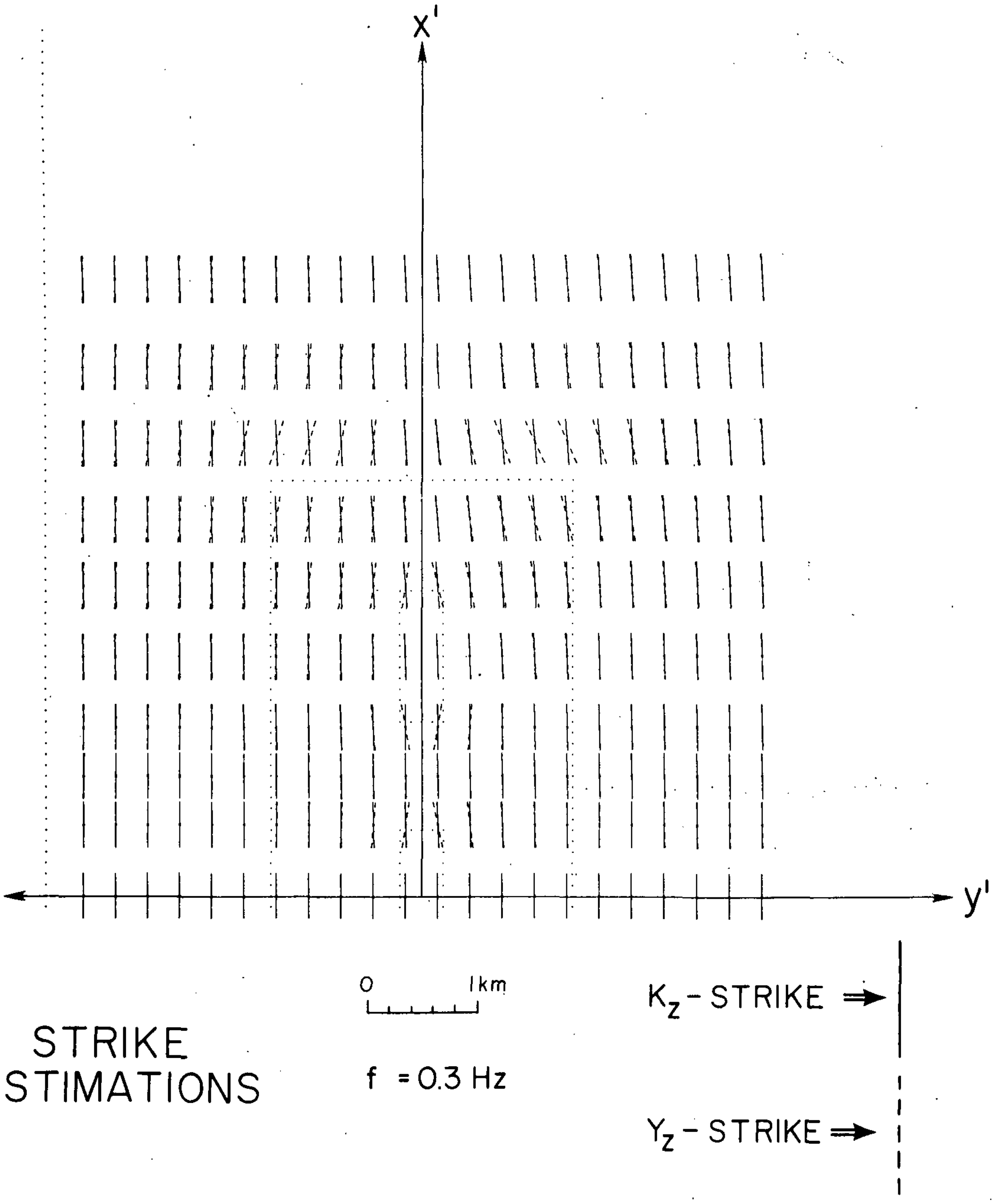

Figure 16a. Azimuths of MT strike estimations around 3-D prism of Figure 15 based upon maximizing $|K_{zy}|$ and $|Y_{zx}|$.

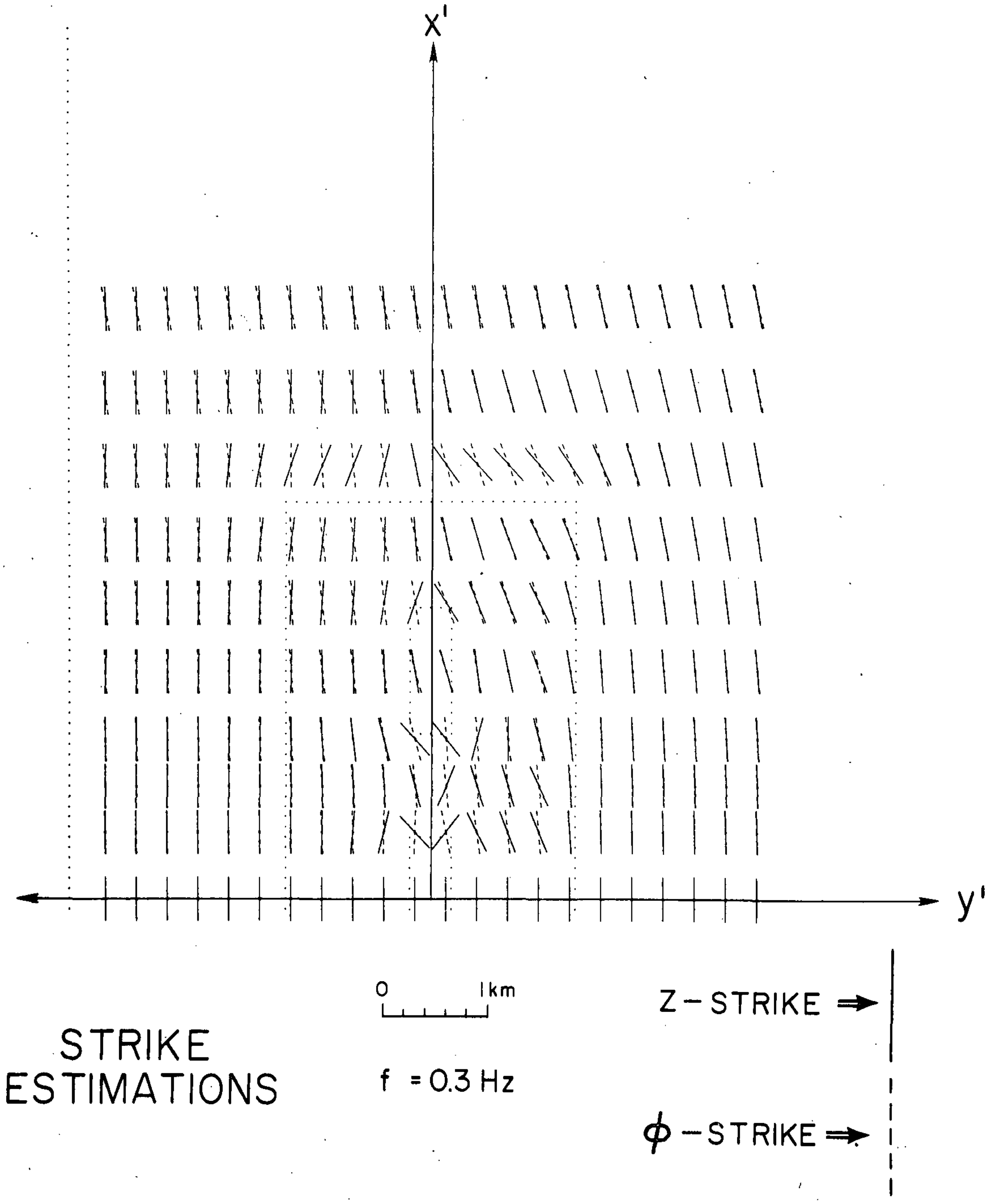

Figure 16b. Azimuths of MT strike estimations around 3-D prism of Figure 15 based upon maximizing $|Z_{xy}|$ and $|\phi_{xy}|$.

hand, contributions of the secondary magnetic field of the small structure of Figure 15 are insufficient to affect $\tilde{K}_Z(\bar{r})$ noticeably. K_Z-strike values have a range of 5° (-5° to 0° from x'-axis).

Principal axes determined by maximizing the magnitude of an off-diagonal impedance element (Z-strike) are most severely disturbed by small-scale lateral inhomogeneities. Variations in this azimuth encompass -43° to +39° from the x'-axis, a total of 82°. ϕ-strike appears to be altered to a greater degree than K_Z-strike but less than Y_Z-strike by geologic noise. Its values change from -23° to +2°, a variation of 25 degrees. In actuality, the impedance phase anomaly existing over the small structure alone approaches 3° while that of the large body alone in the area of the small approaches 20°. An inadequacy in our choice of a representative smaller feature is reflected by this. Observed impedance phase anomalies at RHS over the thermal anomaly due to near-surface conductive inhomogeneities appear to fall below 3° at 10 Hz, a frequency over a decade higher than that of our computations. The scale of variable hydrothermal alteration at RHS may appear substantially smaller than the models we have used, in an electromagnetic sense. We expect this explains some of the distortion in ϕ-strike in that the smaller hypothetical feature is still contributing actively to the overall phase response. Also, the amplitude of the electric field anomaly due to the small inhomogeneity will increase somewhat as frequency diminishes such that Y_Z-strike, and Z-strike for that matter, disturbances will be magnified. A rating is given therefore to the four estimators based upon their ability to identify major geoelectric trends in the face of geoelectric noise. In increasing order of ability they are Z-strike, Y_Z-strike, ϕ-strike and K_Z-strike.

Apparent Resistivities and Impedance Phases: By referring to Figure 17, one can compare the effects of the smaller feature versus the effects of the valley prism on the apparent resistivity. At the frequency of 0.3 Hz, profiles of ρ_{xy} and ρ_{yx} for receivers to the right of the center of the valley model and parallel to line A-A' in Figure 15 are compared to their 2-D counterparts. The cross section of resistivity structure beneath A-A;, which also applies to the 2-D model is shown at the bottom. A considerable difference between profiles of ρ_{xy} for the 3-D and 2-D TE cases is apparent in Figure 17a. While the 3-D and 2-D signatures over the valley prism agree well at 0.3 Hz, as expected from the discussion pertaining to Figure 13a, the finite strike lengths of features in the smaller structure result in a disagreement between 3-D and 2-D resistivities of about half an order of magnitude. The discrepancy is also a function of position. Profiles of ρ_{xy} taken nearer the ends of the small interior prisms show variations from the 2-D signature approaching an order of magnitude, as expected from Figure 4. That distortions of observed ρ_{xy} are as great as those of ρ_{yx} at RHS may point out other inadequancies in our theoretical model of Figure 15; intrinsic resistivity anisotropy at RHS, a greater equidimensionality on the part of the alteration and/or non-equivalence of station locations in modeled and observed cases. In the 2-D TE geometry, the anomaly due to the smaller inhomogeneity has virtually vanished. Other model studies, not discussed here, indicate 2-D TE and 3-D ρ_{xy} and ϕ_{xy} computations for such small features

Figure 17. Profiles of ρ_{xy} and ρ_{yx} extending from center of valley prism along line A-A' at x' = 0 through the smaller 3-D structure. The 2-D TE and TM curves are compared as solid lines. Horizontal rows of tiny x's represent the host apparent resistivity of 400 Ω-m. A resistivity section beneath the profile is shown at bottom.

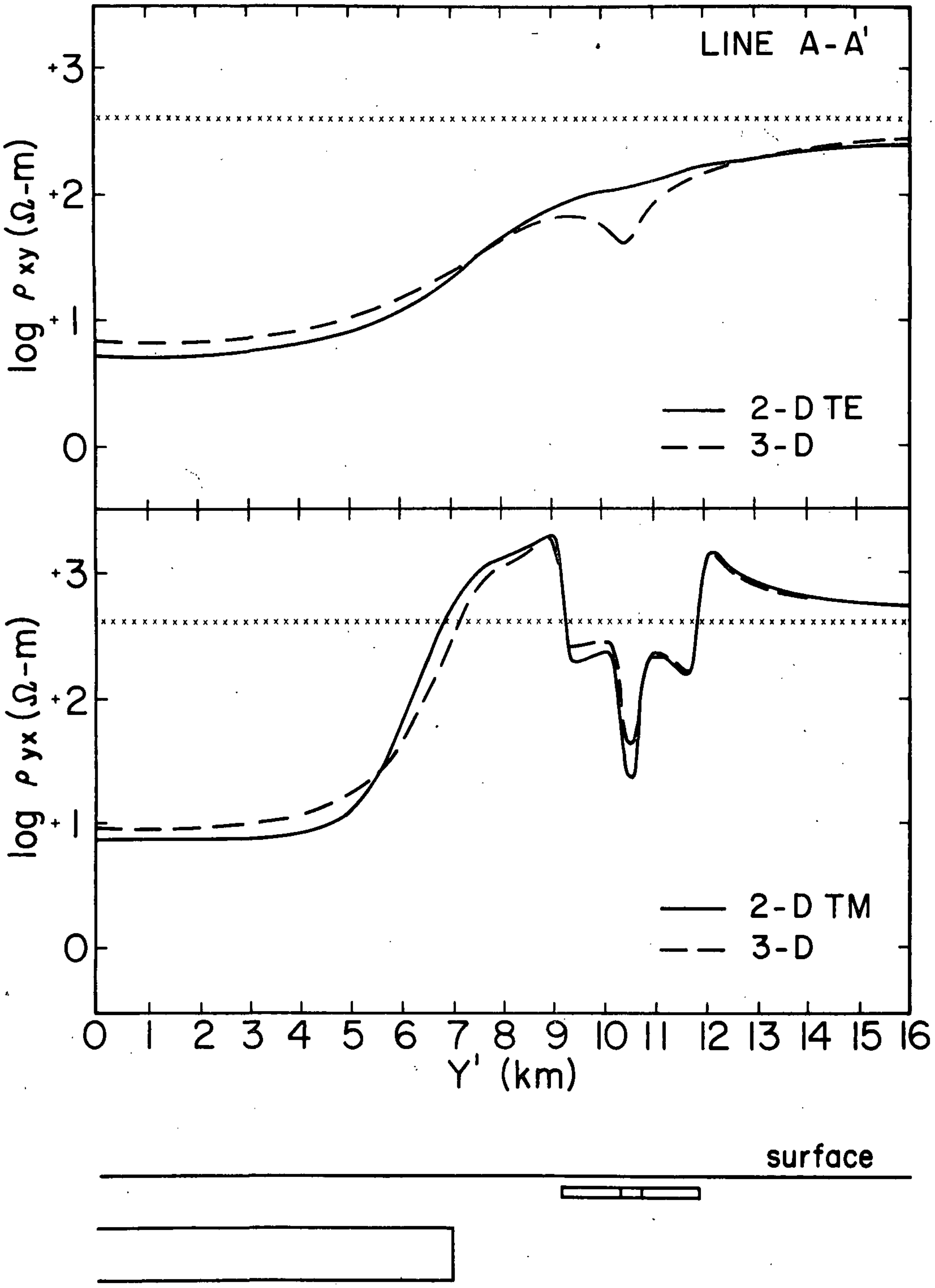
LINE A-A'
log ρ xy (Ω-m)
+3
+2
+1
0
2-D TE
3-D
log ρ yx (Ω-m)
+3
+2
+1
0
2-D TM
3-D
0 1 2 3 4 5 6 7 8 9 10 11 12 13 14 15 16
Y' (km)
surface

disagree significantly below 100 Hz. The presence of small-scale 3-D inhomogeneities has essentially invalidated application of 2-D TE modeling algorithms to all observed data at the Roosevelt Hot Springs.

In Figure 17b, both 2-D TM and 3-D ρ_{yx} curves agree within numerical uncertainty. Regardless of the scale of the structure, the quantities ρ_{yx} and ϕ_{yx} for profiles across elongated, geometrically regular 3-D prisms may be interpreted successfully using a 2-D TM algorithm. Of course, not all profiles of observations will be so favorably located, particularly with respect to the many possible manifestations of near-surface geologic noise. This will certainly lead to errors in the interpretation of these small structures. Generally though, one is not interested in describing such structures with tensor MT measurements; their evaluation is accomplished better and more cheaply using CSAMT or DC dipole-dipole resistivity surveys. Although an extensive model study has not been performed, we don't believe that such errors in the interpretation of small-scale surficial inhomogeneities will lead to systematic errors in the interpretation of deeper features of interest when a 2-D TM algorithm is used in this manner, provided the measurement profiles are properly placed over the deeper target.

Earlier in this section we discussed four strike estimators in connection with the valley prism model in Figure 12 and subsequently showed good agreement between apparent resistivity and phase profiles across and well away from the center of the body for all estimators. In Figure 16, however, Z-strike and K_Z-strike disagree greatly, for example along profile B-B'. If one wished to apply a 2-D TM modeling routine to observed data along this line, should the former or the latter strike estimator be used to judge which data may be treated as the TM mode of measurements? Plots of ϕ_{yx}, which would generally be considered the TM mode of phase, based upon these two estimators appear in Figure 18 and show marked discrepancies, particularly between y' = 10 km and y' = 11 km. Pronounced irregularities in this quantity based upon Z-strike occur along the ends of the most conductive interior prisms where the azimuths of this estimator undergo great variation. These irregularities are really due to the presence of the valley which has caused a regional anisotropy in impedance phase. At this frequency and range of apparent resistivities, our experience in modeling has taught us that such small-scale, moderately large amplitude phase expressions are not physically realizable for two-dimensional 2-D TM geometries and cannot be fit by a 2-D TM algorithm.

On the other hand, the greater uniformity of K_Z-strike yields a phase curve that is much more regular and is close to that due to the valley alone without the presence of the smaller structure. Fluctuations of about 2° appear along the closest approach of line B-B to the interior conductive prisms. A 2-D TM interpretation of ρ_{yx} and ϕ_{yx} along this profile will yield a cross section intermediate between that which is through an interior prism and that which is not. Because of this, we choose a strike direction that is uniform in the face of geologic noise, such as K_Z-strike, as preferable for estimating apparent resistivities and impedance phases to be modeled by a 2-D TM program. In the absence of reliable estimates of the tipper elements, rotation of co-ordinate axes to a uniform direction compatible with

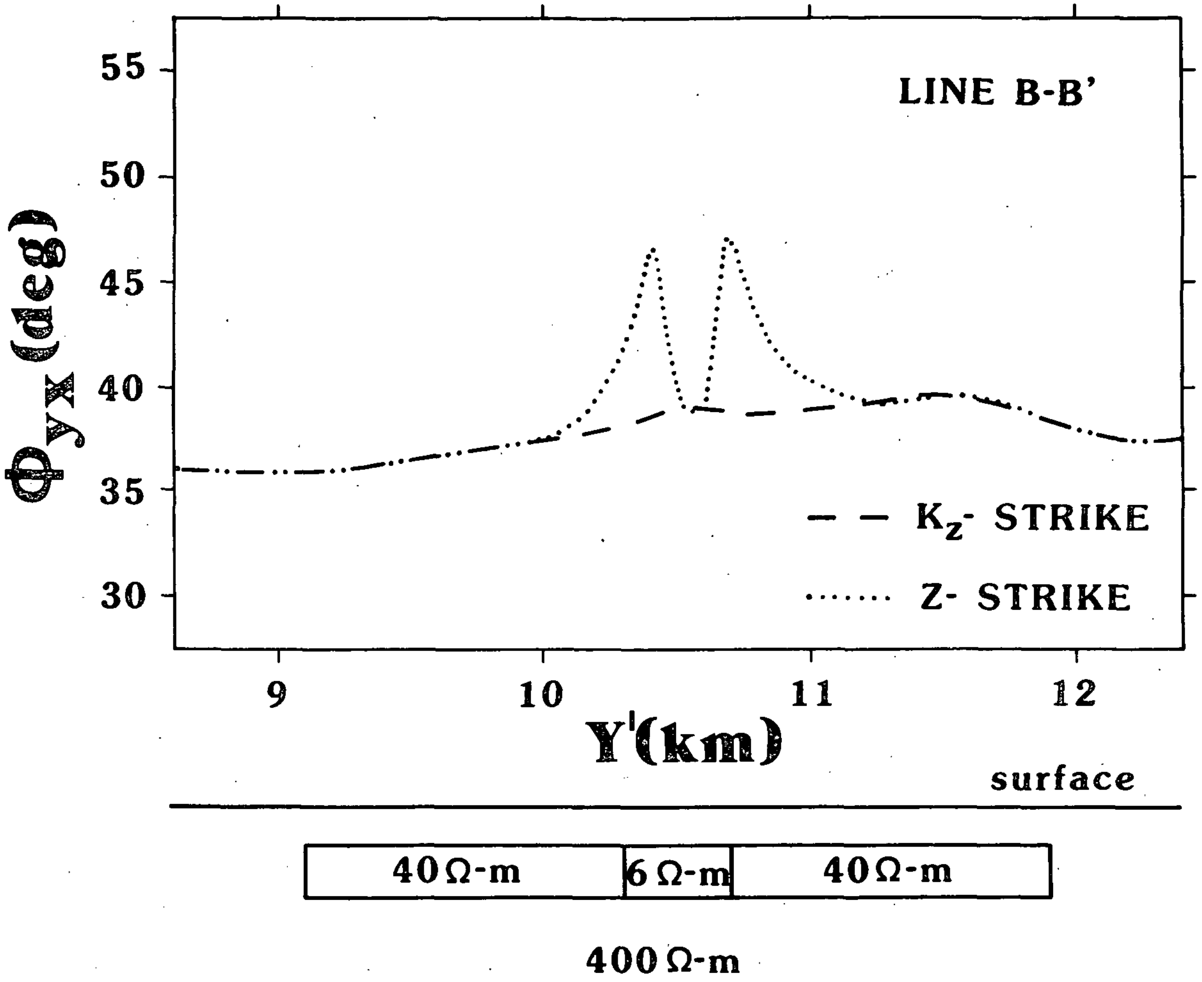

Figure 18. Profiles of ϕ_{yx} directly over the 3-D prism of Figure 15 along profile B-B' based upon estimators K_z-strike and Z-strike. A resistivity section beneath the profile is shown at bottom.

regional geologic trends, if clear regional trends are apparent, should give roughly equivalent results.

Summary of 3-D Model Studies

Both the discussion of theory and the previous model results have pointed out that small, shallow inhomogeneities may lead to MT anomalies as pronounced as those due to a much larger resistivity structure, although the former are much more limited spatially. At relatively high frequencies, rather complicated signatures result, particularly for the phase of the vertical admittance and tipper elements, relating to an outwardly propagating secondary wavefront. At sufficiently low frequencies such that Poisson's equations are approximately the governing relations for fields over and within the solitary 3-D body, the MT quantities are to first order those of a static electric dipole in the earth. For the hydrothermal alteration zone model of Figure 3, these long wavelength conditions are roughly met for frequencies below 1 Hz. Because they involve magnitudes of electric fields, the apparent resistivities and vertical admittance element magnitudes around even small-scale structures approach a non-zero low-frequency limit as shown in Figures 4 and 6. The former in particular varies by a factor approaching forty below 1 Hz. Interpretations of deep structure using 1-D or 2-D TE schemes will be subject to errors directly proportional to the distortions of apparent resistivities caused by such examples of geologic noise. Such distortions to arbitrarily low frequencies do not occur around such small single inhomogeneities as are represented in Figure 3 for the tipper element magnitudes and the phases of all MT functions; anomalies in these quantities appear restricted mostly to frequencies greater than 1 Hz.

For structures of a scale much larger than the average station spacing at RHS, such as the valley sediments, a strong frequency dependence for all MT quantities persists to much lower frequencies than for the alteration zone model, as expected from the discussion of EM scaling. Current-gathering in the valley is reflected in a regional distortion of the electric field affecting all stations at RHS to arbitrarily low frequencies. As shown in Figures 13 and 14, the amplitudes of the apparent resistivity anomalies grow as frequency decreases. Outside the right edge of the valley prism, an apparent resistivity anisotropy of about 30:1 is observed with ρ_{xy} and ρ_{yx} being nearly equidistant from the background resistivity of 400 Ω-m. It is in this vicinity that most of the MT soundings at RHS are located. The apparent anisotropy in soundings caused by the valley is another reason that a one-dimensional interpretation of results is an incorrect and hazardous approach. Two-dimensional TE interpretations are likewise not valid even for the single valley in the absence of any other inhomogeneities due to the presence of boundary charges on the ends. Though these charges are present at all frequencies, their effect upon secondary fields along centrally located profiles becomes most notable for this model below 0.3 Hz. Figures 13 and 14 also show that anomalies in impedance phase, particularly exterior to the valley, are restricted to frequencies above 0.01 Hz such that both ϕ_{xy} and ϕ_{yx} become essentially equal to that of the host medium, which is 45° for our theoretical models. This characteristic will allow us to test an assumption stated in the introduction that inhomogeneities in the RHS area are contained in a regional resistivity profile which is common to all MT soundings there. If significant differences between observed ϕ_{xy} and ϕ_{yx}, or between the shapes of ρ_{xy} and ρ_{yx}, exist below 0.01 Hz then we must reckon with substantial lateral inhomogeneities in the deep or distant crust or upper mantle.

A consideration of small-scale features juxtaposed with larger structure is a necessary one in the treatment of geologic noise. The results displayed in Figure 16 lead us to choose K_Z-strike as the estimator best suited to detecting major geoelectric trends in the face of such noise while Z-strike is considered worst suited. The contributions of geologic noise to the secondary magnetic field become insignificant as frequency diminishes though the converse is true for the secondary electric field. The apparent resistivity profiles of Figure 17 imply that ρ_{xy} would be less distorted than ρ_{yx} around large structures by geologic noise, although this is not borne out by the observations at RHS (Wannamaker, 1978). There are three possible reasons for this. First, station locations in the modeled and observed cases may not be equivalent and by coincidence are such that ρ_{xy} is relatively more affected for the latter. Second, an intrinsic resistivity anisotropy due to fracture anisotropy might lead to near-surface structures that are more conductive in the N-S direction than the E-W direction. Third, individual hydrothermal alteration variations may be more horizontally equidimensional than depicted in Figure 15 which would also account for similar distortions in observed

ρ_{xy} and ρ_{yx}. Below about 100 Hz, which is roughly the upper limit to our measurements at RHS, 2-D TE and 3-D ρ_{xy} signatures disagree significantly for such small-scale geologic noise. This condition, along with the parallel conclusion concerning the valley above, has essentially invalidated the application of 2-D TE algorithms at RHS.

The calculations displayed in Figures 14 and 17 show that profiles of ρ_{yx} and ϕ_{yx} across elongated, geometrically regular 3-D prisms may be interpreted successfully using a 2-D TM algorithm. Although one's observations may not be so favorably placed with respect to geologic noise features, we do not believe that the resultant errors in the evaluation of such noise will lead to systematic errors in the evaluation of deeper features using such a 2-D TM approach, provided the measurement profiles are properly placed over the deeper target. A variety of MT strike estimators may be used to pick which data may be treated as the TM mode of measurements. For interpreting deeper, larger structure in the presence of geologic noise, we favor K_z-strike, an estimator not seriously affected by such noise. In particular, smoother, more physically realizable impedance phase data will result from such a choice as compared to an alternate estimator like Z-strike. If reliable estimates of the tipper elements are not available, rotation of co-ordinates axes to a uniform direction compatible with regional geologic trends, if such regional trends are apparent, should give roughly equivalent results.

OBSERVED MAGNETOTELLURIC DATA AND MODEL RESISTIVITY CROSS SECTIONS

The discussions of theory and three dimensional (3-D) inhomogeneity simulations have established a partial philosophy for evaluating magnetotelluric (MT) measurements in a complicated 3-D environment. The hypothetical prismatic structures were designed on the basis of geological and geophysical evidence independent of the MT data so that the major features of the overall MT response could be anticipated and limitations to 1-D and 2-D interpretation techniques could be pointed out. We proceed now with this insight to further our knowledge of the resistivity structure at Roosevelt Hot Springs (RHS). The natural MT response at RHS is introduced by plan maps of apparent resistivity at two frequencies, which are then compared to the previous 3-D simulations. Subsequently, detailed resistivity cross sections below two, selected, E-W profiles of soundings are computed from properly processed observations using a 2-D TM algorithm. Sensitivity tests of the data to the model show good resolution of many important features but unsatisfactory resolution of other desired structures.

Plan Maps of Apparent Resistivity

In Figures 19 and 20, contour maps of principal apparent resistivities ρ_{xy} and ρ_{yx} are displayed for frequencies of 10 and 0.1 Hz. Consistent with coordinate conventions used in the preceding 3-D model studies, the x-axis of the principal coordinates of the MT impedance tensor is approximately magnetic north (N15°E). These principal quantities are as

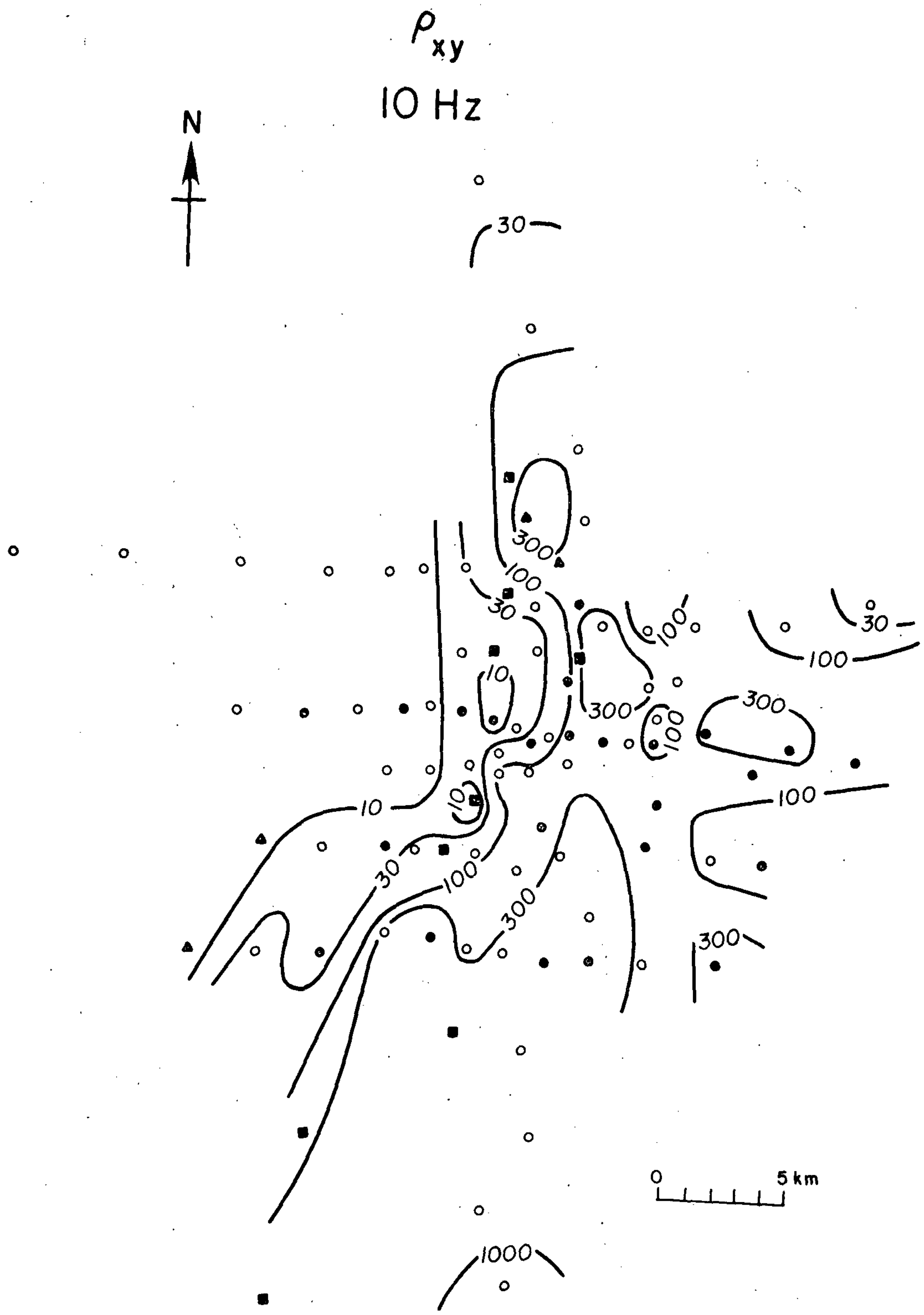

Figure 19. Contours of observed ρ_{xy} and ρ_{yx} at 10 Hz over the RHS survey area. The x-axis of these principal apparent resistivities is approximately magnetic north (N15°E). Contour values are in Ω-m.

ρ_{yx}

10 Hz

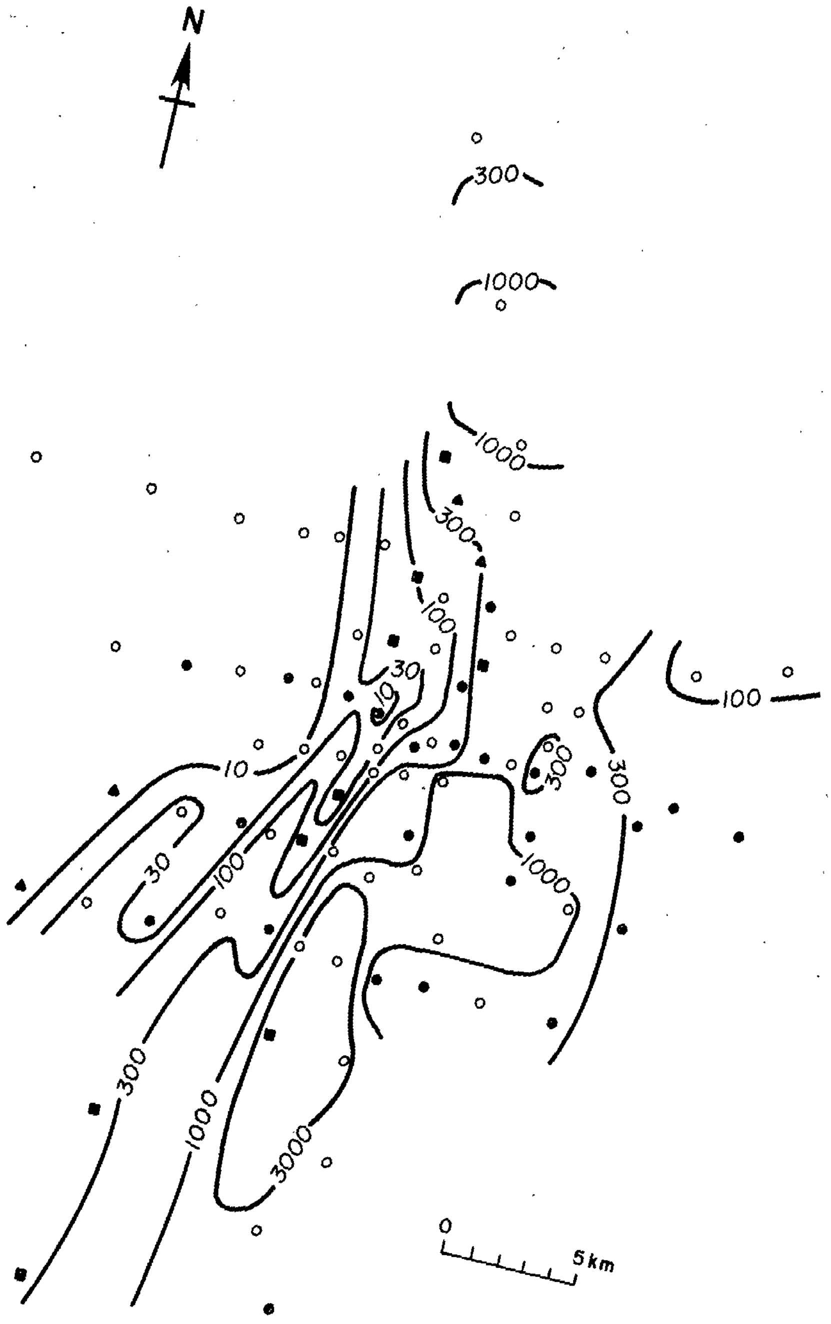
N
300
1000
1000
300
100
30
10
10
30
100
300
1000
3000
100
300
300
1000
0
5 km

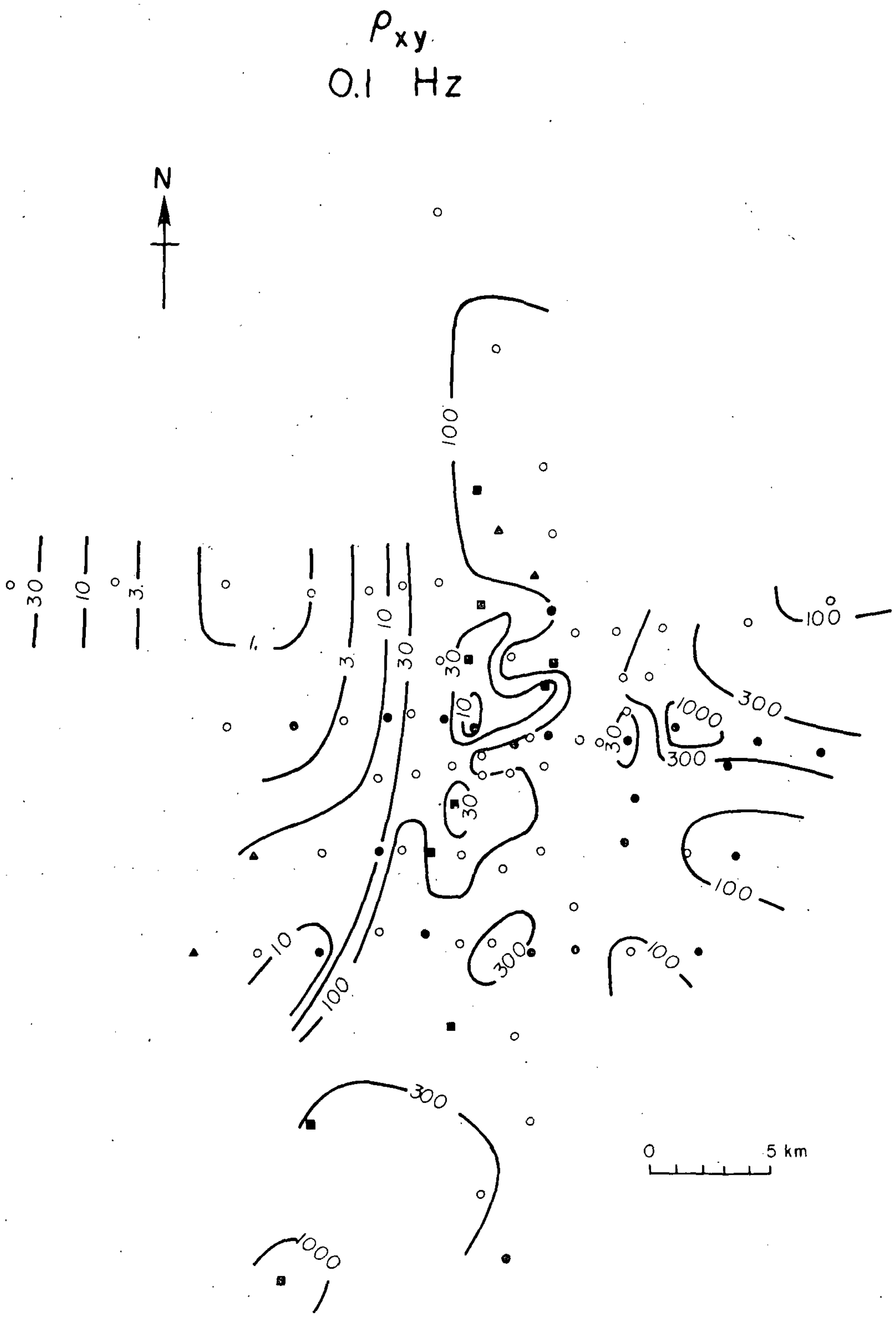

Figure 20. Contours of observed ρ_{xy} and ρ_{yx} at 0.1 Hz over the RHS survey area. Contour values are in Ω-m.

ρ_{yx}

0.1 Hz

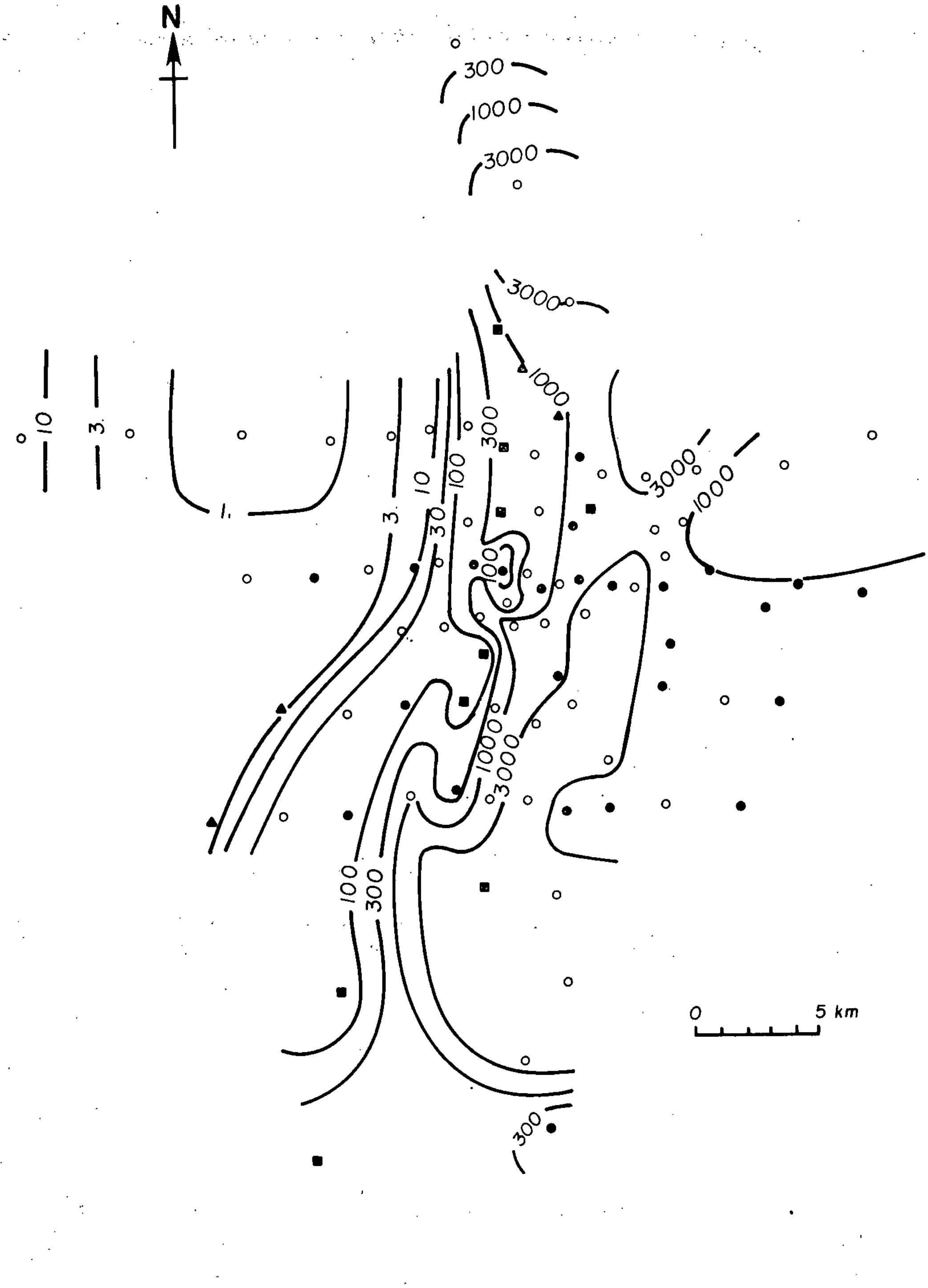
N
300
1000
3000
3000
1000
10
3.
1.
3.
10
30
100
300
100
3000
1000
1000
3000
100
300
300
0
5 km

provided by the contractors and were determined by a computational rotation of the original coordinate directions in order to maximize either the magnitude of an off-diagonal impedance element (Z-strike) or the sum of the magnitudes of both off-diagonal impedance elements (Word et al, 1971); the influence of small-scale geoelectric features at RHS has lead to significant site-to-site variations in these x-axis azimuth estimations. However, major components of the geoelectric makeup are apparent in their effects. On the basis of the vertical H-field relation Y_Z-strike, ρ_{xy} and ϕ_{xy} were generally identified as the transverse electric apparent resistivity and impedance phase while ρ_{yx} and ϕ_{yx} corresponded for the most part to the transverse magnetic mode.

Milford Valley Sediments and Mineral Mountains Horst: A most conspicuous feature of the contour maps of Figures 19 and 20 is the large apparent resistivity low occurring over the unconsolidated, water-saturated valley sediments to the west (Figure 1). We observe here fairly uniform but small values of apparent resistivity, particularly ρ_{yx}. At 0.1 Hz, this quantity falls below 1 Ω-m. At 10 Hz, the approximate constancy of both ρ_{xy} and ρ_{yx} suggests approximate constancy of intrinsic resistivity at shallow depths over the majority of the graben, although the station density is not particularly high in this area. For both quantities, the apparent resistivity values for all sites over the valley lie between 3 and 10 Ω-m.

The pronounced gradient in contours of ρ_{yx} at 0.1 Hz at the east margin of the valley marks the presence of steep rangefront faulting which bounds the sediments on this side. Such a high gradient results from undershoots and overshoots of the total electric field with respect to the incident field as one crosses from the sediments on the west to rock outcrop on the east. This behavior has been demonstrated in Figures 11a and 14a, using the representative valley prism. A less extreme gradient in ρ_{yx} between sites 78-4 and 78-5 of Figure 1 indicates the western limit of the bulk of the sediments, probably also defined by normal faulting. The contours of ρ_{xy}, more widely spaced than those of ρ_{yx} over the eastern edge of the valley, testify to the greater continuity here of total electric field, as suggested by Figures 11b and 14b. This mode of apparent resistivity and impedance phase is expected to be more sensitive to dip of the rangefront faulting than ρ_{yx} and ϕ_{yx}.

East of the valley over the Mineral Range, apparent resistivities at 10 Hz have magnitudes in the hundreds of Ω-m, with ρ_{yx} generally slightly greater than ρ_{xy}. Although this overall anisotropy implies some effect from the valley sediments, these values should be roughly representative of the average resistivity of the slightly weathered, mainly granitic rocks within 2-3 km of the surface. At 0.1 Hz however the ratio of ρ_{yx} to ρ_{xy} is around 20, denoting a strong influence of the graben. Moreover at the lower frequency, ρ_{xy} is less than, while ρ_{yx} is greater than, the corresponding quantities at 10 Hz. This tendency for the valley-induced, mountain responses ρ_{xy} to decrease and ρ_{yx} to increase with decreasing frequency is in keeping with the results of Figures 13 and 14, where similar behavior occurs as frequencies fall below 0.3 Hz. An added complication with the field data however is the regional layered profile which in general alters the geometry and overall level of the ρ_{xy} and ρ_{yx} signatures from what they are for a half-space host.

Thermal Anomaly Area: With regard to the small-scale but large amplitude anomalies of apparent resistivity within the thermal anomaly (see Figure

1), it is obvious from the maps of either principal resistivity that sites 76-4, 77-14, 77-15, 78-31, and 78-51 were located in close proximity to small, low resistivity zones of hydrothermal alteration. Probable pronounced anomalies in apparent resistivity due to these structures persisting to arbitrarily low frequencies were predicted by the calculations of Figure 4. The plan maps of ρ_a indicate however that distortions of ρ_{xy} are as great as those of ρ_{yx} by these features, a result not anticipated by Figure 17. Possible reasons for this have already been given. As described by Ward and Sill (1976), there are several such conductors coinciding with the peak of the thermal anomaly and our station density is insufficient to sample adequately the contributions of all zones to the total MT response. We must therefore live with significant spatial aliasing of the total electromagnetic signature right over the volume of earth that we are most interested in understanding. These anomalies of high spatial frequency content tend to obscure the response of any deeper structure of interest so that the presence of any economic thermal reservoir or deep heat source is not obvious from Figures 19 and 20. However, we do possess some control on the near-surface resistivity structure from prior DC resistivity modeling and a recently completed controlled-source audiomagnetotelluric (CSAMT) survey (Sandberg et al, 1980) which has been used to guide the MT modeling effort.

One-Dimensional Interpretation Attempts

Observed Data and 1-D Models: The boundary polarization charges occurring over lateral inhomogeneities have serious effects on interpreted structure calculated using 1-D or 2-D TE algorithms, since such routines do not include boundary charges in their formulations. We demonstrate the deleterious effects of small-scale, near-surface conductors upon 1-D interpretations in particular by examining a north-south trending line of soundings that spans the thermal anomaly area. Values of principal apparent resistivity ρ_{xy} over the entire observed frequency range appear for this selected line in the upper half of Figure 21. This quantity was identified by our contractors as transverse electric on the basis of principal axis estimations involving Z-strike (or equivalent) and either Y_Z-strike or K_Z-strike, this identification is expected considering the results of Figure 12. Due to geologic noise structures however, as described earlier, these axes have significant inconsistencies. The stations themselves lie close to the eastern border of the Milford Valley sediments and locations of individual sites may be deduced from Figure 1. The apparent resistivities appear as a pseudosection; log frequency defines the ordinate and horizontal distance defines the abscissa for a contour plot of ρ_{xy}. The major feature of the pseudosection is the complicated low resistivity pattern persisting to the lowest observed frequencies directly over the thermal anomaly area. Assuming that the proposed thermal reservoir and deep heat source exist beneath the thermal anomaly area, then the MT response one observes in Figure 21 will be a composite of the responses of these two features along with the responses of the valley, the regional profile and the near-surface variable alteration, the last represented in Figures 3 and 15.

In the lower half of Figure 21 are presented interpreted continuous 1-D intrinsic resistivity profiles based upon a simple analytic inversion scheme (Boehl et al, 1977; Stanley et al, 1977). The comparison of these

Figure 21. Observed apparent resistivity (ρ_{xy}) pseudosection and continuous 1-D inversion results for N-S trending profile of stations over thermal anomaly area. Contour values for pseudosection are in Ω-m. Continuous inversion results plotted on a logarithmic scale with a reference value in Ω-m given for each sounding (note elaborated scale for station 77-16).

OBSERVED ρ_{xy} (Ω-m)

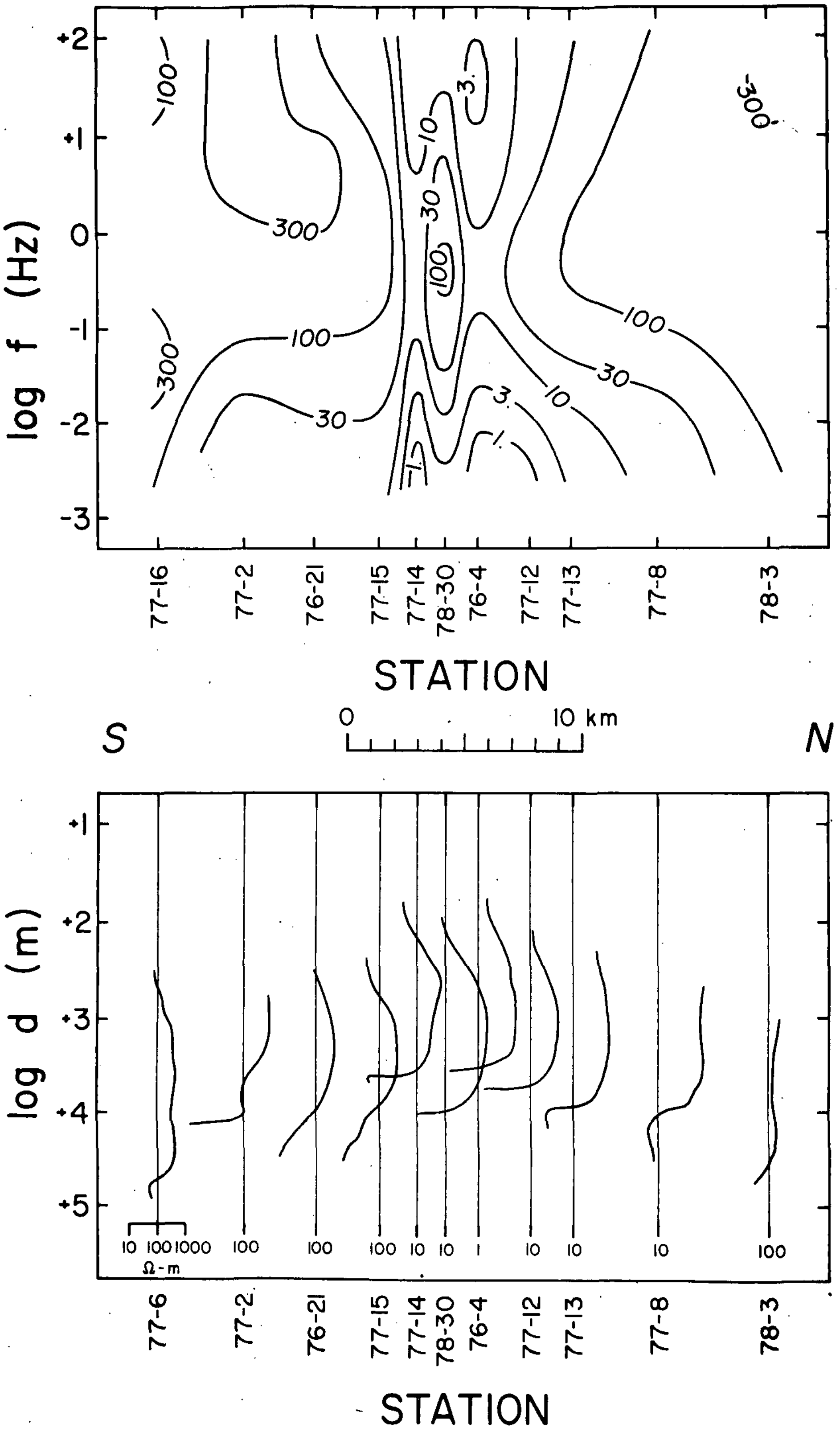

continuous profiles with layered inverse models computed from a given sounding seems reasonably close (Wannamaker, 1978). The character of these inferred continuous resistivity profiles as one crosses the thermal anomaly from one end of the line of stations to the other is very interesting. For every station, the intrinsic resistivities at the greatest depths, corresponding to the lowest frequencies, at which the profiles can be computed appear to be decreasing quite rapidly with increasing depths. Under the thermal area, however, depths at which these decreases occur are particularly shallow; 3 to 10 km as compared to 15 to 40 km as one examines sites closer to the ends of the line. These calculations imply that anomalously conductive structure exists in the deep to intermediate crust below the thermal area, perhaps representing a partially molten magma chamber that is the heat source for the geothermal system. We maintain nevertheless that the much greater part of this inferred structure is an artifact of the 1-D inversion approach and is actually induced by the near-surface resistivity structure associated with hydrothermal alteration.

<u>2-D Model and Effects of Shallow Resistivity Structure</u>: The depression of total electric field, and hence both ρ_{xy} and ρ_{yx}, directly over moderately small conductive 3-D prisms, such as in Figures 3, 15 and the smaller of those in A-1, lasts to arbitrarily low frequencies. This depression generally becomes more severe as frequencies decrease although the discussion of Figures 3, 15 and A-1 indicates that below about 1Hz, this depression has roughly reached a frequency independent limit. These hypothetical prisms are representative of a zone of overall decreased resistivity associated with brine-saturated and hydrothermally altered rocks and sediments within the thermal anomaly at RHS. The factors $|1+P^{o}_{xx}|$

and $|1+P^{o}_{yy}|$ of equations (17a) and (29) may be substantially less than one due to this electric field reduction so that both log ρ_{xy} and log ρ_{yx} vs log f plots are simply translated downwards along the ρ_a axis from the ρ_a plot that would result from measurements over the layered earth host alone. One may infer then from the genral expression for the n-layered impedance (Ward, 1967, p 120) and equation (29) that the model layer resistivities which are calculated by a 1-D inversion of ρ_{xy} or ρ_{yx} mesured within near-surface conductive prisms will be less than those of the actual layered host by multiplicative factors $|1+P^{o}_{xx}|^2$ or $|1+P^{o}_{yy}|^2$ respectively (also see Larsen, 1977). Furthermore, the layer interface depths calculated from such distorted soundings will be shallower than those of the true host by multiplicative factors $|1+P^{o}_{xx}|$ and $|1+P^{o}_{yy}|$ respectively.

To show computationally that the near-surface, low resistivity structure associated with the thermal anomaly is mostly responsible for the apparently anomalously conductive structure in the intermediate to deep crust below the thermal anomaly, as implied by the continuous 1-D inversions of Figure 21, requires an algorithm which can include boundary polarization charges and a layered earth host in its formulation. Our 3-D integral equation routine is not sufficiently general at this time to allow modeling of prisms in a layered host. However, the finite N-S strike extent of the near-surface resistivity structure just described can be simulated approximately using a 2-D TM algorithm. Using this 2-D program, we have calculated the resistivity cross section of Figure 22 and the ρ_a pseudosection in the upper half of Figure 23 in an attempt to match the observations. A comparison that is generally close between pseudosections of Figures 21 and 23 has been obtained, particularly concerning the

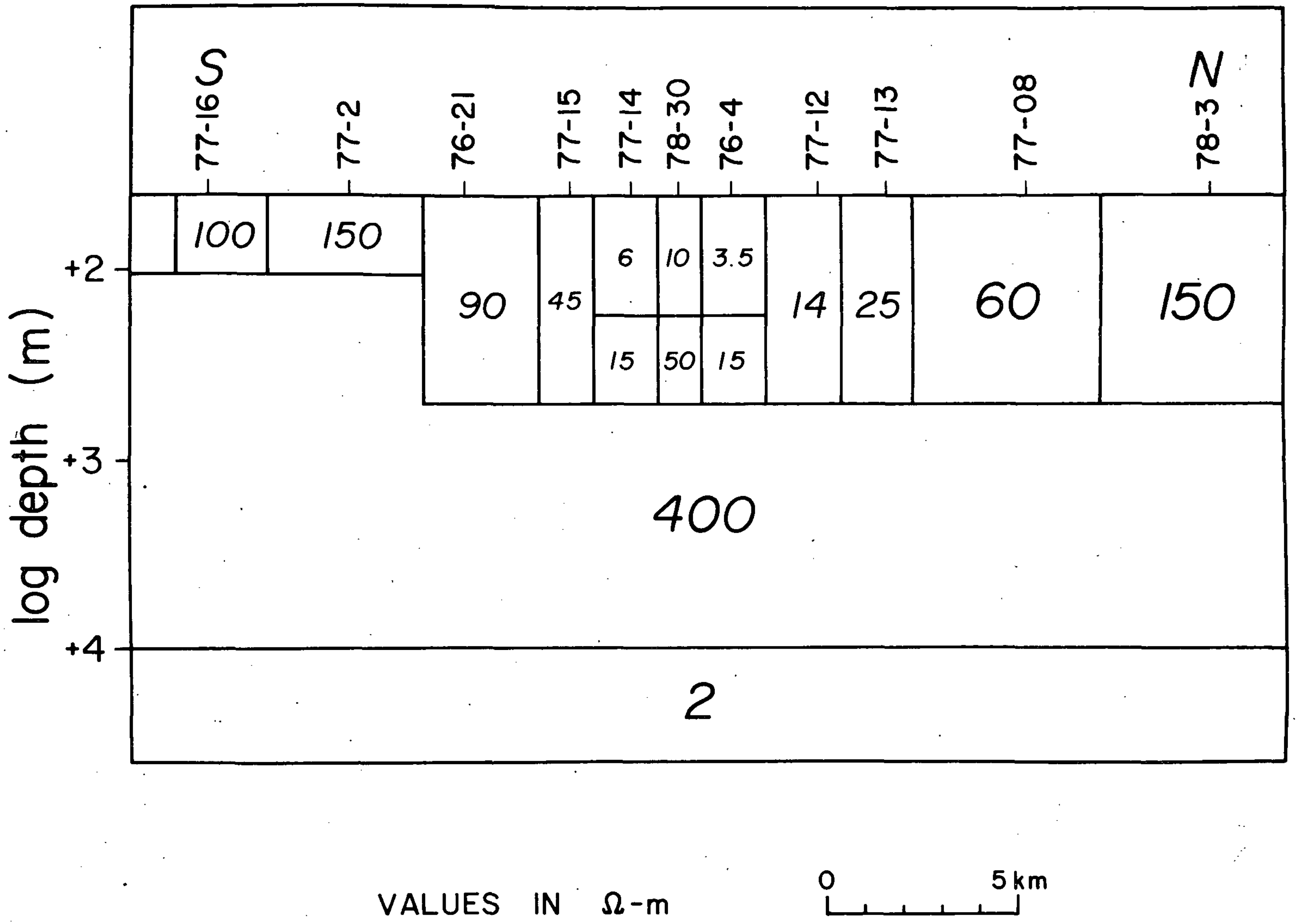

Figure 22. Finite element resistivity section computed using lateral inhomogeneities in only the upper 500 m to fit the observations in the top half of Figure 21. Values of individual media in Ω-m.

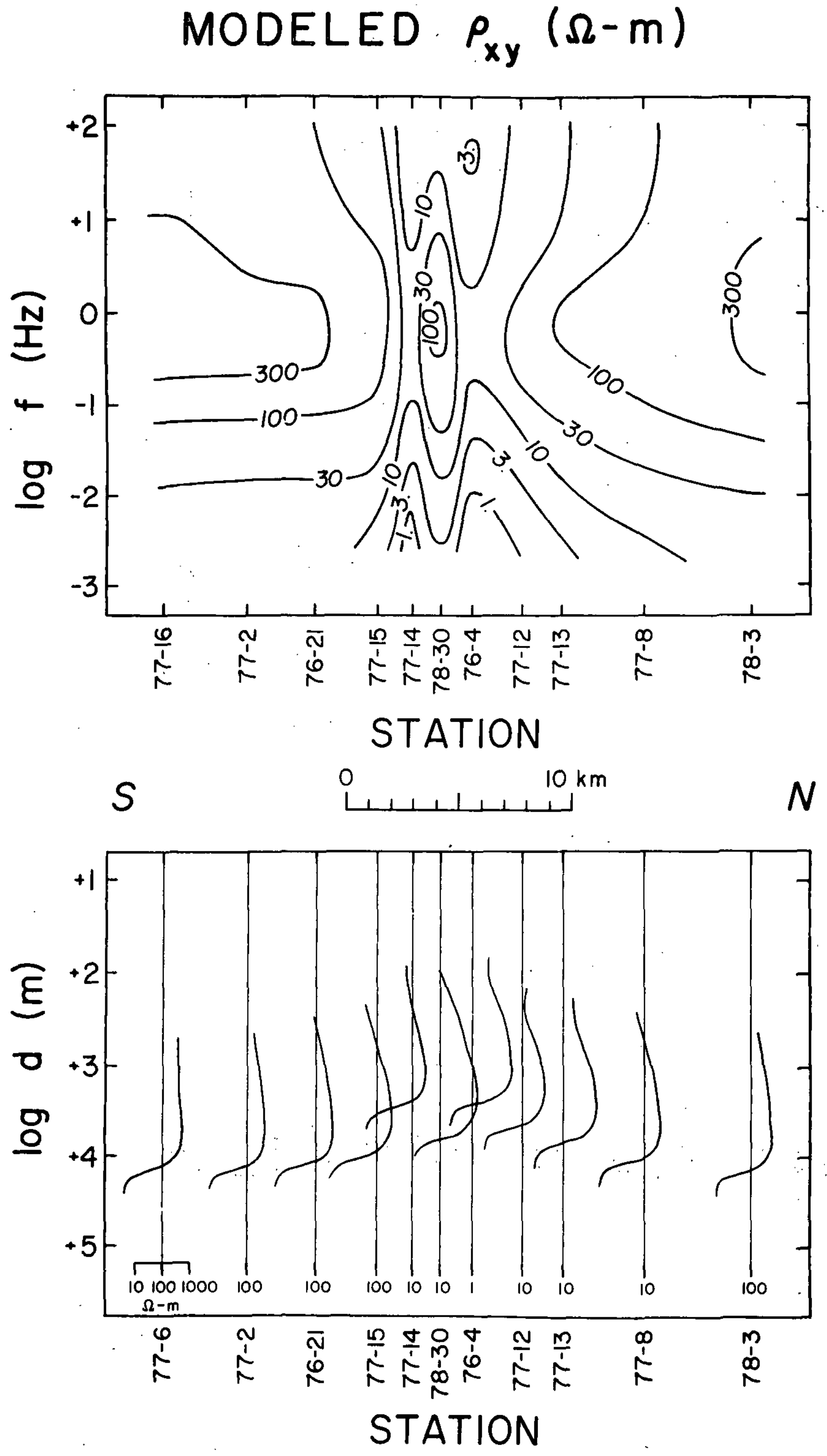

Figure 23. Computed apparent resistivity (ρ_{xy}) pseudosection and continuous 1-D inversion results corresponding to the finite element model of Figure 22. Conventions are as for Figure 21.

resistivity lows directly associated with the thermal anomaly area, using lateral inhomogeneities which extend no deeper than 500 m. One must conclude from this that many important characteristics of MT observations to arbitrarily low frequencies can be determined by very shallow structure.

We note at this point the progression of resistivities of the layered host in Figure 22 from 600 Ω-m over the depth interval 1 to 20 km to 2 Ω-m at greater depths. This behavior can be explained for the most part as a combination of the effects of the regional layered profile and the Milford Valley sediments. As will be discussed later, we believe the true resistivities of the layers of the regional profile are much higher than shown in Figure 22 and the depths to the most conductive units are much greater. Now the length of the line of soundings considered in this exercise is about 25 km, which is less than the N-S strike extent of the valley sediments of 35 to 40 km. As shown in Figures 13a and 17, this valley causes a regional depression of the roughly N-S component of electric field and hence ρ_{xy} for soundings that would be located along the majority of its side. The valley and this depression of ρ_{xy} is not allowed for by the 2-D TM routine that yielded Figure 22 and so falsely conductive and shallow units of the regional profile were inferred. Of course this regional depression of electric field by the valley has affected the 1-D inversion results as well.

To complete this investigation, we invert the computed sounding data to yield the continuous intrinsic resistivity profiles in the lower portion of Figure 23. The ensemble of profiles bears an overall similarity to that in the lower half of Figure 21 with the implication of anomalously conductive structure existing in the deep to intermediate crust directly underneath the thermal area. One must conclude that false conductivities and falsely shallow interface depths will be generated from a 1-D inversion scheme using ρ_a and ϕ data measured over 3-D near-surface conductive structure. In particular concerning geothermal systems, the near-surface conductivity structure within a thermal area created by the upward convection of hot brines with attendant hydrothermal alteration of rocks and alluvium may itself be the cause of an apparent but false conductor beneath the system, suggestive of a partially molten heat source, if the true complexity of this shallow conductivity makeup is not properly accounted for.

We do not mean by these discussions to imply disfavor, necessarily, with the notion of deep 3-D resistivity structure beneath RHS. Substantial disagreements exist between the computed and observed pseudosections of Figures 21 and 23 as well as between the 1-D intrinsic resistivity profiles calculated from modeled and measured results, although some of these may be due to inconsistencies in the measurement coordinate directions from site to site. A serious opinion on such a matter may be formed only after all of the observed MT data at RHS have been evaluated with algorithms taking into measure the three-dimensionality of the entire ensemble of features that may affect that data. We do believe nevertheless that a 1-D approach to the interpretation, which is prone to misrepresentations due to the three-dimensionality of the environment at RHS, is no way to attempt to describe this same environment.

Observed Apparent Resistivity and Impedance Phase Pseudosections

The limitations of our 3-D integral equation routine have stopped us to this time from interpreting all the MT data at the RHS in a completely satisfactory manner. However, a partial evaluation with 2-D algorithms is possible under the restricted conditions to which such algorithms apply. The discussion accompanying Figures 14 and 17 recommends interpretation of part of that mode of the MT data identified as ρ_{yx} and ϕ_{yx} with a 2-D TM algorithm. Our research group has developed such a program capable of calculating multifrequency ρ_{yx} and ϕ_{yx} results for complicated resistivity cross sections within layered hosts (Rijo, 1977; Stodt, 1978). To make use of this algorithm we have chosen profiles of stations B-B' and C-C' of Figure 1 as meeting the necessary criteria. The two profiles trend nearly perpendicular to the margin of the bulk of the valley sediments, as evidence by geologic mapping and gravity and by the steep gradient in apparent resistivity contours of Figure 20b. They are also, for the most part, rather centrally located with respect to the northern and southern limits of the valley, also on the basis of mapping and gravity.

The observations ρ_{yx} and ϕ_{yx} for these two lines appear in Figures 24 and 25, also as pseudosections. In keeping with the discussion surrounding Figures 16 and 18, the coordinate axes for all sites in these profiles lie in a uniform direction which is approximately N15°E. Such an azimuth is compatible with preferred geologic trends indicated by the previously mentioned mapping and geophysical surveys along with some of the better quality K_z-strike estimations. Picking uniform coordinate directions has greatly smoothed certain aspects of the observed data, particularly the low-frequency values of impedance phase as anticipated by the discussion of Figure 18.

<u>Line B-B'</u>: We discuss first details of the pseudosections of line B-B'

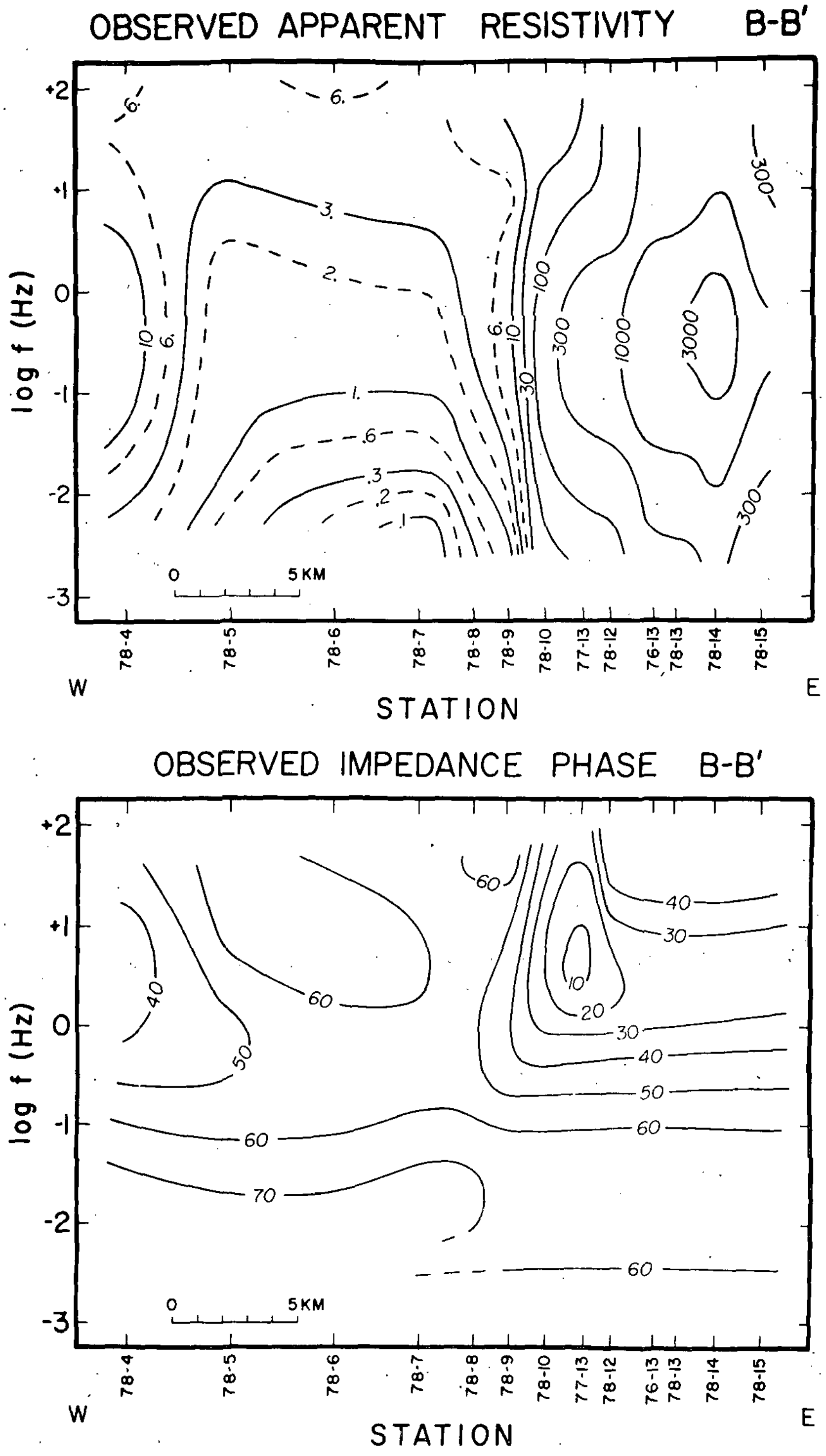

Figure 24. Observed apparent resistivity and impedance phase pseudosections for profile B-B' of Figure 1. Contours of ρ_{yx} are in Ω-m while those of ϕ_{yx} are in degrees.

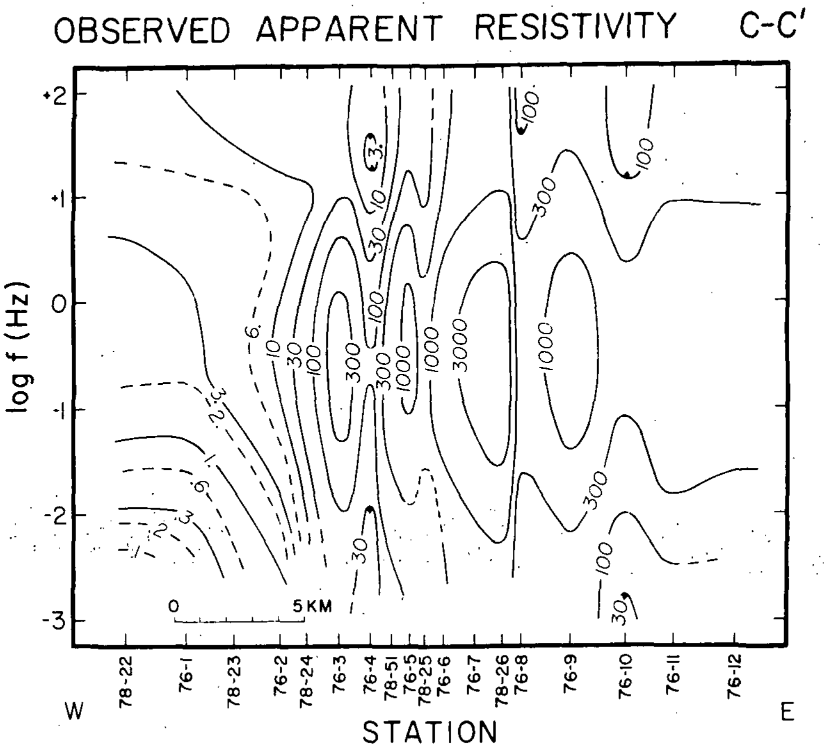

OBSERVED APPARENT RESISTIVITY C-C'

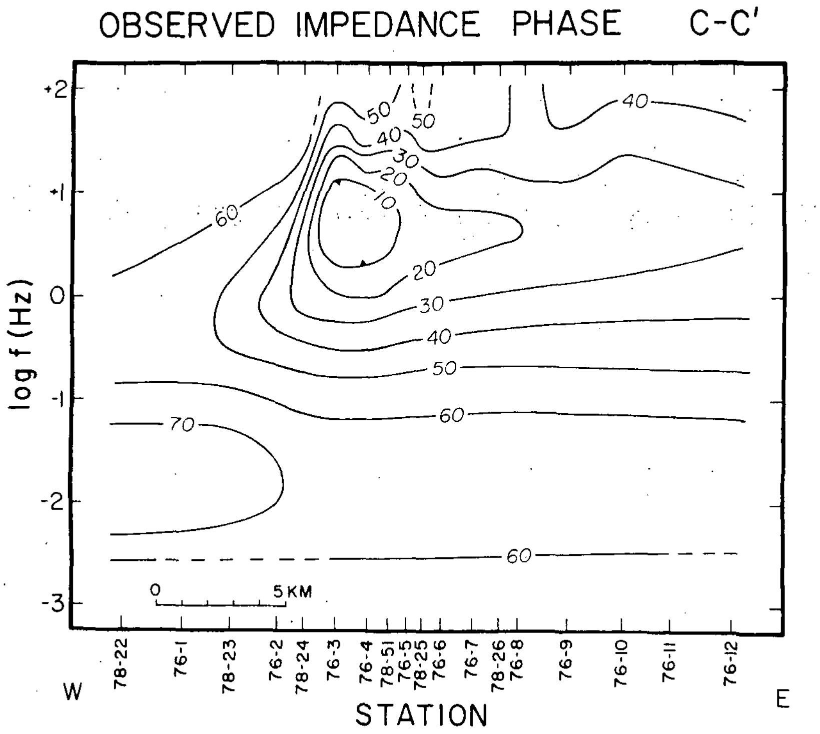

OBSERVED IMPEDANCE PHASE C-C'

Figure 25. Observed apparent resistivity and impedance phase pseudosections for profile C-C' of Figure 1. Contours as in Figure 24.

since it lies north of the thermal area and is expected to be affected by just the valley and regional layered structure and not significantly by features directly related to the geothermal system. The observed results for this line exhibit a virtually classic horst-graben response for the TM mode and are qualitatively similar to the computations of Figure 14. Within the margins of the conductive vallley sediments, apparent resistivities for stations 78-5 to 78-8 (Figure 24) are monotonically decreasing functions as frequency decreases, falling from somewhat over 3 Ω-m at 10 Hz to below 0.1 Ω-m at very low frequencies for station 78-7. Impedance phase values remain above 45° here with a maximum exceeding 70° at low frequencies. As shown by the plan maps of apparent resistivity in Figure 20b, substantial gradients in ρ_{yx} at mid to lower frequencies are responses due to the rangefront faulting bounding the sediments between sites 78-4 and 78-5 and between 78-8 and 78-10. Likewise, gradients in impedance phase in Figure 24 at the same locations at mid to high frequencies are further responses to the same structures.

Again referring to Figure 24, high apparent resistivities, often exceeding 1000 Ω-m are observed for the mountain soundings east of and including station 77-13; a maximum in the contour values is reached at mid frequencies (0.3 Hz). If one examines the shapes of the apparent resistivity curves on a log ρ_{yx} vs log frequency plot for individual stations in the mountains, they are all very similar although the amplitudes of ρ_{yx} at a given frequency vary in excess of an order of magnitude from station to station. This variation in the overall level of the soundings is due to near-surface resistivity fluctuations which are in turn due to changes in the rock porosity and/or pore water saturation and chemistry. This is yet another indication that a straight-forward application of one-dimensional inversion algorithms will yield confusing and erroneous conclusions. The impedance phase contours of Figure 24, somewhat less featured over the mountains than those of the apparent resistivity, undergo a minimum near 20° at upper-central frequencies (∿3 Hz) and a maximum of almost 70° at lower frequencies (∿0.01 Hz).

We should perhaps state at this time that the major differences between the computed results of Figure 14 and the observations of Figure 24 can be accounted for by the differences in the hosts of the lateral inhomogeneities for the two cases; that of the model of Figure 10 is a uniform half-space while that of the natural structure at RHS varies with depth. It is this regional layering that is primarily responsible for the very lowest values of ρ_{yx} and the higher values of ϕ_{yx} at low frequencies over the valley. It is also the cause of the maxima in apparent resistivities for the mountain stations at mid freqencies along with the minima of impedance phases at upper-central frequencies and their maxima at lower frequencies. The regional profile will be discussed in detail later in this report.

Line C-C': Many similarities but some important differences exist between the observed data of B-B' and C-C', the latter of which is now considered (Figure 25). This line straddles the thermal anomaly of Figure 1 and three producing steam wells. The profile of stations extends only about half way across the bulk of the valley sediments so that the entire valley signature is not observed. However, the monotonic decrease of apparent resistivities over the sediments along with impedance phase values exceeding 45° everywhere with a low-frequency maximum above 70° is obvious for stations

78-22 to 78-23. Furthermore, between soundings 78-23 and 76-3, the major rangefront faulting again results in a steep gradient in apparent resistivities at mid to low frequencies and a gradient in impedance phases at mid to high frequencies.

The observations for the mountain sites of line C-C', which are those east of and including station 76-5, are generally very similar to those of B-B'. The range of apparent resistivities at a given frequency for these soundings is about the same with maxima at mid frequencies of over 1000 Ω-m appearing for some soundings. The impedance phase pseudosections appear very close.

The major characteristics peculiar to the pseudosections of line C-C' are seen for soundings directly over the thermal area nearby to the east of the margin of the Milford Valley sediments. For the higher frequencies above 30 Hz, the apparent resistivities of stations 76-3, 76-4 and 78-51 of Figure 25 are modest to low in amplitude and descend with decreasing frequency. The impedance phase pseudosection, exhibiting some relief in this frequency range, takes on values that overall are greater than 45°. However, in the frequency interval 10 to 1 Hz for these three sites, the apparent resistivities are now rising relatively very rapidly as frequency diminishes while the impedance phase values are below 10°. It has been our experience that such MT function behavior often is indicative of a resistive body at depth. We have paid special attention to attempting to fit this data with our 2-D TM program since such resistive structure beneath the thermal area would have controversial geological ramifications. Below 1 Hz, the shapes of the individual apparent resistivity curves and values of impedance phase are essentially the same as those of soundings on line B-B' which are at equivalent distances to the east of the bulk of the Milford Valley sediments.

Calculated Pseudosections and Model Cross Section

Procedural Considerations: We next examine calculated ρ_{yx} and ϕ_{yx} pseudosections along with the model resistivity cross sections that resulted from application of our 2-D TM finite element modeling algorithm. The calculated MT functions were obtained not using any programmed iterative method such as that described by Jupp and Vozoff (1977) but instead by trial-and-error calculation and comparison of the MT forward problem results yielded by our algorithm to the observations. Alterations in any of the parameters of the cross sections at a given iteration were conceived mentally and this process muddled along until a satisfactory fit of the calculated results to the observed was effected. This sort of modeling can be very laborious for complicated data sets. Approximately 200 man-hours of effort and 12 hours of calculation time on a Univac 1108 computer were required to achieve the fit. Such requirements of course would vary according to the computer resources, the size and complication of the given data set and upon the experience of the interpreter.

We would also like to bring up a couple of points that were kept in mind while the modeling took place which concern uniqueness of final models and resolution of certain of its parameters. Any resistivity cross section which is modeled by our finite element routine consists of a variety of adjoining, straight-sided polygons each with a uniform interior resistivity. There is some question as to the correctness of application of this type of model to the real-world. Clearly, variations in hydrothermal alteration of earth materials, in pore water content and salinity and in temperature are likely to be smooth functions of position. However, other structures such as fault-bounded masses of conductive alluvium and perhaps a partially molten magma chamber acting as a deep heat source for a geothermal system would have sharp boundaries. Given, furthermore, that the algorithm is reasonably fast and easy to implement on a computer, we have presumed that in instances where the resistivity boundaries in the earth are gradational that the flat-sided, computed model whose MT functions fit the observations is, in some sense, close to the actual structure. Model uniqueness problems can be treated by a combination of three things; a high station density in each profile, a wide spectrum of data in each sounding, and data to sufficiently high frequencies at each sounding. By sufficiently high frequencies we mean that both apparent resistivities, ρ_{xy} and ρ_{yx}, and impedance phases, ϕ_{xy} and ϕ_{yx}, have converged to common values above a given frequency. For this high frequency range, the earth will probably be effectively one-dimensional, allowing us to set the near-surface intrinsic resistivities close to their true values. Such isotropic behavior occurs for frequencies above 3 Hz for the valley stations and above 30 Hz for the mountain sites.

The finite element cross sections which will be introduced shortly may appear overly complicated to some observers. Technically, every vertex of every polygon in any such cross section is considered a parameter yet we do not pretend that every vertex in the sections we will be discussing is even moderately resolvable. In other words, we admit that straight-sided polygons may not be the most frugal way of describing the earth and so any sensitivity tests of the data to our computed resistivity model will involve families of vertices that comprise geologically important media in the subsurface.

Goodness of Fit and Cross Sections for Line B-B'.: The computed ρ_{yx} and ϕ_{yx} pseudosections pertinent to line B-B' appear in Figure 26. About all that needs to be said about this is that the computed (Figure 26) and observed (Figure 24) pseudosections for this line agree within data scatter almost everywhere. Examples of typical data scatter will be forthcoming in a discussion of sensitivity tests.

The complicated finite element cross section representing resistivity structure beneath line B-B' appears in Figure 27. The section as we show it in this diagram extends to a depth of only about 3 km although the measurements are sensitive to resistivity structure to depths in excess of 100 km. Figure 27 details just the lateral inhomogeneities beneath B-B' that appear to be affecting these particular measurements; below a bit over 2 km a layered regional profile which is common to both lines B-B' and C-C' appears to be the only resolvable geoelectric structure. This layered regional profile will be discussed at length later in this report but for now we examine solely the upper-level multidimensional resistivity makeup as we see it.

A major feature of the cross section of Figure 27 is one of low to modest resistivity extending about 17 km west of site 78-9. It corresponds to a sequence of conductive sediments which occupy the Milford Valley. The resistivities of units within 140 m of the surface range from 3.5 to 18 Ω-m and with depth pass into a low resistivity medium of 1.1 Ω-m to a maximum depth of around 650 m beneath station 78-7. Deeper still lies a great

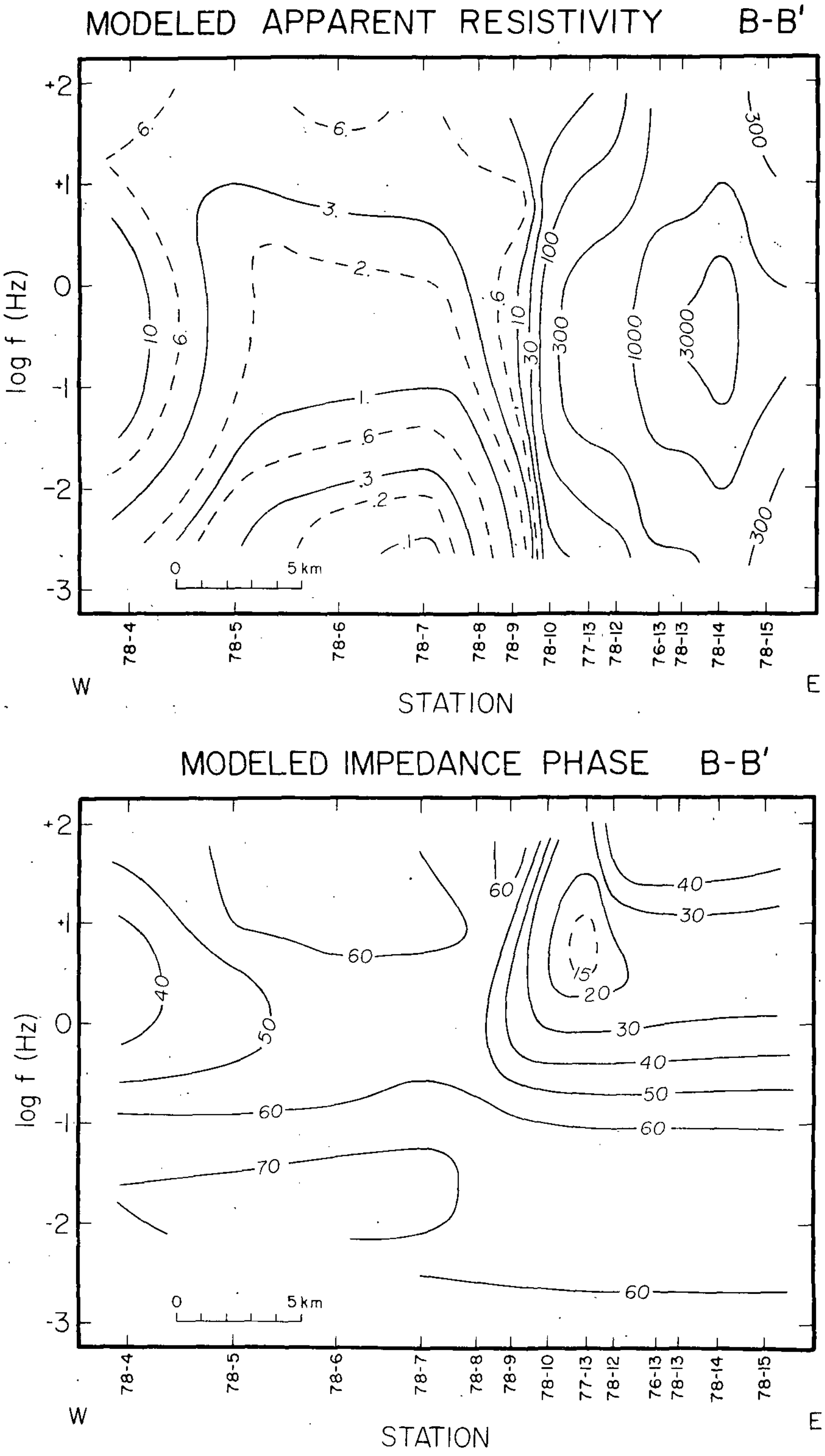

Figure 26. Computed apparent resistivity and impedance phase pseudosections for model finite element section for profile B-B' of Figure 1. Contours as in Figure 24.

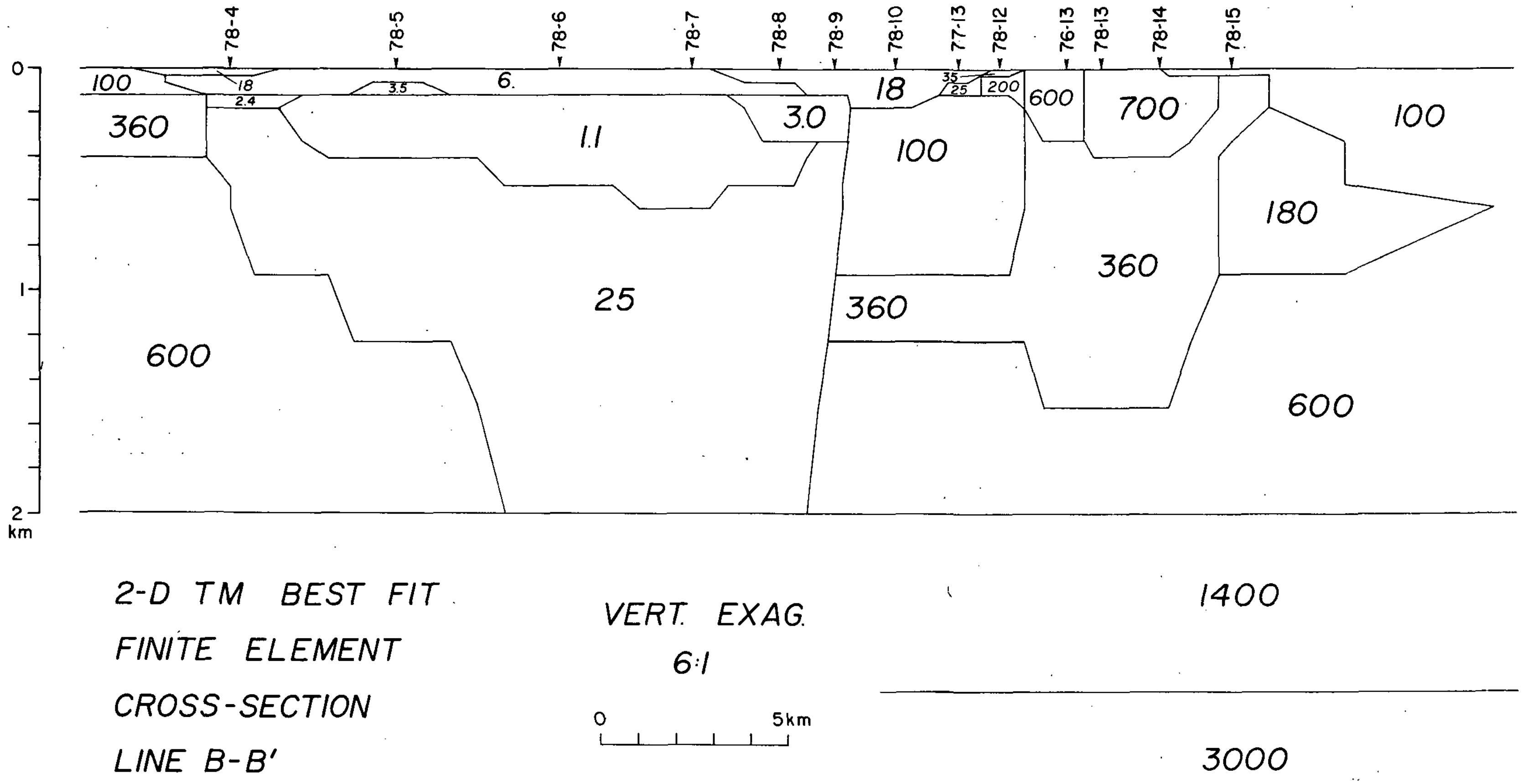

Figure 27. Best 2-D TM finite element section fitting the observations for profile B-B' of Figure 1. Values of individual media are in Ω-m. Vertical exaggeration is 6:1.

thickness (>1 km) of modest resistivity material (25 Ω-m) although the depth extent of this material is poorly resolved. This group of media beneath the valley soundings is interpreted as being bounded on its western and eastern margins by steeply dipping interfaces. Though the actual dips are not well resolved, particularly for the western margin, a dip greater than 60° to the west is favored for the eastern limit.

The values of resistivity believed to exist to a depth of about 2 km beneath the mountain sites of this line are shown in the section to lie in the hundreds of Ω-m. Indeed, for stations 76-13, 78-13 and 78-14 of Figure 27, one observes a drop from 600-700 Ω-m near 400 m depth to 360 Ω-m whereafter resistivity rises through 600 and 1400 Ω-m to 3000 Ω-m. The units of 1400 and 3000 Ω-m below 2 km are the start of the purely layered sequence comprising the regional profile below this line.

Goodness of Fit and Cross Sections for Line C-C': The computed pseudosection for line C-C' shown in Figure 28 matches the observed pseudosection of Figure 25 reasonably well, but some difficulties with stations 76-3, 76-4 and 78-51 directly beneath the thermal area have been encountered. For these three sites, impedance phases below 10° could not be achieved for the computed results between 10 and 1 Hz, in fact they do not fall far below 20°, unless unrealistic subsurface geoelectric structure is invoked. Furthermore, the calculated apparent resistivities here below 10 Hz could not be made as large as those observed. This particular lack-of-fit will be elaborated upon in some upcoming sensitivity tests.

The same basic structure as on line B-B' is seen for the finite element cross section for line C-C' in Figure 29, except of course for some features peculiar to the thermal anomaly area of Figure 1. The

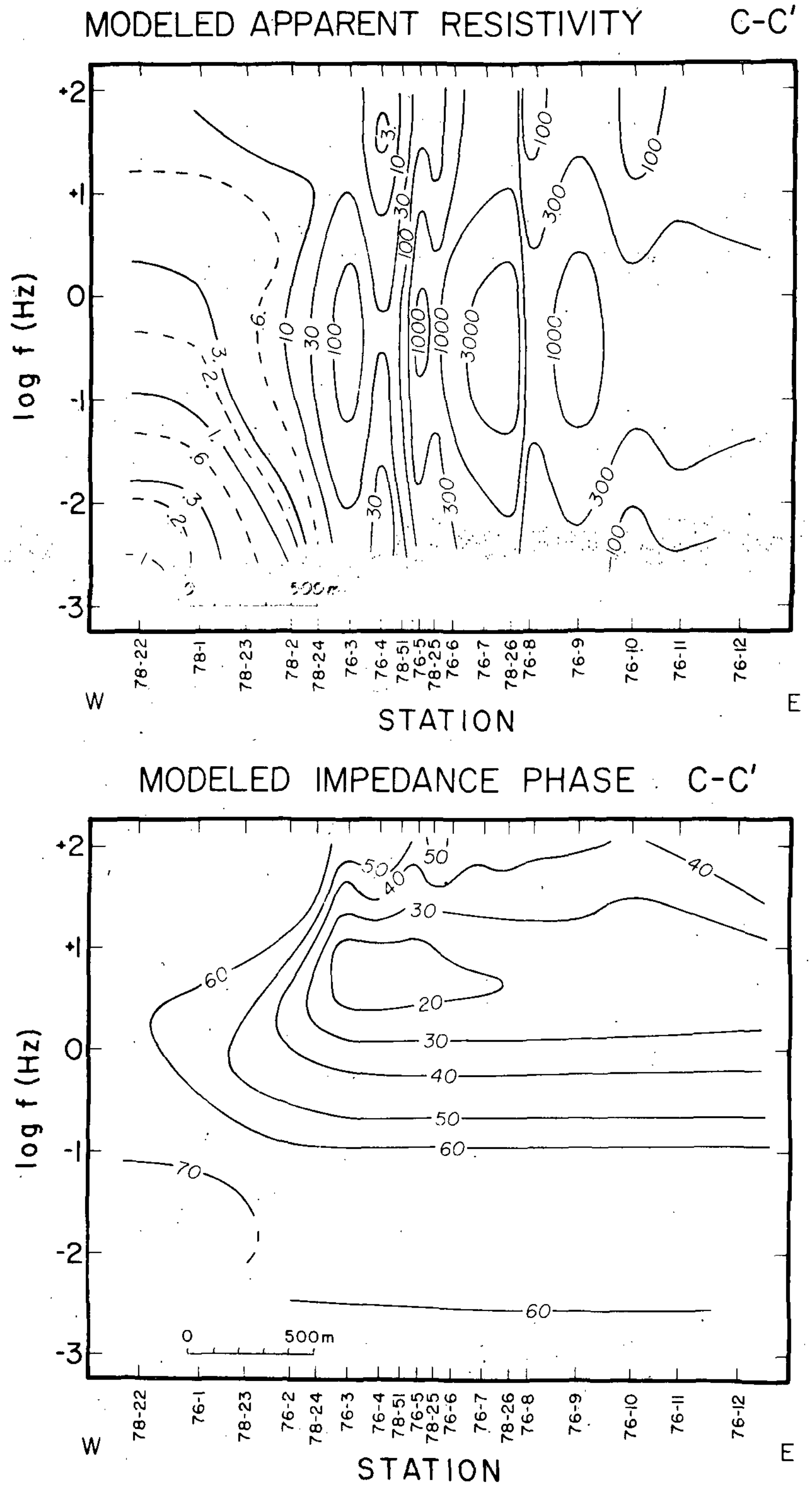
MODELED APPARENT RESISTIVITY C-C'

MODELED IMPEDANCE PHASE C-C'

Figure 28. Computed apparent resistivity and impedance phase pseudosections for model finite element section for profile C-C' of Figure 1. Contours as in Figure 24.

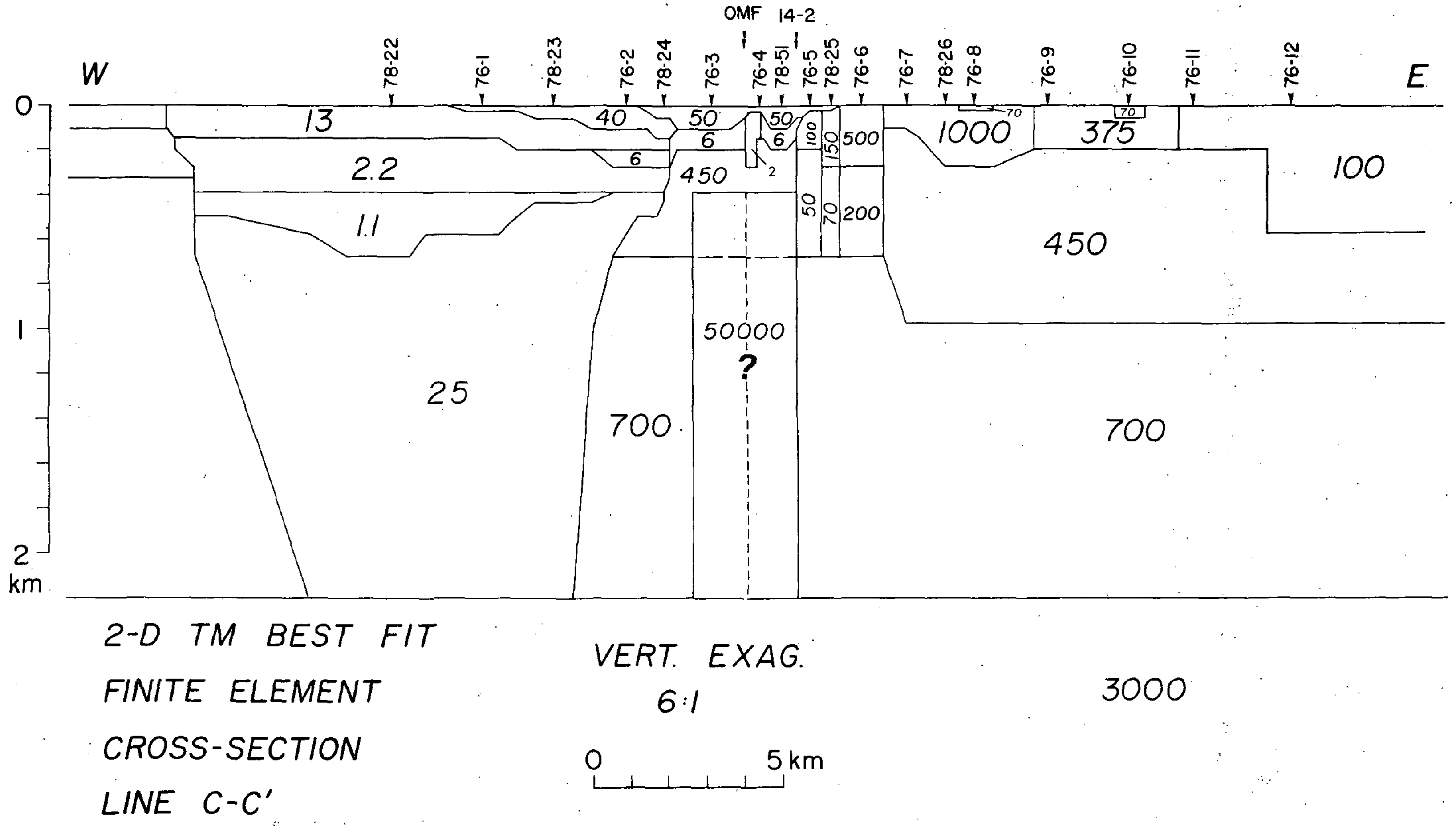

Figure 29. Best-fit 2-D TM finite element section fitting the observations for profile C-C' of Figure 1. Conventions as in Figure 27.

resistivities of units within 200 m of the surface beneath the valley stations of C-C' range from 6 to 40 Ω-m and as well as for line B-B' pass into lower resistivity material of 1.1 to 2.2 Ω-m to a maximum depth of around 650 m beneath station 78-22. Also, a modest resistivity medium (25 Ω-m) appears to exist at yet greater depth to at least 2 km. It should be mentioned now that the westernmost limit of this conductive series of valley sediments on line C-C' of Figure 29, some 6 km west of station 78-22, is not resolved by our MT measurements but instead is constrained by gravity data and seismic refraction modeling (Carter and Cook, 1978; Gertson and Smith, 1979). Shifting this margin by ±2 km in an east-west sense from its present depiction appears to have no significant effect upon the calculated MT values. Concerning the eastward margin of this conductive series, the somewhat less steep gradient in observed ρ_{yx} and ϕ_{yx} contours between sites 78-23 and 78-24 of Figure 25 than between sites 78-9 and 78-10 of Figure 24 implies the less abrupt, somewhat stepped transition in Figure 29 between the more conductive material of the Milford Valley and the relatively resistive material beneath much of the thermal area and Mineral Mountains.

Values of intrinsic resistivity in the hundreds of Ω-m in the upper 2 km or so are also seen beneath the mountains sites of line C-C'. The medium of 3000 Ω-m below 2-2 km heralds the onset of the 1-D regional profile below C-C'. It is emphasized at this time that the regional resistivity layering below 2-3 km is common to both lines C-C' and B-B' and provides equally excellent fits to the observations of both lines, this being a reassuring circumstance.

As stated earlier, line C-C' straddles the thermal anomaly area as shown in Figure 1 and the major justification for this MT survey is the possible delineation of resistivity structure, perhaps relating to an economic brine reservoir or a deep-seated heat source driving the convective system, beneath this thermal area. Stations 76-3, 76-4 and 78-51 of Figure 1 were occupied directly over the thermal anomaly and the Opal Mound Fault, the latter denoted by OMF in Figure 29. In the upper 300 m of the finite element section, the resistivity progresses downward from 50 Ω-m material of 100 m maximum thickness through more conductive units (2-6 Ω-m) into a resistive medium of 450 Ω-m. This interval of the cross section is determined primarily by observations at frequencies greater than 10 Hz. The limits to the small volume of least resistivity (2 Ω-m) beneath station 76-4 are not resolvable with the MT measurements since they are measurably affecting only the data of site 76-4. Instead, this unit was defined in conjunction with DC resistivity and controlled source audiomagnetotelluric measurements (Ward et al, 1978; Sandberg and Hohmann, 1980) in order to fit the observations at station 76-4.

The usefulness of small-scale electrical and electromagnetic surveys in detailing the shallow, low resistivity volume of earth beneath the thermal area should be stressed. The average MT station spacing across the thermal area on line C-C' is about 1 km. While being a rather high density compared to other MT surveys, this average spacing is inadequate to sample the complicated MT response over the thermal area, particularly the variable hydrothermal alteration centered near the Opal Mound Fault. Some model uniqueness problems can be avoided if control on the near-surface resistivity structure can be obtained. CSAMT especially appears to be a rapid, inexpensive means of gaining such control and the good agreement between interpreted geoelectric cross sections in this area for the measurements of Sandberg and Hohmann (1980) and our study points out how complimentary to MT is this active source technique. It turns out in addition that our MT cross section in Figure 29 in the upper 300 m agrees satisfactorily with those of Ward and Sill (1976) and Tripp et al (1978) for dipole-dipole surveys in this area. Three independent electrical methods give similar estimates of the resistivity structure within 300 m of the surface so that we have confidence that the true, natural structure here bears a strong resemblance to that shown in Figure 29.

If one continues downward in this area of the figure one encounters a highly resistive (50,000 Ω-m) prism at a depth of 400 m. The width of this feature is 3 km and it extends to a depth of 2.2 km. The frequency range over which MT supplies information on the depth and intrinsic resistivity of this prism appears to be around 1 to 10 Hz. Recall from earlier discussion that over this frequency interval the observed impedance phase is some 10° less than the computed and that below 10 Hz, the modeled apparent resistivity could not be made as large as the observed. Since such an extreme resistor could arouse controversy over its geological significance, a closer examination of the lack of fit of calculated to observed data plus parameter sensitivity tests are imperative.

We note briefly from the calculated resistivity cross sections that the data do not appear to detect lateral resistivity inhomogeneities existing below a depth of 2-3 km for either line B-B' or C-C'. In other words, ρ_{yx} and ϕ_{yx} for these lines are not sensitive to the presence of any large, lateral resistivity contrasts which may be associated with a deep-seated, perhaps partially molten heat source that drives the convective system. It is certainly fair to question the detectability of any such deep structure with these particular MT quantities and we shall return to this matter at a later point in this writing.

Sensitivity Tests of Structure for Line C-C': To examine more closely the problem of the 50,000 Ω-m prism displayed in Figure 29, we have plotted the observed apparent resistivity and impedance phase data points for station 76-4 in Figure 30. The data points are generally of very high quality and we note that a later reoccupation of this site by remote reference MT instruments (Gamble et al, 1979) gave ρ_{yx} and ϕ_{yx} data points whose mean values at a given frequency appeared identical to those which may be deduced from Figure 30 when the site coordinate axes are made coincident. Hence we accept the very low values of ϕ_{yx} near 5° around 6 Hz as being real and not a problem with data quality. The solid curves in the diagram are computed values of ρ_{yx} and ϕ_{yx} at station 76-4 for the cross section of Figure 29 with the 50,000 Ω-m unit present. As pointed out before in the comparison of observed and computed pseudosections for line C-C', there exists a significant lack of fit of modeled to observed data over the thermal area for much of ϕ_{yx} and the great majority of ρ_{yx}.

Magnifying the resistivity of this prism further has no appreciable effect upon the computed curves. If one increases substantially the lateral extent of this unit along with changing the resistivity structure of the previously described upper 300 m of the section here, the overall percent squared difference between the observed and calculated pseudosections in general and the respective MT quantities for station 76-4 in particular may be reduced, although not satisfactorily removed, as suggested by Vozoff (1980, pers. comm.). There would be two deleterious

Figure 30. Observed data points of ρ_{yx} and ϕ_{yx} for sounding 76-4 along with sensitivity test computations. Solid curves are calculated using the best fit cross-section of Figure 29. The curves of long dashes result when the 50,000 Ω-m unit was removed while the curves of short dashes result when this resistive body was replaced by a narrower conductor of 10 Ω-m resistivity.

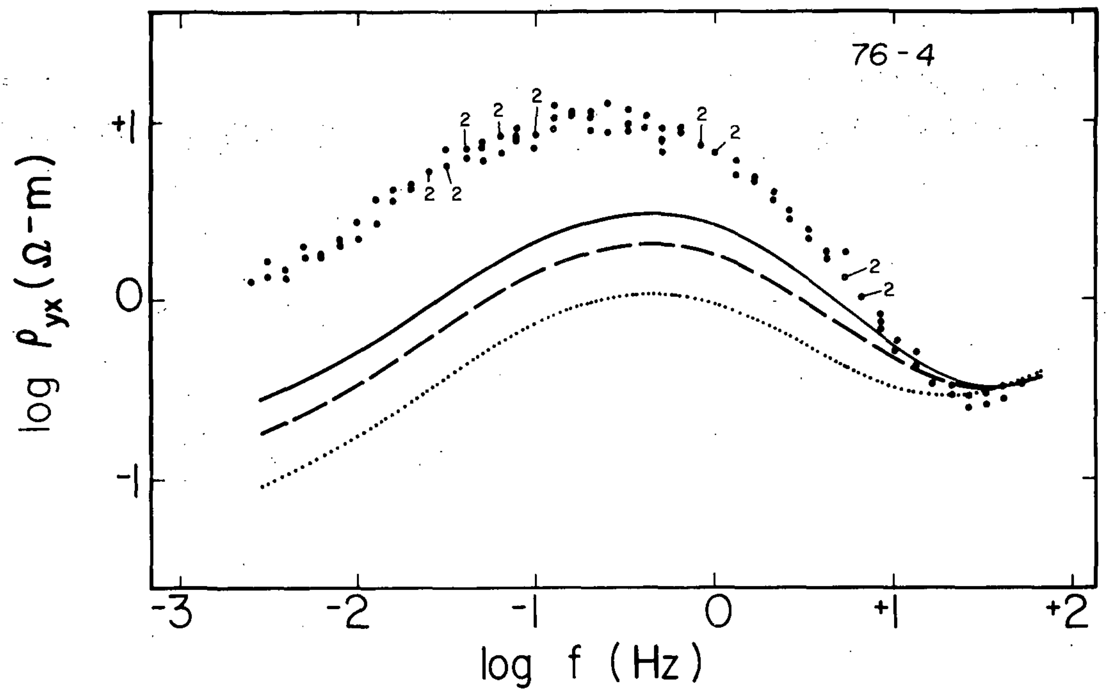
76 - 4
log ρyx (Ω-m)
+1
0
-1
-3
-2
-1
0
+1
+2
log f (Hz)
2
2
2
2
2
2
2
2
2

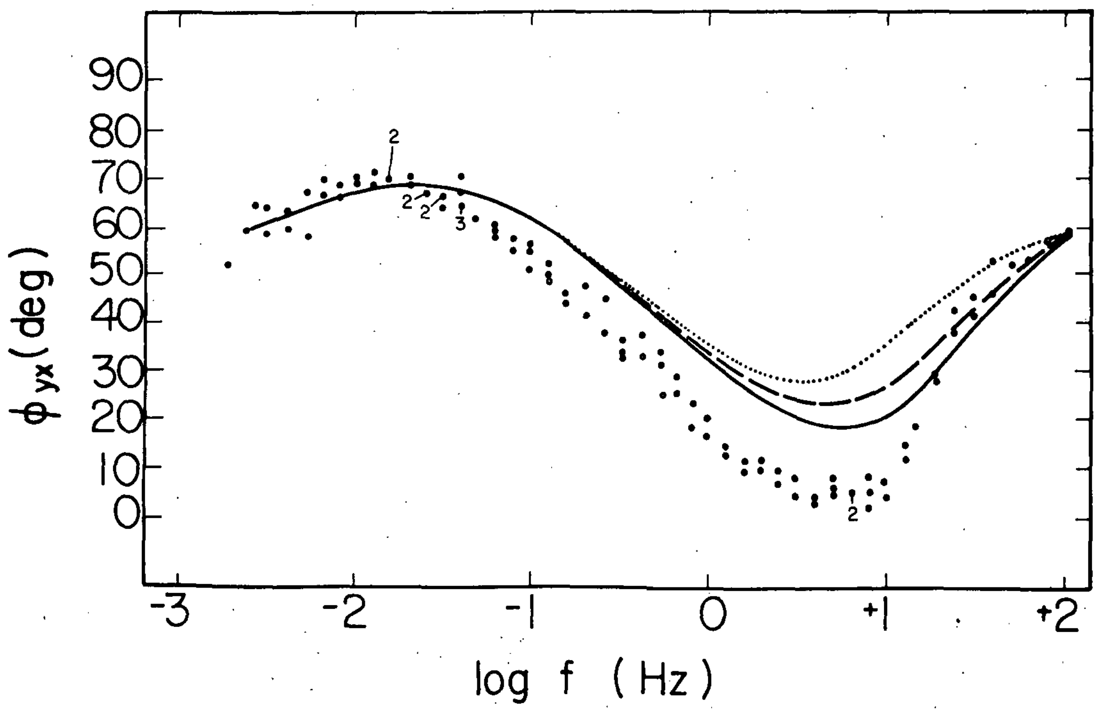
φyx (deg)
90
80
70
60
50
40
30
20
10
0
-3
-2
-1
0
+1
+2
log f (Hz)
2
2
2
3
2

side effects that lead us to reject such an action. First, increasing substantially the lateral extent of the prism introduces some lack of fit to the data of sites west of 76-3 and east of 78-51 such that the data of more than just the three soundings over the thermal area become problematical. Second, we are against altering the structure in the upper 300 m of this area as we now believe we have three independent sets of electrical data that would verify this part of the section.

To show to what extent the highly resistive prism as we depict it in Figure 29 minimizes the lack of fit of computed to observed results, we removed it and replaced it by 450 and 700 Ω-m material, above and below the horizontal line of long dashes, and then recomputed the MT response. The curves of long dashes in Figure 30 are the result. One may conclude from this that imposition of a very resistive prism will improve the agreement between observed and calculated values, however the lack of fit in both instances is so severe that we are reluctant to propose that such resistive material actually exists at depth beneath the thermal anomaly for this profile.

We have also tested the sensitivity of the MT measurements of this profile to a buried conductor. Downward continuation of the observed heat flow anomaly at RHS suggests a depth to major heat sources of 400 m with a width of roughly 1.5 km extending eastward from the Opal Mound Fault (Wilson and Chapman, 1980). This roughly constitutes the eastern half of the resistive prism previously discussed as is defined by the vertical line of short dashes in Figure 29. If one hypothesizes that the region of major heat sources corresponds to a reservoir saturated with hot brine, of 10% porosity due to randomly oriented fractures and containing 0.1 N NaCl fluids at 250°C, Archies Law estimates an intrinsic resistivity to the region of well under 10 Ω-m. Hence we have assigned 10 Ω-m to the east portion of this original resistor while the remainder received values of 450 and 700 Ω-m, again applying above and below the horizontal dashed line of Figure 20. The recomputed response for this site is given by the curves of short dashes in Figure 30 and the lack of fit is nearly twice that due to the resistive prism at depth.

This presently unassailable poorness of fit is perplexing. During the process of trial-and-error simulation of the data, a great many combinations of parameters were attempted with no success. We submit that application of a 2-D transverse magnetic modeling program is inappropriate for describing the relatively limited scale and likely complexly 3-D resistivity geometry especially related to the economic thermal reservoir. An as yet unconceived 3-D effect, quite possibly involving the valley sediments as we shall explain later, is believed responsible for the troublesome measured signature in this area of this profile. We are convinced that an algorithm which can model 3-D resistivity structure in a layered earth is essential for understanding the MT response of any economic thermal reservoir and it is toward this goal that some of our ongoing effort is progressing.

Regional Resistivity Layering: As alluded to in the writing on the MT function pseudosections and the model resistivity cross sections, the inhomogeneities in the upper 2 to 3 km appear to be contained in an apparently 1-D regional profile specific to the Roosevelt Hot Springs thermal area. The profile as we see it appears in Figure 31 along with some alternate crust and upper mantle models used in sensitivity tests

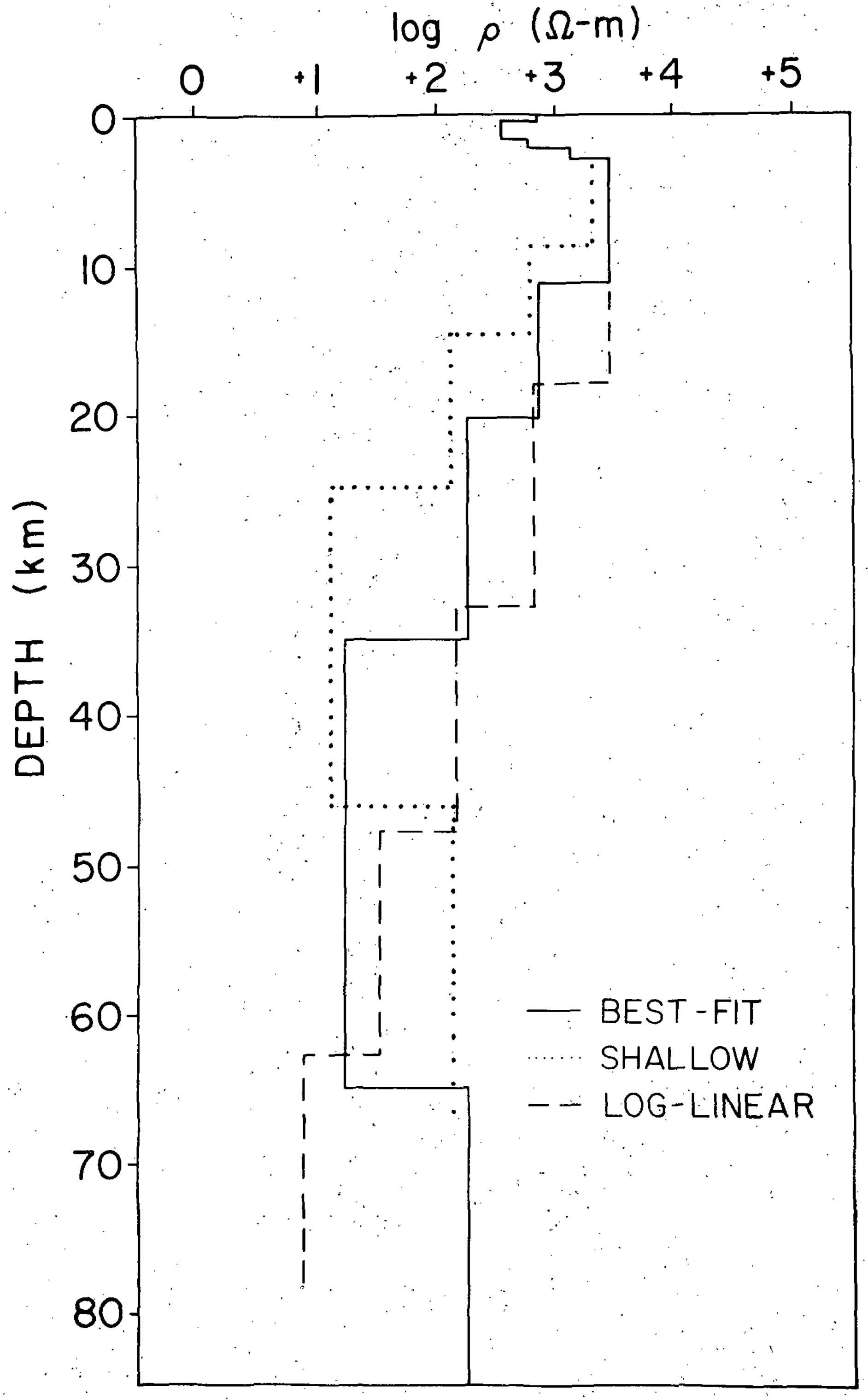

Figure 31. Best-fit 2-D TM finite element model of the 1-D regional profile of the Great Basin crust and upper mantle (solid line) in the RHS area. Alternate regional profiles used in sensitivity tests are shown with long and short dashes.

explained below. The simultaneous modeling of the regional layered profile and the upper crustal lateral inhomogeneities using the 2-D TM algorithm has made allowance for the distortion of the observed ρ_{yx} and ϕ_{yx} data by these lateral inhomogeneities, such as the conductive valley sediments, from those data that would result from measurements over the regional 1-D profile alone. It will be shown that a straightfoward one-dimensional inversion of the observations leads to inconsistent and unreasonable estimates.

The sequence in the uppermost 2 or 3 km in Figure 31 applies only to station 76-13 of line B-B' (Figure 28), which has been used in the sensitivity tests, and will differ depending upon which station is examined. Here, resistivity at first decreases from 600 to 360 Ω-m at 400 m depth and henceforth increases rather sharply to 3000 Ω-m by 3 km depth. From here on downwards, the sequence applies generally for any sounding at RHS. Subsequently below 11 km, the resistivity falls, probably we believe in a smooth manner not immediately apparent from the sharp interfaces required for our algorithm, to some 200 Ω-m at 35 km. An abrupt drop to 20 Ω-m material is encountered next, which seems to remain uniform to a depth of 65 km where an equally abrupt rise to 200 Ω-m introduces a basal half-space.

Observed data points of ρ_{yx} and ϕ_{yx} are plotted in Figure 32 for station 76-13 of Figure 1. The calculated response of our best-fit finite element model which combines Figures 28 and 31 is the solid curves of Figure 32, which seems very agreeable with the trends of the observed data points. The goodness-of-fit and observed data quality are typical of the dozen sites in the two lines which lie over resistive rocks of the mountain

Figure 32. Observed data points of ρ_{yx} and ϕ_{yx} for sounding 76-13 of line B-B' along with sensitivity test calculations. Solid curves are computed using the best-fit regional model of Figures 27 and 31. The curves of long dashes correspond to the Log-Linear model of Figure 31 while the curves of short dashes result from the Shallow model of Figure 31.

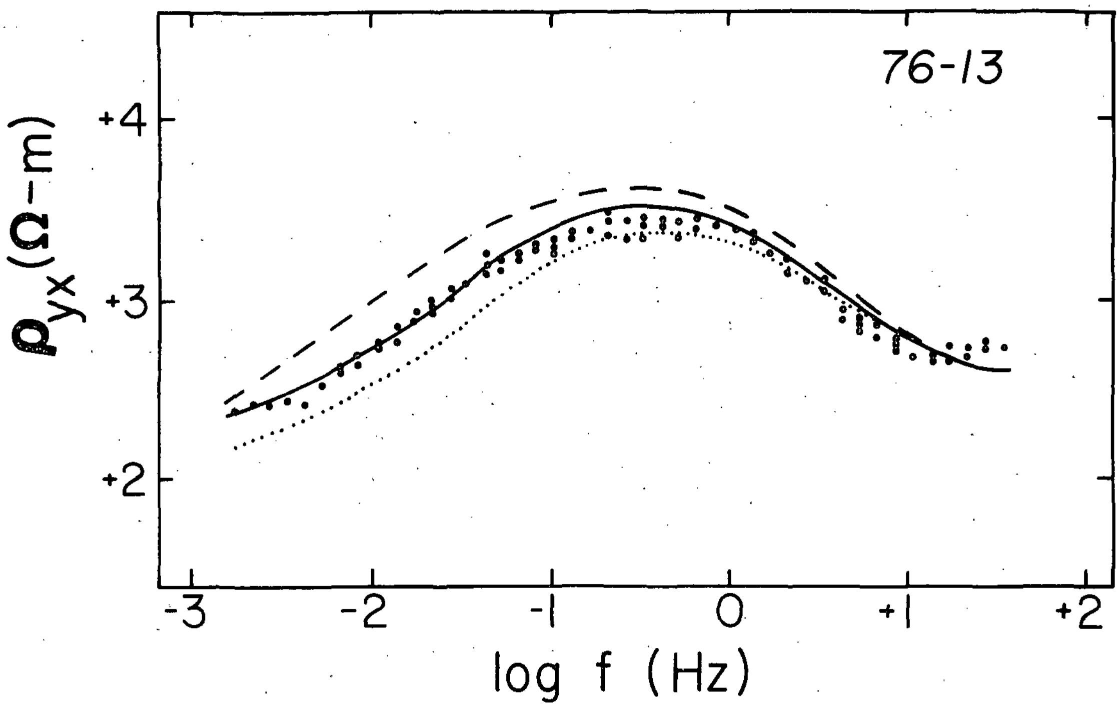
76-13
+4
+3
+2
ρyx(Ω-m)
-3
-2
-1
0
+1
+2
log f (Hz)

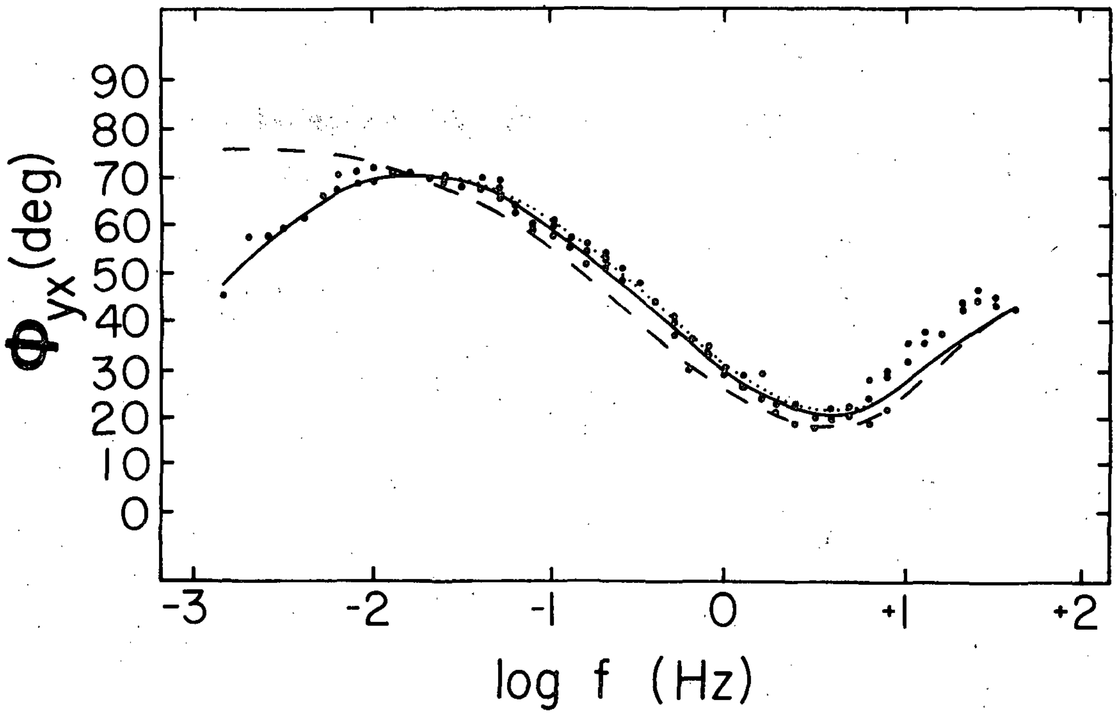
90
80
70
60
50
40
30
20
10
0
Φyx(deg)
-3
-2
-1
0
+1
+2
log f (Hz)

pluton. As stated before, it is the layered crust and upper mantle regional host which governs major features of the total MT signature. The steep increase in resistivity from 2 to 3 km accounts for the general rise in apparent resistivities and for the impedance phases falling near 20° from 10 Hz down to 1 Hz. Below 0.3 Hz, the decrease in resistivity for depths below 11 km leads to decreasing apparent resistivities along with phases greater than 45° with the factor of ten drop at 35 km depth responsible for the steepest gradient in ρ_{yx} and the values ϕ_{yx} approaching 70° below 0.06 Hz. The thickness of this deep 20 Ω-m layer together with the rise in resistivity below 65 km causes the apparent resistivity data to flatten out and the phase data to fall, particularly below 0.003 Hz. We note that a few soundings, not on either line B-B' or C-C', in our survey possess accurate data points below 0.001 Hz and these exhibit a genuine rise in ρ_{yx} and a fall in ϕ_{yx} below 40° indicative of a substantial resistivity rise at the greatest depths to which the observations seem sensitive.

Sensitivity Tests of Regional Layering: Sensitivity tests of the model regional profile are important as its character may be an indicator of physical and chemical conditions in this area of the eastern Great Basin. As a first test, let us examine the overall scale of the layering. By shrinking the depths and resistivities of individuals by 30% such that the layer contrasts and conductivity-thickness products remain constant, we arrive at the sequence drawn with dots, labeled the Shallow regional model in Figure 31. The recomputed curves of ρ_{yx} and ϕ_{yx} in Figure 32 are likewise dots. A preference for one of the choices cannot be formed on the basis of the impedance phase alone since the difference in the best-fit and shallow calculated responses is much smaller than data scatter. The fit appears significantly worse however for the apparent resistivity and we reject the shallow regional model as an alternative. An F-test (Jenkins and Watts, 1968) of the lack of fit of the computed results to the observations has not been conducted for the shallow or other models examined here. Instead we have simply disqualified by inspection those structures whose computations lie well outside the observations over a wide frequency range.

Also considered is a regional 1-D profile of different shape. A structure whose log resistivity decreases linearly with depth (labeled the Log-Linear model in Figure 31) and whose conductivity-thickness product down to 75 km is close to that of the best-fit model is plotted with dashes. At 0.002 Hz, about the lowest frequency at which we have reliable data for station 76-13, computations using this log-linear composition do not appear sensitive to any high-contrast structure below about 75 km. Such a profile shape has a particular geological significance, as will be expanded upon in the next section. Its calculated response for station 76-13 appears also as dashes in Figure 32. Computed apparent resistivities significantly higher than observed are the yield. This is due in part to the effects of the valley sediments. For the log-linear layering above around 0.3 Hz, the valley sediments act as though contained in a relatively more resistive host than for our best-fit choice. Hence the upward distortion of ρ_{yx} by the valley from that which would result from the layering alone is relatively larger for the log-linear host than for the best-fit host. Calculated phases for the log-linear case are lower than the measured ones down to 0.01 Hz but cross and asymptote at about 75° at the lowest frequencies. The substantial disagreement in character of the observed and computed soundings here causes us to rule out the log-linear possibility.

Results of a specific sensitivity test on the 20 Ω-m layer from 35 to 65 km, though not plotted in this report, indicate that the thickness (t) and the conductivity (σ) are not highly correlated estimates. Varying the conductivity of the layer while keeping σt constant indicated a permissible range of resistivity of 12 to 30 Ω-m before a significant lack of fit to the observations, particularly ϕ_{yx} between about 0.06 and 0.005 Hz, was noted.

The data of station 76-13 is now used to evaluate the direct applicability of a 1-D inverse algorithm (Petrick et al, 1977) to the estimation of the regional resistivity profile in this area. In Figure 33 we have replotted ρ_{yx} and ϕ_{yx} as well as the complementary quantities ρ_{xy} and ϕ_{xy}. As anticipated by the hypothetical results of Figures 13 and 14, the valley sediments cause a serious apparent resistivity anisotropy for stations in close proximity to it. The observations of both modes of apparent resistivity and impedance phase were transformed by the above-mentioned 1-D algorithm to give estimates of regional layer thicknesses and intrinsic resistivities. It is emphasized that a direct 1-D inversion disregards the distorting effects of the valley and hence is expected to yield highly suspect models.

In Figure 34, the layered estimates provided using the pairs (ρ_{yx}, ϕ_{yx})and (ρ_{xy}, ϕ_{xy}), respectively, are plotted as dashed and dotted lines and are seen, except for the upper 2 km or so, to not match at all with our best-fit choice that was obtained through use of the 2-D TM program. We

Figure 33. Observed data points of ρ_{yx}, ρ_{xy}, ϕ_{yx} and ϕ_{xy} for sounding 76-13. Curves of long and short dashes indicate the good fit to the data that may be obtained by using a 1-D layered inverse routine, although the resultant layered models were dismissed as unrealistic. Solid curve appearing between data points correponds to the 1-D forward problem using the best-fit regional profile of Figure 31. Its placement with respect to the observations demonstrates the severe regional ρ_a anisotropy induced by the valley.

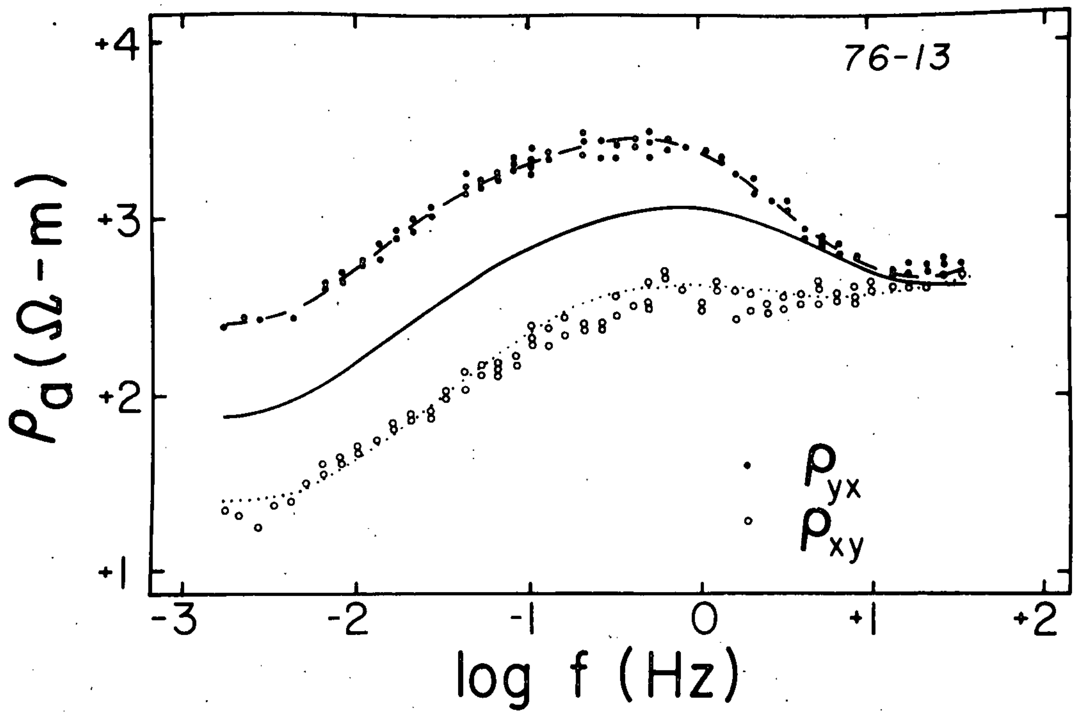
76-13
ρa (Ω-m)
+4
+3
+2
+1
-3
-2
-1
0
+1
+2
log f (Hz)
• ρyx
∘ ρxy

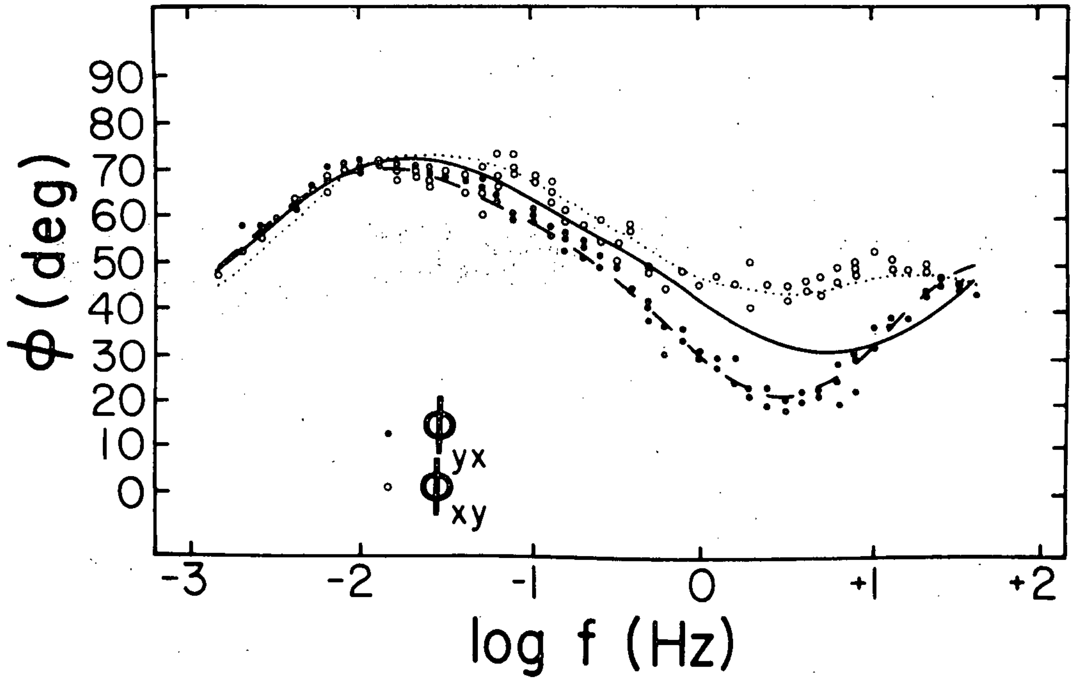
φ (deg)
90
80
70
60
50
40
30
20
10
0
-3
-2
-1
0
+1
+2
log f (Hz)
• φyx
∘ φxy

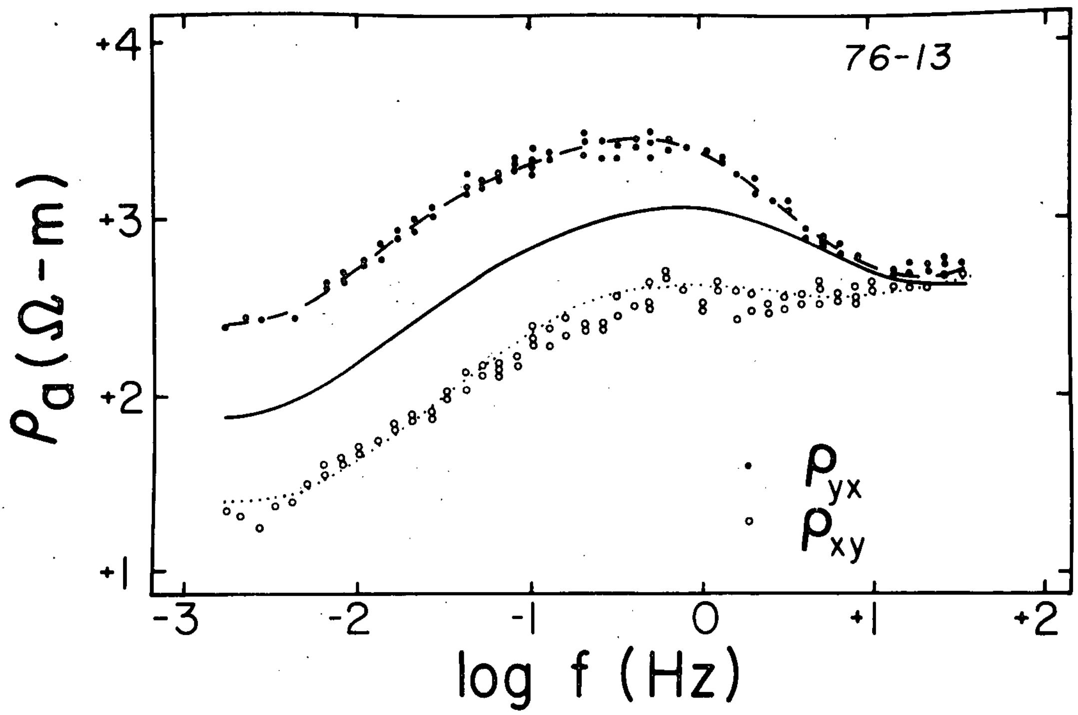
76-13
ρ_a (Ω-m)
+4
+3
+2
+1
-3
-2
-1
0
+1
+2
log f (Hz)
• ρ_{yx}
○ ρ_{xy}

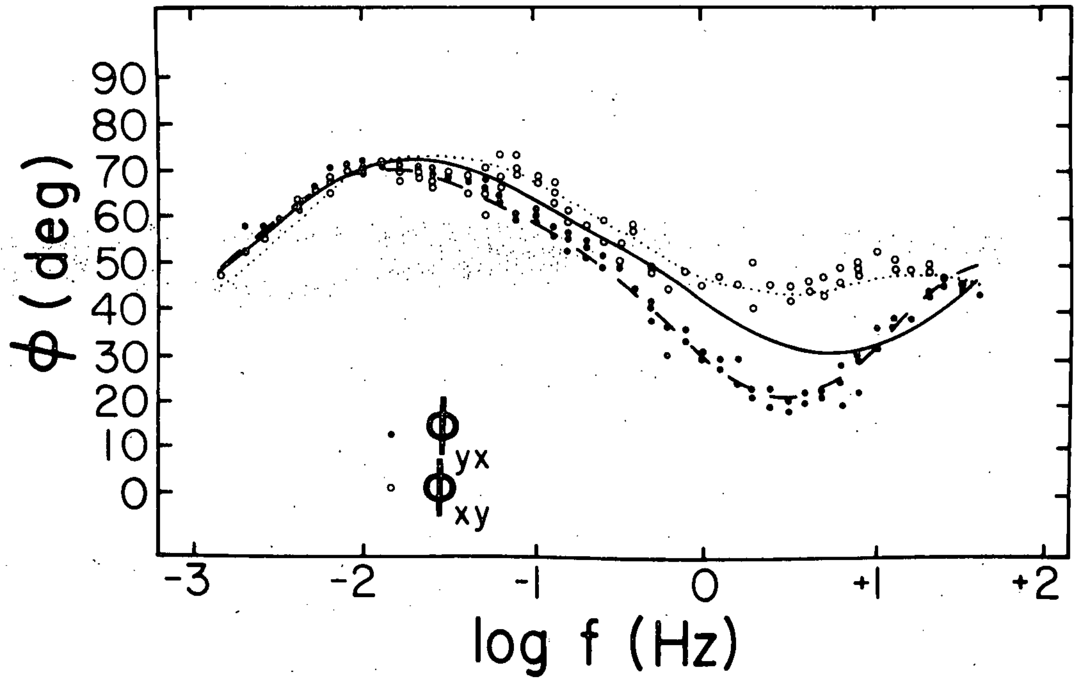
ϕ (deg)
90
80
70
60
50
40
30
20
10
0
-3
-2
-1
0
+1
+2
log f (Hz)
• ϕ_{yx}
○ ϕ_{xy}

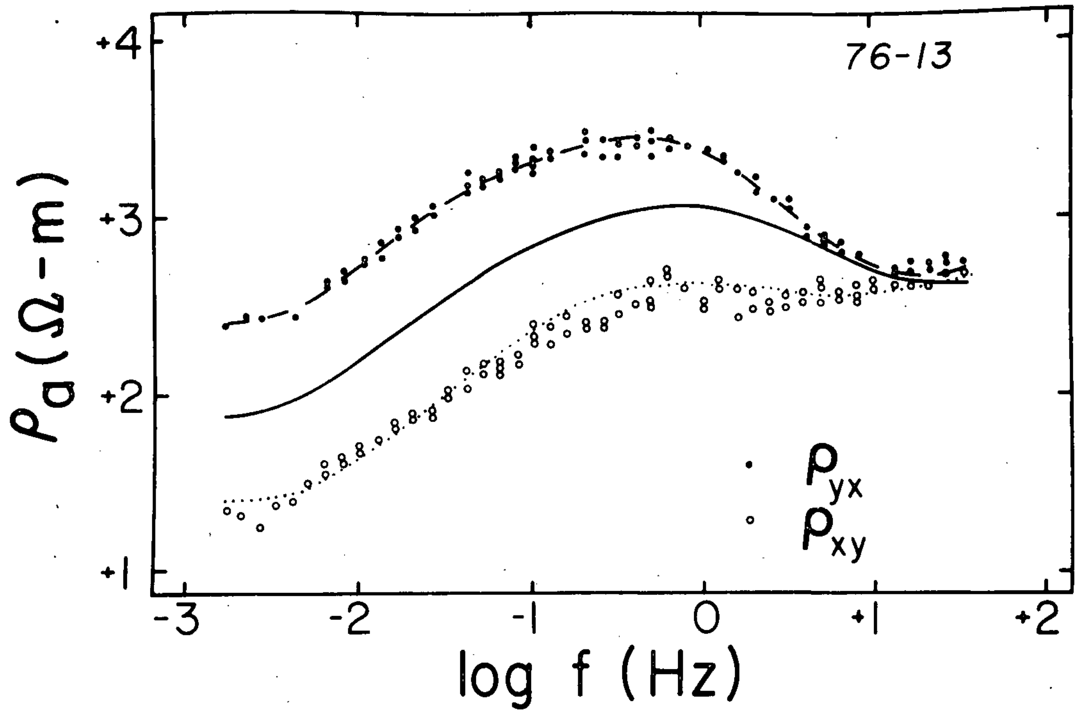
76-13
ρ_a (Ω-m)
+4
+3
+2
+1
-3
-2
-1
0
+1
+2
log f (Hz)
• ρ_{yx}
∘ ρ_{xy}

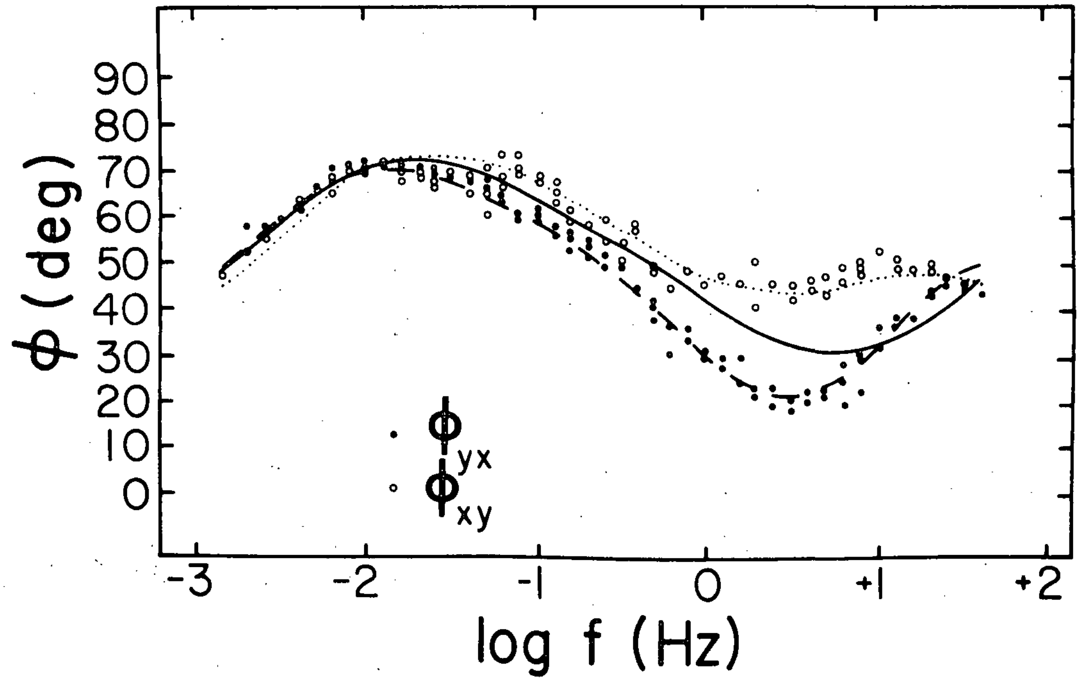
ϕ (deg)
90
80
70
60
50
40
30
20
10
0
-3
-2
-1
0
+1
+2
log f (Hz)
• ϕ_{yx}
∘ ϕ_{xy}

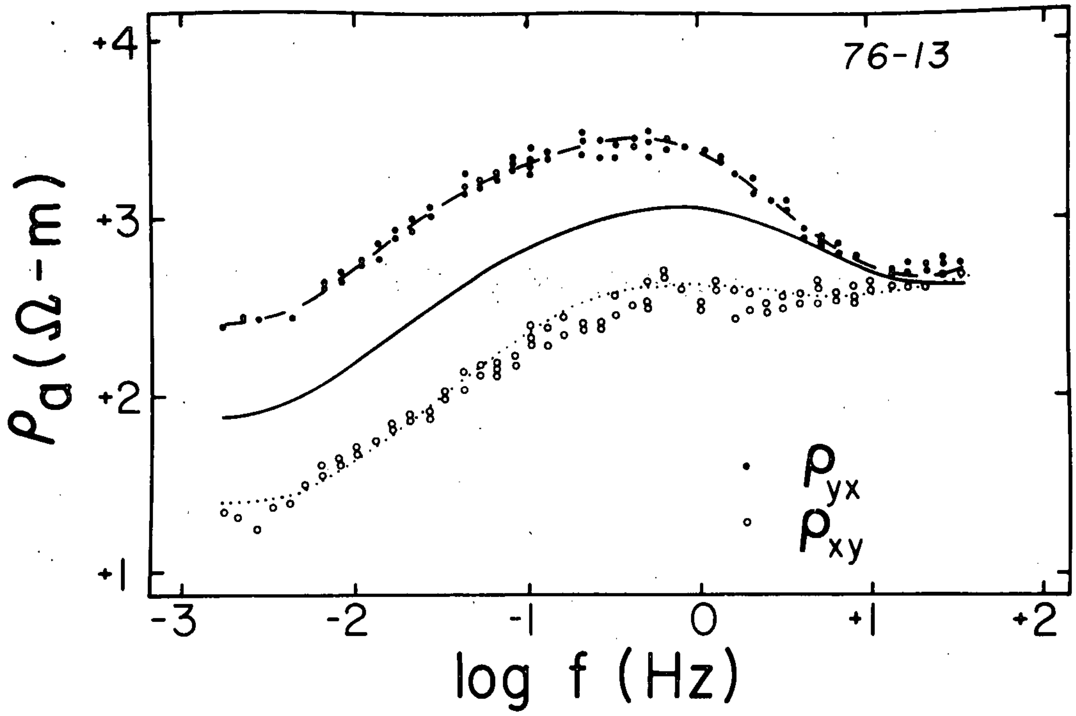
76-13
$\rho_a (\Omega\text{-m})$
+4
+3
+2
+1
-3
-2
-1
0
+1
+2
log f (Hz)
• ρ_{yx}
∘ ρ_{xy}

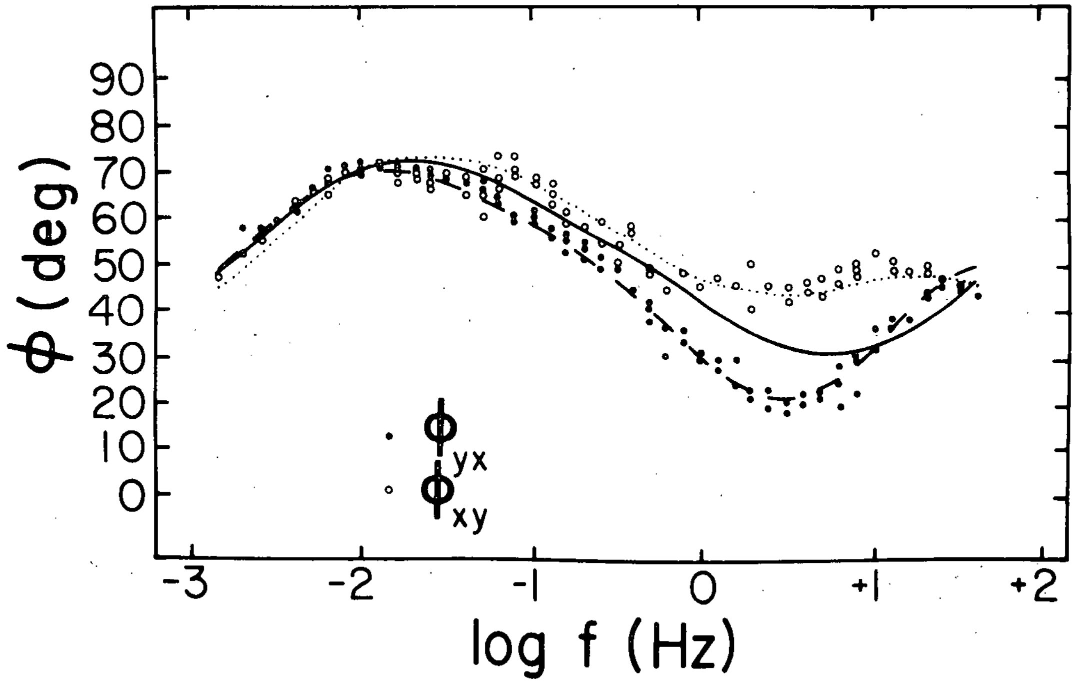
ϕ (deg)
90
80
70
60
50
40
30
20
10
0
-3
-2
-1
0
+1
+2
log f (Hz)
• ϕ_{yx}
∘ ϕ_{xy}

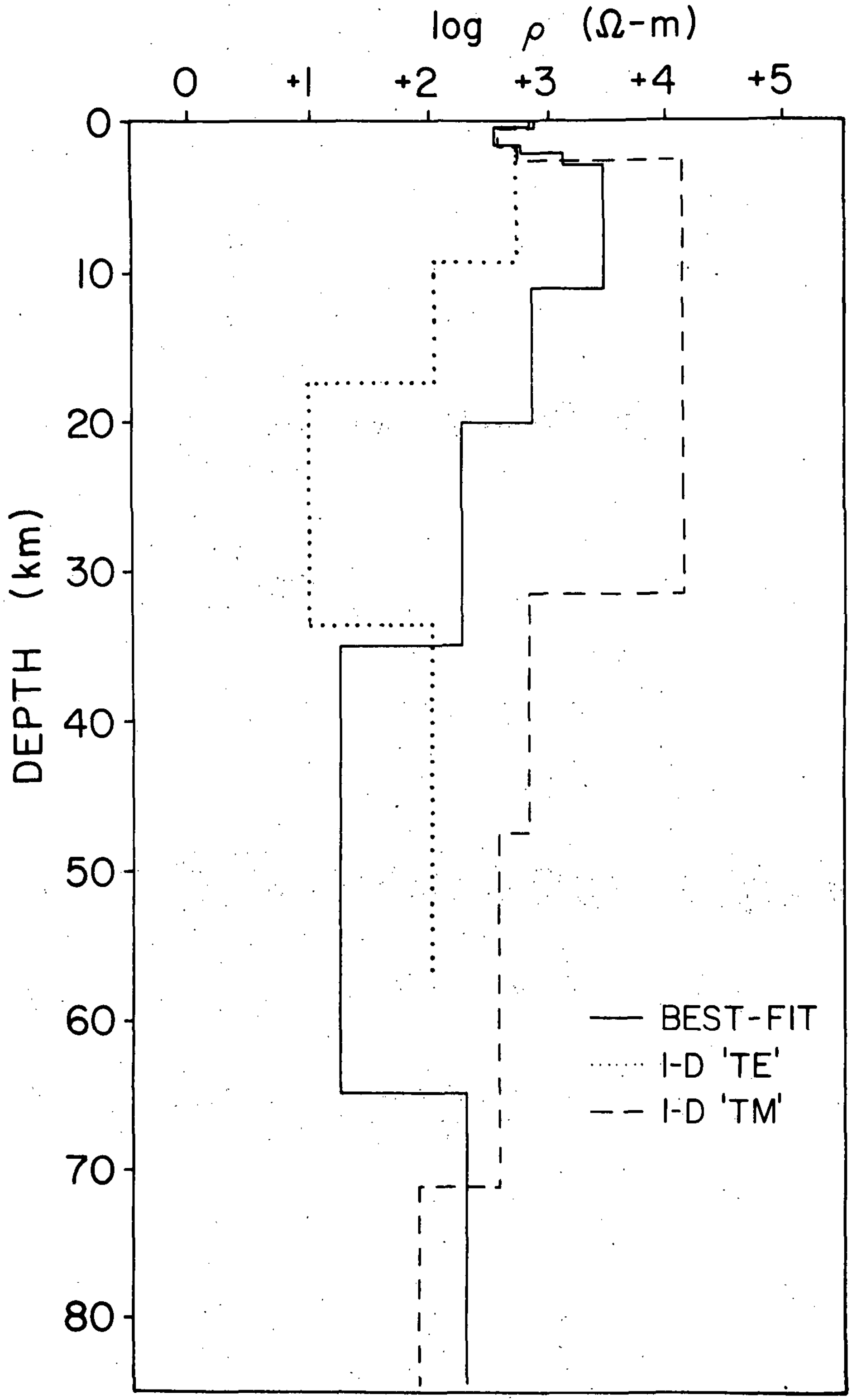

Figure 34. Best-Fit regional resistivity profile for the RHS thermal area compared to 1-D layered inverse models obtained from ρ_{xy} and ϕ_{xy} (dots) and ρ_{yx} and ϕ_{yx} (dashes).

point out however that the fit to the observations that the 1-D algorithm provides for (ρ_{yx}, ϕ_{yx}) and (ρ_{xy}, ϕ_{xy}) is very close, as evidenced by the dashed and dotted computed curves that pass through the data points of Figure 33. Within certain limits, it is not difficult to fit a 1-D model to data from a 3-D environment but the worth of such a model is very questionable.

We see that the 1-D inversion model layers computed from ρ_{yx} and ϕ_{yx} in Figure 34 are distorted and generally much thicker and more resistive than our best-fit choice. The 1-D layers computed from ρ_{xy} and ϕ_{xy} are generally much thinner and less resistive than our best-fit structure. The differences between our optimal profile and those obtained by 1-D inversions are substantially greater than those between the optimal model and the alternate layerings discussed in Figures 31 and 32, which we have already ruled unacceptable. To make matters worse, the models that result from 1-D inversions vary from site to site over the Mineral Mountains and the thermal anomaly area due not only to differences in distance of a given MT site from the valley but also due to the distorting effects of small-scale, near-surface inhomogeneities that are particular to a given site.

As a final step, we have taken our best-fit regional model as calculated using the 2-D TM routine and computed the purely 1-D soundings of apparent resistivity and phase as if there were no lateral inhomogeneities whatsoever. This has been plotted in Figure 33 as the solid curves. These fall roughly half-way between the observations (ρ_{yx}, ϕ_{yx}) and (ρ_{xy}, ϕ_{xy}) and demonstrate convincingly the severe effect of a valley full of conductive sediments. A 1-D interpretation approach is not valid in an environment with such severe lateral inhomogeneity as this one.

Plotting both modes of apparent resistivity and impedance phase in Figure 33 allows a test of our initial assumption that an effectively one-dimensional regional resistivity profile exists as a host for the lateral inhomogeneities which exist within 2-3 km of the surface at RHS. Below 0.01 Hz in this diagram, both ϕ_{yx} and ϕ_{xy} have converged to common values and ρ_{yx} and ρ_{xy} have shapes that are essentially identical. In actuality, such a convergence has occurred for all four apparent resistivities and impedance phases formed from the four impedance elements below this frequency for all stations over the Mineral Mountains away from the thermal anomaly area. Equation (29) indicates for sufficiently low frequencies that all four quantities ρ_{ij} become magnitude-scaled images of the apparent resistivity of the layered earth host and all ϕ_{ij}'s converge to the impedance phase of the host. The model studies shown in Figures 13 and 14 suggest that for the stations over the Mineral Mountains east of the Milford Valley, this low frequency limit reached by about 0.01 Hz, provided the valley is responsible for the differences in frequency dependence between any of ρ_{ij} or ϕ_{ij}. We believe this is in keeping with the majority of the observations at RHS, as exemplified in Figure 33, so that any possible lateral inhomogeneities in the deep or distant crust or upper mantle in the RHS area are not severe. This conclusion must be qualified somewhat for stations over the thermal anomaly area. The low frequency limit in this particular area does not occur until below at least 0.003 Hz and this is due exclusively to anomalous behavior in ρ_{xy} and ϕ_{xy}, and not in ρ_{yx} and ϕ_{yx} which were modeled to give Figures 27 and 29. Interpretation of these special features of the data must await development of our 3-D numerical algorithm to accommodate bodies in a layered earth.

The regional layering we show in Figures 31 and 34 must of course have some horizontal bounds. Hence, this structure is strictly speaking a lateral inhomogeneity, though the effects of its horizontal bounds must be rather restricted if a layered regional structure is consistent with the TM mode of data of all sites of lines B-B' and C-C' and both modes of data below about 0.01 Hz. This behavior of the observed data implies that such lateral bounds should be far removed or should be close to equidistant on the order of 50 km or more in any direction from the group of stations we have at RHS. Recall furthermore for frequencies above 0.01 Hz, which pertains mainly to the regional layering above 35 km depth including the entire crust, that the shapes of the apparent resistivity curves (ρ_{xx}, ρ_{xy}, ρ_{yx}, ρ_{yy}) and the values of the impedance phases (ϕ_{xx}, ϕ_{xy}, ϕ_{yx}, ϕ_{yy}) at a given station are not the same. From this portion of the observations it is conceivable that an interpretation of ρ_{xy} and ϕ_{xy}, and other MT quantities requiring an algorithm modeling 3-D bodies in a layered earth, will uncover large-scale (several tens of km wide) lateral inhomogeneity in the lower levels of the crust which is not apparent in the TM observations we have modeled to date. Considering however that a single layered structure below 2-3 km at RHS is compatible with the TM mode of all sites in lines B-B' and C-C', we believe that such widespread inhomogeneity in the deep crust or upper mantle, should it exist, is a rather special case which has not seriously affected our estimates of the profiles of Figures 31 and 34. Nevertheless, as explained in the upcoming discussion of tectonic significance of the regional profile, any such lateral inhomogeneity may have an important bearing on the geothermal system at RHS and should be investigated with additional MT soundings.

GEOLOGICAL IMPLICATION OF MODEL RESISTIVITY STRUCTURE

Discussion of the resistivity structure beneath lines B-B' and C-C' is divided into three areas: Milford Valley sediments and Mineral Mountains horst, structure beneath the thermal anomaly area and the regional resistivity profile. These sections relate in turn mainly to the distribution of regional geoelectric inhomogeneities in the Great Basin due for the most part to Miocene to present lithospheric extension, to special structure in geothermal systems involving anomalously high temperatures and active hydrothermal convection and to the average chemical composition and physical conditions as a function of depth in this area of the eastern Great Basin.

Milford Valley Sediments and Mineral Mountains Horst

Regional Extensional Tectonics and Morphology: The geoelectric sections of Figures 27 and 29 are dominated at least volumetrically by the water-saturated, unconsolidated, low-resistivity sediments filling the Milford Valley graben. This valley is only one example of dozens of such NNE trending deposits of alluvium characteristic of the Basin-Range structural province (Stewart, 1978). The onset of regional lithospheric extension as early as 20 m.y. ago (Late Cenozoic, mid-Miocene) along an approximately WNW axis has yielded elongate, normal fault-bounded portions of the crust that underwent relative uplift to form horsts or mountain ranges and relative subsidence to form grabens or valleys. Cumulative extension to date may range from 10% to 35% for the province as a whole. Whether the normal faulting defining these portions is downward-flattening (listric) or essentially planar is a matter of debate (Christiansen and McKee, 1978; Stewart, 1978), though movement seems likely to incorporate a substantial amount of strike-slip motion (Smith, 1978). The province overall has also undergone late Cenozoic uplift of from one to three kilometers.

The greatest amounts of overall uplift (up to 3 km) as well as present-day active extension occur in the Great Basin subprovince of the Basin-Range, an area comprised predominantly of Nevada and western Utah (Stewart, 1978). Furthermore, active seismicity, a thin crust, mapped crustal extensions and high heat flow suggest that the eastern margin of the Great Basin, including the Roosevelt Hot Springs, has experienced a particularly high rate of normal faulting over the past 10 m.y. or longer (Smith, 1978; Christiansen and McKee, 1978; Eaton et al, 1978; Lachenbruch and Sass, 1978). Hypocentral depths in this area appear restricted for the most part to less than 15 km implying that extensional deformation below this is not brittle but instead characteristic of a ductile deep crust and upper mantle (Smith, 1978). This concentration of spreading has led to especially deep alluvial fills (up to 3 km) in grabens, and the Milford Valley is no exception. As extension progressed continuously in the eastern Great Basin, Tertiary to present day alluvium has been deposited continuously in the evolving grabens from the evolving ranges. The mechanisms driving the formation of horst-graben morphology are the subject of much conjecture. Mantle upwelling models have been considered by Stewart (1978) and Eaton et al (1978) while Atwater (1970), Christiansen and McKee (1978) and Smith (1978) have advanced plate interaction scenarios. The previous tectonic conditioning of the Basin-Range lithosphere is likely important in the two mechanisms and both theories call upon basalt production, thermal expansion and/or mineralogical phase changes to be causes of the overall province uplift.

Predominantly alkalic basaltic and bimodal basalt-rhyolite volcanism appears to have begun contemporaneously with WNW lithospheric extension about 17 m.y. ago along a north-trending belt of dikes and flows in central Nevada and southern Oregon and Idaho (Christiansen and McKee, 1978). By 14 to 12 m.y. ago however, volcanism appears to have spread across the entire Great Basin to its present margins. Since 12 to 10 m.y. ago, activity seems to have been successively concentrated near the edges of the Great Basin and excluded from a growing central region located mainly in Nevada (Christiansen and McKee, 1978; Ward et al, 1978). As the concentration of volcanism near the Great Basin margins occurred, tholeiitic as well as alkalic basalts began to appear, although the former are volumetrically subordinate (Leeman and Rogers, 1970).

Igneous, metamorphic and sedimentary rocks formed the original basement for the Mineral Mountains horst and Milford Valley graben. The horst is defined by various Paleozoic and Mesozoic sedimentary rocks to the south and southeast, small amounts of Cambrian and Cretaceous sediments to the north and the large Mineral Mountains batholith in the central portion east of the thermal anomaly area at RHS (Ward et al, 1978; Nielson et al, 1978). K-Ar age dating summarized by Evans (1980) for the Mineral Mountains pluton shows a range from less than 10 m.y. to 22 m.y. indicating a complex thermal history for the pluton involving probable reheating events. Hintze (1973) assigns an Oligocene age to this batholith. Small outcrops and xenoliths of amphiboite and biotite gneiss basement rocks (Precambrian?) appear nearby and to the south of the thermal area. Examples of Oligocene rhyolitic ash-flow tuffs also lap onto the Paleozoic and Mesozoic rocks at the southeast corner of the horst and Eocene (?) and Oligocene conglomerates and extrusive volcanics outcrop in the Cricket - North San Francisco Mountains and Star Range to the north and west of RHS (Hintze, 1973). Finally, various Late Tertiary and Quaternary basalts and rhyolites, discussed subsequently in more detail, also exist around and on the crest of the Mineral Mountains (Ward et al, 1978; Evans and Nash, 1978).

The maximum relief between the surfaces of the Milford Valley and the mountains is about 1400 m but for the most part topography in the area is not severe. The various Precambrian to Oligocene rocks just described likely define the basement below the unconsolidated sediments in the graben. Alluvium was deposited here from various surrounding mountain ranges in response to ongoing extension since Miocene time but, in addition, Pleistocene Lake Bonneville lacustrine sediments also reside. Hintze (1973) describes as many as ten cycles of transgression and regression by this body of water from as long as 100,000 years ago to less than 10,000 years ago. It is probable that several cycles of such flooding have left the very clay-rich material observed in at least the upper few hundred meters of the Milford Valley; the eastern shoreline of the last transgression is apparent some 5 km west of the peak of the thermal anomaly (Mower and Cordova, 1974; Ward et al, 1978). Some intercalated coarser alluvium from the surrounding ranges was also likely deposited between cycles, especially near the edges of the valley.

Correlation of Resistivity Structure with Geology: The range of interpreted intrinsic resistivities of 200 to 1000 Ω-m within 2 km of the surface along lines B-B' and C-C' east of stations 77-13 and 78-25 (Figures 27 and 29, respectively) over the modestly inhomogeneous rocks of the Mineral Mountains horst is typical of that for well-indurated rocks. The Mineral Mountains is considered to be a hydrologic recharge area for convective waters in the geothermal system (Wilson and Chapman, 1980; Rohrs and Bowman, 1980; Smith, 1980) so that rock pore waters here, derived at least partly from rainfall, should be considered fairly fresh. Also, rock porosity here is likely made up of planar rock fractures plus more tortuous intergranular pores. Published experiments on the bulk resistivity of crystalline rocks due to electrolytic conduction in aqueous pore fluids as a function of temperature and pressure have been compiled by Brace (1971). It was concluded that bulk rock resistivities are determined typically by conduction through pores and that the empirical Archie's Law applies, i.e.

$$\rho = \rho_W \phi^{-m} \tag{70}$$

where ρ is the bulk resistivity, ρ_W is the fluid resistivity, ϕ is the fractional porosity and m is the tortuousity coefficient which is near two. However, due to ionic substitution and broken atomic bonds, the constituent silicate minerals generally possess a net negative charge, thereby creating on the boundaries of the minerals a layer of cations attracted from the solution and ultimately leading to an enhanced surface conductivity (Brace, 1971). Furthermore, the circulation of pore waters, even fairly fresh ones, in the upper few kilometers of the crust facilitates some alteration, particularly of feldspars to clay minerals, leading to a supply of exchangeable cations adsorbed to the surface of the clay minerals (Grim, 1968). The contribution of surface conduction to bulk resistivity is described approximately by the relation due to Waxman and Smits (1968),

$$\sigma = (\sigma_W + BQ_V)\phi^{+m} \tag{71}$$

where $\sigma = 1/\rho$ is the bulk conductivity, $\sigma_W = 1/\rho_W$ is the fluid conductivity, ϕ and m are as defined for Archie's Law, B is a factor which takes into account the dependence of the mobility of the excess surface cations on the pore fluid concentration (Sm^2/eq) and Q_V is the concentration of excess surface cations per unit pore volume (eq/m^3). The factor $(\sigma_W + BQ_V)$ can be considered the effective electrolyte conductivity for an Archie's Law dependence. Surface conduction becomes increasingly important when pore passages are small and the fluid is of low ionic strength, conditions which apply generally to the rocks of the Mineral Mountains, so that bulk resistivity might be lowered by an order of magnitude or more from that simply predicted by equation (70) (Brace, 1971). For fresh pore waters typically of a few tens of ohm-meters, intrinsic resistivities of 200 to 1000 Ω-m could correspond to porosities of around a few percent. East of soundings 78-15 and 76-11 of lines B-B' and C-C' in Figures 27 and 29, moderate resistivity substance reaching depths of a few hundred meters is not well discerned due to limited station density but can be explained as a mixture of rubbly Quaternary basalt flows associated with the Cove Fort KGRA and coarse, partially saturated alluvium (Evans, 1977). At depths somewhat greater than 2 km under either line of stations in Figures 27 and 29, the rise in resistivity to 3000 Ω-m, corresponding also to the start of the apparently 1-D regional profile, is likely related to basement rocks with porosities below 1%.

Much lower resistivities from a few tens of ohm-meters down to about 1 Ω-m west of stations 77-13 and 76-3 on lines B-B' and C-C' of Figures 27 and 29 correspond probably to Tertiary to present-day alluvium and clays deposited in the Milford Valley graben. The relation (71) is still appropriate for describing bulk resistivity for these materials though the porosities and clay contents are much higher than in the rocks of the Mineral Mountains. The media in Figures 27 and 29 beneath stations 78-4 to 77-13 and 78-22 to 76-3 ranging from 6 to 40 Ω-m within 200 m of the surface possibly represent surficial clays, sands and gravels which are partially or completely water-saturated. Looking deeper, the most conductive (1.1-2.2 Ω-m) units are believed to correspond to predominantly clay-rich Lake Bonneville sediments. Sensitivity tests, not described in this report, of data for the valley stations suggests that the 650 m maximum depth shown to the base of this feature is an estimate likely accurate to within ±200 m. Below 650 m, the 25 Ω-m substance observed in both cross sections probably relates to unconsolidated to semiconsolidated pre-Bonneville alluvium and perhaps volcanics extending downwards to the Oligocene and older basement rocks. The boundary between the Tertiary alluvium and the older rocks may be an electrically "soft" one; if earlier Tertiary volcanics and conglomerates appearing in the Cricket-North San Francisco Mountains stratigraphic sections exist just below the alluvium, a gradation in resistivity from about 25 Ω-m to several hundreds of Ω-m may occur as one descends into plutonic or pre-Cenozoic rocks. As stated earlier, even if the depth extent of this 25 Ω-m medium is sharply bounded, it can be resolved with rather little confidence based upon the transverse magnetic observations alone. We believe however that ρ_{xy} and ϕ_{xy}, which require an algorithm accommodating 3-D bodies in a layered earth, would be more sensitive than ρ_{yx} and ϕ_{yx} to depth to bottom of this material.

The steeply dipping interfaces which bound the valley sediment sequence on the west and east are interpreted to represent major normal faulting. A single fault surface on the eastern side will fit the data for line B-B' although a more stepped boundary is implied by the data for C-C', one just east of station 78-24 and one just west of station 76-2 in Figure 29. The magnitudes of dips are poorly resolved but steep inclinations are favored. As in the case of the depth extent of the valley media, ρ_{xy} and ϕ_{xy} should be affected more than ρ_{yx} and ϕ_{yx} by variations in dip.

Independent geophysical evidence is supportive of our conclusions concerning the horst-graben morphology at RHS. Direct-current electrical surveys described by Ward and Sill (1976), Tripp et. al (1978) and Ward et al (1978) have shown resistivities in the range 200-1000 Ω-m for the rocks in the upper few hundred meters of the

Mineral Mountains. The DC resistivity results over the valley sediments do not resolve well any depths to interfaces but show resistivities substantially below 5 Ω-m. Refraction seismic measurements discussed by Gertson and Smith (1979) show a rise in V_p over the Mineral Mountains from 4.0 to 5.5 km/s over the depth interval 1.5 to 2.0 km. This correlates well with our interpreted rise in resistivities here from a few hundred to 3000 Ω-m near 2 km depth which we believe represents a pressure-induced decrease in pore and fracture porosity. Below the Milford Valley, three media were delineated by the refraction method. The uppermost medium, of a maximum thickness of 700 m and possessing a V_p of 1.8 km/s, compares closely with our low resistivity media of 1.1 to 2.2 Ω-m and probably reflects the presence of the clay-rich Lake Bonneville material. Deeper, a unit with a V_p of 4.0 km/s extends to a depth of about 2 km, although the bottom of this unit is not well-determined by the refraction survey. It likely corresponds to the 25 Ω-m medium shown here in Figures 27 and 29 which in turn relates to pre-Bonneville alluvium and perhaps volcanics. As explained previously with regard to the interpreted resistivity, this boundary may be acoustically gradational. The lowermost medium of V_p = 6.7 km/s must represent very well-indurated rocks, perhaps indicating that the graben basement is made up mainly of Precambrian gneisses. As shown for resistivity in Figures 27 and 29, the eastern valley margin is interpreted by the refraction technique to be steeply dipping and rather abrupt.

A steep east margin to the sediments is suggested as well by a pronounced gravity gradient here (Carter and Cook, 1978). Assuming a uniform alluvium-bedrock density contrast of 0.5 gm/cm^3, Carter and Cook modeled their observations with a valley fill of about 1.5 km. Such a uniform contrast is unrealistic in light of the multi-layered valley section described by the MT and refraction seismic studies. Gertson and Smith (1979) have shown that a multilayered valley is consistent with the gravity observations.

Structure Relevant to the Thermal Anomaly Area

The discussion accompanying Figure 29 has shown that our greatest difficulty in fitting the observations with a 2-D TM algorithm occurred for stations directly over the thermal area in Figure 29 and so we have some misgivings about correlation of some of the resistivity structure below the thermal area with geology and physical conditions. After a description of heat flow, geology and geochemistry relevant to possible electric structure around and within the thermal area, some tentative conclusions based upon resistivity structure concerning the thermal reservoir and deep heat source will be noted.

Heat Flow, Geology and Geochemistry of the Thermal Area: Temperature profiles and heat flow values for 53 drill holes outline a N-S elongated area of anomalous heat flow (>100 mWm^{-2}) integrating to nearly 70 megawatts (MW) roughly centered upon the Opal Mound Fault, a controlling NNE trending fracture (Ward et al, 1978; Wilson and Chapman, 1980). The 400 mWm^{-2} heat flow contour, considered a criterion for an economic geothermal prospect, encloses an area of about 57 km^2 as shown in Figure 1. Downward continuation of the heat flow signature by Wilson and Chapman (1980) suggests a depth to top of major heat sources, assumed to correspond to the top of the thermal reservoir, of about 450 m and that the heat sources are restricted to an area approximately 6 km long (NNE direction) by 1.5 km wide. Dip and depth extent of the heat sources were unresolved.

Drilling has indicated that the actual heat sources are steeply dipping fractures (Ward et al, 1978). Based upon surface geological mapping and drilling results, Nielson et al (1978) emphasize that the geothermal system is controlled by four major fault sets. Representative members of the first three sets described here appear in Figure 11 of Ward et al (1978). The first two systems are steeply dipping and trend NW and NNE, respectively. The economic brine- and vapor-producing zones seem localized along these fractures where some production wells have been drilled to depths near 2 km. The third set, steeply dipping E-W faults, possibly represents the effects of deep-seated regional stresses (Nielson et al, 1978). These faults may contribute to the influx of fresh cold waters into the convective system and may serve to limit the southern extent of the thermal reservoir. The fourth system consists of one or more listric denudation faults with shallow westward dips and a normal sense of displacement. The producing fracture zone is for the most part contained in the upper block(s) of this faulting which appears to predate the producing fractures. Yusas and Bruhn (1979) argue that the NW and NNE fracture sets observed away from the producing zones result mainly from cooling and contraction of the Mineral Mountains pluton. The concentration of such fractures that define the producing zone in the upper block(s) of the denudation faulting may result from displacement along such faulting coupled with strength anisotropies induced by the contraction of the pluton.

Pervasive hydrothermal alteration of rocks and sediments is apparent around the RHS thermal anomaly area (Ward et al, 1978; Parry et al, 1980). Surficial alteration is most concentrated along the NNE-trending Opal Mound Fault forming a zone roughly 6 km long and a few hundred meters wide. Sulfide-bearing sodium chloride thermal brines (ionic strength = 0.1 to 0.2) rise convectively along fractures and cool near the surface by conduction and steam separation. Near-surface alteration consists of opaline sinter, massive opal, siliceous sinter-cemented alluvium, native sulfur and iron sulfide minerals. A high pH alteration assemblage of muscovite, quartz and chlorite with calcite is superimposed in disequilibrium upon a low pH assemblage of alunite, kaolinite, montmorillonite and muscovite. Alteration of primary feldspars and mafic minerals to clays appears most intense within 200 to 400 m of the surface. A less abundant assemblage of K-mica, chlorite, calcite, K-feldspar and pyrite in gneiss and plutonic rocks was noted in wells approaching 2 km in depth and 2 km away from the Opal Mound Fault, but alteration intensity appears correlated with individual fractures and small scale granite and microdiorite dikes (Ballantyne, 1980). The lack of alteration of primary minerals in unfractured igneous and metamorphic rock may be the result of its low porosity and permeability.

Ward et al (1978) document the distribution and ages of the Late Tertiary and Quaternary volcanism in west-central Utah which include the 600 year old basalt eruption at Ice Springs some 90 km northeast of the RHS thermal area near Fillmore, Utah. In addition to the Late Miocene (7.9 m.y.) rhyolite on the west flank of the Mineral Mountains south of the thermal area, 7.6 m.y. old basalt outcrops on the southern flank of the mountains and the Cove Creek volcanic center some 25 km north of the thermal area contains basalts and rhyolites ranging in age from 0.97 to 2.5 m.y. Within 15 km of the thermal area, Quaternary basalts and andesites associated with the Cove Fort KGRA, of age 0.1 to 1.1 m.y., lie on the eastern flank of the Mineral Mountains.

Of possible significance to the Roosevelt Hot Springs are the two, 0.8 m.y. old rhyolite flows and ten, 0.6 to 0.5 m.y. old rhyolite domes, all of high silica contents, present in the central Mineral Mountains east and southeast of the thermal area (Evans and Nash, 1978). Using Fe-Ti oxide and two-feldspar geothermometers, temperatures of 785° C in the flows and 650°C in the domes were estimated. Estimates of P_{H_2O}, a dominant variable determining melting temperature and electrical resistivity, for the rhyolite magmas range from about 150 to 800 bars indicating that the melts contained substantial water but were not saturated. Significant amounts of fluorine (0.3 to 0.4 wt.%) were also detected. Overall, the dome magma appears to have been cooler and drier than that of the flows and may, but not necessarily, have evolved from the flow-forming magma (Ward et al, 1978).

The exact relationship of the repeated volcanism in the eastern Great Basin, especially the rhyolite volcanism in the Mineral Mountains, to the ultimate heat source of the Roosevelt Hot Springs activity is not known. One theory regarding geothermal system heat sources does not relate directly to igneous activity but holds that groundwaters circulating deep in Great Basin crust with characteristic, regional temperature-depth profiles and subsequently rising to the surface along permeable fracture systems are sufficient to produce the observed temperatures and heat flows in the geothermal area. Background heat flow values in this region of the eastern Great Basin exceed 90 mWm^{-2} (Bodell et al, 1980), corresponding roughly to a regional geotherm of 40°C/km. This concept has been applied successfully to the Monroe, Utah, KGRA (Kilty et al, 1980) where water, probably residing at temperatures somewhat over 100°C in a sandstone aquifer, rises from a depth of about 2 km along steep fractures to give the observed, surface thermal manifestations. There are difficulties in applying this idea to RHS since temperatures near 270°C are observed in some wells (Ward et al, 1978). This requires efficient circulation of groundwater to depths exceeding 7 km. In a previous section relating resistivity cross sections to the horst-graben morphology, a rise in interpreted resistivity from a few hundred to 3000 Ω-m and in estimated V_p from 4.0 to 5.5 km/s at depths around 2 km was believed to correspond to a marked decrease in fracture pososity. Furthermore, rock mechanics experiments cited by Yusas and Bruhn (1979) indicate that extensional fractures formed in response to cooling and contraction of the Mineral Mountains pluton, believed to be those dominating fracture porosity at RHS, cannot develop under confining pressures exceeding 1 kilobar (∿3 km depth). A depth of about 2.5 km to a lower impermeable boundary has also been used by Smith (1980) to model interbasin groundwater flow in this area. Hydraulic permeabilities to depths exceeding 7 km are probably not high enough for the deep circulation model to adequately explain the thermal anomaly at RHS.

A second model for the primary heat source of a high-temperature (>200°C) geothermal system receiving much consideration is proposed by Smith and Shaw (1975) and, for the eastern Great Basin, invokes a direct relation between the system and the bimodal basalt-rhyolite eruptions that are generally nearby (Lipman et al, 1978; Evans and Nash, 1978). Smith and Shaw (1975) argue that a high-level (<10 km) magma chamber is required to form thermal anomalies of economic interest and that, for continental volcanic occurrences, such chambers are observed to be rhyolitic. Crustal melting to yield upper-level rhyolite magmas is due to a combination of high regional heat flow and the intrusion(s) of basaltic magma, formed by partial fusion in the upper mantle, into lower levels of the crust. For water-dominated geothermal systems such as RHS, White (1957) suggests that observed thermal waters are a mixture of hot (∿700°C), dense, solute-rich (mainly NaCl) vapors driven upward from the cooling, silicic magma that condense in circulating meteoric water (also White et al, 1971; Burnham, 1979a). To counter conductive and convective heat losses, a continual reinjection of basaltic magma from deep crust or mantle levels may be the ultimate heat supply for upper level rhyolite magmatic and geothermal systems persisting for over 100,000 years (Smith and Shaw, 1975).

After reasonable allowances for background Great Basin heat flow, local hydrologic recharge and discharge and exothermic alteration reactions at RHS, Ward et al (1978) estimate the net heat flow near 60 MW may be supplied by steady-state conduction from a body near 700°C (just above the wet granite solidus) having lateral dimensions of the Mineral Mountains pluton at a depth of 7 km. Such a body could alternately exist at shallower depths in the crust beneath RHS but would have to be smaller, particularly if hydrothermal convection is an important heat transfer mechanism. For a heat source of a given depth to have a temperature that is more or less steady-state, it is reasonable to conclude that it remains partially molten by the previously defined resupply of heat from greater depths. Conductive cooling of a chamber without a resupply of heat since the rhyolite dome emplacement is insufficient to maintain a thermal budget of 60 MW for 0.5 m.y. (Ward et al, 1978). The numerical simulations involving hydrothermal convection of Cathles (1977) suggest that 50,000 years is sufficient time for cooling of typical silicic intrusions. The above discussion does not rule out the possibility that the heat source for the present-day thermal activity at RHS is not a chamber that has evolved more or less continuously from that which supplied the 0.5 m.y. old domes but instead has resulted from an independent intrusion of basaltic magma into the deep to intermediate crust.

Near-Surface Resistivity Structure: The thermal and hydrological regime beneath the thermal anomaly has resulted in resistivity structure in the upper 300 m that affects the MT observations in this area to arbitrarily low frequencies, as evidenced by the earlier 3-D model studies as well as Figures 15, 27 and 29 concerning line C-C'. In the upper 300 m of the finite element section beneath stations 76-3, 76-4 and 78-51 of Figure 29, the resistivity progresses downward from 50 Ω-m material of 100 m maximum thickness through 2-6 Ω-m material into a resistive medium of 400 Ω-m.

The intrinsic resistivity of the earth materials in this part of the section is defined in terms of the brine chemistry, surface conduction contributions and porosity by equation (71). The uppermost 50 Ω-m material is correlated with alluvium, of typical porosities 15-30%, which may be completely or partially water-saturated. Some alteration of feldspars to clays is inevitable in the weathering process producing the alluvium so that a significant contribution from clay surface conduction is likely. The 6 Ω-m material encountered next in Figure 29 beneath stations 76-3 and 78-51 probably represents saturated and hydrothermally altered alluvium and/or bedrock. This is particularly true for the 6 Ω-m substance beneath site 76-3 where Ward and Sill (1976) and Wilson and Chapman (1980) point to thermal brines leaking westward from the Opal Mound Fault to the Milford Valley. The small volume of 2 Ω-m material beneath station 76-4 is interpreted as an intensely altered, porous and brine-saturated fracture zone extending for a limited distance east of the Opal Mound Fault. Ward and Sill (1976) have estimated that the presence of hydrothermal clay in typical amounts at RHS can lower resistivities by a factor of two to four. In conjunction with hot brines, enhanced surface conduction has led to a volume of earth some 10 km (N-S) long by 4 km (E-W) wide extending a few hundred meters downward that is significantly lower in intrinsic resistivity from the relatively unaffected surrounding rock and sediments. As brought out earlier in connection with Figures 17 and 21 through 23, depression of the total electric fields, and hence ρ_{xy} and ρ_{yx}, over the above defined shallow volume of earth will cause falsely low layer resistivities and falsely shallow depths to interfaces if a 1-D inverse algorithm is applied to MT data taken within this volume to interpret the character of a deeper layered sequence. Both the upper 300 m of these geoelectric sections and the correlation of this resistivity to geology using MT agree with those deduced from DC resistivity and CSAMT investigations.

Detectability of the Thermal Reservoir: Although they severely affect the MT response in their vicinity, the near-surface conductive features just described are not of direct interest to us and essentially comprise annoying geologic noise. We are very interested however in delineating any possibly economic thermal reservoir beneath such noise. Unfortunately, model sensitivity tests described by Ward and Sill (1976) showed that targets at 500 m beneath the thermal area would remain unresolved by the dipole-dipole surveys.

The resistivity medium of Figure 29 that would correspond most closely to the suggested volume of major heat sources of Wilson and Chapman (1980) is that of 50,000 Ω-m at a depth of 400 m beneath stations 76-3, 76-4 and 78-51. The depth and eastern limit of the resistivity structure agrees well with those of the heat source volume of Wilson and Chapman but the western extent of the former is about 3 km as opposed to 1 1/2 km for the latter. The depth extent of the highly resistive unit is poorly resolved though a deep extent fits the data marginally better. Recall that the agreement between observed and modeled data in Figures 25, 27 and 30 for line C-C' for the pertinent three MT stations over the frequency range that is most affected by the 50,000 Ω-m prism is quite unsatisfactory.

The bulk resistivity relation (71) is still applicable for a thermal reservoir with minor qualification. The structural mapping of Nielson et al (1978) and Yusas and Bruhn (1979) indicate that extensive planar fractures are the dominant factor determining porosity so that the tortuousity coefficient m should be closer to unity. Also, the fractures have a considerable width, often on the order of millimeters or more, although microfractures may be common; the contribution from surface conduction could be minor (Brace, 1971). It is assumed that the intrinsic resistivity of the minerals is very high (>10^6 Ω-m) at temperatures characteristic of the RHS geothermal system in the upper 2 km (<300°C). Hence, the resistivity of the pore fluids is the controlling variable for a given fracture porosity. To achieve resistivities of 50,000 Ω-m, as we model in Figure 29, requires pore filling intrinsic resistivities on the order of 10^4 Ω-m. This would imply special P-T conditions, namely that vapor dominates volumetrically over liquid in the economic thermal reservoir.

Quist and Marshall (1968) have measured the specific conductivities of NaCl brines as a function of temperature and pressure and their data on 0.1 N fluids, representative of those in wells at RHS KGRA, have been constructed into Figure 35. This P-T diagram shows intrinsic brine resistivities as solid contours (values in Ω-m, dashed where uncertain). Included is the fluid boiling curve as a dotted line ending at the critical point at X (Souririjan and Kennedy, 1962). The critical point for this brine is a mere 5°C and 10 Bars higher than for

Figure 35. Pressure-temperature diagram showing contours of intrinsic resistivity of a 0.1 N NaCl fluid representative of thermal brines observed at the Roosevelt Hot Springs. The boiling curve of the brine is shown with dots while the critical point is at X. Contours are in Ω-m. Included also is the temperature log of US 14-2, assuming hydrostatic pressure. Compiled from data of Quist and Marshall (1968) and Souririjan and Kennedy (1962).

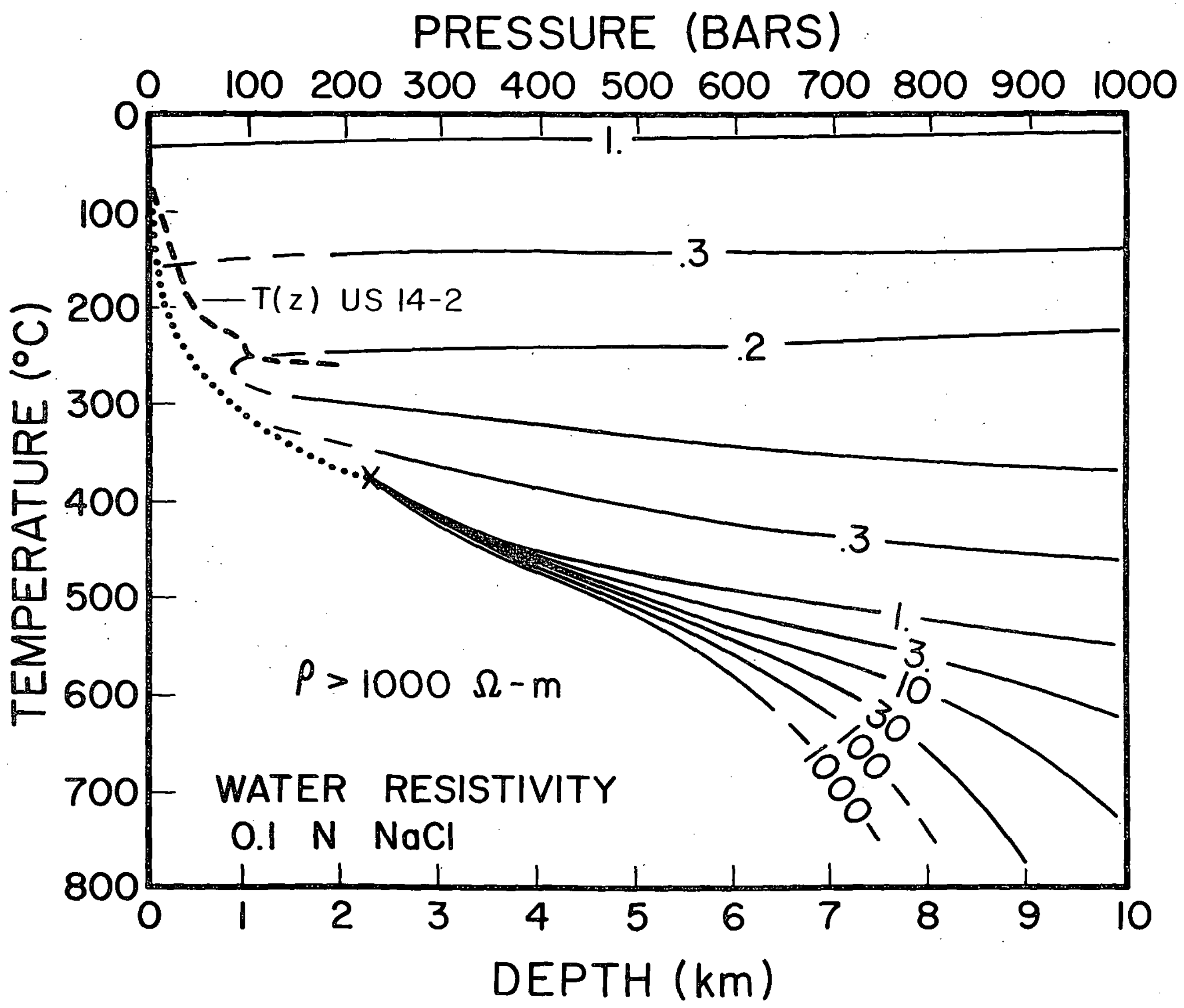
PRESSURE (BARS)
0
100
200
300
400
500
600
700
800
900
1000
TEMPERATURE (°C)
0
100
200
300
400
500
600
700
800
DEPTH (km)
0
1
2
3
4
5
6
7
8
9
10
1.
.3
.2
.3
1.
3.
10
30
100
1000
T(z) US 14-2
ρ > 1000 Ω-m
WATER RESISTIVITY
0.1 N NaCl

pure water. Quist and Marshall (1968) also show that resistivity is close to a linear function of concentration for solutions of 0.1 N strength or less.

At temperatures near 300°C and pressures over 100 bars in Figure 35, a resistivity minimum for the brine below 0.2 Ω-m is observed expanding towards higher pressures. At this temperature, water viscosity is at a minimum meaning ion mobility is near a maximum. If 0.1 N NaCl brines are representative throughout the postulated reservoir, then this represents an absolute lower limit on the reservoir bulk resistivity (100% porosity!). For temperatures in the vapor region above the boiling curve, the solubility and degree of dissociation of NaCl is drastically reduced resulting in resistivities in excess of 10^4 Ω-m. These latter P-T conditions seem imperative if a medium of 50,000 Ω-m resistivity really exists beneath the thermal area in rocks of substantial fracture porosity. To be complete, we note for Figure 35 that the increasing resistivities for temperature above 300°C and pressures above 500 bars are in response to a fall in the dielectric constant of water and hence in the degree of dissociation of the charge carriers Na^+ and Cl^-. Supersaturation of NaCl is not obtained in this P-T regime and thus it must be denied as a reason for increased resistivity (Souririjan and Kennedy, 1962).

Independent geological and geophysical evidence does not support the notion of vapor zones beneath the thermal anomaly at RHS. Cathles (1977) has shown that, during evolution of the hydrothermal convection within and surrounding a shallow intrusion, P_{H_2O} remains close to hydrostatic throughout. We assume therefore that measured temperature-depth profiles at RHS may be plotted as a function of equivalent pressure in Figure 35. The temperature profile in well US 14-2, shown in Figure 29 to pass along the eastern edge of the 50,000 Ω-m to a depth of 1902 m, is seen in Figure 35 to be on the average 70°C too cool for the solution to be above the boiling curve and of intrinsically high resistivity. Another well of interest, US 72-16 of total depth 375 m, lies some 6 km south of line C-C' but would project only a few hundred meters east of station 76-4. Presuming hydrostatic pressures again, the temperature profile for this hole (not shown in Figure 35) is essentially coincident with the boiling curve (Wilson and Chapman, 1980). However, Rohrs and Bowman (1980) argue that circulation in this well has resulted in post-drilling temperatures in excess of those existing before drilling. According to White et al (1971) the high chloride contents of the 0.1 N NaCl brines encountered in both near-surface and deep wells would make the Roosevelt Hot Springs a liquid water-dominated geothermal system.

Concerning resistivity structure now, there is a possible alternate explanation for the observed anomaly of very small ϕ_{yx} and steeply increasing ρ_{yx} for decreasing frequencies for stations 76-3, 76-4 and 78-51. Examination of Figure 20b, ρ_{yx} at 0.1 Hz, along with the residual gravity anomaly map of Carter and Cook (1978) indicates that the trend of the rangefront faulting that bounds the bulk of the valley sediments on their eastern side changes from a dominantly N-S trend, as pertains to line B-B', to one approximately S45°W for stations south of 78-28 in Figure 1. We believe that frequency-dependent current-gathering effects nearby but just to the east of such a corner in the valley sediments may result in anomalously low ϕ_{yx} and steep ρ_{yx} such as we were unable to reproduce in Figure 27. Similar frequency-dependent current-gathering phenomena were observed near the corners of the platelike 3-D model of Figure 10, though we did not discuss them earlier in the text. Values of ϕ_{yx} at 0.3 Hz at a receiver location $x' = 18$ km, $y' = 7$ km for Figure 10 using ϕ-strike to determine the x-axis are about 25° as opposed to about 37° for ϕ_{yx} at $x = 0$ km, $y = 7$ km, where agreement with the 2-D TM results occurs. The difference is about 12° and at a higher freequency, say 3 Hz, the difference may exceed 20°. A less sharp corner, 135° instead of 90° which is more applicable to the trend of the Milford Valley just described, may produce a less severe difference at 3 Hz, ten or so degrees as opposed to 20°. Twelve degrees is approximately the lack of fit we are faced with in the frequency range 1 to 10 Hz for the above problematic three stations.

In light of this possible 3-D effect and the lack of supportive independent evidence, we cannot endorse the notion of a zone of highly resistive vapor beneath the thermal anomaly area. We do however still favor the earlier conclusion given in the section on sensitivity tests of structure beneath line C-C', which is that a conductive prism of regular geometry corresponding to the zone of major heat sources of Wilson and Chapman (1980) does not exist below the thermal anomaly. Delineation of any economic thermal reservoir using MT will be an involved process owing to the finite strike extent of this reservoir along with those of the valley sediments and the near-surface, variable hydrothermal alteration. If the reservoir is elongated in a N-S direction, as the pattern of producing wells and heat flow values suggest, the quantities ρ_{xy} and ϕ_{xy} should be more sensitive to it than ρ_{yx} and ϕ_{yx}, which we have modeled in Figure 29. The vertical H-field relations $\tilde{Y}_z(\overline{r})$ and $\tilde{K}_z(\overline{r})$ should also be useful. Interpretation of these quantities requires an algorithm that can model 3-D bodies in a layered earth. A further complication we must be aware of concerning the reservoir is variable intrinsic resistivity anisotropy, as suggested by the fracture density recordings of Yusas and Bruhn (1979).

Detectability of the Deep Heat Source: The deep heat source in which we are interested presumably corresponds to a partially molten silicic magma chamber in the upper crust formed in response to high regional heat flow and injection(s) of basaltic magma into the intermediate to deep crust from the upper mantle (Smith and Shaw, 1975). This chamber, if it exists, may have a high resistivity contrast with its host rocks but, if it is located beneath the thermal anomaly, its magnetotelluric response will have superimposed upon it the response of the near-surface resistivity structure and any signature possessed by the economic thermal reservoir.

The conductivity of partially molten granite as a function of P_{H_2O} and T was measured by Lebedev and Khitarov (1964). For water pressures in excess of 1 kilobar and temperatures over 700°C, granitic partial melts were shown to have intrinsic resistivities below 1 Ω-m. This would provide a sizeable contrast with lower temperature, unmelted host rocks conceivably having resistivities over 1000 Ω-m (Brace, 1971). An Archies Law dependence like equation (70) is expected to apply for partial melts if conduction in an interconnected liquid phase dominates over conduction in the crystalline residue; Lebedev and Khitarov (1964) unfortunately do not correlate their conductivities with percentage of melt phase. Conduction in silicic melts is ionic, involving mainly the univalent cations Na^+ and K^+ which provide charge balance for the individual but highly polymerized feldspar structural units (Burnham, 1979b). These alkali charge carriers must move from unit to unit to enable conduction. Water may enter and greatly depolymerize the melt by partial hydrolysis and exchange of H^+ for Na^+ and K^+ in the feldspar units. This exchange greatly enhances mobility of the alkali ions and resultant increases of conductivity may approach four orders of magnitude for H_2O-saturated silicic liquids (ibid.). The dissolution of HF in silicic magmas is by the same partial hydrolysis and cation exchange mechanism as for H_2O. HF is in fact more soluble than H_2O so that, given its substantial presence in the magmas producing the domes and flows over the Mineral Mountains, fluorine may be important in lowering resistivities in any postulated, present-day magmatic heat source for RHS.

Silicic magmas in nature, however, are rarely water-saturated. An average of 2-3% H_2O by weight has generally been observed by Wyllie (1977) and Burnham (1979a) indicating that only a limited amount of water was available to the system that generated the magmas. This observation must be kept in mind when considering any possible silicic magma chamber at RHS. Below a few kilometers in the crust, interstitial water is presumably subject to the same load as the minerals so that $P_{H_2O} = P_{total}$ to a good approximation, even under all metamorphic conditions but regional granulite facies (Winkler, 1979, p

15-27). Hence, the minimum melting temperature of a source region is not affected at a given depth by the volume of free water but the total amount of melt produced is. This point was duly noted by Feldman (1976) and Stanley et al (1977). Since presumably water cannot diffuse quickly enough through pores in the country rock to keep the increasing melt phase saturated, P_{H_2O} will subsequently fall as the melt fraction in a given source region increases with increasing T and the limited available water is dissolved and diluted by the melt. Evans and Nash (1978) stress that the magmas forming the flows and domes over the Mineral Mountains were water-undersaturated. The water-saturated conditions considered by Lebedev and Khitarov (1964) represent a special case that applies in natural systems only at low melt fractions near the beginning of melting. Otherwise use of their data may underestimate temperatures corresponding to the bulk resistivity of a granitic partial melt in the crust. One must know the absolute content of free H_2O in the rock since this will determine the volume and conductivity of the liquid phase.

The experiment of Lebedev and Khitarov (1964) also shows very high subsolidus granite conductivities for $P_{H_2O} > 4$ kb and temperatures around 600°C. In an attempt to explain this aspect of the data of Lebedev and Khitarov, geochemical reactions producing alteration minerals, which in turn supply exchangeable cations for the solution, were invoked to decrease bulk resistivity by Stanley et al (1977) and reaffirmed by Jiracek et al (1979). We cannot agree. Stanley et al (1977) do not say which alteration minerals are involved to lower the resistivity so we consider gibbsite, pyrophyllite, kaolinite, paragonite and muscovite as these are the commonest hydrous alteration products in granitic rocks (Helgeson et al, 1978). The existence of all these minerals except muscovite is ruled out as they are not stable under P_{H_2O} - T conditions as extreme as 4 km and 600°C (ibid.). The cation exchange capacity of muscovite is very small, less than 10 meq/100 gm (Grim, 1968, p 204), and hence would have to be volumetrically abundant in the sample of Lebedev and Khitarov (1964) to materially affect bulk resistivity. Experiment shows that two reaction mechanisms are available to form muscovite from granitic compositions. First, a stable assemblage of muscovite plus quartz may be produced at the water pressures and temperatures of interest by reaction of K-feldspar, pure water and corundum or aluminosilicate (kyanite or sillimanite). The latter Al-rich minerals are generally not observed in granites owing to the manner in which granitic liquids are initially formed and crystallized (Winkler, 1979, p 329-339). Hence, abundant secondary muscovite cannot form in this manner. Alternately, a reaction producing muscovite and quartz just from K-feldspar and water that conserves aluminum is possible (Helgeson et al, 1978). Hydrogen ion is consumed from the water in exchange for potassium ion. The waters used by Lebedev and Khitarov (1964) were fresh; unless enormous amounts of such water were circulated through their granite sample while the conductivity measurements were made, only trace amounts of muscovite would be produced.

As evidence for the formation of alteration minerals under deep crustal conditions, Stanley et al (1977) cite rock mechanics experiments in which water-pressurized (300 bars), compressed (500 bars), heated (400°C) and fractured granite permeabilities were observed to decrease by a factor of 50 over a period of 10 hours and by a factor of 500 after 10 days. This considerably lower water pressure and temperature lies within the stability fields of various clay minerals but, as in the case of muscovite, the lack of aluminum sources or abundant water containing H^+ disfavors the significant synthesis of these minerals. The dissolution of granitic minerals, particularly quartz, from sharp corners at fracture intersections and their precipitation on flatter fracture surfaces could reduce fracture permeabilities substantially. A reduction in permeability serves to localize water in the rock but, since no increase in molar volume occurs in dissolution and precipitation, no water overpressures occur to enhance partial melting, as also suggested by Stanley et al (1977). The results of Brace et al (1968) show the close inverse relation between permeability and bulk resistivity. Even if physiochemical conditions are suitable for the formation of hydrous alteration minerals, their formation will not generate H_2O overpressures; the total molar volume of the reactants, K-feldspar plus aluminosilicate plus water or K-feldspar plus water, is greater than that of the alteration products, muscovite plus quartz or clay minerals plus quartz. The breakdown of hydrous minerals to yield water rather than the formation of hydrous minerals by consuming water is responsible for increasing P_{H_2O} and the promotion of melting (Winkler, 1979, p 316-319).

As regards the data of Lebedev and Khitarov (1964), it is unjustifiable to consider the high, sub-solidus conductivities near

600°C and above 4 kb H_2O pressure in terms of an Archie's Law dependence or any other mixing law involving a conductive aqueous electrolyte in a resistive mineral matrix. Figure 35 indicates that above about 300°C, aqueous solution resistivities increase rather than decrease with temperature, and hence so would bulk rock resistivities controlled by this mechanism. Lebedev and Khitarov (1964) show subsolidus resistivities that decrease monotonically with increasing T. This leads us to suspect that some solid-state conduction mechanism involving silicates like K-feldspar, plagioclase and quartz under high temperatures and water pressures may be important. A possible mechanism for enhancing anhydrous mineral conductivities in the solid-state at high water activities is noted by us in a later discussion in this report on conduction mechanisms related to the regional resistivity profile.

As regards our magnetotelluric interpretation, no lateral resistivity inhomogeneities were resolved below a depth of 2-3 km on lines B-B' and C-C' in Figures 27 and 29 by the MT quantities ρ_{yx} and ϕ_{yx}. Presuming that a partially molten silicic magma chamber possesses a high resistivity contrast with the host rock, we may place limits upon its east-west dimensions. In our experience with transverse magnetic modeling of conductive, rectangular prisms, a sizeable anomaly in ρ_{yx} or ϕ_{yx} (>10% of background values) is not produced if the depth to the top of the prism is substantially greater than its width, regardless of the resistivity contrast. These are wide but definite limits to any such possible prism. It seems possible however that a magma chamber may be elongated in a roughly N-S direction parallel to regional Great Basin faulting trends. Basaltic intrusions that led to crustal melting may rise along such regional zones of weakness resulting in elongated magma chambers. In this instance, ρ_{xy} and ϕ_{xy} should be much more sensitive than ρ_{yx} and ϕ_{yx} to such a chamber. Anomalous behavior in ρ_{xy} and ϕ_{xy} over and to the southeast of the thermal anomaly area was noted earlier in the report implying localized deep structure. As in the case of the brine reservoir, interpretation of the effects of any high contrast deep heat source upon ρ_{xy} and ϕ_{xy} will require an algorithm that can model 3-D bodies in a layered earth and we cannot comment further on this aspect of the observations at this time.

Other geophysical evidence cited for a possible magma chamber at RHS is based upon gravity and teleseismic P-wave data. A prominent gravity saddle, of amplitude near 20 mgal (Carter and Cook, 1978), coincident with the Mineral Mountains pluton has been speculated as due to a low-density silicic magma chamber. However, the plutonic rocks themselves may have a density contrast of about 0.1 gm/cm^3 with the metamorphic and sedimentary rocks into which they were intruded, providing an alternate explanation for the saddle. Robinson and Iyer (1979) have modeled a N-S elongated zone of low velocity (5-7% contrast) centered under RHS extending from a depth of 5 km to the base of the crust that corresponds well in horizontal extent with the gravity saddle of Carter and Cook (1978). Robinson and Iyer (1979) prefer a zone of low fraction ($\sim$2%) partial melt in the crust over a 0.1 to 0.15 gm/cm^3 density contrast between the plutonic rocks and their denser host to explain their low velocity region since the extent of the low velocity anomaly does not correspond well with the outcrop area of the granitic rocks. In our opinion, however, there is no good reason to assume that the horizontal cross section of a batholith should remain effectively constant with depth. We conclude that there is no direct, independent, geophysical evidence, other than the thermal budget arguments given in the section on heat flow, geology and geochemistry of the thermal area, of a present-day igneous heat source beneath RHS, even though we have postulated the existence of one.

The Regional Resistivity Profile

Electrical Conduction Mechanisms Relevant to the Regional Profile: To correlate the regional resistivity profile of Figures 31 and 32 to the tectonic environment of the eastern Great Basin, we must turn to laboratory investigations of the electrical properties of earth materials under a variety of physiochemical conditions. Electrolytic conduction in aqueous pore fluids, solid-state semiconduction in minerals and electrolytic conduction in partial melts must be considered.

The experiments summarized by Brace (1971) covered a sufficiently wide temperature and pressure range to allow construction of a laboratory-derived regional resistivity profile for the Basin-Range province using the best estimate of the conductive geotherm known at that time (Roy et al, 1968). Electrolytic conduction in aqueous pore passages will dominate bulk rock resistivity in typical Basin-Range crust to depths of 15 km or so according to the Waxman-Smits relation (71). Though the pore electrolyte conductivity will rise by up to a factor of five as temperatures of 300°C are reached at several kilometers depth, the pressure-induced decrease in porosity causes bulk resistivity to increase from hundreds or thousands of Ω-m near the surface to conceivably several tens of thousands of Ω-m by 15 km depth.

As increasing temperatures are encountered with depth in the crust, solid-state semiconduction in minerals will come to dominate pore conduction in determining bulk resistivity. The fundamental modes of semiconductive transport relevant to silicates were discussed by Hamilton (1965). An Arrhenius exponential temperature dependence is invariably observed with activation energies generally increasing discontinuously with increasing temperature as different charge transport mechanisms dominate for different temperature ranges. Brace (1971) has compiled semiconduction experimental results by various workers on many dry rocks and minerals. Olhoeft (1979) has also released a partial translation of the work of Parkhomenko and Bondarenko (1972). The three orders of magnitude spread in conductivity at a given temperature exhibited by these publications is due to differences in mineralogy, variations in composition of a given mineral type and the diversity of experimental conditions.

Several authors (e.g. Duba et al, 1974; Schock et al, 1977) have shown that crystal conductivities may be significantly affected by the oxygen fugacity (f_{O_2}) of the crystal environment. The concentrations of conduction band electrons, valence band holes, electrons hopping between ions of different valence, variations in transition metal valence and anion and cation vacancies and interstitials are all potentially sensitive to f_{O_2} (Stocker, 1978). From crystalographic bonding and band-gap energy considerations, Stocker (1978) favors donation of electrons to the conduction band from oxidation of Fe^{+2} to Fe^{+3} as an important process in enstatite, although the laboratory results he discussed indicate more than one conduction mechanism is at work. Duba and Heard (1980) invoke oxygen defects as the major charge carriers in olivine. Although published research on semiconduction under controlled atmospheres has been restricted to minerals representative of the upper mantle, it is probable that oxidation state is a controlling variable for crustal minerals as well. The ambient f_{O_2} for the crust appears to lie close to the quartz-fayalite-magnetite (QFM) buffer, though this mineral assemblage itself is not responsible (Winkler, 1979, p 23). The great majority of minerals considered by Brace (1971) and Olhoeft (1979) were measured in air, conditions not representative of those in the crust. Even if experimental atmospheres are properly controlled, given the diverse mineralogy of the crust, it is problematic whether resistivity soundings which reflect semiconduction mechanisms will be useful for estimating temperature profiles in the crust. Though the conductivity ranges shown by Brace (1971) and Olhoeft (1979) are wide, they do indicate that for temperatures below 600°C, resistivities of dry minerals should lie in the hundreds or thousands of ohm-meters.

In the previous discussion on detectability of the deep heat source at RHS, we expressed disfavor with the concept of alteration reactions significantly enhancing bulk conductivities in the intermediate and deep crust. High values of P_{H_2O} and T may nevertheless enhance solid-state semiconduction in otherwise anhydrous crustal minerals by providing charged defects, such as H^+, OH^-, H_3O^+, etc., which enter the crystal lattice. Duba and Heard (1980 and written com.) invoke this mechanism to explain the order of magnitude increase in olivine conductivity, specifically below 1000°C, when the H_2-CO_2 buffer is used to control f_{O_2} as opposed to the CO-CO_2 buffer. Similar experiences concerning creep rates in silicates have been summarized by Goetze (1977). Duba (1976) shows that the effects of lattice disorder on the electrical conductivity of dry albite at slightly subsolidus temperatures may be substantial and it seems possible that incorporation of additional hydrous defects into solid minerals may occur by a mechanism analogous to that due to Burnham (1979b) for silicic liquids. Electrical conductivity measurements on anhydrous crustal minerals like K-feldspar, plagioclase and quartz as a function of P_{H_2O} and T (and f_{O_2}), corroborated by creep rate determinations, would establish the possible importance of such a mechanism in explaining low resistivity layers in stable crusts (e.g. Van Zijl, 1977; Connery et al, 1980), which cannot be considered in terms of dry mineral solid-state conduction or partial melting. Since $P_{H_2O} \approx P_{total}$ in typical crust at depth, downward increasing temperatures and water pressures may result in a rapid rise in hydrous defect concentrations incorporated into crystal lattices. Substantial depletions in water content such that $P_{H_2O} << P_{total}$ below 25 km or so, indicating the presence of high grade metamorphic terrains (Winkler, 1979, p 256-275), may determine the lower interface of such crustal layers. Enhanced conductivity in hydrous amphiboles has been alluded to by Feldman (1976), Jiracek et al (1979) and Connery et al (1980) as a cause of such low resistivity layers. As pointed out by these authors, there is a scarcity of experimental data on amphiboles, but the limited results shown by Olhoeft (1979) do not support the notion of high amphibole conductivities in the intermediate temperature range 350-650°C. As another possible means of enhancing solid state crustal conductivities, we propose that significant charged defect concentrations may be the result of active, ductile deformation and thermal metamorphism, such as are occurring in the eastern Great Basin. Deviatoric stresses are known to greatly enhance metamorphic reaction rates (Winkler, 1979, p 25).

Unlike crustal minerals, since olivine is by far the dominant mineral of the upper mantle, careful determinations of its conductivity as a function of T and f_{O_2} may be fruitful in calculating mantle geotherms using resistivity profiles estimated from surface measurements like MT. The ambient oxidation state of the upper mantle is in some dispute, heterogeneity in this variable is possible. Measurements of f_{O_2} for basaltic magmas originating in the mantle generally lie near the QFM buffer (Carmichael et al, 1974, p. 329; Haggerty, 1979; Evans and Nash, 1979). However oxidation state determinations on peridotite xenoliths in lavas and kimberlites show values that are much more reducing than QFM, generally lying near the magnetite-wustite or wustite-iron buffers (Sato, 1972; Sato, 1977; Arculus and Delano, 1980; Ulmer et al, 1980). A comparison of the olivine data of Duba et al (1974) for f_{O_2} near the QFM boundary with the data of Duba and Heard (1980) for f_{O_2} near the iron-wustite boundary using identical buffering agents (H_2-CO_2) shows the former results near a half an order of magnitude more conductive at a given temperature. One must be aware also that the trace amounts of H_2O which have received considerable study in peridotite partial melt experiments (Wyllie, 1979) may also contribute to lower solid-state mantle resistivities, as explained earlier in connection with crustal minerals.

In light of the Late Tertiary to Recent, predominantly alkalic basalt eruptions in the eastern Great Basin, it should not be surprising if partial melt distributions in the upper mantle contribute to our regional resistivity profile. As with aqueous electrolytic conduction in rock pores, interconnection of a low resistivity (1 Ω-m) melt phase in a residual crystal matrix of a resistivity generally greater by two or more orders of magnitude will determine bulk resistivity (Shankland and Waff, 1977). An Archie's Law dependence is hence expected. Conduction in basaltic liquids is ionic, involving mainly Mg, Fe and Ca, analogous to conduction in granitic melts discussed previously. Laboratory determinations of bulk resistivity may follow two basic approaches. First, this resistivity may be directly measured on a sample for P-T conditions between solidus and liquidus (e.g. Rai and Manghnani, 1978a). The porosity or percent melt phase correponding to a particular bulk resistivity is not considered. In the second approach, the conductivity of only the basaltic melt phase is measured. If an appropriate physical model of melt connectivity can be had, a liquid-solid mixing law will give bulk resistivity.

We follow the latter approach since published experimental data concerning it appear more comprehensive. Careful measurements at 1 atm pressure on dry basaltic liquids by Waff and Weill (1975) show these conductivities are only a slight function of composition and are virtually independent of f_{O_2}. The effect of total confining pressure on melt conductivities appears to be small (Shankland and Waff, 1977). The results of Waff and Weill (1975) are very similar to those of Rai and Manghnani (1978b), giving us confidence that we have a good handle on melt phase conductivity as a function of T, P_{total} and f_{O_2}. However, depolymerization and reduction in viscosity of basaltic melts, as in granitic melts, by small amounts of H_2O can be substantial (Carmichael et al, 1974, p 142-147) so that we are concerned about possible amplifications of conductivity by trace amounts of water. This effect must be ignored for the time being due to lack of published experimental data. Regarding liquid geometry, we believe the work of Bulau et al (1979) and Waff and Bulau (1979) has established a model of equilibrium melt connectivity at upper mantle pressures and temperatures. The formation of initial liquids is at triple edge junctions of peridotitic minerals and melt interconnection appears complete for fractions above 1%; the Hashin-Strickman upper bound for bulk conductivity is likely the most applicable liquid-solid mixing model (Waff, 1974). Such a distribution and interconnection of initial basaltic liquids has been supported by recent independent experiments (Vaughn and Kohlstedt, 1980; D. H. Eggler, 1980, pers. com.).

Physical Model for the Regional Profile: Our best-fit, crust and upper mantle resistivity profile appears in Figure 36 along with laboratory-derived estimates of bulk resistivity of relevant earth

Figure 36. Best-fit crust and upper mantle resistivity profile for RHS compared to physical model using aqueous electrolytic conduction in rock pores, solid state semiconduction in minerals and electrolytic conduction in partial melts in conjunction with thermally conductive geotherm using data of Bodell et al (1980). Dotted crustal bounds use the aqueous electrolytic and solid-state conduction data compiled by Brace (1971). The line of short dashes represents buffered olivine measurements of Duba et al (1974), though f_{O_2} (labeled here for T = 1200°C) may be higher here than typical mantle conductions. The curves of long dashes and long and short dashes correspond to melt fraction determinations of Wyllie (1971) and Ringwood (1975) along with liquid phase conductivity measurements of Waff and Weill (1975) and melt fraction geometry models of Waff (1974) and Waff and Bulau (1979). Individual numbers on the partial melting curves indicate percentage of liquid phase.

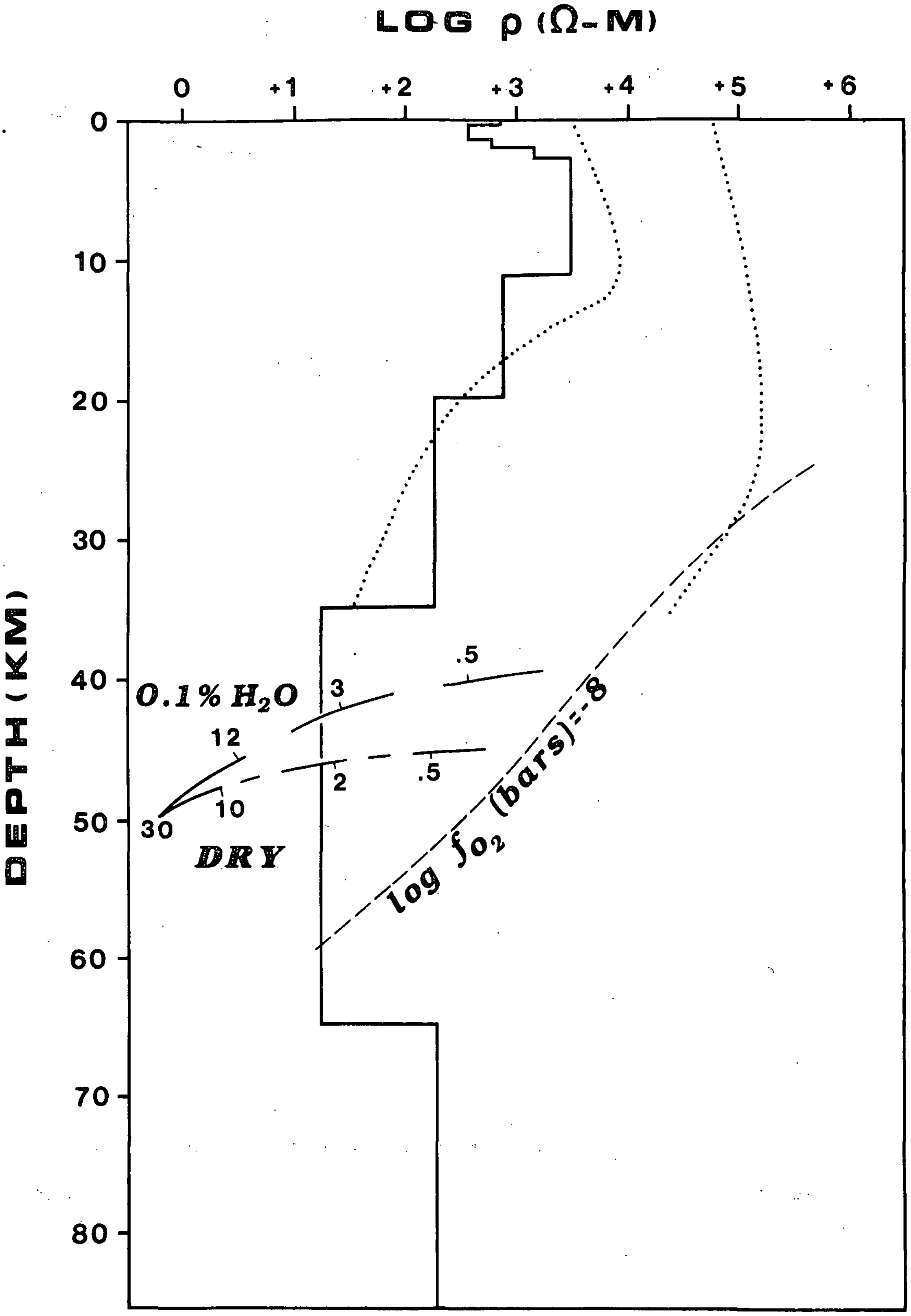
LOG ρ (Ω-M)
0
+1
+2
+3
+4
+5
+6
DEPTH (KM)
0
10
20
30
40
50
60
70
80
0.1% H₂O
3
.5
12
2
.5
10
30
DRY
log fo₂ (bars)=-8

materials. As stated before, the upper 2-3 km of this profile are relevant just to station 76-13 of line B-B' in Figure 27, below this the profile is common to all sites of lines B-B' and C-C' and presumably all other sites of RHS of Figure 1. Concerning the upper part of the profile, we note a rise in resistivity from a few hundred to around 3000 Ω-m by 3 km depth. In the discussion of horst-graben morphology, this initial rise in resistivity was mainly correlated to a pressure-induced closing of fractures. Our layered earth profile implies that increasing pressures from 3 to 11 km depth do not result in significant further increases in resistivity. In this regime, the Waxman-Smits relation (71) for aqueous electrolytic conduction in pores is applicable. The dotted curves lying at higher resistivities in the upper 10-15 km have been borrowed from the Basin-Range regional profile derived by Brace (1971) from laboratory experiments. In addition to the overall higher values, Brace's resistivities increase more gradually than in our best-fit model in this depth range. However, in view of the significance of fracture porosity in the upper 2 km at RHS and uncertainties in average porosity and groundwater chemistry, we are not greatly disturbed by this disagreement.

Over the depth interval 11 to 35 km in Figure 36, the regional resistivity decreases in a gradual manner from 3000 Ω-m to 200 Ω-m. We have modeled this decline with layers due to the nature of our algorithm but we believe the actual variation to be smooth. The dotted curves in Figure 36 using data of Brace (1971) have been extrapolated to 35 km and indicate that a solid-state semiconduction mechanism should be dominant. This lower section differs somewhat from the original derivation of Brace as we have incorporated an eastern Great Basin, thermally conductive geotherm determined from the information of Lachenbruch and Sass (1978) and Bodell et al (1980) as opposed to the cooler temperature profile of Roy et al (1968) used by Brace (1971). It should be emphasized that great uncertainties in this geotherm exist due to uncertainties in surface heat flow, the distribution of radiogenic heat production and the role of mass transfer in an actively extending lithosphere. The lower bound of Brace's estimate agrees well with our model. That our profile lies near the more conductive bound of Brace (1971) is not surprising; Brace considered only dry minerals under uniform pressures whereas we have pointed out the possible importance of extra, charged defects under conditions of high P_{H_2O}, active ductile extension and thermal metamorphism.

Seismic refraction experiments place the base of the crust in the RHS area at somewhat less than 30 km depth (Smith, 1978). Thus, the low resistivity layer of 20 Ω-m extending from 35-65 km depth must lie in the upper mantle. For comparison, the anticipated solid-state resistivity of a dominantly olivine mantle, using the Red Sea Peridot sample of Duba et al (1974) and the already defined conductive geotherm is shown as the sloping line of short dashes in Figure 36. f_{O_2} for this olivine sample was near the QFM buffer, its value in bars at 1200°C is labeled with the curve. This is perhaps too oxidizing compared to typical mantle, yet it is difficult to say if the olivine of Duba et al (1974) is representative of typical olivine crystals (see Schock et al, 1977). We therefore consider it no more than an approximate standard of solid-state conduction in the upper mantle of the eastern Great Basin by which we compare our regional profile. The solid-state values are generally more resistive than 20 Ω-m until a depth of 60 km is reached. Much more disagreeable however is the discrepancy in shapes between the solid-state and our best-fit profiles. In a mantle whose dominant mineralogical phase is olivine and whose temperatures increase downward, the Arrhenius temperature dependence does not allow rises in intrinsic resistivity with depth, which is why we considered such a geometry in the sensitivity tests of Figure 31.

It follows that we must entertain the idea of an isolated partial melt to explain the 20 Ω-m layer from 35-65 km depth. The conductivity of basaltic liquids, the Hashin-Strickman upper bound for bulk conductivity, and percent melt phase estimations as a function of P_{total} and T, and hence of depth, are combined with the thermally conductive geotherm. This gives the curves of expected bulk peridotite resistivity of long and long with short dashes in Figure 36. The upper curve pertains to peridotite containing 0.1 wt % H_2O and is based upon the percent melt fraction determinations of Green (1971) and Ringwood (1975). The lower curve pertains to dry peridotite and incorporates experimental work of Wyllie (1971, p 205; 1979). Both invoke an olivine solid-state matrix conductivity using the data of Duba et al (1974), though the matrix only affects bulk conductivities materially below 1% liquid. The small numbers adjacent to each curve mark the percent melt fraction and suggest that convergence in melt fraction for damp and dry peridotite does not occur until percentages in excess of ten are reached. However, as Wyllie (1979) states, these percent melt fractions, and particularly the role of trace amounts of H_2O, are not well determined by direct experimental evidence. Uncertainties in the percent melt fraction at a given pressure that correspond to a particular temperature would result in some upward or downward shift in the partial melt resistivity curves from where we place them. Nevertheless, the partial melt fraction that relates to a specified bulk resistivity is little affected; witness the value of 3% applicable at the 20 Ω-m layer for the damp peridotite as opposed to 2% for the dry case. We do worry that trace amounts of water in the source rock, which are preferentially incorporated into the melt, may importantly lower viscosity and thus resistivity of the liquid phase and bulk resistivity for a given melt fraction. As regards the apparently basal half-space, whose resistivity we believe is at least 200 Ω-m, a solid-state mechanism in the dominantly olivine rock is adopted with conduction in partial melts no longer figuring in bulk resistivity.

Tectonic Significance of the Regional Profile: Some important remarks may be made concerning tectonics and responses of other geophysical methods in the Great Basin from our physical model of the regional resistivity profile. For instance, the 5-15 km crustal low velocity zone of Smith (1978) cannot be correlated with a crustal low resistivity layer, as has been attempted by other authors in different geological environments (e.g. Connery et al, 1980). The 3000 Ω-m resistivity unit of Figure 36 lying in the depth range 3 to 11 km is in fact the closest medium. The increase in pore pressure advanced by

Smith (1978) is not inconsistent with these high resistivities.

The lack of isolated low resistivity layers in the crust also rules out the presence of a widespread region of interconnected silicic partial melt in this region. The eastern Great Basin thermally conductive geotherm we consider suggests that incipient fusion of granite in the presence of water may occur at depths of 20 km or so in this area; if such temperatures do exist, the absolute water content of this volume of the crust may be insufficient to produce enough melt phase for interconnection to occur. In addition, along the line of reasoning of Hyndman and Hyndman (1968) and Connery et al (1980), the lack of a high resistivity layer in the very deepest parts of this crust does not support the possibility of a zone of severe dehydration signaling high-grade, granulite facies metamorphism (Winkler, 1979, p. 256-275). However, if such a layer were less than about 5 km thick, it would likely not be resolvable on the basis of our measurements (Madden, 1971). Our regional profile for the intermediate to deep crust is consistent with downward increasing temperatures and one conductivity mechanism; solid-state semiconduction in minerals with a possible enhancement of charged defects due to ductile extension, thermal metamorphism and values of P_{H_2O} that increase monotonically with depth.

It has been explained that we have difficulty estimating lateral limits to the regional layering, though it is apparent that some exist. As a variation on the hypothesis of Smith and Shaw (1975), it is conceivable that basaltic igneous activity in the lower levels of the crust is distributed horizontally, perhaps as a collection of dikes and sills, rather than or in addition to an isolated dike-dike intrusion below RHS itself (see Lachenbruch and Sass, 1978). Such a distribution would result in a widespread zone of heating, on the order of several tens of kilometers wide. Though present-day heat flow measurements don't resolve patterns on this scale, the eastern Great Basin, which is 200-300 km wide, is anomalously hot and volcanically active. The hypothetical volume of higher temperature could be an important contributor of heat to RHS. Magnetotelluric measurements may not detect the intrusions per se but the heating of this part of the crust could increase its electrical conductivity due to a variety of solid-state mechanisms. We do not believe that crustal lateral inhomogeneities several tens of kilometers wide which may be roughly centered below RHS have seriously affected our estimation of the regional resistivity profile of Figure 36. In light of the possible significance of this heated region to the geothermal system, an additional two, E-W trending profiles of stations located about 50 km east and west respectively of RHS is recommended to describe the existence of the region.

We believe that the 20 Ω-m layer in Figure 36 extending from 35 to 65 km depth is a volume of low fraction ($\sim$2%) partial melt in peridotitic rocks of the upper mantle. It is however fair to question whether the upper and lower bounds to such a volume are abrupt, as our layered model presumes, or diffuse. It is well known that unless the liquid phase is highly interconnected, its contribution to bulk resistivity is negligible (Waff, 1974). Thus we expect a rapid drop in bulk resistivity as we cross the boundary from a region of incipient but poorly interconnected melting to a region of virtually complete interconnection. The difference in volume melt fractions between the two regions could be less than 1% (Waff and Bulau, 1979). We believe it is plausible in the absence of direct contradictory evidence to consider resistivity structure in the upper mantle corresponding to small degrees of partial melting as having fairly abrupt upper and lower bounds.

The acoustical indications for partial melting in the eastern Great Basin are not decisive. The relatively thin crust (down to 20 km, 28 km at RHS), lower values of upper mantle V_p (down to 7.4 km/s, 7.6 km/s at RHS), and active seismicity support the independent evidence of concentrated lithospheric extension and high heat flow, which are both conducive to partial melting (Smith, 1978). It is difficult nonetheless to resolve from refraction profiling variations in these seismic parameters whose horizontal extents are less than about 100 km, though regional P-wave delay studies resolved a volume of low velocity in the upper 200-300 km of the mantle of SW Utah including RHS (Smith, 1978). The interpreted upper mantle compressional and shear wave velocity structures of Archambeau et al (1969), Burdick and Helmberger (1978) and Priestley and Brune (1978) show a Great Basin low velocity zone residing from 65 to 170 km depth, which is much greater than that of the conductive layer we have advanced. We are not alarmed by this discrepancy; these seismic determinations apply for the Great Basin as a whole while we believe the profile of Figure 36 is relevant to a limited portion of its eastern margin. It is concluded that our regional profile and its corresponding physical model are not inconsistent with the seismic evidence to date.

We should also like to point out that the laboratory evidence for substantial anomalies in seismic velocity, especially V_p, in melt fractions of a few percent or less in the upper mantle is not clear (Goetze, 1977; Wyllie, 1979). It is specifically not apparent that the equilibrium melt distribution we described previously results in a measureable reduction in bulk modulus from that of the complete solid (Waff and Bulau, 1979). In view of the fact that 2% liquid phase will likely cause an order of magnitude reduction of bulk peridotite resistivity, we argue that electrical conductivity is a more reliable indicator of low fraction partial melts in a tectonically active area like the Great Basin than are the acoustical properties of such rock. In addition, though the MT observations at RHS are only sensitive to the regional resistivity profile at that location, we are reasonably confident that an E-W extension of these MT soundings could delineate horizontal variations in zones of conductive mantle partial melting in the Great Basin within some tens of kilometers. Both physical property contrasts and geometric limits of such tectonically significant zones should be resolved more accurately by magnetotellurics than by other geophysical methods including seismics.

A reservoir of magma in the upper mantle supporting the repeated basaltic and bimodal volcanic activity which has occurred in the eastern Great Basin for at least the past 10 m.y. is implied by the 20 Ω-m layer of Figure 36, although we do not address the question of how the liquid in a 2% partial melt separates from its host mineral matrix. The vast majority of Late Cenozoic basalt eruptions in western Utah were stated to be alkalic. Petrogenetic schemes based on worldwide occurrences of basalts indicate that alkalic melts form from low degrees of partial melting (<10%) in a depth range of 35 to 80 km (Ringwood, 1975; Wyllie, 1979). Leeman and Rogers (1970) interpret a depth range of 40 to 60 km for production of alkalic basalts in the Basin-Range which is in excellent agreement with the deep conductive layer we have modeled. That the Great Basin low velocity zone, which is generally believed by petrologists to be a region of incipient fusion producing basaltic melts (e.g. Wyllie, 1979), is substantially deeper than this does not distress us for the same reason as above; Late Cenozoic volcanic activity in this subprovince has been severely limited to its margins, which have been discussed as anomalous in several ways. Though we admitted that the horizontal bounds for our deep conductive layer are not resolved by the group of MT stations at RHS, surface manifestations of Quaternary volcanic activity suggest a N-S trending reservoir in the eastern Great Basin whose E-W extent is on the order of 200 km (Christiansen and McKee, 1978). It is proposed that this 35-65 km reservoir of magma would also supply the intermediate to deep crustal basaltic injections which heat and perhaps induce melting of crustal rocks resulting in deep igneous heat sources for high-temperature geothermal systems such as the Roosevelt Hot Springs, as per Smith and Shaw (1975).

The magmatic models of heat flow by Lachenbruch and Sass (1978) have shown that a thermally conductive geotherm will correctly describe the temperature profile associated with a given surface heat flow down to the region where partial melting exists; thereafter the geotherm is increasingly overestimated by a purely conductive model. The existence of this zone of partial melting hence casts additional suspicion on the applicability of a thermally conductive goetherm in this part of the eastern Great Basin to depths of more than about 40 km. The computation of a correction to the upper mantle geotherm using our resistivity profile of Figure 36 may be complicated somewhat by the presence of trace amounts (~0.1 wt %) of water; such water clearly reduces the temperatures of incipient fusion by over 100°C. Green (1971) and Ringwood (1975, p 143-157) hold that up to several percent melt phase can be produced below the dry peridotite solidus in the presence of 0.1% H_2O. Wyllie (1971, p 190-208) argues that no more than 1-2% melt is possible below the dry solidus under these conditions and that greater liquid production requires temperatures in excess of the dry melting curve. Much controversy has been generated by the opinions of Green and Ringwood (see Wyllie, 1979) and we adopt the dry solidus henceforth to represent temperatures that produce electromagnetically detectable partial melts of >2%.

We propose, considering the uncertainties in our regional profile and particularly the surface heat flow observations, that the top of our deep conductive layer and the expected intersection at 43 km of the dry peridotite solidus as in Figure 36 are in reasonable agreement. Hence, a conductive geotherm model appears to be an adequate description of the temperatures to a depth of about 35 km. This is of course ignoring the mass transfer contribution related to the actively extending, ductile deep crust, as described by Lachenbruch and Sass (1978), This contribution, although finite, is not resolved by the electrical and heat flow measurements we consider here. At 35 km depth at the bottom of the conductive layer, the dry peridotite solidus implies temperatures near 1250°C. At 65 km depth at the bottom of the conductive layer, the dry solidus implies temperatures near 1400°C, a higher temperature due to the increased pressure (Wyllie, 1979). It is reassuring to note that the mathematical model of bulk resistivity we use here gives temperatures that are in good agreement with those from direct bulk resistivity determinations on spinel lherzolite of Rai and Manghnani (1978a), provided a first-order correction to their data for pressure is made (Wyllie, 1979). The electromagnetically estimated temperature of about 1400°C at 65 km is in contrast to the much higher temperature in excess of 1700°C that would be predicted here by a purely conductive geotherm in the RHS area. If this purely conductive geotherm is imposed below 65 km depth, subsolidus temperatures are never reached again, in fact the peridotite liquidus of Wyllie (1979) would be encountered.

Concerning the relatively resistive basal half-space we have interpreted in Figure 36, the value of 200 Ω-m assigned was stated to be a lower limit due to the scarcity of very low frequency data points. If a temperature of 1400°C is assigned to the uppermost part of this resistive medium, the solid-state olivine data of Duba et al (1974) and Duba and Heard (1980) imply a resistivity range of 200 to 650 Ω-m, depending on the f_{O_2} adopted. Given the uncertainties, this slightly higher range is consistent with our data; accurate apparent resistivity and impedance phase estimates down towards 10^{-4} Hz would be required to substantiate the actual values at this depth. The above discussions lead us to believe that estimations of percent melt fraction, and temperature distributions in the upper mantle provided melting occurs, can also be made with confidence from resistivity structure. The interpretation of direct measurements of surface heat flow is susceptible to large uncertainties in regional and local hydrology as well as in the distribution of radiogenic heat production and mass transfer contributions in an extended and actively extending lithosphere.

Basin-Range to Colorado Plateau Transition: Late Cenozoic deformation has for the greater part bypassed the Colorado Plateau physiographic province with the exception of an overall uplift of about 3000 m occurring as recently as 5-10 m.y. ago (Stewart, 1978). Crustal thicknesses are around 45 km but upper mantle P-wave velocities do not seem very high, $\sim$7.8 km/s, though there is a lack of deep refraction results in this province (Smith, 1978). Concerning deeper structure, the interpretation of Archambeau et al (1969) places a low velocity zone at not much greater depth than for the Great Basin, around 80 km as compared to 65 km. This somewhat, but not severely, less developed LVZ is not quite consistent with the very low observed surface heat flow ($\sim$50 mWm^{-2}, Bodell et al, 1980). If uplift of the Colorado Plateau as recently as 10 m.y. ago was accompanied by an amplification of the existing LVZ as well as a sudden rise in heat flux in the upper mantle below the crust, little effect upon surface heat flow would be observable at the present day (Lachenbruch and Sass, 1978). Extensional deformation marks the transition of this province to the Rio Grande Rift on the east and the Great Basin on the west. The Great Basin border has been investigated geophysically using aeromagnetics (Shuey and others, 1973), refraction seismics (Smith, 1978) and heat flow (Bodell et al, 1980). All of these interpretations place the tectonic boundary some 50 km east of the physiographic boundary, or about 100 km east of the Roosevelt Hot Springs.

Magnetovariational anomalies reflecting lateral changes in upper mantle resistivity structure along a traverse from eastern Nevada to eastern Colorado were considered by Porath (1971b). The models that fit this variational data are widely non-unique pointing out the limited resolution of this technique. The data is, however, in agreement with a conductive axis beneath the Wasatch Fault Zone at depths near 30 km. The variational observations are hence supportive of the notion of a roughly N-S trending reservoir of partial melting in the eastern Great Basin. In the model favored by Porath (1971b), this conductive axis is superimposed upon the stepped transition from a relatively thick (45 to 190 km depth-extent), conductive Great Basin LVZ to a somewhat thinner (80 to 190 km depth extent), conductive LVZ beneath the Colorado Plateau. Though we must remain aware of model non-uniqueness, the upper mantle below the Colorado Plateau appears significantly more conductive from the variational data than does that of the stable Great Plains to the east, which suggests that present surface heat flows in the former may not represent thermal equilibrium. Porath (1971b) used solid-state semiconduction as the dominant mechanism explaining all features of his models, however our discourse indicates that partial melting is important at least in the eastern Great Basin.

To demonstrate a possible magnetotelluric response of the Basin-Range to Colorado Plateau transition, we consider the hypothetical construction in the lower section of Figure 37. The regional profile at RHS of Figure 36, with slight simplification in its upper 3 km, has been retained for the Basin-Range up to a presumed boundary 100 km to the east of RHS. A much more resistive profile is employed for most of the upper 65 km of the Colorado Plateau, reaching a 50:1 contrast over much of this interval This profile results from the combination of a rough geotherm based on the heat flow observations of Bodell et al (1980) with the lower resistivity bound of the solid-state compilation of Brace (1971), which we have found to correspond with the crustal portion of our regional profile of Figure 36. A decrease in resistivity contrast to 2:1 between the two provinces below 65 km is chosen given the uncertainties in the correctness of purely conductive geotherms with increasing depth and whether thermal equilibrium in the Colorado Plateau is in effect. While this is obviously a crude model, we believe it is sufficently representative and gives useful estimates of magnitudes and lateral extents of expected MT responses.

In the upper half of Figure 37, we show the TM mode apparent resistivity and impedance phase responses at 0.3 and 0.003 Hz. The amplitudes of the anomalies in both quantities is greater for the

Figure 37. Hypothetical 2-D resistivity structure representing Basin-Range to Colorado Plateau provincial transition. Structure for Basin-Range portion is based on the regional profile of Figure 36. The Roosevelt Hot Springs is located 100 km to the west of the boundary and is marked at the surface as RHS. Resistivity values of individual media are in Ω-m.

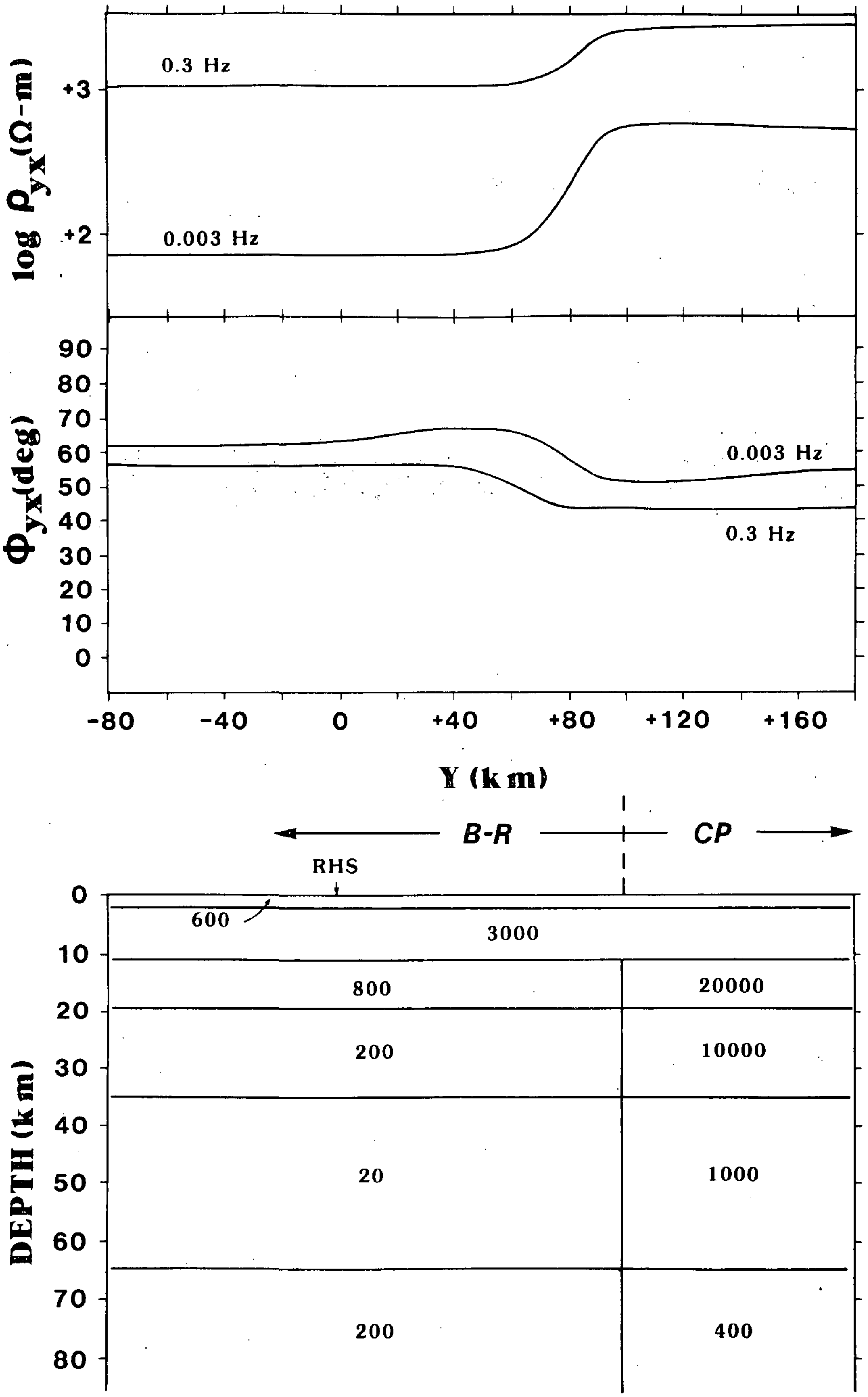
log ρ_{yx}(Ω-m)
+3
+2
0.3 Hz
0.003 Hz
Φ_{yx}(deg)
90
80
70
60
50
40
30
20
10
0
0.003 Hz
0.3 Hz
-80
-40
0
+40
+80
+120
+160
Y (km)
B-R
CP
RHS
DEPTH (km)
0
10
20
30
40
50
60
70
80
600
3000
800
20000
200
10000
20
1000
200
400

lower frequency than for the higher, particularly in ρ_{yx} which undergoes about an order of magnitude increase from the Basin-Range to the Colorado Plateau. It should be pointed out that the majority of the change of the MT response from one province to the other occurs on the conductive Basin-Range side to the west of the tectonic boundary over a distance of 60-80 km. Impedance phase variation across the transition at 0.003 Hz approaches 20°, higher than the difference between background phases for the two provinces. A negligible effect of the boundary is observed at the Roosevelt Hot Springs as was anticipated in the earlier discussion on sensitivity tests of the regional profile.

This exercise has shown that an easily detectable magnetotelluric response should accompany the progression of the Basin-Range to the Colorado Plateau. In fact, in light of this demonstration and our previous discourse on the regional profile at RHS, we believe a series of MT measurements along an ESE trend from central Nevada to near the Four Corners area, properly designed and modeled to account for severe upper crustal lateral inhomogeneities such as graben sediments, would contain much information on the tectonics and physical state of the Great Basin interior, its eastern margin and the Colorado Plateau. These have all been shown to be unique geological environments. The magnetotelluric method, with its sensitivity to amplitudes and phases of E-fields, should be the superior electrical technique for detailed resolution of intrinsic resistivity to depths of 300 km or more for frequencies as low as 10^{-4} Hz.

CONCLUSIONS OF MAGNETOTELLURIC MODELS OF THE ROOSEVELT HOT SPRINGS

The discourses on MT theory and 3-D model studies make clear the abundant deleterious consequences of polarization charge or current-gathering phenomena around finite strike length structures. These phenomena manifest themselves in sizeable distortions of the total electric field magnitude around 3-D structures to arbitrarily low frequencies regardless of the orientation of the incident field or the size of the body. The MT quantities most seriously affected by electric field distortions are the apparent resitivities and vertical admittance element magnitudes. Anomalies in tipper element magnitudes and the phases of all MT quantities diminish at low frequencies however; for small-scale features of a few hundred meters characteristic length and low to moderate resistivity contrasts, anomalies in these functions generally appear important only for frequencies in excess of about 1 Hz. This may encourage use of these latter MT functions in order to observe more directly the presence of larger and perhaps more interesting structure buried beneath small-scale geologic noise.

For structures of a scale much larger than the average station spacing at RHS, such as the valley sediments, a strong frequency dependence for all MT quantities persists to much lower frequencies than for geologic noise features such as surficial hydrothermal alteration, as expected from the discussion on EM scaling. Current-gathering in the valley is reflected in a regional distortion of the electric field affecting all stations at RHS to arbitrarily low frequencies. Exterior to the valley considered by itself, 3-D model studies indicate differences in ϕ_{xy} and ϕ_{yx} or in the shapes of ρ_{xy} and ρ_{yx} from those of any 1-D host enclosing the valley are effectively restricted to frequencies above 0.01 Hz. The severe anisotropy in ρ_a soundings caused by the valley along with abundantly distributed, small-scale geologic noise features has invalidated 1-D and 2-D TE interpretation approaches to accurate resistivity assessment over the entire frequency range of observations at the Roosevelt Hot Springs. However, centrally located profiles of ρ_{yx} and ϕ_{yx} across elongated, geometrically regular 3-D prisms may be interpreted successfully using a 2-D TM algorithm. When geologic noise exists over or around such elongated 3-D bodies, a uniform coordinate direction based upon MT strike estimators, for instance K_z-strike or ϕ-strike, not affected to arbitrarily low frequencies by current-gathering in such geologic noise or based upon regional geologic trends should be used to define which data may be treated as the TM mode.

That 1-D and 2-D interpretation schemes have very limited applicability in tectonically disturbed areas like the Basin-Range is born out by observed magnetotelluric data. In particular for geothermal systems in this province, current-gathering in the near-surface conductivity structure within a thermal area, created by the upward convection of hot brines with attendant hydrothermal alteration of earth materials, may itself be the cause of an apparent but false deep conductor beneath the system, suggestive of a partially molten heat source, if ρ_a soundings within this shallow structure are interpreted with a 1-D inverse algorithm. However, we have had some success with modeling observed values of ρ_{yx} and

ϕ_{yx}, where the x-axis is uniform and parallel to major Basin-Range faulting trends for all stations, for two E-W profiles, one north of the thermal area and one directly across it using our 2-D TM algorithm. From these two profiles, detailed estimates of resistivity structure related to horst-graben morphology were possible; as far as the majority of soundings at RHS are concerned, the Milford Valley graben sediments comprise the single most important lateral resistivity inhomogeneity with resistivities of clay-rich, sedimentary material as low as 1 Ω-m. A presumably three-dimensional effect however has resulted in a serious lack of fit of calculated to observed MT quantities for stations directly over the thermal area. A major change in the trend of the eastern margin of the valley sediments just to the west of the thermal area may be the cause of such a 3-D effect. Hence our search for any possible economic thermal reservoir to this point must be considered unsuccessful. Also, no lateral resistivity inhomogeneities below 3 km in the RHS area are apparently affecting our observed TM mode of data. Our search for a deep, presumably magmatic heat source driving the convecting system as well must be considered unsuccessful at this time. Unless at least one horizontal dimension of any conductive deep heat source is substantially greater than its depth, this source does not appear resolvable with MT measurements. Nevertheless given the preferred orientation of structure in the RHS area, the quantities ρ_{xy} and ϕ_{xy} in conjunction with vertical H-field functions, and not ρ_{yx} and ϕ_{yx} which we have modeled, should be most sensitive to the presence of any resistivity structure associated with the thermal reservoir or the deep heat source. Interpretation of these former quantities necessitates an algorithm that can model 3-D bodies in a layered earth, a routine towards which we are presently working.

Our greatest advance in the interpretation of the MT observations concerns the regional, apparently one-dimensional resistivity structure of the crust and upper mantle beneath RHS to depths in excess of 100 km. It is this regional profile which governs major features of the total magnetotelluric signature. Resistivities of a few hundred to a few thousand Ω-m in the upper 10-15 km of this crust are determined by aqueous electrolytic conduction in pore fluids and along mineral surfaces. Thereafter, the monotonic decrease in resistivities from 3000 to 200 Ω-m at about 30 km depth is consistent with downward increasing tempratures and one conductivity mechanism; solid-state semiconduction in minerals with a possible enhancement of charged defects due to ductile extension, thermal metamorphism and values of P_{H_2O} that increase monotonically with depth through the crust. No isolated conductive layers within the crust, possibly representing a widespread zone of interconnected silicic melt or abnormally high water contents, have been detected.

The 20 Ω-m layer existing from around 35 to 65 km depth is suggestive of a reservoir of ∿2% partial melt in peridotitic rocks of the upper mantle in the eastern Great Basin. This interpretation is in agreement with observed magnetovariational anomalies and petrogenetic modeling of worldwide and Basin-Range occurrences of alkalic basalts. This reservoir may have supported the repeated basaltic and bimodal volcanic activity in the eastern Great Basin for at least the past 10 m.y. It may also supply the intermediate to deep crustal basaltic injections which heat and perhaps induce crustal melting resulting in silicic igneous heat sources for high-temperature geothermal systems such as the Roosevelt Hot Springs. The presence of this conductive layer in the upper mantle also suggests that a thermally conductive geotherm model will adequately estimate temperatures through the crust but increasingly overestimates temperatures as one proceeds into the mantle, in particular giving temperatures over 1700°C at 65 km as opposed to something less than 1400°C implied by the dry peridotite solidus and the base of the conductive layer.

We believe that our discussions of the regional resistivity structure have shown that the magnetotelluric method, with its sensitivity to amplitudes and phases of E-fields, should be the superior technique for detailed resolution of intrinsic resistivity structure to depths of 300 km or more for frequencies as low as 10^{-4} Hz. A high bulk physical property contrast, the lateral resolution of such contrast and the mathematical relation of this bulk property to percent melt phase are more apparent for resistivity than for other geophysical indicators including acoustical ones. A series of MT measurements along an ESE trend from central Nevada to near the four state corners area, properly designed and modeled to account for severe upper crustal lateral inhomogeneities such as graben sediments, would contain much information on the tectonics and physical state of the Great Basin interior, its eastern margin and the Colorado Plateau. These three areas have been shown to be unique geological environments. Given the precise present-day determinations of the dry peridotite solidus, delineation of the limits of a partial melt in the upper mantle will also mean a delineation of the geotherm that is not possible from surface measurements of heat flow. This will include addressing the question of whether the Colorado Plateau is close to a thermal steady state.

APPENDIX A

Numerical Test of the Coupled Body Approximation

A number of conclusions in the section on MT theory are based upon an approximate analysis of the coupling between a large and a small structure. The applicability of this estimation to modeling structure at RHS is tested using the two body ensemble of Figure A-1. A small platelike conductor, 1800 m wide by 7 km long by 350 m thick with a depth to the top of 350 m, lies next to a much larger and less resistive feature 15 km wide by 36 km long by 1 1/2 km thick with a depth to the top of 1 1/2 km. The intrinsic resistivity of the smaller structure is 40 Ω-m while that of the larger is 3 Ω-m. Both reside in a half-space host of 400 Ω-m resistivity and the frequency of excitation is 0.3 Hz. The two features represent the area of near surface manifestations of resistivity contrast coincident with the thermal anomaly along with the Milford valley sedimentary fill.

Initially, the scattering current distribution in the small and large plates coupled together was calculated for two polarizations of incident electric field. Subsequently a numerical integration of equation (10) was performed over the scattering currents in just the small plate to obtain the secondary fields at the surface due only to the small body. These fields we will refer to as the "true" secondary fields due to the small body. Next, the scattering current distribution within and the secondary fields over the large body and small body were calculated separately, again for two polarizations of $\vec{E}_i^o$. The secondary fields calculated over the small body in the absence

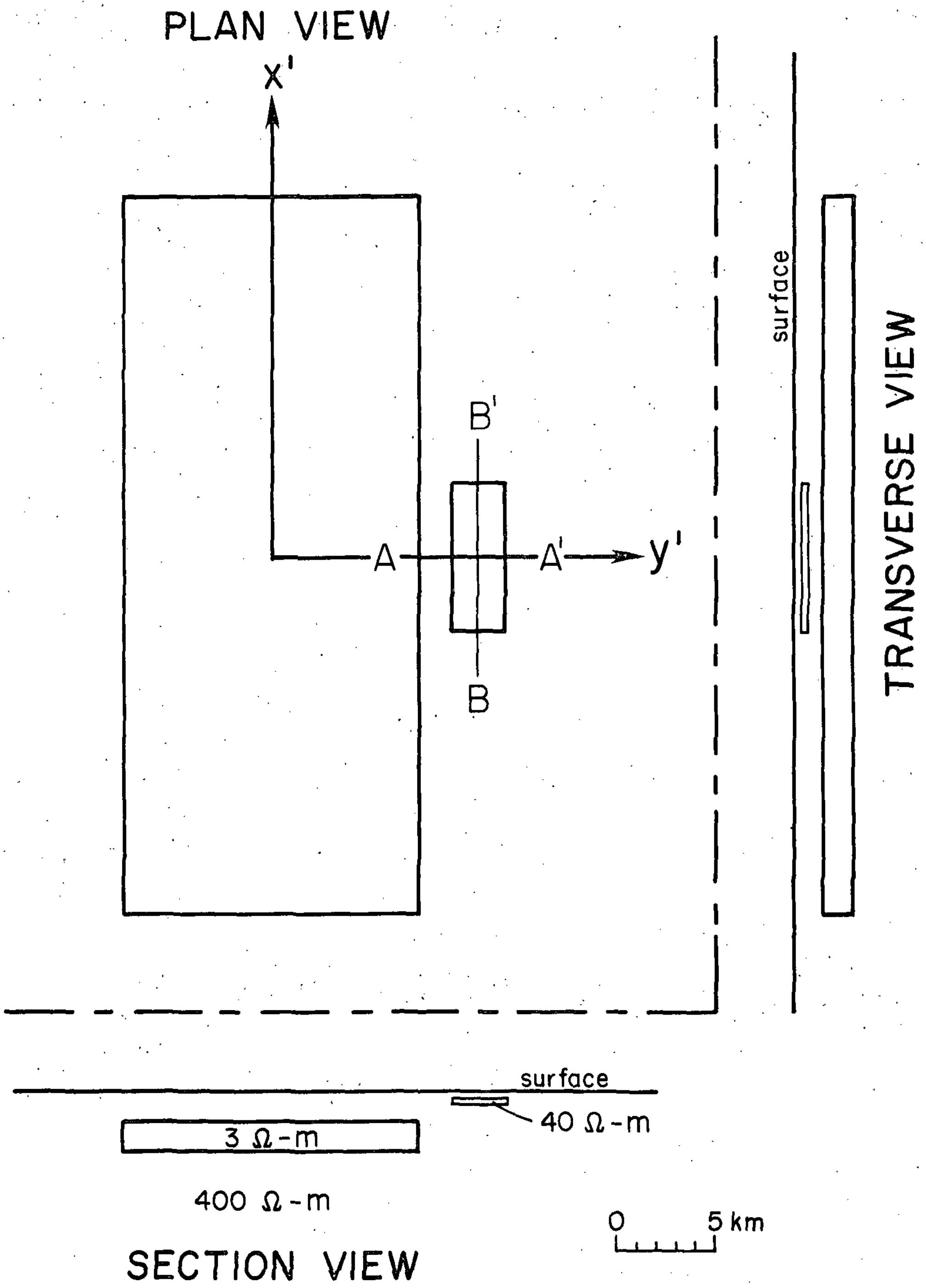

Figure A-1. Multiple body construction used to test the coupled body approximate analysis. Dimensions may be inferred from the scale or taken from main text.

of any larger feature will be referred to henceforth as the "unperturbed" fields. Finally, an estimate of the secondary fields scattered by the small body in the presence of the large one resulted from application of relation (58a) and (58b), these being referred to subsequently as the "estimated" fields. In essence, the total fields around the large body alone are used as approximate incident fields for the small body.

Plots of the true, unperturbed and estimated secondary fields at 0.3 Hz for the profiles A-A' and B-B' of Figure A-1 appear in Figures (A-2), (A-3) and (A-4). Results plotted in these diagrams are labeled according to whether the secondary field is electric or magnetic, whether it is in the x' or y' direction and whether it is due to the first or the second polarization of $\vec{E}_i^o$. For example, EXS1 refers to a secondary electric field oriented in the x'-direction due to the first polarization of incident field. The first polarization of $\vec{E}_i^o$ is directed along the x'-axis while the second is along the y'-axis. The comparison between true and estimated fields appears to be quite close for all components, nowhere is it worse than 10% and in general it is much better. Slight asymmetries in the true EYS2, HYS1 and HZS1 are due to slight asymmetries in the scattering current within the small plate, which in turn is due to its proximity to the large body. Due to our assumption of uniform source fields over the small body, the estimated fields must be symmetrical across axes of the small prism. Both the true and the estimated secondary fields disagree substantially with the unperturbed fields. Hence, a simple addition of the unperturbed fields over the small body alone to the total fields over

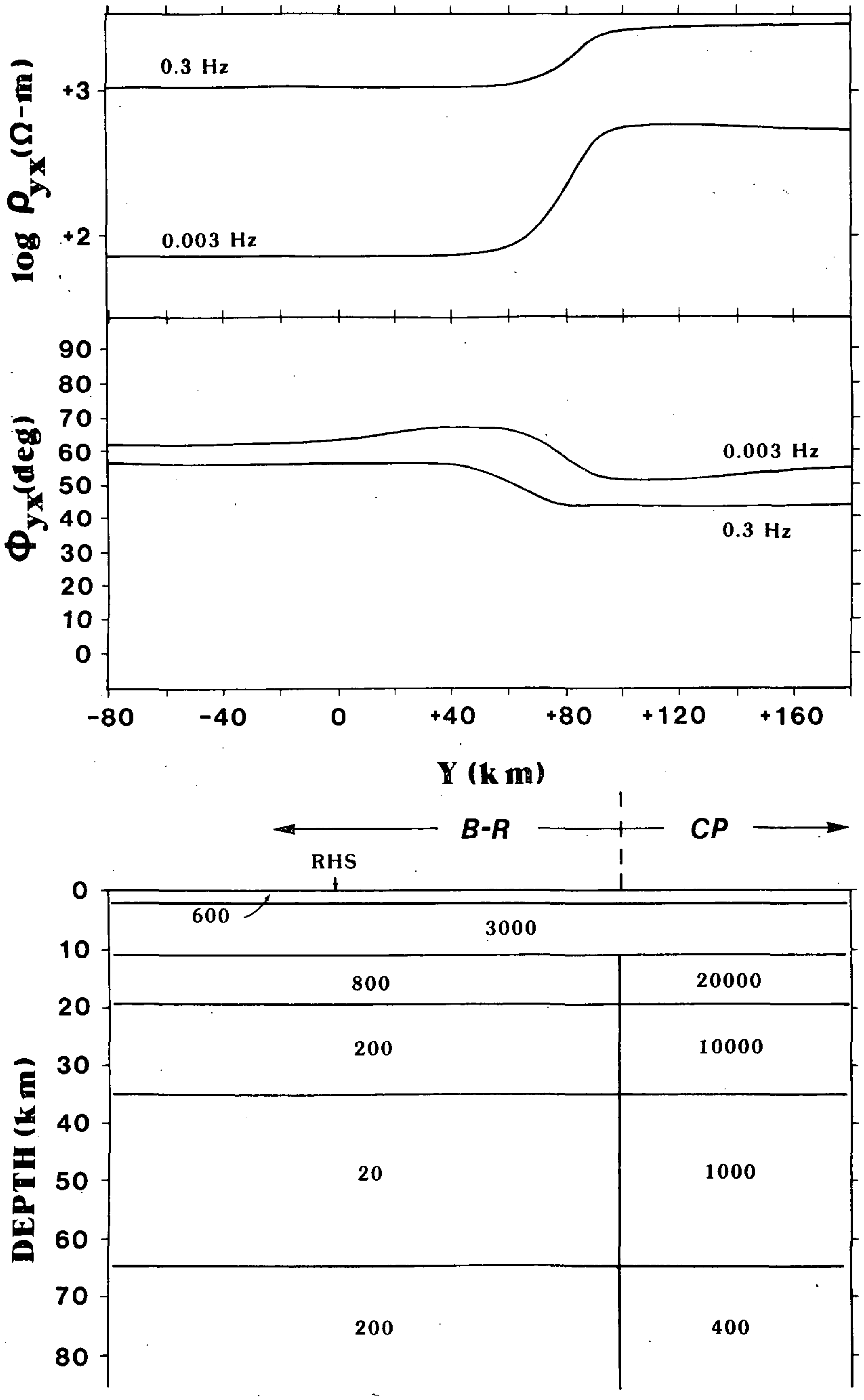
log ρ_{yx}(Ω-m)
+3
+2
0.3 Hz
0.003 Hz
Φ_{yx}(deg)
90
80
70
60
50
40
30
20
10
0
0.003 Hz
0.3 Hz
-80
-40
0
+40
+80
+120
+160
Y (km)
B-R
CP
RHS
DEPTH (km)
0
10
20
30
40
50
60
70
80
600
3000
800
20000
200
10000
20
1000
200
400

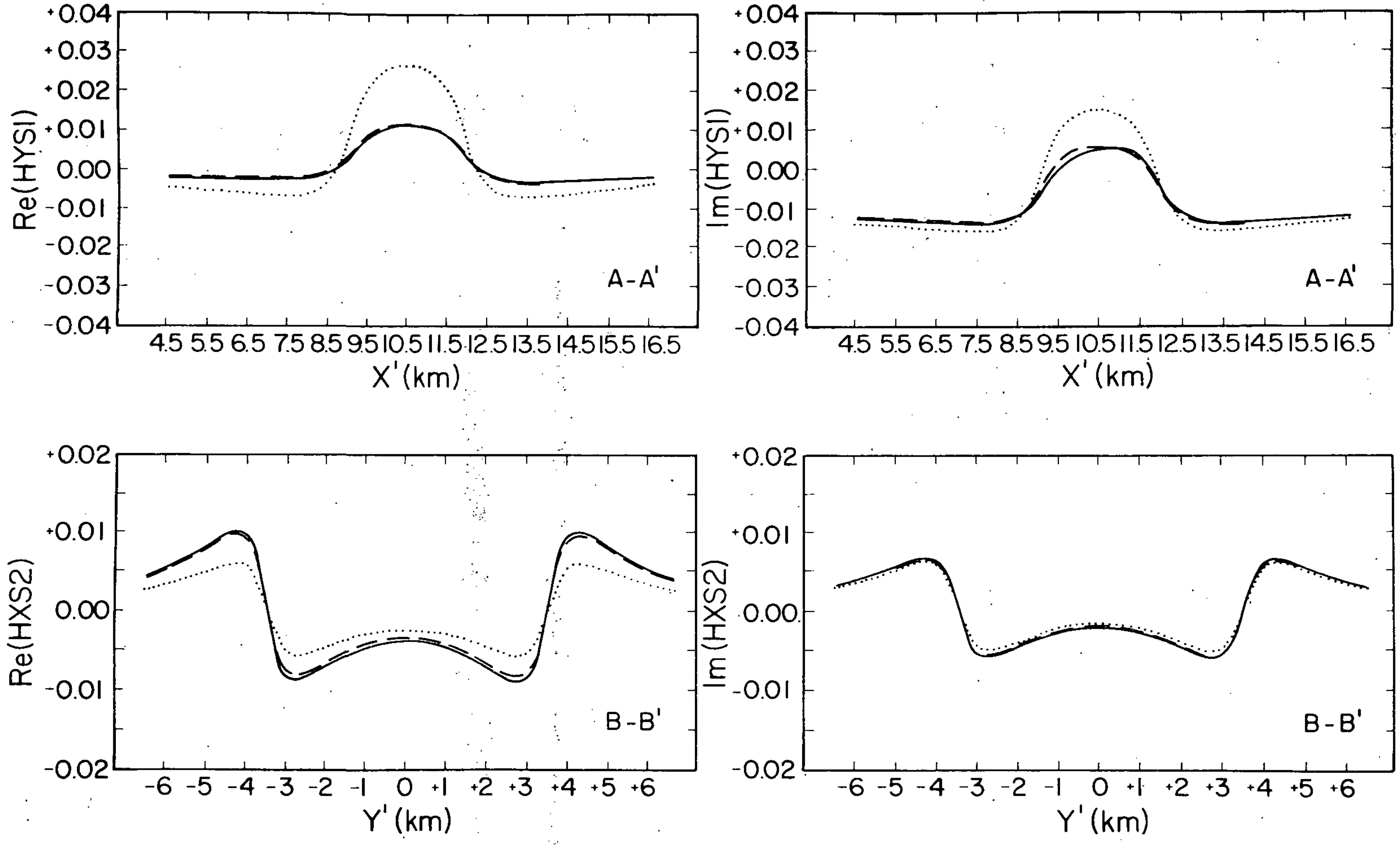

Figure A-3. Plots of true (solid lines), unperturbed (dotted lines) and estimated (dashed lines) secondary horizontal magnetic fields over the smaller plate like conductor. The values of the real and imaginary parts have each been normalized by $|\vec{H}_i|$.

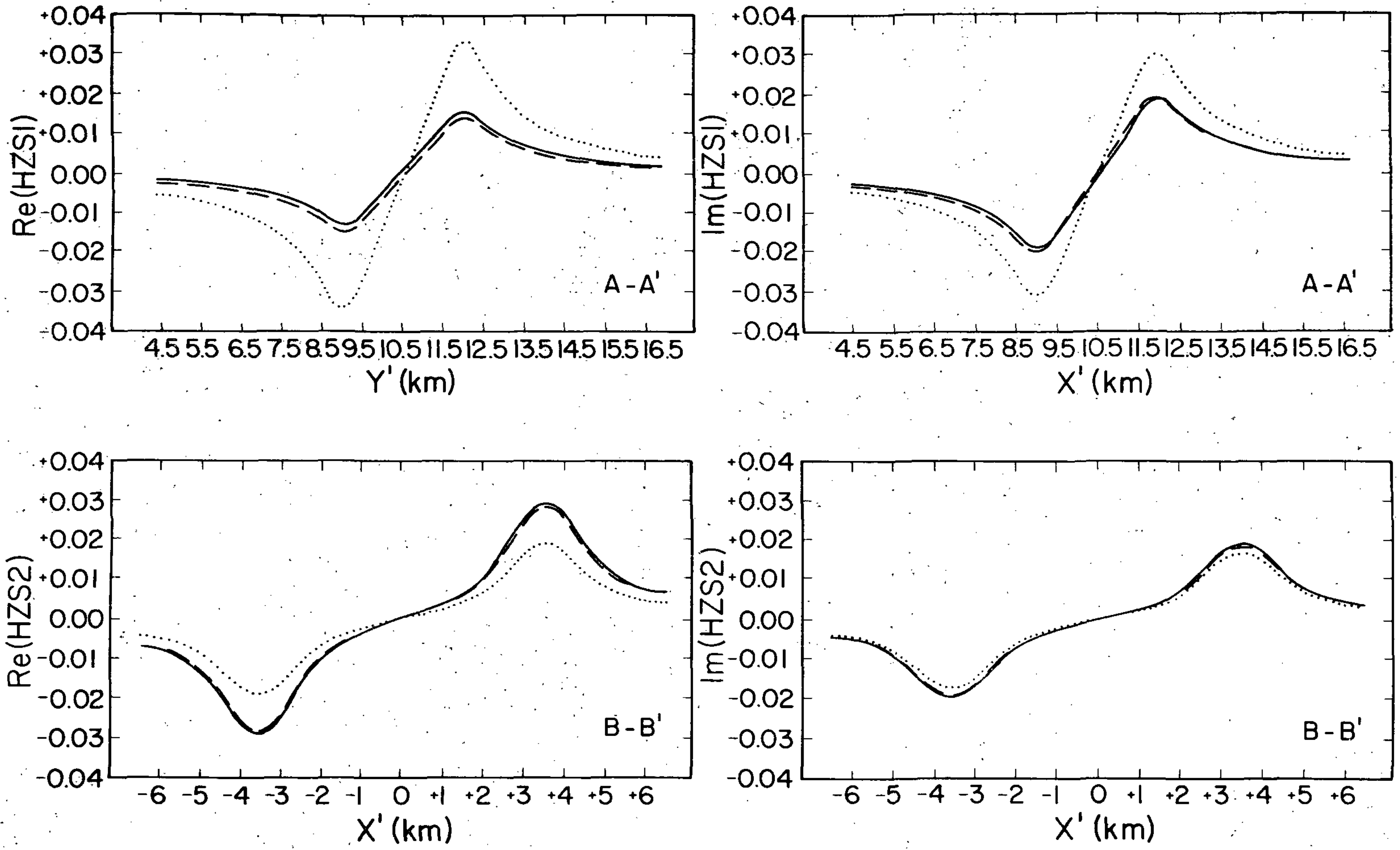

Figure A-4. Plots of true (solid lines), unperturbed (dotted lines) and estimated (dashed lines) secondary vertical magnetic fields over the smaller plate like conductor. The values of the real and imaginary parts have each been normalized by $|\vec{H}_i^o|$.

the large body alone will yield a relatively poor approximation to the total response of the two structures together. The total fields over the large body by itself in effect alter the magnitude and rotate the phase of the unperturbed fields over the small body to give the true secondary fields.

REFERENCES

Archambeau, C. A., Flinn, E. A., and Lambert, D. G., 1969, Fine structure of the upper mantle: J. Geop. Res., 74 (25), p. 5825-5865.

Arculus, R. J., and Delano, J. W., 1980, Intrinsic oxygen fugacities of the earth's mantle: a new approach and results for spinel peridotites: abstract of paper submitted to the Eleventh Lunar and Planetary Science Conference, March 17-21.

Atwater, T., 1970, Implications of plate tectonics for the Cenozoic tectonic evolution of western North America: Geol. Soc. Am. Bull., 81, p. 3513-3535.

Ballantyne, J. M., 1980, Geochemistry of sericite and chlorite in well 14-2 Roosevelt Hot Springs geothermal system and in mineralized hydrothermal systems: DOE/DGE topical report, 78-28391.a.1.6, 92 p.

Berdichevskiy, M. N., and Dmitriev, V. I., 1976, Distortion of magnetic and electrical fields by near-surface lateral inhomogeneities: Acta Geod., Geop. et Mont. Acad. Sci., 11, p. 447-483.

Bodell, J., Chapman, D. S., Clement, M. D., and Darling, R., 1980, Basin and Range-Colorado Plateau heat flow results from Utah: EOS Transactions, 61 (17), p. 363.

Boehl, J. E., Bostick, Jr., F. X., and Smith, H. W., 1977, An application of the Hilbert transform to the magnetotelluric method: Elec. Geo. Res. Lab. Rep., Univ. of Texas at Austin, 98 p.

Brace, W. F., 1971, Resistivity of saturated crustal rocks to 40 km based on laboratory measurements, In The Structure and Physical Properties of the Earth's Crust, ed. by J. G. Heacock, American Geophysical Union Mono. 14, p. 243-256.

Brace, W. F., Walsh, J. B., and Frangos, W. T., 1968, Permeability of granite under high pressure: J. Geop. Res., 73 (6), p. 2225-2236.

Bulau, J. R., Waff, H. S., and Tyburczy, J. A., 1979, Mechanical and thermo-dynamic constraints on fluid distribution in partial melts: J. Geop. Res., 84 (B11), p. 6102-6108.

Burdick, L. J., and Helmberger, D. V., 1978, The upper mantle P velocity structure of the western United States: J. Geop. Res., 83 (B4), p. 1699-1712.

Burnham, C. W., 1979a, Magmas and hydrothermal fluids, In Geochemistry of Hydrothermal Ore Deposits, ed. by H. L. Barnes, John Wiley and Sons, New York, p. 71-136.

_____, 1979b, The importance of volatile constituents, In The Evolution of the Igneous Rocks: Fiftieth Anniversary Perspectives, ed. by H. S. Yoder, Jrs., Princeton Univ. Press, p. 439-482.

Carmichael, I. S. E., Turner, F. J., and Verhoogen, J., 1974, Igneous Petrology: McGraw-Hill International Series in the Earth and Planetary Sciences, McGraw-Hill, Inc., 739 p.

Carter, J. A., and Cook, K. L., 1978, Regional gravity and aeromagnetic surveys of the Mineral Mountains and vicinity, Millard and Beaver Counties, Utah: DOE/DGE Final Report, 77-11, Univ. of Utah, 178 p.

Cathles, L. M., 1977, An analysis of the cooling of intrusives by groundwater convection which includes boiling: Econ. Geol., 74, p. 804-826.

Christiansen, R. L., and McKee, E. H., 1978, Late Cenozoic volcanic and tectonic evolution of the Great Basin and Columbia intermontane region, In Cenozoic Tectonics and Regional Geophysics of the Western Cordillera, ed. by R. B. Smith and G. P. Eaton, Geo. Soc. Am. Mem. 152, p. 283-311.

Connery, J. E. P., Nekut, A., and Kuckes, A. F., 1980, Deep crustal electrical conductivity in the Adirondacks: J. Geop. Res., 85 (B5), p. 2603-2614.

Duba, A., 1976, Are laboratory electrical conductivity data relevant to the Earth? Acta Geod., Geop. et Mont. Acad. Sci., 11, p. 485-495.

Duba, A., Heard, H. C., and Schock, R. N., 1974, Electrical conductivity of olivine at high pressure and under controlled oxygen fugacity: J. Geop. Res., 79 (11), p. 1667-1673.

Duba, A., and Heard, H. C., 1980, Effect of hydration on the electrical conductivity of olivine: EOS Transactions, 61(17), p. 404.

Eaton, G. P., Wahl, R. R., Prostka, H. J., Mabey, D. R., and Kleinkopf, M. D., 1978, Regional gravity and tectonic patterns: their relation to Late Cenozoic epeirogeny and lateral spreading in the Western Cordillera, ed. by R. B. Smith and G. P. Eaton, Geol. Soc. Am. Mem. 152, p. 51-91.

Evans, S. H., Jr., 1977, Geologic map of the central and northern Mineral Mountains, Utah: Tech. rep., 77-7, DOE/DGE contract EY-76-S-07-1601, Univ. of Utah.

_____, 1980, Summary of potassium/argon age dating - 1979: Topical Rep., 78-28392.a.11.1, DOE/DGE contract DE-AC07-78-ET-28392, Univ. of Utah, 23 p.

Evans, S. H., Jr., and Nash, W. P., 1978, Quaternary rhyolite from the

Mineral Mountains, Utah: DOE/DGE Topical Report, 77-10, Univ. of Utah, 59 p.

_____, 1979, Petrogenesis of xenolith-bearing basalts from southeastern Arizona: Am. Mineralogist, 64, p. 249-267.

Feldman, I. S., 1976, On the nature of conductive layers in the earth's crust and upper mantle: Geoelectric and Geothermal Studies, KAPG Geophysical Monograph, ed. by A. Adam, Akademiai Kiado, p. 720-730.

Gamble, T. D., Goubau, W. M., and Clarke, J., 1979, Magnetotellurics with a remote reference: Geophysics, 44 (1), p. 53-68.

Gertson, R. C., and Smith, R. B., 1979, Interpretation of a seismic refraction profile across the Roosevelt Hot Springs, Utah and vicinity: DOE/DGE Topical Report 78-1701.a.3, Univ. of Utah, 116 p.

Goetze, C., 1977, A brief summary of our present day understanding of the effect of volatiles and partial melt on the mechanical properties of the upper mantle, In High Pressure Research; Applications in Geophysics, ed. by M. H. Manghnani and S. Akimoto, Academic Press Inc., New York, p. 3-23.

Grant, F. S., and West, G. F., 1965, Interpretation Theory in Applied Geophysics: McGraw-Hill Book Company, Toronto, 584 p.

Green, D. H., 1971, Composition of basaltic magmas as indicators of conditions of origin: application to oceanic volcanism: Phil. Trans. Royal Soc. London, A 268, p. 707-725.

Grim, R. E., 1968, Clay Mineralogy: McGraw-Hill International Series in the Earth Sciences, 695 p.

Haggerty, S. E., 1978, The redox state of planetary basalts: Geop. Res. Letters, 5(6), p. 443-446.

Hamilton, R. M., 1965, Temperature variation at constant pressures of the electrical conductivity of periclase and olivine: J. Geop. Res., 70 (2), p. 5679-5692.

Harrington, R. F., 1961, Time-Harmonic Electromagnetic Fields: McGraw-Hill Electrical and Electronic Engineering Series, McGraw-Hill Book Company, New York, 480 p.

Helgeson, H. C., Delaney, J. M., Nesbitt, H. W., and Bird, D. K., 1978, Summary and critique of the thermodynamic properies of rock-forming minerals: Am. Jour. Sci. 278-A, 229 p.

Hintze, L. F., 1973, Geologic History of Utah: Brigham Young Univ. Geology Studies, 20, pt. 3, 181 p.

Hohmann, G. W., 1975, Three-dimensional induced polarization and electromagnetic modeling: Geophysics, 40 (2), April 1975, p. 309-324.

Hohmann, G. W., and Ting, S. C., 1978, Three-dimensional magnetotelluric modeling: DOE/DGE Final Report, 77-15, Earth Sciences Lab., Univ. of Utah Research Institute, 48 p.

Hyndman, R. D., and Hyndman, D. W., 1968, Water saturation and high electrical conductivity in the lower continental crust: Earth and Plan. Sci. Letters, 4, p. 427-432.

Jenkins, G. M., and Watts, D. G., 1968, Spectral Analysis and Its Application: Holden-Day Series in Time Series Analysis, Holden-Day Inc., 525 p.

Jiracek, G. R., Ander, M. E., and Holcombe, H. T., 1979, Magnetotelluric soundings of crustal conductive zones in major continental rifts, In Rio Grande Rift: Tectonics and Magmatism, ed. by R. E. Riecker, American Geophysical Union, p. 209-222.

Jones, F. W., and Vozoff, K., 1978, The calculation of magnetotelluric quantities for three-dimensional conductivity inhomogeneities, Geophysics, 43 (6), p. 1167-1175.

Jupp, D. L., and Vozoff, K., 1976, Discussion on "The magnetotelluric method in the exploration of sedimentary basins" by K. Vozoff: Geophysics, 41 (2), p. 325-328.

_____, 1977, Two-dimensional magnetotelluric inversion: Geop. J. R. Ast. Soc., 50, p. 333-352.

Kemmerle, K., 1977, On the influence of local anomalies of conductivity at the earth's surface on magnetotelluric data: Acta Geod., Geop. et Mont. Acad. Sci., 12, p. 177-181.

Kilty, K., Chapman, D. S., and Mase, C. W., 1979, Forced convective heat transfer in the Monroe Hot Springs geothermal system: J. of Volcanology and Geothermal Res., 6, p. 257-277.

Kurtz, R. D., and Garland, G. D., 1976, Magnetotelluric measurements in eastern Canada: Geop. J. R. Ast. Soc., 45, p. 321-347.

Lachenbruch, A. H., and Sass, J. H., 1978, Models of an extending lithosphere and heat flow in the Basin and Range province, In Cenozoic Tectonics and Regional Geophysics of the Western Cordillera, ed. by R. B. Smith and G. P. Eaton, Geol. Soc. Am. Mem. 152, p. 209-250.

Lajoie, J., and West, G. F., 1976, The electromagnetic response of a conductive inhomogeneity in a layered earth: Geophysics, 41 (6A), p. 1133-1156.

Larsen, J. C., 1975, Low frequency (0.1-6.0 cpd) electromagnetic study of the deep mantle electrical conductivity beneath the Hawaiian Islands: Geop. J. R. Ast. Soc., 43, p. 17-46.

_____, 1977, Removal of local surface conductivity effects from low frequency mantle response curves, Acta Geod. Geop. et Mont. Acad. Sci., 12, p. 183-186.

Lebedev, E. B., and Khitarov, N. I., 1964, Dependence on the beginning of melting of granite and the electrical conductivity of its melt on high water vapor pressure, Geokhimiya, 3, p. 195-201.

Leeman, W. P., and Rogers, J. J. W., 1970, Late Cenozoic alkali-olivine basalts of the Basin-Range province, USA: Contr. Min. and Petrol., 25, p. 1-24.

Lipman, R. W., Rowley, P. D., Mehnert, H. H., Evans, S. H., Jr., Nash, W. P., and Brown, F. H., 1978, Pleistocene rhyolite of the Mineral Range, Utah: geothermal and archeological significance: J. Res. of U.S.G.S., 6 (1), p. 133-147.

Lorrain, P., and Corson, D. R., 1970, Electromagnetic Fields and Waves: W. H. Freeman and Co., San Francisco, 706 p.

Madden, T. R., 1971, The resolving power of geoelectric measurements for delineating resistive zones within the crust, In The Structure and Physical Properties of the Earth's Crust, ed. by J. G. Heacock, American Geophysical Union Mono. 14, p. 95-105.

Mower, R. W., and Cordova, R. M., 1974, Water resources of the Milford area, Utah, with emphasis on groundwater: State of Utah Department of Natural Resources Technical Publication no. 43, 106 p.

Nielson, D. L., Sibbett, B. S., McKinney, D. B., Hulen, J. B., Moore, J. N., and Samberg, S. M., 1978, Geology of Roosevelt Hot Springs KGRA, Beaver County, Utah: DOE/DGE Topical Report, 78-1701.b.1.1.3, Earth Sciences Lab., Univ. of Utah Research Institute, 120 p.

Olhoeft, G. R., 1979, Electrical conductivity from 200 to 1000°C for 264 rocks and minerals from data in Parkhomenko and Bondarenko, 1972: U. S.G.S. Open File Rep. 79-846, 23 p.

Parkhomenko, E. I., and Bondarenko, A. T., 1972, Electroconductivity of rocks at high pressures and temperatures: Moscow, Nauka Press, 279 p.

Parry, W. T., Ballantyne, J. M., Bryant, N. L., and Dedolph, R. E., 1980, Geochemistry of hydrothermal alteration at the Roosevelt Hot Springs thermal area, Utah: Geochim. et Cosmochim. Acta, 44, p. 95-102.

Petrick, W. R., Pelton, W. H., and Ward, S. H., 1977, Ridge regression inversion applied to crustal resistivity sounding data from South

Africa: Geophysics, 42 (5), p. 995-1005.

Porath, H., 1971a, A review of the evidence on low-resistivity layers in the earth's crust, In The Structure and Physical Properties of the Earth's Crust, ed. by J. G. Heacock, American Geophysical Union Mono. 14, p. 127-144.

_____, 1971b, Magnetic variation anomalies and seismic low-velocity zone in the western United States: J. Geop. Res., 76 (11), p. 2643-2648.

Price, A. T., 1973, The theory of geomagnetic induction: Phys. of the Earth and Plan. Int., 7, p. 227-233.

Priestly, K., and Brune, J., 1978, Surface waves and the structure of the Great Basin of Nevada and western Utah: J. Geop. Res., 83 (B5), p. 2265-2272.

Quist, A. S., and Marshall, W. L., 1968, The electrical conductances of aqueous sodium chloride solutions from 0 to 800°C and at pressures to 4000 bars: J. Phys. Chem., 71 (2), p. 684-703.

Rai, C. S., and Manghnani, M. H., 1978a, Electrical conductivity of ultramafic rocks to 1820 Kelvin: Phys. of the Earth and Plan. Int., 17, p. 6-13.

_____, 1978b, Electrical conductivity of basalts to 1550°C, In Proc. of Chapman Conference on Partial Melting in the Earth's Upper Mantle, ed. by H. J. B. Dick, Oreg. Dep. Geol. Miner. Ind., Bull. 96, p. 219-232.

Reddy, I. K., Rankin, D., and Phillips, R. J., 1977, Three-dimensional modeling in magnetotelluric and magnetic variational sounding: Geop. J. R. Ast. Soc., 51, p. 313-325.

Rijo, L., 1977, Modeling of electric and electromagnetic data: Ph.D. Thesis, Dept. of Geology and Geophysics, Univ. of Utah.

Ringwood, A. T., 1975, Composition and Petrology of the Earth's Mantle: McGraw-Hill International Series in the Earth and Planetary Sciences, McGraw-Hill Inc., 618 p.

Robinson, R., and Iyer, H. M., 1979, Delineation of a low-velocity body under the Roosevelt Hot Springs geothermal area, Utah, using teleseismic P-wave data: U.S.G.S. unpublished manuscript, 26 p.

Rohrs, D. T., and Bowman, J. R., 1980, A light stable isotope study of the Roosevelt Hot Springs thermal area, southwestern Utah: Topical Rep., 78-1701.a.1.5., DOE/DGE contract ET-28392-46, 89 p.

Rooney, D., and Hutton, V. R. S., 1977, A magnetotelluric and magnetovariational study of the Gregory Rift Valley, Kenya: Geop. J. R. Ast. Soc., 51, p. 91-119.

Roy, R. F., Blackwell, D. D., and Birch, F., 1968, Heat generation of plutonic rocks and continental heat flow provinces: Earth and Plan. Sci. Letters, 5, p. 1-12.

Sandberg, S. K., and Hohmann, G. W., 1980, Controlled-source audiomagnetotellurics in geothermal areas: Topical rep. DOE/ID/12079-5, DOE/DGE contract DE-AC07-80ID12079, Univ. of Utah, 85 p.

Sato, M., 1972, Intrinsic oxygen fugacities of iron-bearing oxide and silicate minerals under low total pressure, In Studies in Mineralogy and Precambrian Geology, ed. by B. R. Doe and D. K. Smith, Geol. Soc. Am. Mem. 135, p. 289-307.

_____, 1977, Oxygen fugacity of the mantle environment, In Proc. of Chapman Conference on Partial Melting in the Earth's Upper Mantle, ed. by H. J. B. Dick, Oreg. Dep. Geol. Miner. Ind. Bull. 96, p. 309.

Schock, R. N., Duba, A. G., Heard, H. C., and Stromberg, H. D., 1977, The electrical conductivity of polycrystalline olivine and pyroxene under pressure, In High Pressure Research, Applications in Geophysics, ed. by M. H. Manghnani and S. Akimoto, Academic Press Inc., New York, p. 39-51.

Shankland, T. J., and Waff, H. S., 1977, Partial melting and electrical conductivity anomalies in the upper mantle, J. Geop. Res., 82 (33), p. 5409-5417.

Shuey, R. T., Schellinger, D. K., Johnson, E. H., and Alley, L. B., 1973, Aeromagnetics and the transition between the Colorado Plateau and Basin Range provinces: Geology, 1, p. 107-111.

Smith, L., 1980, A model study of the regional hydrogeologic regime, Roosevelt Hot Springs, Utah: Topical Rep., 78-28392.a.10, DOE/DGE contract DE-AC07-78ET/28392, 30 p.

Smith, R. B., 1978, Seismicity, crustal structure and intraplate tectonics of the interior of the western Cordillera, In Cenozoic Tectonics and Regional Geophysics of the Western Cordillera, ed. by R. B. Smith and G. P. Eaton, Geol. Soc. Am. Mem. 152, p. 111-144.

Smith, R. L., and Shaw, H. R., 1975, Igneous-related geothermal systems, In Assessment of Geothermal Resources of the United States - 1975, U.S.G.S. Circ. 726, p. 58-83.

Souririjan, S., and Kennedy, G. C., 1962, The system H_2O-NaCl at elevated temperatures and pressures: Am. J. Sci., 160, p. 115-141.

Stanley, W. D., Boehl, J. E., Bostick, Jr., F. X., and Smith, H. W., 1977, Geothermal signficance of magnetotelluric soundings in the Snake River Plain -- Yellowstone region: J. Geop. Res., 82 (17), p. 2501-2514.

Stewart, J. H., 1978, Basin and Range structure in western North America: a review, In Cenozoic Tectonics and Regional Geophysics of the western Cordillera, ed. by R. B. Smith and G. P. Eaton, Geol. Soc. Am. Mem. 152, p. 1-31.

Stocker, R. L., 1978, Variation of electrical conductivity in enstatite with oxygen partial pressure: comparison of observed and predicted behavior: Phys. of the Earth and Plan. Int., 17, p. 34-40.

Stodt, J. A., 1978, Documentation of a finite element program for solution of geophysical problems governed by the inhomogeneous 2-D scalar Helmholtz equation: NSF Program Listing and Documentation, Univ. of Utah, 66 p.

Stratton, J. A., 1941, Electromagnetic Theory: McGraw-Hill International Series in Pure and Applied Physics, McGraw-Hill Book Company, 615 p.

Swift, G. M., Jr., 1967, A magnetotelluric investigation of an electrical conductivity anomaly in the southwestern United States, Ph.D. Thesis, Massachusetts Institute of Technology, 211 p.

Ting, S. C., and G. W. Hohmann, 1980, Integral equation modeling of three-dimensional magnetotelluric quantities, manuscript accepted for publication in Geophysics.

Tripp, A. C., Ward, S. H., Sill, W. R., Swift, Jr., C. M., and Petrick, W. R., 1978, Electromagnetic and Schlumberger resistivity sounding in the Roosevelt Hot Springs KGRA: Geophysics, 43 (7), p. 1450-1469.

Ulmer, G. C., Rosenhauer, M., and Woermann, E., 1980, Glimpses of mantle redox conditions: EOS Transactions, 61 (17), p. 413.

Van Blaedel, J., 1961, Some remarks on Green's dyadic for infinite space: IRE Trans. on Antennas and Propagation, 9, p. 563-566.

Van Zijl, J. S. V., 1977, Electrical studies of the deep crust in various tectonic provinces of southern Africa, In The Earth's Crust, ed. by J. G. Heacock, American Geophysical Union Mono. 20, p. 470-500.

Vaughn, P. J., and Kohlstedt, D. L., 1980, Solid-melt structure in a partially melted olivene-basalt mixture: EOS Transactions, 61 (17), p. 396.

Vozoff, K., 1972, The magnetotelluric method in the exploration of sedimentary basins: Geophysics, 37 (1), p. 98-141.

Waff, H. S., 1974, Theoretical considerations of electrical conductivity in a partially molten mantle and implications for geothermometry: J.

Geop. Res., 79 (26), p. 4003-4010.

Waff, H. S., and Bulau, J. R., 1979, Equilibrium fluid distribution in an ultramafic partial melt under hydrostatic stress conditions: J. Geop. Res., 84 (B11), p. 6109-6114.

Waff, H. S., and Weill, D. F., 1975, Electrical conductivity of magmatic liquids: effects of temperature, oxygen fugacity and composition: Earth and Plan. Sci. Letters, 28, p. 254-260.

Wannamaker, P. E., 1978, Magnetotelluric investigations at Roosevelt Hot Springs and Mineral Mts area, Utah: Topical rep., 78-1701.a.6.1, DOE/DGE contract EY-78-S-07-1701, Univ. of Utah, 53 p.

Ward, S. H., 1967, Electromagnetic theory for geophysical application: Mining Geophysics, v. II, Tulsa, SEG, pp. 10-196.

Ward, S. H., Parry, W. T., Nash, W. P., Sill, W. R., Cook, K. L., Smith, R. B., Chapman, D. S., Brown, F. H., Whelan, J. A., and Bowman, J. R., 1978, A summary of the geology, geochemistry and geophysics of the Roosevelt Hot Springs thermal area, Utah. Geophysics, 43 (7), p. 1515-1542.

Ward, S. H., and Sill, W. R., 1976, Dipole-dipole resistivity surveys, Roosevelt Hot Springs KGRA: NSF Technical Report, 76-2, Univ. of Utah, 29 p.

Waxman, M. H., and Smits, L. T. M., 1968, Electrical conductivities in oil-bearing shaly sands: Trans. Soc. Pet. Eng., 243, p. 107-123.

White, D. E., 1957, Magmatic, connate and metamorphic waters: Bull. Geol. Soc. Am., 68, p. 1659-1682.

White, D. E., Muffler, L. J. P., and Truesdell, A. H., 1971, Vapor-dominated hydrothermal systems compared with hot-water systems, Economic Geology, 66, p. 75-97.

Wilson, W. R., and Chapman, D. S., 1980, Thermal studies at Roosevelt Hot Springs, Utah: manuscript accepted for publication in Geophysics.

Winkler, H. G. F., 1979, Petrogenesis of Metamorphic Rocks: Fifth Ed., Springer-Verlag Inc., New York, 348 p.

Word, D. R., Smith, H. W., and Bostick, F. X., Jr., 1971, Crustal investigations by the magnetotelluric impedance method, In The Structure and Physical Properties of the Earth's Crust, ed. by J. G. Heacock, American Geophysical Union Mono. 14, p. 145-167.

Wyllie, P. H., 1971, The Dynamic Earth: Textbook In Geosciences, John Wiley & Sons, New York.

Wyllie, P. H., 1977, Crustal anatexis: an experimental review: Tectonophysics, 43, p. 41-71.

Wyllie, P. H., 1979, Petrogenesis and the physics of the earth, In The Evolution of the Igneous Rocks: Fiftieth Anniversary Perspectives, ed. by H. S. Yoder, Jr., Princeton Univ. Press, p. 483-520.

Yusas, M. R., and Bruhn, R. L., 1979, Structural fabric and in-situ stress analyses of the Roosevelt Hot Springs KGRA: Topical Rep., 78-1701.a.6.5.1, DOE/DGE contract DE-AC07-78ET28392, 62 p.